Cellular Mechanisms of Neurovascular Breakdown and Neuronal Dysfunction Following Recurrent *Group A Streptococcus* Infections in Mice

Maryann Priscilla Platt

Submitted in partial fulfillment of the
requirements for the degree of
Doctor of Philosophy
under the Executive Committee
of the Graduate School of Arts and Sciences

COLUMBIA UNIVERSITY

2019

ABSTRACT

Cellular Mechanisms of Neurovascular Breakdown and Neuronal Dysfunction Following Recurrent *Group A Streptococcus* Infections in Mice

Maryann Priscilla Platt

Autoimmune encephalitic (AE) syndromes represent a unique manifestation of autoimmunity: the immune system recognizes the brain as foreign, and interferes with neuronal function. AE syndromes are characterized by hallucinations, paranoia, anxiety, seizures, and autonomic dysregulation, and progress over a matter of weeks as autoantibodies targeting the brain bind more densely to their CNS targets. Development of AE has been linked to peripheral tumors and infection, both of which provide structural mimetics to CNS antigens to incite an immune response in the periphery. How these brain-specific antibodies reach the CNS remains unclear.

In rare cases, Group A *Streptococcus* (GAS, *S. pyogenes*) infections can cause CNS autoimmunity targeting the basal ganglia, termed post-infectious basal ganglia encephalitis (BGE), manifesting as motor (Sydenham's chorea) and psychiatric (Pediatric Autoimmune Neuropsychiatric Disorders Associated with Streptococcus, PANDAS) abnormalities. In a mouse model of post-infectious BGE, we have shown that repeated intranasal GAS infections generate robust T cell infiltration into the CNS, concomitant with blood-brain barrier breakdown, microglial activation, and olfactory synapse degradation. However, the different T cell subtypes that enter the brain, how they enter the CNS, and their relative contributions to neural dysfunction and neuroinflammation remain unclear.

Th17 lymphocytes are heavily implicated in many autoimmune diseases, but whether the inflammatory post-infectious BGE reaction induces functional deficits in odor processing and requires Th17 lymphocytes was unknown. Here we demonstrate that mice lacking Th17

lymphocytes display both reduced BBB impairment and antibody infiltration. Furthermore, multiple GAS infections induce deficits in odor processing, which are partially ameliorated in Th17 cell-deficient mice. Notably, neuroinflammation and some excitatory synaptic loss persist, due to the presence of Th1 lymphocytes. Th17 lymphocytes are therefore critical for both selective CNS entry of autoantibodies and neural circuit impairment during post-infectious BGE. By examining the regulation of chemokine ligand expression in GAS-inoculated mice, we determined that CCL20/CCR6 and CCL2/CCR2 chemokine axes are implicated in T cell homing to the brain. In chemokine receptor mutant *CCR6*$^{+/-}$ *CCR2*$^{-/-}$ mice, T cell infiltration is reduced by 86.2%, and microglial activation is blunted. These findings suggest that CCL2/CCR2 and CCL20/CCR6 signaling may play a role in T cell homing to the brain and neuroinflammation. Finally, we first assessed behavioral and immune responses in two different GAS exposure models. It was clear that while behavioral abnormalities can be recapitulated in mice given subcutaneous GAS immunizations, this elicited relatively weak cellular and humoral immune responses. By contrast, mice given intranasal GAS inoculations showed minimal behavioral abnormalities, but elicited robust humoral and cellular immune responses.

Taken together, these data demonstrate the pivotal role of Th17 lymphocytes in brain pathology and olfactory processing deficits after recurrent GAS infections in our mouse model. Our intranasal inoculation model supports the conclusion that post-infectious BGE is autoimmune in nature, despite the absence of behavioral symptoms in this model. Using multiple mouse models of post-infectious BGE may allow us to study distinct facets of disease pathogenesis. Finally, this work underscores the ability of T cells to incite neuroinflammation, provides a useful clinical diagnostic test in olfactory functional assessments, and lends support to T cell immunotherapy strategies in patients with post-infectious BGEs.

Table of Contents

List of Figures

Chapter 1

Chapter 2

Chapter 3

Chapter 4

Appendix A

Appendix B

Appendix C

Acknowledgements

First and foremost, I would like to thank my PI, Dritan Agalliu, for being probably the most fitting mentor I could have asked for to oversee my PhD. He has been patient with me over the years, taking time to troubleshoot experiments and discuss future directions, even with my less-than-fully-baked ideas. Dritan provided technical support at the bench, worked late nights in lab alongside me, and encouraged me to take advantage of scientific and cultural opportunities both in Irvine and New York. He has been so supportive scientifically and on a personal level as a mentor, and I admire his commitment to training all of his mentees. I am a better scientist and a better person for having been in Dritan's lab. I rate him a 5/5 for PhD mentors.

I thank my thesis committee members, Drs. Ai Yamamoto, Lori Zeltser, and Christoph Kellendonk, for mentoring me over the years and taking me in after moving from UC Irvine to Columbia. Their helpful comments and constructive criticism helped shape this project for many years, and I am grateful they were willing to serve on my committee for its duration. Many thanks go to Dr. Zsuzsanna Fabry for serving as my outside examiner.

For their moral support and help in troubleshooting, I'd like to acknowledge members of the Agalliu lab since my joining in 2014: Drs. Sarah Lutz, Justin Lengfeld, Jenna Mazzoni, Saptarshi Biswas, and Azzurra Cottarelli; Sanjid Shahriar, Francesca Garretti, Joon Kim, Julian Smith, and Sigal Kofman. For preliminary studies on the PANDAS project, I'm indebted to Dr. Erica Smith, Martin Hsu, and Daniel Knowland, whose analyses built the legs for this thesis to stand on. Ongoing work by Tyler Cutforth, Nicole Ampatey, and Charlotte Wayne drives this project forward in both the human and mouse worlds, connecting bench to bedside. I look forward to reading about your discoveries in the coming years. I am grateful for the undergraduates I trained that contributed to this project: Alison Tran at UC Irvine, Fernanda Pacheco at Columbia

University, and Sarah Chaudhry at Barnard College performed hours of sectioning and imaging for their own projects.

Thank you to our collaborators at the University of Minnesota and at Duke University. Work done in collaboration with Pat Cleary and Thamotharampillai Dileepan at the University of Minnesota forms the basis for many of these studies. I'd also like to thank the Franks lab at Duke University for taking me in not once, but twice, and letting me monopolize their recording rig for seven total weeks. Kevin Bolding, Shiva Nagappan, Brendan Ryu, and of course Kevin Franks provided invaluable guidance on surgery, recording, and data analysis, as well as moral support. Many, many thanks go out to my friend Dr. Rachel Cohen in Durham for housing me and sharing her running routes, oatmeal, chicken, and sweet potatoes.

I'm grateful to the faculty and students in the INP program at UC Irvine, as well as my adopted cohort at Columbia that took me in after the move to New York, and to the many neuroscientist friends I gained on both coasts. Encouragement from previous mentors, especially Drs. Lynn Westling, Jan Naegele, Glenn Rosen, and Al Galaburda, helped me see that science was a viable path, and inspired me to follow my passion.

For all their support and love, I'd like to thank my parents, my family, and my friends. My parents helped me move across the country not once, but twice for graduate school, listened to my elevator pitch at every holiday for six years, and provided unending moral support. To my nieces and nephew, may you follow your passions as far as they lead you; to my sister Katy and my brother Jody, thank you for blazing every trail, constantly striving for more, and for showing me what pursuit of passion looks like. To my boyfriend Tony, thank you for your bottomless support, for relishing victories large and small, and for talking about every single piece of data here.

I would like to thank the parents of children with PANDAS who initially motivated me to work on this project. Your perseverance in the face of adversity is truly inspiring; I am honored to have played a small role in your lives. Finally, I have to thank the thousands of research animals who sacrificed their lives for this work, and for basic and translational research that underlies all scientific discovery.

Preface

Portions of Chapter 1 in this work, describing immune dysfunction in autoimmune encephalitis and routes of antibody and immune cell entry into the CNS, are slightly expanded from a published review article [50]. Text, figures, and tables from this article have been updated to include discoveries since its publication.

Some experiments were performed partly or wholly by other members of the Agalliu laboratory. Erica Smith generated cDNA from olfactory tissues, performed the chemokine screen, and assisted with behavioral analysis for intranasally inoculated mice. Erica also performed some initial pilot experiments in the *CCR6* and *RORγt* mouse lines not described here. Charlotte Wayne performed flow cytometry for cytokine expression in lymphocytes from $CCR2^{+/-}$ and $CCR2^{-/-}$ mice. Nicole Ampatey performed much of the Th17 analysis in $CCR6^{+/-}$ and $CCR6^{-/-}$ mice. Alison Tran helped perform much of the behavioral and histological analyses on subcutaneously immunized mice; Fernanda Pacheco analyzed BBB breakdown after subcutaneous GAS immunization, and Sarah Chaudhry analyzed the spatial distribution of the Th17 fraction in the brain, in addition to frequent assistance with genotyping.

This work is dedicated to my two whip-smart, independent grandmothers: Mary Anne and Priscilla.

Chapter 1: Autoimmune encephalitic syndromes linked to infection

Antibody-mediated autoimmunity, the hallmark of several autoimmune encephalitides (AE) that produce movement and psychiatric disorders, is triggered when antibodies recognize neuronal epitopes as foreign proteins [1-3]. Antibodies directed against neuronal antigens can arise in the periphery when target proteins are expressed ectopically on tumor cells. Disease pathogenesis involves three distinct facets: (1) peripherally-generated antibodies capable of cross-reacting with neuronal epitopes (2) that gain access to targets in relevant brain regions, and (3) persist in the brain long enough to perturb neuronal signaling. First, what initially prompts autoantibody formation remains a subject of debate, although there is evidence for two main triggers: (1) ectopic neuronal epitope expression on peripheral tumors, and (2) infectious triggers. The link between N-methyl-D-aspartate (NMDA) receptor encephalitis and ovarian teratoma ectopically expressing the antigen was reported in the initial description of NMDA receptor encephalitis (NMDARE) by Dalmau and colleagues [4, 5]. AE has also been linked to various infectious triggers, including bacteria, viruses, fungi, and other parasites [6-8]. However, an underlying infection is the causative agent in only a small fraction of AE cases; in about half of cases, a trigger is never identified [9-11].

The blood-brain barrier (BBB) normally excludes circulating antibodies from the CNS [12, 13], including CNS autoantibodies present in a minority of the healthy population, from cross-reacting with neuronal epitopes [14, 15]. While mechanisms of BBB breakdown are well-documented in multiple sclerosis (MS), a CNS autoimmune disease where T cells and antibodies target CNS myelin, it is unclear how peripherally-generated antibodies against brain targets might access the parenchyma in AE. Spatial breakdown of the BBB may be indicative of symptomatology, given that antibody reaction with different brain structures will produce different

symptom spectra (e.g., motor symptoms induced by BBB breach and antibody deposition in the basal ganglia vs memory impairment from barrier leakage in the hippocampus). Frank brain lesions are uncommon in AE patients, and brain imaging is frequently normal [16-18], indicating that antibody entry into the brain may result from dynamic, short-term BBB breakdown.

Many AE syndromes have protracted clinical courses because of frequent misdiagnosis. It remains unclear how peripherally-generated autoantibodies persist in the CNS; either the BBB is continually permeable to antibodies allowing their continuous entry into the CNS, or plasma cells or B cells enter the brain parenchyma and synthesize antibodies intrathecally, allowing for disease persistence after resolution of BBB breakdown. In this chapter, I will review development and disease course in various AE disorders, what we have learned from animal models of AE, and the role of the immune system in these and other CNS autoimmune diseases.

1.1 Autoimmune encephalitis disease pathogenesis

Since the discovery of NMDA receptor linkage to AE by Dr. Josep Dalmau in 2007, many clinical and basic discoveries have defined some general mechanisms of these diseases [2, 4, 5, 17-21]. Dozens of neuronal targets of AE have been identified since, and most of these proteins are surface receptors involved in synaptic transmission (**Figure 1.1**). However, some targets are expressed intracellularly. In about half of all AE cases, an underlying cause is never identified. These cases are typically diagnosed as limbic encephalitis (LE) with no demyelinating lesions, or acute disseminated encephalomyelitis (ADEM), an inflammatory demyelinating disease with no infectious involvement. Diagnosis of autoimmune or other encephalitides can be challenging, and symptoms can involve a host of motor, affective, and psychological presentations. A subacute onset of fever, confusion, personality changes, memory loss, seizures, and weakness or ataxia are

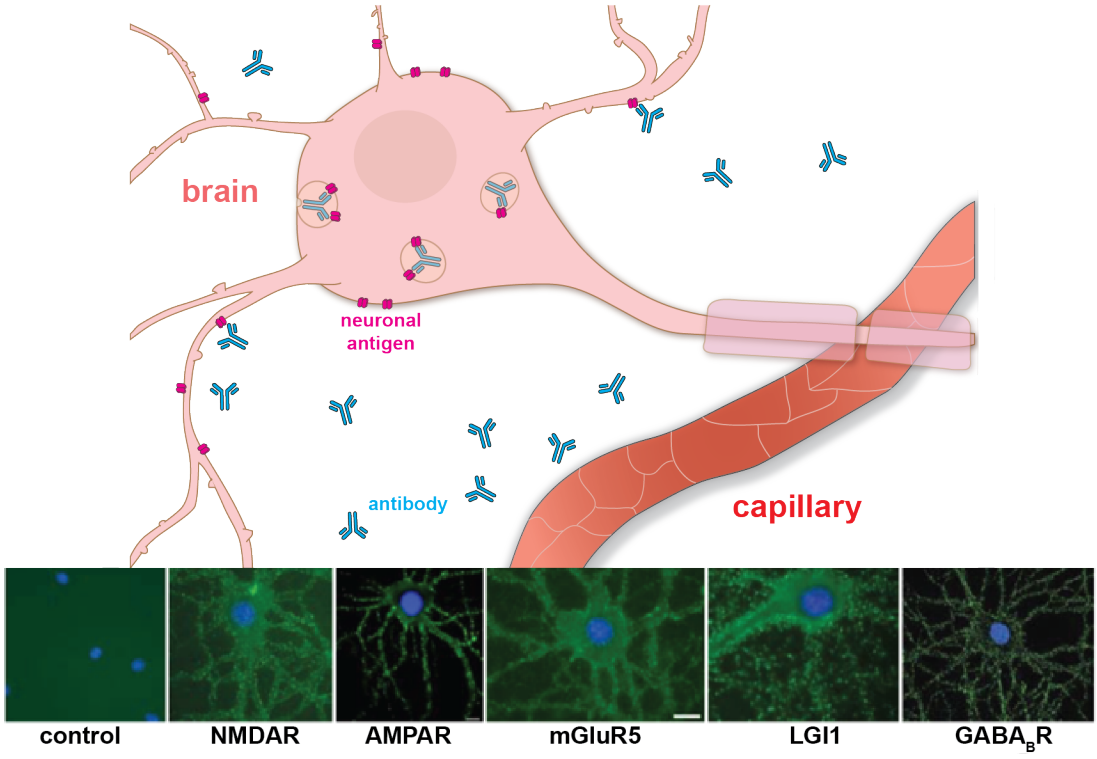

Figure 1.1 Pathogenesis of autoimmune encephalitis. Autoimmune encephalitis occurs when antibodies specific for brain epitopes enter the CNS, where they bind target antigens and interfere with neuronal signaling. Many distinct autoantibody targets have been identified to date, with selected examples of antibodies from CSF reacting with neurons *in vitro* [22].

common, with slight variations in both presentation and symptom onset. CSF pleocytosis is a hallmark of AE, but clinical presentation can also vary with age, as seen in Herpes virus encephalitis and NMDARE [23, 24]. Frequently, imaging studies of acute AE patients are either nonspecific or unremarkable, differentiating these syndromes from multiple sclerosis (MS) and other encephalopathies, where PET or MRI often reveals classical lesions [16]. Brain MRI aids in differential diagnosis between different encephalitic syndromes and MS, as ADEM typically presents with abrupt onset and symmetrical lesion areas usually involving the thalamus, while MS onset is more gradual, with distinct, non-symmetrical lesions that involve the brainstem [25]. Lesions in LE patients are typically bilateral and involve the medial temporal lobes [18]. ADEM and other AE disorders will sometimes have a history of infection or vaccination preceding

symptom onset, which can also aid in narrowing down specific autoantigens that may trigger disease.

Initial identification of several AE syndromes stemmed from links to specific cancer populations. The original cohort of NMDARE patients all presented with both psychosis symptoms as well as ovarian or mediastinal teratomas. These tumors contained neural tissue ectopically expressing NMDAR NR2 subunits on the tumor surface, which provides a potential initiation point for autoimmunity outside the CNS [4]. In a cohort of $GABA_B$ receptor encephalitis patients, 50% had small cell lung cancer ectopically expressing the antigen [26]. Morvan syndrome and limbic encephalitis have also been linked to thymoma in a subset of patients (19-30%) [27, 28]. In patients with tumors and ensuing paraneoplastic syndrome, removal of the inciting tumor is necessary for treatment [4, 17, 29-32]. Immunotherapy alone without tumor resection frequently results in deterioration [17, 32].

Several precipitating infectious triggers have also been identified recently, including bacteria, viruses, and, rarely, fungi. Specifically, AE has been linked to Group A *Streptococcus* (GAS, *S. pyogenes*) bacteria [33, 34], influenza virus [35], Japanese encephalitis virus [8, 36], Herpes virus [24, 37-39], and fungi [40]. Herpes virus has been linked to later development of NMDARE in a subset of patients [24, 37]. These are all quite common pathogens, and tend not to cause encephalitis in healthy, immunocompetent individuals. Infectious triggers such as GAS are hypothesized to cause autoimmunity by either direct molecular mimicry of GAS antigens and autoantigens, or by recurrent inflammation combined with BBB breach that allows aberrant immune targeting of the CNS.

Presence of autoantibodies in serum is an imperfect diagnostic tool. First, it has been estimated that approximately 2-10% of the healthy population have circulating anti-brain

antibodies [14, 15, 41]. It is also possible to isolate antinuclear antibodies from ~30% of the healthy population [15, 42], and anti-endothelial cell antibodies from ~2% of healthy patients [43]. Second, the BBB normally excludes circulating antibodies from the brain parenchyma, limiting their pathogenic power. Presence of autoantibodies in the CSF is a more specific indicator of AE, with much greater sensitivity and specificity than serum antibodies [18]. These important findings raise the question of how CNS barriers, including the BBB, break down during AE to allow circulating autoantibodies into the brain parenchyma.

Genetic studies have shown linkages to several loci in AE patient cohorts. Several immune alleles confer specific risk for AE syndromes, specifically, major histocompatibility complex-II (MHC-II) alleles. Anti-LGI1 encephalitis is highly associated with 27 SNPs, most significantly with a 13.66-fold odds ratio in patients carrying the rs2858870 SNP in HLA-II. Imputation of HLA alleles in this cohort showed linkage to DRB1*07:01, DQA1*02:01 and DQB1*02:02 [44]. In a separate cohort, HLA DRB7 and DRB4 were strongly linked to non-tumor anti-LGI1 encephalitis patients, but not patients with tumors [45]. In a German NMDARE cohort, HLA typing showed linkage to MHC II allele B*07:01 [44], but no HLA allele associations were identified in a Korean cohort [46]. No significant linkages were identified between the two AE syndrome cohorts [44]. This implies that different AE syndromes may develop via unique genetic vulnerabilities, perhaps tied to risk factors for infection or specific neoplasms.

1.1.1 Group A Streptococcus triggers robust immune responses and autoimmune encephalitis

While the evidence that microbial infections trigger for AE is limited, Group A *Streptococcus* (GAS, *S. pyogenes*) infections cause autoimmune sequelae in many target tissues, including heart, kidney, or CNS that are manifested as acute rheumatic fever (ARF),

glomerulonephritis, or Sydenham's chorea, respectively [47]. ARF is the most common of these outcomes, and while its prevalence has waned with the advent of antibiotics, it remains a public health concern in many developing countries. The most prominent risk factors for ARF include overcrowded living conditions, undernutrition, and family history of rheumatic fever or rheumatic heart disease [48]. Patients typically develop fever, arthralgia, lethargy, and/or chest pain, which is treated with antibiotics and anti-inflammatory drugs to resolve latent infection and inflammation. Preventative treatments for ARF primarily involve antibiotics to treat preceding GAS pharyngitis, which limits the burden on the immune system. Several vaccines against GAS are being developed, but large variation among serotypes has hindered progress on this front [49].

Untreated GAS infections have long been linked to later development of movement disorders in a minority of children, as identified in 1686 by Thomas Sydenham [50]. Sydenham's chorea (SC) presents in a minority of children as uncontrolled, jerky movements of the arms, legs, trunk, or face, sometimes in conjunction with rheumatic fever. It was not until 1998 that Dr. Susan Swedo at the National Institutes of Mental Health (NIMH) described a subset of 50 children from a larger cohort of SC patients with acute psychiatric symptoms, which she termed *P*ediatric *A*utoimmune *N*europsychiatric *D*isorders *A*ssociated with *S*treptococcus (PANDAS) [34]. Her description of PANDAS maintains a close association with prior GAS infection, but presents with psychiatric symptoms rather than purely motor disturbances characteristic of SC [34]. In patients, post-*Streptococcal* autoimmunity can have a wide variety of symptoms. Children presenting with the following symptoms are considered for a PANDAS diagnosis: swift or overnight onset of symptoms; pediatric patient age; bedwetting or urinary urgency; obsessions or compulsions; separation anxiety; choreiform movements; and changes in mood or behavioral disturbances [34]. There has been some resistance to PANDAS diagnosis clinically, and controversy still persists.

Clinicians have raised objections for a multitude of reasons, namely: reliance on a list of unvalidated criteria for differential diagnosis; no specific laboratory tests; weak genetic associations; lack of direct evidence of autoimmunity; and the prevalence of GAS infections in children complicated separation of PANDAS from pediatric onset of Tourette's disorder or obsessive-compulsive disorders (OCD) [51-54]. Careful consideration of obsessive-compulsive OCD, Tourette's, and rheumatic fever must be ruled out before considering a diagnosis of PANDAS.

1.1.2 Human genetics in SC and PANDAS

It is hypothesized that predisposition to post-*Streptococcal* autoimmunity has a genetic component, since rheumatic heart disease, Sydenham's chorea, and PANDAS are sex-skewed [34, 47, 49]. ARF affects both sexes equally, but later development of rheumatic heart disease is skewed toward to females [55]. SC tends to affect girls more, but PANDAS is more prevalent in boys [56]. Females are more prone to autoimmune diseases in general, so it comes as little surprise that there would be a sex linkage in these diseases. Genome wide association studies (GWAS) have implicated major histocompatibility class (MHC) class I and class II alleles in ARF, SC, AE, ADEM, multiple sclerosis, and systemic lupus erythematosus risk [25, 57-59]. Specifically, HLA DRB1*15:01 has been linked to SC, MS, SLE, and ADEM, identifying a common genetic risk factor in this group of autoimmune diseases [59, 60]. HLA alleles DRB1*15:01, DRB1*15:03, DQB1*06:02, DQA*01:02, and DPA*03:01 also confer risk in MS and ADEM [25, 61]. Conversely, HLA DQB1*06:02 is protective for rheumatic heart disease in adult populations, rheumatic fever, SC, and recurrent GAS tonsillitis in children [59, 60, 62] Genetic linkage to ARF is also strong for several cytokine and other immune effector molecules, as well as Fc receptor

gene polymorphisms (FcγRIIA-R/R-131 and FcγRIIA-R/H-131 polymorphisms) [57, 59, 63-69]. Small numbers of patients with SC or PANDAS limits the power GWAS studies for genetic susceptibility, but future studies using whole exome sequencing and gene burden analysis methods to probe candidate pathways may provide an avenue to identify genetic risk factors for these diseases.

Since GAS is posited to be the initiating agent in causing autoimmunity in PANDAS and SC, it is important to link infectious agents with later development of psychiatric illness. Several studies using large population registers have demonstrated a link between childhood infections and psychiatric disorders later in life. The first linked childhood GAS infections of later development of mental disorder, specifically OCD and tics (relative risk 1.51 and 1.35, respectively) in a Danish population. Non-Streptococcal infections also increased relative risk of OCD and tics, but to a lesser extent (1.28 and 1.25, respectively) [70]. The second found that in a Taiwanese population, severe or recurrent GAS infections raised relative risk for tics and ADHD (1.63 and 1.16, respectively) later in life [69]. Finally, among a Danish population, increasing numbers of antibiotic agents used on a particular patient raised relative risk for psychiatric hospitalization and prescription of psychotropic medication later in life [71]. Recent GWAS studies have also demonstrated a genetic predisposition for recurrent childhood infections linked to SNPs in the TNFα and IL-6 genes [6, 56, 72, 73]. Alleles conferring risk (HLA DRB1*01:01, DRB1*07:01) and protection (HLA DQB1*06:02) specifically for recurrent GAS infections in children were recently identified [62]. These population-based studies support a link between childhood infections and later development of psychiatric diseases. Since GAS is an obligatory human pathogen, genetic predisposition towards both recurrent primary infections and GAS-induced autoimmunity can cause long lasting effects much later in life than previously thought.

1.1.3 GAS genetics and Superantigens

Bacterial infections generate an antibody pool targeting various epitopes on the bacterial surface. It is hypothesized that a small subset of antibodies produced during GAS infections are the initial causative agents for the subsequent autoimmunity [63, 74, 75]. This is hypothesized to occur via molecular mimicry, where structural similarity between the targeted bacterial and self-antigens promotes cross-reactivity [76-78]. Structural similarity between the coiled-coil region of cardiac myosin and the antigenic M protein on the bacterial surface may promote cross-reaction of M-specific antibodies with myosin (**Figure 1.2a**). Mutated GAS strains have been generated where irregularities in M coiled-coil structure are smoothed; these strains induce antibodies with less cross-reactive affinity for myosin, as well as decreased binding to serum fibrinogen and inflammatory effects [79]. Further studies using sera from PANDAS and SC patients support cross-reactivity with dopamine D2 receptor (**Figure 1.2b**), neuronal lysoganglioside, and tubulin

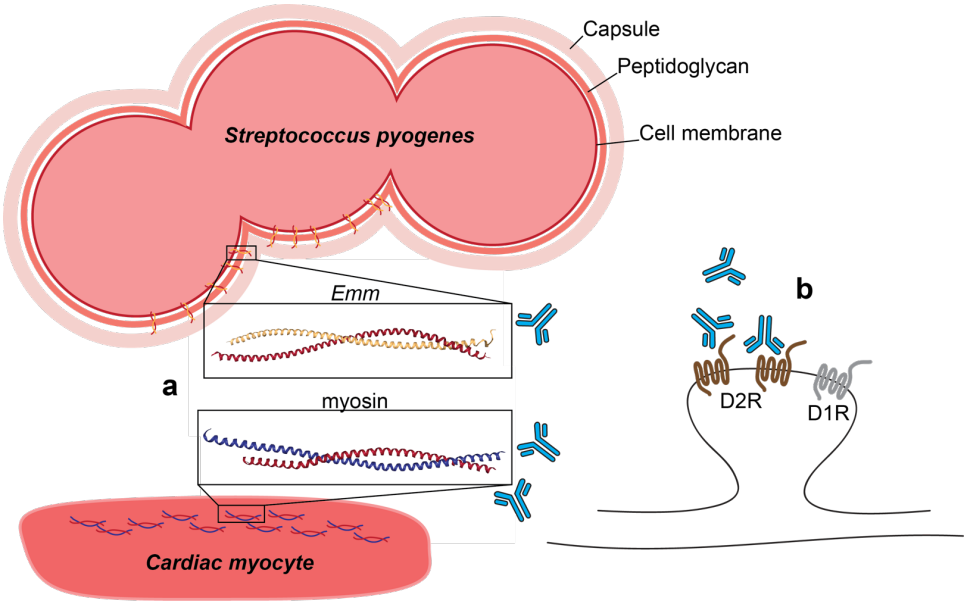

Figure 1.2 Schematic of cross-reactive antibodies from recurrent GAS infections. **a** In rheumatic fever, structural similarity between GAS *Emm* protein and cardiac myosin is thought to underlie cross-reaction by molecular mimicry. **b** Autoantibodies target the dopamine D2 receptor in Sydenham's chorea.

[10, 63, 80, 81]. *Ex vivo* studies with also showed cross-reactivity between patient sera and cholinergic neurons in the striatum, providing another potential target for autoantibody binding in the basal ganglia [82]. Furthermore, epitope spreading after the initiation of autoimmunity could lead to numerous cross-reactive antibodies stemming from an inflammatory environment [65].

One study on a rat model of rheumatic heart disease (rat autoimmune valvulitis) showed an increased infiltration of cardiac tissue by T cells and macrophages, as well as cardiac arrhythmia, after increasing numbers of immunizations with recombinant M protein. This study examined changes in endothelial cell expression of vascular cell adhesion molecule-1 (VCAM-1), which is required for adhesion of immune cells to endothelial cells, after exposure to inflammatory factors in sera from immunized rats. *In vitro* restimulation led to upregulated VCAM-1 expression, suggesting that T cells may use VCAM-1 to arrest on cardiac vasculature and infiltrate the activated endothelium. [83]. While other microbes may exert a similar effect on the immune system, direct evidence of immune sensitization leading to autoimmunity is lacking.

Strain differences in GAS bacteria have also been postulated to contribute to variability in both prevalence and manifestation of GAS-induced autoimmunity. Broad groups of *emm* genes refer to their tropism for particular organs; A, B, and C strains are considered particularly specialized to the throat, while D strains are specialized to skin, and E is broadly pathogenic [63, 84]. Expression and antigenicity of superantigen proteins (SAgs), which induce a massive cytokine release from T cells upon binding and recognition, varies between GAS strains. In clinical isolates from different types of GAS infections (invasive, pharyngitis, and acute rheumatic fever cases), SpeB SAg activity was markedly lower in the ARF clinical isolates, suggesting that a balance between different SAgs is important for development of autoimmunity [85]. Children with recurrent GAS tonsillitis have markedly reduced antibody titers against SpeA, indicating faulty or

incomplete antibody production against the pathogen [62]. SAgs bind to the portion of the β-chain T cell receptor that does not undergo V(D)J recombination, allowing activation of a huge number of T cells [86]. SAgs also bind to and activate MHC-II on antigen presenting cells, although less efficiently than SAg binding to the Vβ T cell receptor (TCR) [63]. SAgs bind to human MHC-II much more efficiently than mouse MHC-II, providing an important caveat for the present studies. Because GAS is an exclusive human pathogen, it will be important to extend these findings using a mouse line in which the MHC-II gene is humanized.

Robust immune reactions to GAS are necessary to fight infection and clear bacteria from host tissues. Interaction of human genetic predisposition towards autoimmunity in general, family history of GAS-induced autoimmunity (including ARF), and GAS strain genetics may all contribute to increased risk for GAS-induced AE disease. In addition, BBB breakdown independent of bacterial infection seems to be an important contributor to disease. These studies emphasize that the contribution of the immune system to PANDAS and SC pathogenesis needs to be more fully elucidated.

1.2 Blood-brain barrier function in health and disease

The blood-brain barrier (BBB) encompasses several unique properties of brain endothelial cells (BECs) that limit trafficking of a variety of blood-borne solutes such as ions, nutrients, toxins, proteins, immune cells, and antibodies into the brain parenchyma to allow for proper neuronal function [12, 87]. The BBB is comprised of three main characteristics. First, expression of tight junction (TJ) proteins effectively seal together adjacent BECs, preventing leakage of serum proteins through the paracellular space. Second, basal rates of transcytosis are very low in BECs, and proteins that form fenestrae are not expressed, limiting bulk transport by vesicular trafficking

through BECs. Third, expression of specialized transmembrane transporters on the BEC membrane facilitates trafficking of nutrients such as glucose into the parenchyma, and limits transit of waste products or potential toxins (**Figure 1.3a**) [88]. BBB properties regulate the ionic composition of brain interstitial fluid, allowing for proper neuronal function. Glial cells are closely associated with the EC basolateral face, with astrocyte endfeet covering the outer face of ECs, and pericytes spaced sporadically along the vessel length. Astrocytes play a large role in regulating water balance and ionic composition of the neuronal milieu, and can signal directly to neurons, ECs, and adjacent astrocytes via gap junctions [89]. This section reviews the cellular and molecular composition of various barrier interfaces insulating the brain parenchyma from circulating blood, as well as mechanisms of barrier breakdown in inflammation and disease states.

1.2.1 Mechanisms of BBB dysfunction in neuroinflammatory diseases

Barrier function of CNS endothelial cells can be impaired by several factors: inflammatory cytokines, hormones (e.g., epinephrine), and substances of abuse (e.g., alcohol, cocaine, and methamphetamine) [11, 89]. Tight junction (TJ) complexes are comprised of tetraspanin integral membrane proteins Claudin5 and Occludin, which interdigitate on their extracellular loops to seal the walls of adjacent BECs together (**Figure 1.3a**) [12, 87]. These transmembrane proteins are linked via scaffolding proteins such as ZO-1 and Cingulin to the actin cytoskeleton [90]. In the healthy CNS, TJ complexes are subject to low rates of turnover through membrane recycling machinery [91, 92]. In disease states, however, rates of TJ internalization increase, and TJ strands become vulnerable to formation of gaps between adjacent ECs (**Figure 1.3b, Figure 1.4c**) [91-93]. In inflamed BECs *in vitro*, TJ proteins show a punctate, rather than continuous, pattern around cell - cell junctions, corresponding to an increase in vesicular endocytosis [94]. In CNS

neurological diseases such as stroke and MS, TJs can be internalized within the BEC by forming 1-3 μm - long protrusions perpendicular to the direction of the TJ strand [91]. Internalization of TJ proteins Claudin5, Occludin, and ZO-1 can occur via Clathrin-dependent (Occludin, ZO-1) or Caveolin1^{+} vesicle-dependent (Claudin5, Occludin, ZO-1) mechanisms [90, 95]. In an animal model of MS (experimental autoimmune encephalomyelitis, EAE), live imaging of tight junctions in the spinal cord showed that TJs are remodeled initially by formation of protrusions before the

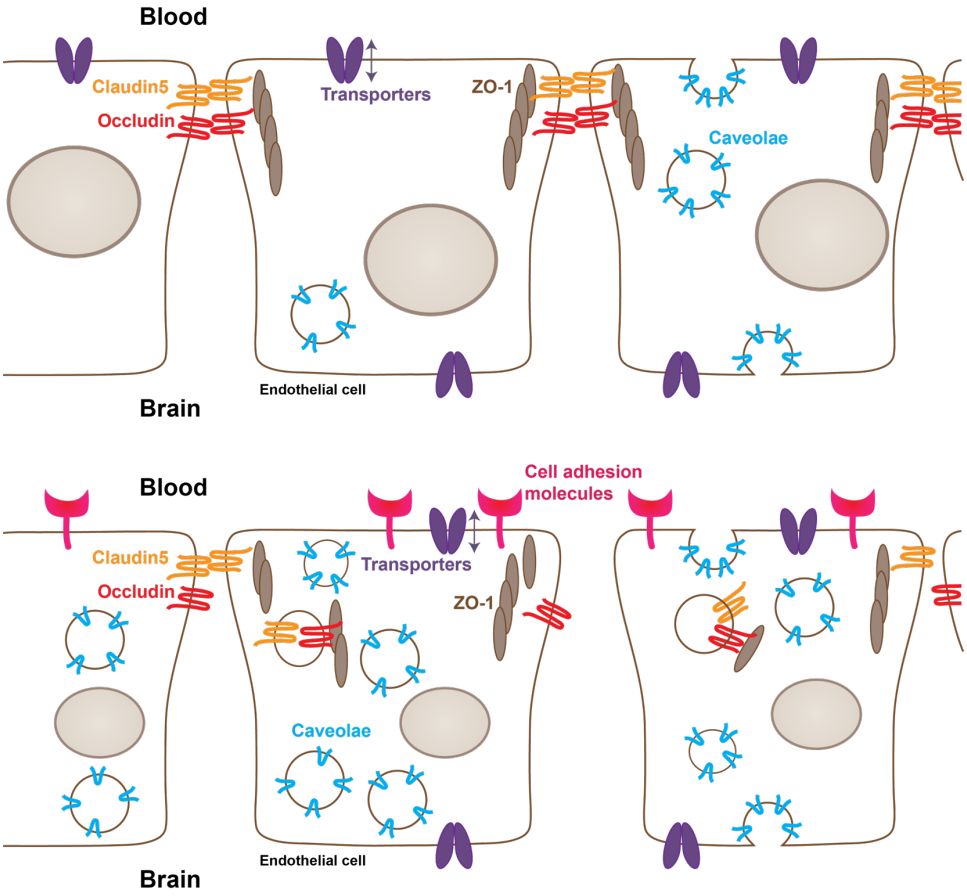

Figure 1.3 Molecular components of the blood-brain barrier in brain endothelial cells (BECs). In healthy vasculature (top), ECs limit bulk diffusion of solutes from blood into brain by expression of tight junction proteins that seal together adjacent ECs, as well as suppressing transcytotic vesicular transport. Specialized transporters and pumps permit active and passive transport of select solutes. Under inflammatory conditions (bottom), tight junction proteins are internalized, and caveolae and cell adhesion molecules are upregulated, promoting BBB permeability.

onset of clinical signs, followed by gap formation at the peak of disease, corresponding to the degree of BBB damage [92]. Similarly, ZO-1 internalization precedes EAE symptom onset and indicates future lesion formation [94]. Although TNFα induces gaps in TJs by upregulating NF-κB and myosin light-chain kinase *in vitro*, which induce internalization of TJs via $Cav1^+$ vesicles [96, 97], several in vivo studies have failed to demonstrate a role of $Cav1^+$ vesicles in remodeling TJs in neurological disease models [91, 92].

Inflammatory cytokines can act directly on TJ proteins to destabilize them, and IL-6 is elevated in many CNS inflammatory diseases [98]. Inflammatory cytokines can degrade TJs, change their phosphorylation state, or affect turnover rate. In EAE, monocytes induce expression of tissue plasminogen activator (tPa) by activated ECs, which proteolytically degrades Occludin [99]. Th17 cells secrete inflammatory cytokines IL-17A and IL-22, which directly disrupt TJs [100]. IL-1β indirectly destabilizes TJs by upregulating Matrix Metalloprotease-9, whereas VEGF-A degrades both Claudin-5 and Occludin [101, 102]. These cytokines have been shown to disrupt BBB function during neuroinflammation in stroke and EAE, but it is unclear whether they are upregulated in AE. Recent cytokine profiling of CSF from patients with viral or autoimmune encephalitis revealed that several Th1 cytokines (TNFα, IFNγ, CXCL9, and CXCL10) were upregulated after viral encephalitis, but not in AE [98]. Healthy brain vasculature expresses low levels of leukocyte adhesion molecules such as vascular cell adhesion molecule-1 (VCAM-1), intercellular adhesion molecule-1 and -2 (ICAM-1 and ICAM-2), and activated leukocyte cell adhesion molecule (ALCAM) which are upregulated in neuroinflammation to promote T cell trafficking into the parenchyma [103, 104]. Cell adhesion molecules influence TJ stability, as deletion of ALCAM leads to decreased expression of several TJ proteins including ZO-1, Occludin, and Claudin5, resulting in increased BBB permeability [105].

Changes in transcytosis can also increase BBB permeability (**Figure 1.3b**). Increased rates of transcytosis are responsible for barrier permeability at early (~6 h), as well as later (48 h) time points post-stroke in a mouse model for the disease (t-MCAO) [91]. EAE studies in *Caveolin-1*$^{-/-}$ mice have demonstrated preferential trafficking of some T cell subtypes (Th17 lymphocytes) *through* ECs rather than *between* them via disrupted TJs during initiation of disease [92]. Notably, some Th1 lymphocytes preferentially traffic via Cav1^{+} vesicles in EAE [92]. *Caveolin-1*$^{-/-}$ mice show reduced EAE clinical scores and demonstrate decreased CD4^{+} cellular infiltrate compared to wild-type (WT) littermates [106]. While caveolar transcytosis is less selective, receptor-mediated endocytosis facilitates transport of specific cargo across BECs in vesicles (e.g., the transferrin receptor and the insulin receptor bind transferrin-iron complexes and insulin, respectively). This pathway has been co-opted to enhance biological treatment passage across the BBB by fusing drugs to receptor targets via a Trojan horse mechanism [107, 108]. Biological therapies using fusion proteins have been used to treat murine models of stroke, lysosomal storage disorders, Alzheimer's disease, and glioma [107]. Transcytosis can also occur through Clathrin-dependent mechanisms, although these vesicles seems to be less important for immune cell trafficking [95]. Taken together, there seems to be interplay between transcytotic leakage machinery and other inflammatory signals in BECs.

Transporters work ceaselessly to supply neurons with nutrients, ions, and gases needed for neuronal transmission, and to remove toxins from the CNS. ECs express a wide variety of transporters on their apical (vessel-facing) and basolateral (brain-facing) surfaces, including the glucose transporter GLUT1. Perhaps the largest superfamily of transporters is the ATP-binding cassette (ABC) superfamily, which encompasses 48 members grouped into 7 subfamilies. ABC transporters are especially efficient pumps that move xenobiotics and metabolites against their

concentration gradient, and can function as importers or exporters [109]. Notably, in a recent study, even physical disruption of TJs by focused ultrasound could not overcome the action of ABC transporters to deliver the tyrosine kinase inhibitor erlotinib in humans [110]. Mutations in transporter genes cause several serious conditions, including cystic fibrosis, Tangier disease, and Stargardt disease [88, 109]. In the CNS, mutations that interfere with the function of ABCA transporter genes, including cholesterol transporters ApoE and ApoA-I, are particularly associated with Alzheimer's disease [109]. Conversely, brain tumor cells frequently upregulate expression of multidrug resistance ABC transporters, which block drug treatment [109].

Endothelial cells are particularly vulnerable to endotoxins secreted by infectious agents. Antigenic surface proteins on Gram-positive bacterial and lipopolysaccharide from Gram-negative bacteria change EC barrier properties [111]. Environmental toxins (e.g., bis(tributyltin) oxide) and food additives can increase BBB permeability, as evidenced by serum protein leakage studies [112]. The gut microbiome also modulates barrier function [113]. Inflamed astrocytes and microglia antagonize each other to amplify release of cytokines IL-1β, TNFα, IL-1α and MIP-1α, leading to breakdown of the EC monolayer [114]. In AE cases with many autoantibodies in the blood circulation, transient BBB permeability by TJ breakdown, transcytosis, or Fc-mediated transport may provide opportunistic access to brain targets.

1.2.2 Glial contributions to BBB structure and function

Interactions between endothelial cells, astrocytes, and pericytes are critical for BBB development and maintenance. Astrocyte endfeet completely encircle CNS blood vessels, and pericytes are spaced evenly along the vessel length. Close association with both of these cell types are required for acquisition and maintenance of CNS barrier properties [115]. During embryonic

development, pericytes invade the CNS together with sprouting endothelial cells starting on embryonic day (E) 12, prior to birth of astrocytes at E18 [116]. Pericyte-deficient *Pdgfrβ*$^{-/-}$ embryos showed incomplete tight junction formation, vessel permeability to tracers, and increased expression of cell adhesion molecules that are normally downregulated over the course of barrier maturation [116]. Wnt/β-catenin signaling in ECs shapes the vascular tree [117], and then pericytes help suppress genes that promote fenestration in peripheral vessels, thus promoting acquisition of barrier properties. Pericytes form adherens junctions with ECs via expression of N-cadherin (Cadherin-2) to maintain their close association to the vessel wall [115]. Astrocytes help control the flux of ions, water, and nutrients by expressing ion and water transporters (e.g., Aqp-4), as well as maintaining BEC barrier properties throughout adulthood by secreting Wnts, retinoic acid, sonic hedgehog, and Angiopoietin-1 [13]. Inflamed astrocytes and microglia antagonize each other to amplify release of cytokines IL-1β, TNFα, IL-1α and MIP-1α, leading to breakdown of the EC monolayer *in vitro* [114]. Astrocytes are also required for recovery from injury, where they proliferate and form a glial scar that limits immune cell infiltration, BBB leakage, and regrowth of neurites through damaged brain areas [118].

1.2.3 Regional variability in BBB permeability

The BBB is not uniformly restrictive over the entirety of the CNS vasculature. Several studies suggest that endothelial barriers in the brain and spinal cord (SC) are functionally different, based on differences in expression of some barrier-specific proteins and their functional permeability. ECs in the SC have lower levels of adherens junction (Cadherin-5 and β-catenin) and tight junction (Occludin, ZO-1) proteins, as well as increased permeability to small molecular weight tracers, compared to brain endothelium [119]. ECs in the brain and SC also differ in their

affinity for immune cells. Activated encephalitogenic T cells in the cervical SC rapidly arrest on vasculature without crawling, whereas in the brain, T cells roll along brain ECs before arresting. Adhesion in the SC is mediated by interaction of α4-integrin and VCAM-1 to arrest, followed by LFA-1 to transmigrate through the vessel wall [103, 120]. Higher expression of sphingosine-1-phosphate receptor in SC ECs may also facilitate immune cell transmigration as compared to other CNS regions during EAE [121]. Within the brain, the olfactory bulb (specifically the olfactory nerve layer) and neurogenic niches also have relatively higher baseline permeability compared to other CNS regions (excepting the circumventricular organs that have leaky blood vessels); vessels in these regions become highly permeable following viral infections [122-124], which may predispose them to infiltration of immune cells or antibodies in addition to viral particles. Neurons in the circumventricular organs actively sample osmolality and hormone levels in the blood, and thus would be hindered by presence of a barrier. These brain regions display high vascular permeability in healthy animals [125].

1.2.4 Blood-cerebrospinal fluid barrier (BCSFB)

Epithelial cells within the choroid plexus form a tight barrier termed the blood-cerebrospinal fluid barrier that restricts diffusion of serum proteins and immune cells from the leaky blood vessel of the choroid plexus into the cerebrospinal fluid (CSF) [126]. The molecular composition of tight and adherens junctions within the BCSFB is slightly different from junctions in the BBB, with Occludin and ZO-1 expressed in both barriers, but with mainly Claudin1 and E-Cadherin expressed in choroid plexus epithelial cells [126, 127]. Several key junctional proteins are present in choroid epithelial cells at high levels both in embryonic and adult stages, suggesting this barrier matures early in development [128]. These junctions creates a physical barrier to

paracellular diffusion and polarizes epithelial cells with distinct luminal and abluminal components (**Figure 1.4a**). Additionally, epithelial cells of the BCSFB express transporter proteins that regulate transit of certain plasma proteins and ions across this barrier and maintain the composition of CSF [127, 128]. The BCSFB is less tightly regulated than its brain counterpart, and is more easily permeabilized in disease states. During EAE, Th17 cells cross the BCSFB

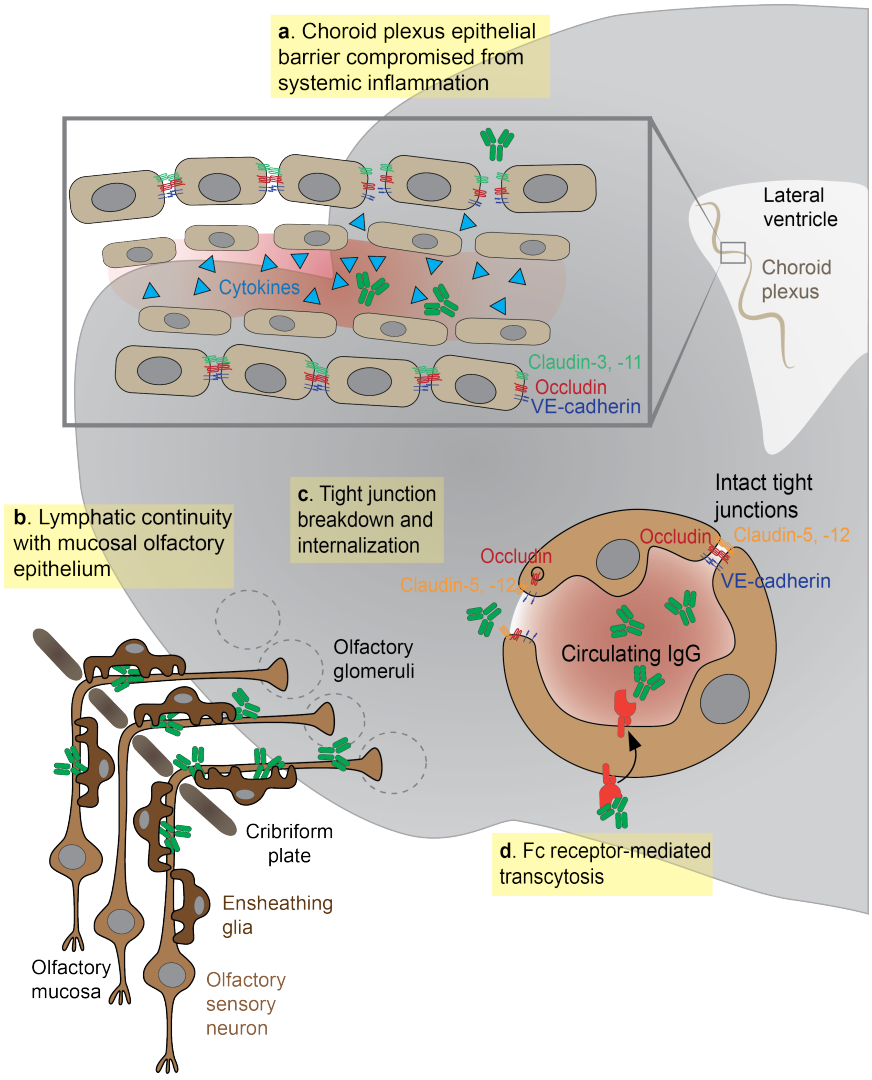

Figure 1.4 Four main hypothesized routes of IgG leakage in AE. **a** Choroid plexus epithelial cells are vulnerable to inflammatory cytokines, promoting leakage of solutes into the CSF. **b** The olfactory route along olfactory axons has been shown to preferentially transport viruses into the brain, as well as providing a route for therapeutic delivery. **c** Blood vessels break down in multiple ways in inflammation, allowing spatially and temporally restricted leakage into the brain. **d** Fc receptors on endothelial cells maintain a low concentration of IgG in the parenchyma; this concentration gradient may reverse in disease states. Reprinted from [50].

several days before BBB damage in the "first wave" of T cell entry into the CNS [129]. This entry step is essential for initiating the CNS immune response, as demonstrated by EAE resistance in *CCR6*- deficient mice where Th17 cells that cannot cross the BCSFB [129]. In mouse models of systemic lupus erythematosus (SLE), VCAM-1 and ICAM-1 expression is elevated on choroid epithelium, and large populations of B and T immune cells infiltrate the choroid [130-132]. Interestingly, there is variability in T cell and B cell infiltration between different spontaneous SLE mouse strains, indicating that distinct disease mechanisms may be at play in the human condition [131]. The role of infiltrating immune cells is still debated, but the BCSFB is clearly activated and disrupted by increased cytokine expression [130, 132-134]. In a mouse model of neuroinflammatory lupus, the choroid plexus becomes permeable via the transcellular route, as tight junctions remain intact. Immune cells can also cross the BCSFB in this mouse model, and later in disease, the choroid plexus may function as a tertiary lymphoid structure [135]. It is possible that B cells or antibodies cross this barrier more efficiently than the BBB and enter the CSF, but data from *in vitro* and animal models are lacking.

1.2.5 Olfactory nerve projections into the brain as a route for immune cell entry

The proximity of the olfactory bulb to the nasal mucosa makes it both a vulnerable niche to insult and infection of the brain, and an attractive option for delivery of therapeutics that cannot otherwise traverse the BBB [136, 137]. Many viruses and bacteria co-opt the olfactory route for brain infection, and more than 40 substances have been shown to enter the brain in this manner (**Figure 1.4b**) [138, 139]. Viruses such as the Venezuelan equine encephalitis virus initially infiltrate the CNS via olfactory sensory neuron axons, where they induce BBB permeability, thus promoting a second wave of infection as virion particles enter the brain from the leaky vasculature

[140]. Herpes simplex virus-1 infection is very prevalent, and can asymptomatically infect the brain via the olfactory or hematogenous route, with olfactory transmission more common in younger patients [37]. A subset of patients develops acute encephalitis, which can be treated with antivirals, but leaves the brain vulnerable to secondary sequelae [37, 141]. In children, Herpes simplex encephalitis is more commonly a result of primary infection, but in adults, maintenance and reactivation of viral reservoirs in neurons is hypothesized to be the driving cause of encephalitis [37]. Recent linkage of HSE with later development of NMDARE provides an intriguing link between infectious trigger and encephalopathies. The neurotrophic Nipah virus also infects hamster olfactory sensory neurons, then travels from the OB along olfactory circuitry before spreading throughout the brain [142]. Finally, after an initial injury to nasal mucosa, *Staphylococcus aureus* infects olfactory sensory neurons and spreads to the OB within 6 hours [143].

In addition to pathogen infection, the intranasal route has been successfully used to deliver drugs, large proteins, and stem cells into the brain [136], largely due to rapid diffusion via perivascular spaces [144]. The intranasal route is particularly suited to access the brain for several reasons: diffusion along heavily vascularized nasal mucosa that also contains lymphatic vessels; direct transport along olfactory sensory axons; and direct transport via the trigeminal nerve into the brainstem. Although the nasal mucosa is heavily vascularized, the mean capillary density and relative permeability to hydrophilic tracers is significantly greater in the respiratory epithelium of the nose than the olfactory sensory regions; sensory regions of the OE thus provide easier access to the brain due to slower clearance rates into the blood stream [145]. Interestingly, the olfactory route is also used by immune cells to exit the CNS through the OB in a CCL19- and CCL21-dependent manner and drain to deep cervical lymph nodes in order to dampen CNS-specific

immune responses in the periphery [146-148]. There are no data, however, on whether antibodies are transported via the olfactory route to gain access to the CNS from sites of infection in the olfactory mucosa.

1.3 Immune system activation in autoimmune encephalitis

Aberrant immune responses underlie AE pathogenesis, and multiple facets of the immune system may play a role in disease initiation and progression. Two main branches of the immune system function in tandem to clear infections. First, the innate immune system is ontologically older and functions much the same way each time it encounters a pathogen. Macrophages and NK cells are the main cellular components of the innate immune system, and macrophages are the main phagocytes recruited to infection. Common protein motifs on the surfaces of pathogens bind complement proteins, which are constantly circulating in the bloodstream [149]. Complement signaling quickly amplifies after binding invading pathogen, which recruits other immune cells to the site of infection. Complement deposition on invading pathogens marks them for destruction and facilitates antigen presentation to the adaptive immune system.

Second, the adaptive immune system, comprised of cellular (dendritic cells, T cells) and humoral (B cells and antibodies) arms, is capable of "remembering" previous pathogens and mounting an expedited immune response when re-exposed to the same challenge. Dendritic cells (DCs) of the cellular adaptive immune system continuously patrol the body, phagocytose debris, and return with processed antigen to lymph nodes to activate a cellular response to an invading pathogen. In the lymph nodes, DCs form an immunological synapse with immature T cells, which prompts T cells to terminally differentiate, leave the lymph node, and navigate to the site of infection. Once there, T cells encounter their cognate antigen and secrete inflammatory molecules

(cytokines) directing other immune cells to neutralize the pathogen and clean up cellular debris. DCs also activate B cells to express antigen-selective receptors, and once they encounter their cognate antigen, B cells secrete pathogen-specific antibodies [149, 150]. antibodies bound to pathogen facilitate clearance by other phagocytic cells. B cells can then differentiate into plasma cells, which secrete large quantities of antibody and then usually die within a few days [151]. However, a subset of both T and B cell populations recruited to an infection will persist and can be rapidly recruited to fight the same pathogen at a later time. Thus, the immune system adapts to more efficiently neutralize pathogens it has encountered before. Aberrant responses by the adaptive immune system seem to underlie the major causes of AE; reviewed here are major cellular components of the immune system (B cells, T cells, microglia/macrophages, and dendritic cells) and their links to AE, as well as molecular signaling pathways thought to be implicated in immune cell trafficking in AE.

1.3.1 Aberrant antibody production and B cells

B cell homing in antibody-driven neuroinflammatory diseases has been a topic of significant interest, given that B cells and plasma cells secrete antibodies. B cells are implicated in the pathogenesis of several CNS autoimmune disorders by the persistent presence of oligoclonal immunoglobulin G (IgG) in cerebrospinal fluid (CSF). Approximately 95% of MS patients have oligoclonal IgG bands, and the presence of IgM bands (approximately 40% of MS patients) is predictive of poor clinical outcomes. B cell targeted therapy like Rituximab is currently the most effective MS treatment, indicating a role for B cells in pathogenesis of the human condition [152]. B cells are efficient antigen presenting cells (APCs), and evidence suggests that MS patient-derived B cells present self-antigen more competently than healthy B cells, indicating that B cells

also contribute to pathogenesis in an antigen-dependent manner. Finally, B cells from MS patients secrete inflammatory cytokines (TNFα, IFNγ, IL-12, and IL-6) that direct T cell differentiation, thus influencing the T cell population in the CNS [152]. Therapies that target B cells but not plasma cells are effective in improving clinical outcomes, indicating that antibody-independent B cell activities play a role in disease progression. Some mouse models of MS, including EAE, are T cell driven diseases, which limits translation of mouse data on the role of B cells in EAE disease course to humans [153].

In AE syndromes, the question of B cell infiltration in the CNS is less clear than it is in MS/EAE literature. Oligoclonal bands are present in CSF samples from neuropsychiatric systemic lupus erythematosus (NPSLE) [133], NMDARE [154, 155], and Sydenham's chorea [156], implying the presence of intrathecal antibody synthesis. NMDARE postmortem or biopsy brain samples have also showed $CD138^{+}$ infiltrates near choroid plexus, around blood vessels and in the brain parenchyma [157], with a very small fraction of monoclonal antibodies derived from NMDARE patient CSF B cells (9/170, 5.3%) specific for NR1 [158]. However, seroprevalence of NMDAR antibodies in healthy patient populations (5-15%, increasing with age) complicates study of these autoantibodies [159]. One study of immune cells in tonsils removed from PANDAS patients showed elevated expression of TNFα and eotaxin-3, and decreased expression of IP-10, IL-8, IL-17A, IFNγ, and IL-12 compared to non-autoimmune GAS pharyngitis patient tonsils [160]. There was no difference in CD19, BAFF, or BAFFR expression (B cell and B cell subset markers) in PANDAS tonsils [161], and no studies to date have examined immune cell populations in PANDAS CNS. Efficacy of steroid and plasma exchange therapies in PANDAS patients suggest that if B cells or plasma cells are involved, they are probably producing autoantibodies peripherally, and the antibodies themselves infiltrate the BBB, and that B cells remain excluded

from the parenchyma [162]. In animal models of PANDAS, B cell chemokine *CCL19* mRNA is upregulated 3.6-fold in olfactory bulb, and *CCL21* is upregulated 16-fold compared to healthy controls, but no B cells were detected in CNS tissues by immunohistochemistry (Maryann Platt, see Chapter 4). The extent to which B cells or plasma cells drive PANDAS pathogenesis remains unclear, and if they act systemically or within the CNS parenchyma to either produce antibodies or present antigen.

1.3.2 T cell-driven brain autoimmunity

T cells differentiate into one of several terminal subsets from naïve precursors in response to antigen presentation by dendritic cells. Each T cell subset is induced by different cytokines in conjunction with unique transcription factors (**Figure 1.5**). Evidence from human and rodent models of MS and AE strongly implicate $CD4^+$ and $CD8^+$ T cells in various steps in pathogenesis. EAE, driven by $CD4^+$ T cells, provides robust evidence that different populations of T cell infiltrate in the CNS are capable of initiating and propagating disease [92, 100, 106, 163-165]. Recent data also demonstrate that different populations of T cells preferentially traffic through TJs or $Cav1^+$ vesicle transport, suggestive of different adhesion molecule profiles [92, 106]. T cell subtypes express unique panels of chemokine receptors and different inflammatory cytokines, so recruitment of mixed T cell populations results in heterogenous inflammatory cytokine pools local to inflammation. GAS infections in mice trigger robust Th1 and Th17, but minimal Treg and Th2 populations in the nose [166]. Strains of mice with knockout of either T cell subpopulations or cytokine genes have delineated specific roles for T cell subtypes (Th1, Th17, Tregs) and inflammatory cytokines (IL-17 family, IL-1β, IFNγ, GM-CSF) [97, 164, 165, 167-172]. Specifically, it has been shown that IL-17A (or the Th17 cells that secrete this cytokine) are

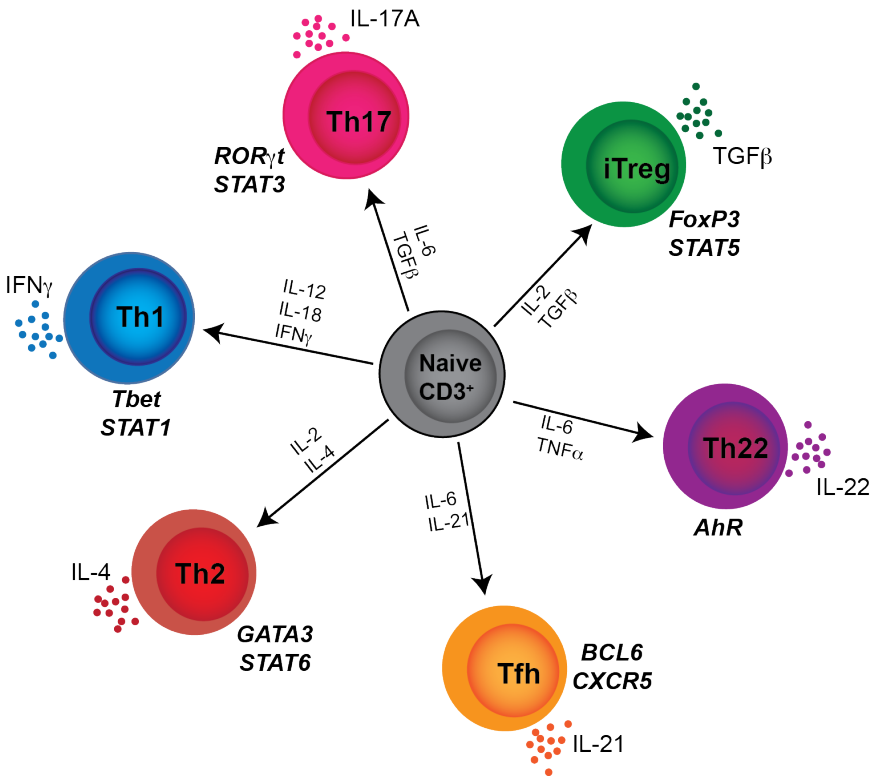

Figure 1.5 Differentiation and effector cytokine production of T cell populations. T cell subtypes are induced to differentiate by unique combinations of transcription factors, resulting in cytokine secretion.

important but not essential for EAE disease initiation and progression; expanded pools of IFNγ-producing cells can inefficiently induce disease [165, 169, 173] . Therefore, Th17 cells play a pivotal role in promoting severe CNS autoimmunity. Th2 cells, characterized by IL-4 production, are anti-inflammatory and have a protective effect on overall disease course, similar to Tregs, which limit activation and proliferation of other T cell subtypes in the inflammatory microenvironment [165]. Indeed, depletion of either of these T cell subtypes increases susceptibility to EAE [167, 174].

In other AE syndromes, Th17 have been shown to play a similar role in exacerbating immune responses. T cells (of unknown subset) can be found in the parenchyma of treatment-refractory NMDARE patient brain samples, and IL-17A levels in CSF correlate with poor disease prognosis and relapse [175, 176]. Mouse models of neuromyelitis optica (NMO) show that primed

Th17 cells are capable of efficiently initiating disease, while primed Th1 are less effective and yield less severe disease [177]. Sera and CSF from acute disseminated encephalomyelitis (ADEM) patients showed elevated levels of Th1- and Th17-associated cytokines, implying a role for autoimmune mechanisms [98]. Taken together, research on both human and mouse neuroinflammatory disorders demonstrates a link between Th17/IL-17 family cytokines and diseases severity. The extent to which Th17 cells are involved in AE pathogenesis remains unclear.

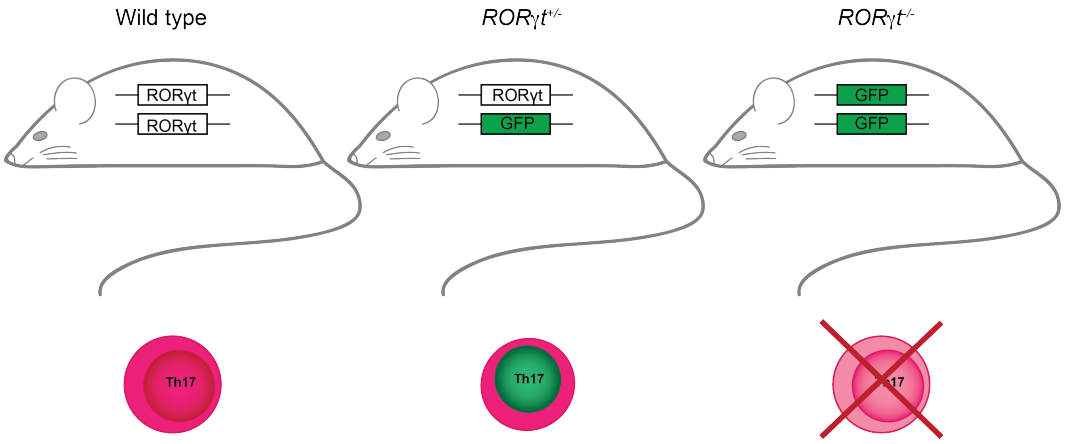

Figure 1.6 Labeling or deletion of Th17 cells in the *RORγt-GFP* mouse line. Heterozygous mice develop normally, and differentiated Th17 cells are labeled with GFP. Homozygotes do not develop Peyer's patches or lymph nodes, and Th17 cells cannot differentiate. Adapted from [178].

One useful genetic tool to provide insight into the role of Th17 cells in these diseases is the *RORγt-eGFP* mouse line [179]. As depicted in **Figure 1.6**, the knockout-knockin mutation in this line has a dual effect: heterozygotes have one copy of *RORγt* replaced with GFP, which labels differentiated Th17 cells with GFP; in homozygous mutant mice, Th17 cells cannot differentiate. This genetic tool allows for assessment of Th17 populations during disease course, and for assessing contribution of Th17 populations to disease pathogenesis.

1.3.3 Microglia and macrophages in neuroinflammatory autoimmune diseases

Microglia are the resident immune cell population of the brain, and can both phagocytose like peripheral macrophages and present antigen like dendritic cells. Microglia express high levels of CX_3CR1 (fractalkine receptor), and are capable antigen presenting cells in their own right. They use innate adaptive signaling (e.g., complement) for both homeostatic purposes (e.g., synaptic sculpting) and in pathogen response [180]. Microglia, like macrophages, also pump out chemokines to activate adaptive immune responses when they sense infection. Throughout development and in adulthood, microglia are highly dynamic, and even at rest continuously sample their extracellular environment to clean up debris and search for inflammatory signals [181].

The role of microglia in the pathogenesis of AE syndromes is unclear. The main roles of microglia seem to be twofold: first, potentiating inflammatory responses from infiltrating immune cells; second, aberrant engulfment of synapses through faulty complement deposition during neuroinflammation. Microglia proliferate in response to systemic inflammation induced by LPS, which may be translatable to inflammation induced by infection [182]. Upon BBB disruption or local inflammation, highly ramified resting microglia round up and shorten their processes to take on a reactive shape [183]. Microglia express chemokine receptors CX_3CR1, CXCR3, and CCR2, and receive the strongest signals from neurons expressing ligands CX_3CL1, CCL21, and CCL2, respectively [184, 185]. Upon activation by inflammatory signals (e.g., fibrinogen from plasma, matrix metalloprotease-9, CCL2, CCL21), activated microglia act as potent phagocytes, and secrete inflammatory factors (IL-1β, TNFα, NOS, and ROS, in classically inflammatory microglia, and VEGF, TGFβ and IL-10 in a more anti-inflammatory context) [183]. These cytokines recruit macrophages, leukocytes, and other microglia to the site of inflammation, potentiating the response. In a mouse model of NPSLE, microglia were shown to mediate aberrant neuronal signaling by release of TNFα in a coculture system [186].

The role of microglia in synapse degradation for AE is unclear. In NPSLE, indirect evidence of interferon-dependent microglial synapse degradation in hippocampi (not due to peripheral immune infiltration) provides one such link [187]. The IFNα/β receptor IFNAR is known to regulate microglial activation state, and inflamed NPSLE brains show increased phagocytosis of tagged tau debris in this model [187]. Close proximity of activated microglia to stripped synapses in a mouse model of post-infectious BGE also supports a role for microglia in aberrant synaptic pruning in disease [93]. More work on the potential roles of microglia in AE diseases is needed.

Perivascular macrophages express similar chemokine receptors as peripheral macrophages, which allows them to present antigen and reactivate lymphocytes in inflammation. Chemokine signaling is probably involved in localization of perivascular macrophages and microglia to their compartments, but the precise mechanisms remain poorly understood [188]. Peripheral macrophages and monocytes are key players in neuroinflammation in EAE models of MS. Their infiltration after BBB breach is well-documented, and they secrete cytokines and chemokines exacerbating damage to the CNS. Assessing the distinct contributions of microglia vs parenchymal macrophages in homeostasis and during neuroinflammatory diseases is a subject of ongoing research, as these two cell types are almost indistinguishable based on morphology and surface marker expression. To date, the only reliable differentiator is TMEM119, which is expressed on mouse and human microglia and absent from infiltrating macrophages [189, 190].

1.3.4 Dendritic cells in neuroinflammatory diseases

Recent work has defined a dendritic cell (DC) niche in CNS inflammation. Many of these results include extensive characterization of infiltrating DCs as separate from CNS-resident

microglia, as activated microglia are capable of presenting antigen and secrete many of the same inflammatory cytokines as DCs. DCs are required for antigen presentation to infiltrating T cells, and can reactivate MOG-directed T cells even in the absence of additional antigen, as shown by elegant selective ablation experiments in putative CNS APC populations [191]. Persistent DC presence in the CNS leads to more severe clinical pathology, indicating that CCR7-mediated signaling is critical to control disease pathogenesis [146]. Vascular endothelial growth factor (VEGF)-mediated lymphangiogenesis in the cribriform plate facilitates chemokine-mediated clearance of DCs that accumulate in the anterior portion of the brain [192]. It is unclear how DCs transmigrate across the BBB, but in EAE many immune cells cross the barrier following its breach by Th17 lymphocytes.

1.3.5 The role of chemokine signaling in immune cell trafficking to the CNS in neuroinflammation

Chemokines are small (8-14 kDa) secreted signaling molecules that bind to GPCR receptors expressed on the surface of immune cells. There are over 50 chemokine ligands and 19 receptors described to date. Chemokine receptors can be promiscuous or exclusive, depending on the receptor and, in some cases, on cell type [193]. Chemokines are classified as CC, CXC, CX_3C, and XC according to sequences of cysteines and intervening amino acids (X) in a conserved region. Some chemokine receptors are constitutively expressed on immune cell populations, while some receptors are upregulated only in inflammatory conditions [193]. Various immune cell populations may constitutively express a receptor that can be transiently induced in other populations, and there is much redundancy and cross-talk built into the signaling system, as demonstrated by **Figure 1.7**. Chemokine signaling connects lymphatic and blood endothelium with the CNS milieu and infiltrating immune cells [12, 194]. Reciprocal signaling is indispensable for initiating

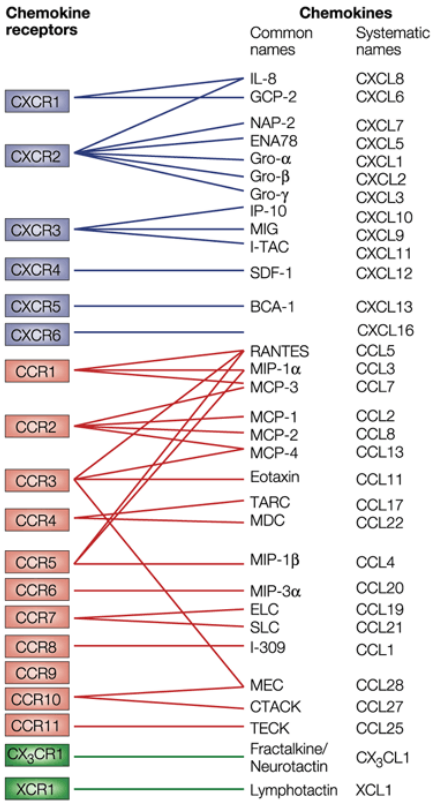

Figure 1.7 Schematic representation of chemokine ligand-receptor binding pairs Chemokines and their receptors can be promiscuous or exclusive. Reprinted from [193].

neuroinflammation and dampening the immune response to control symptoms. Because redundancy is high in chemokine networks, examination of the contribution of individual chemokine/receptor signaling pairs can be a challenge. Once bacterial infection occurs, the adaptive immune system begins to mount a response to destroy the pathogen. Once directed by DCs, T cells migrate from lymph nodes to the site of infection, guided by chemokine cues. Chemokine gradients are maintained by tethering chemokine ligands to the endothelial extracellular matrix or to glycosaminoglycans [188]. Chemokine signaling is essential to pathogenesis of many diseases, including MS, nephritis, atherosclerosis, asthma, and cancer.

Research on T cell trafficking in EAE has clarified the role of chemokines in disease progression, and has been instructive for potential chemokine cues in AE. CCL20/CCR6 signaling is important for EAE initiation and neo-lymphogenesis, and is required for initial entry of Th17 through the choroid plexus during the first wave of T cell entry into the CNS [129]. The second wave of Th1 infiltration is mostly governed by increased CCL2 expression. Over the course of EAE, the inflammatory chemokines CCL2 and CCL5 are upregulated, and constitutive cytokines

CXCL10, CXCL12, CCL19, CCL20 and CCL21 are expressed at higher levels on ECs [188, 195]. Some of these chemokines are also expressed on other cell types during EAE, with CCL2, CXCL12, CXCL19 upregulated in astrocytes, and CXCL19 expressed on microglia [195]. Treg cells harvested from mice with EAE can self-potentiate in areas of active inflammation by secreting both CCL1 and expressing its receptor, CCR8; this effectively dampens local inflammation and suppresses lesion formation [174]. Indirect evidence for antigen-specific T cell recruitment to the CNS in AE was demonstrated using CSF samples from AE patients. Patient CSF was enriched for CCL2 and CXCL10, as well as for white blood cells expressing CXCR3, the cognate receptor for CXCL10 [196]. Taken together, these data detail mechanistic links that tie neuroinflammation seen in AE to generally accepted mechanisms of neuroinflammation and CNS T cell infiltration.

Like T cells, B cells respond to chemokine cues through CCR7 signaling. CCL19 and CCL21 guide B cells to and from draining lymph nodes as needed [193]. Upregulation of CXCL13 near MS lesions [153], and of CCR6 on activated B cells [197] identifies chemokine axes that may be instrumental in B cell recruitment or localization to the brain. Monocytes constitutively express CCR2, and respond to CCL2 secreted by astrocytes to home to inflammatory lesions in MS and EAE [198-200]. Monocyte infiltration is a critical step in EAE pathogenesis, and interrupted CCL2/CCR2 signaling in $CCR2^{-/-}$ mice blunts disease progression. CCL2 is constitutively expressed by neurons at low levels basally. Under hypoxic conditions, neurons will upregulate CCL2 signaling to surrounding microglia, but without increased macrophage populations in the CNS, implying that there may be a threshold of CCL2 required for macrophages to cross the BBB into the brain [184, 188]. In EAE, DCs are recruited to the spinal cord, cerebellum, cortex, and

olfactory bulb in EAE by CCL2/CCR2 interactions [201, 202], and use CCR7/CCL21 and CCL19 signaling to exit the CNS and drain to peripheral lymph nodes [146].

CXCR4 expression is upregulated on $CD19^+$ NPSLE B cells compared to controls, and symptom severity correlated with higher CXCR4 expression and with CNS involvement. Elevated expression of its ligand CXCL12 in kidney glomeruli was highly correlated with lupus nephritis disease severity [203, 204]. However, clinical studies of B cell treatment in NPSLE patient populations are inconclusive in their efficacy, or have low sample sizes.

1.4 Lessons from animal models of autoimmune encephalitis

Numerous rodent studies have expanded our understanding of the molecular events involved in antibody generation and pathogenicity. Rodent models for NMDARE, basal ganglia encephalitis (BGE), GAD65 encephalitis, LGI-1 and Caspr2 encephalitis, and Morvan syndrome vary widely in both their methods of antigen exposure and disease parameters recapitulated. Expansion of the EAE immunization model to expose mice to foreign (or self-) antigens greatly expanded understanding of disease processes [80, 205, 206]. Conversely, passive infusion and adoptive transfer models clarified how autoantibodies harvested from patients may interact with an intact CNS [19, 206-211]. Animal models for post-Streptococcal AE have been focused on demonstrating the ability of GAS to prime development of an autoimmune reaction by stimulating adaptive cellular and humoral immune responses. A summary of current literature on rodent AE models is summarized in Table 1.1, and reviewed here in more depth for several AE subtypes.

Disease	Strain / Species (Sex)	Autoantibody source	Delivery	Immune response	Neural consequences	Reference
SC/PANDAS	SJL mouse (F)	Unknown	Intranasal infection with GAS	Microglial activation and infiltrating CD4+ T cells in OB	Decreased excitatory synapse proteins in olfactory bulb glomeruli	Dileepan et al., JCI 2016
SC/PANDAS	Lewis rat	Induced in model	Subcutaneous immunization with GAS emulsion	Autoantibodies detected against tubulin	Dopamine D2-dependent compulsive grooming; impaired motor coordination; IgG deposition in striatum, thalamus and cortex; IgG-induced elevation of CamKII signaling in cultured neurons	Brimberg et al., Neuropsychopharmacology 2012
SC/PANDAS	SJL mouse	Induced in model	Subcutaneous immunization with GAS emulsion	Specific increase in IgG1 subclass, no change in IgG2 nor IgG3 pool	Increased rearing; decreased motor coordination; impaired olfactory discrimination; improved spatial memory performance; IgG deposition in straitum and cerebellum	Yaddanapudi et al., Molecular Psychiatry 2010
SC/PANDAS	SJL mouse (M)	Adoptive transfer from immunized cohort	Intravenous injection with intraperitoneal LPS	Not analyzed	Increased rearing; IgG deposition in dentate gyrus	Yaddanapudi et al., Molecular Psychiatry 2010
SC/PANDAS	Lewis rat (M)	Induced in model	Subcutaneous immunization with GAS emulsion	Autoantibodies against D1R, D2R and serotonin receptors	Impaired motor coordination; compulsive grooming	Lotan et al., Brain, Behavior, and Immunity 2014
SC/PANDAS	Lewis rat (M)	Adoptive transfer from immunized cohort	Intrastriatal infusion	Not analyzed	Impaired motor coordination; IgG deposition in striatum	Lotan et al., Brain, Behavior, and Immunity 2014
SC/PANDAS	SJL mouse (M)	Induced in model	Subcutaneous immunization with GAS emulsion	Microglial activation in white matter tracts, infiltrating CD4+ T cells	Impaired motor coordiation; repetitive behaviors; increased rearing; excessive lactate; blunted startle response (PPI)	Macri et al., Scientific Reports 2015
SC/PANDAS	SJL mouse (F)	Induced in model	Subcutaneous immunization with GAS emulsion	IgG against complement C4 and α2-macroglobulin	Increased rearing and decreased ambulation; synaptic IgG deposition in deep cerebellar nuclei	Hoffman et al., J Neurosci 2004
SC/PANDAS	C57BL/6 mouse (M and F)	Patient sera	Intrastriatal infusion	Not analyzed	IgG deposition on ChAT+ striatal interneurons, abrogated in sera samples collected after IVIG treatment	Frick et al., Brain, Behavior, and Immunity 2018
SC/PANDAS	BALB/C mice (M)	Commercial anti-GAS IgM and IgG	Subcutaneous injection	Striatal Fc$\alpha\mu$R upregulation	Stereotypy after IgM but not IgG injection; IgM-linked increased cFos reactivity and IgM deposition in striatum and mucleus accumbens	Zhang et al., Brain, Behavior, and Immunity 2012
NMDA receptor encephalitis	Lewis rat	Patient CSF	Bath application to cultured neurons	Not analyzed	Autoantibody-mediated internalization of NMDAR from synapses; selective loss of NMDA-mediated currents	Hughes et al., J Neurosci 2010
NMDA receptor encephalitis	Lewis rat (F)	Patient CSF	Intrahippocampal infusion	Not analyzed	Decreased NMDAR density in hippocampus	Hughes et al., J Neurosci 2010
NMDA receptor encephalitis	C57BL/6 mouse	Patient CSF	Intravenous injection with intraperitoneal LPS; bath application to cultured neurons	Not analyzed	Antibody deposition in hippocampus and cerebellum; decreased Ca2+ flux, loss of synaptic clusters, and reduced NMDA-dependent currents in vitro cutured neurons	Kreye et al., Brain 2016
NMDA receptor encephalitis	C57BL/6 mouse	Patient sera	Intraventricular injection	Not analyzed	IgG deposition in hippocampus; more seizures and higher seizure scores after pro-convulsant challenge; no change in total NMDAR number	Wright et al., Brain 2015
NMDA receptor encephalitis	ApoE-/- or C57BL/6N (M) mouse	Patient sera	Intravenous injection	All autoantibody isotypes affected behavioral assessments and endocytosis	Decreased spontaneous locomotion and increased MK-801-evoked locomotion in ApoE-/- mice, but not WT, treated with autoantibody; increased endocytosis by cultured neurons after autoantibody treatment	Hammer et al., Molecular Psychiatry 2014
NMDA receptor encephalitis	C57BL/6 mouse (M)	Patient CSF or purfied IgG	Intraventricular infusion	Not analyzed	Seizures; reduced excitability of hippocampal CA1 neurons from mice treated with patient CSF	Taraschenko et al., Epilepsia 2019
NMDA receptor encephalitis	C57BL/6J mouse	Patient CSF	Intraventricular infusion	Not analyzed	Reversible memory deficits, anhedonia, and depressive-like behavior without locomotor impairment; hippocampal IgG deposition; decreased NMDAR density in hippocampus	Planaguma et al., Brain 2015
Post-HSV NMDA receptor encephalitis	BALB/C mice (F)	Unknown	Intranasal Herpes simplex virus infection	Anti-NMDAR antibody titers in 4/6 mice	Reduced hippocampal NMDAR density in mice with NMDAR antibodies	Linnoila et al., Neurology Neuroimmunology & Neuroinflammation 2019
Limbic encephalitis (LGI1)	C57BL/6 mouse (M)	Patient sera	Intraventricular infusion	Not analyzed	Hippocampal dentate and CA1 hyperexcitability, impaired LTP in CA1, antibody-dependent memory deficits	Petit-Pedrol et al., Brain 2018
Stiff person syndrome/cerebellar ataxia	Wistar rat (M)	Patient sera	Intracerebellar infusion	Not analyzed	Decreased potentiation from excitatory stimulus trains; decreased NMDA-mediated NO synthesis	Manto et al., Annals of Neurology 2007
Stiff person syndrome/cerebellar ataxia	Wistar rat (M)	Patient sera	Lumbar paraspinal injection	Not analyzed	Abnormal high baseline activity; increased excitability of anterior horn neurons	Manto et al., Annals of Neurology 2007
Stiff person syndrome/cerebellar ataxia	Lewis rat (F)	Patient sera	Intrathecal infusion	Not analyzed	Paralysis; autoantibody-mediated internalization of ampiphysin on GABAergic neurons; decreased GABA release from cultured neurons; increased IPSC frequency and amplitude recorded *in vivo* from hippocampal granule cells	Geis et al., Brain 2010
Stiff person syndrome/cerebellar ataxia	Lewis rat (F)	Patient CSF	Intrahippocampal injection	Not analyzed	No changes in evoked and spontaneous GABAergic transmission in CA1 neurons	Hackert et al., Frontiers in Cellular Neuroscience 2016
Stiff person syndrome/cerebellar ataxia	cultured mouse hippocampal neurons	Patient sera	Bath application	Not analyzed	No changes in evoked and spontaneous GABAergic transmission in cultured hippocampal networks	Stemmler et al., Frontiers in Neurology 2015

Table 1.1 (Previous page) Animal models of AE syndromes and associated immunological and neurological findings. Updated from [50].

1.4.1 Mechanisms of NMDA receptor encephalitis

NMDARE models almost exclusively utilize intracerebral infusion of serum antibodies harvested from acutely ill patients into rodents in an attempt to replicate behavioral symptoms. Infusion of autoantibodies from NMDARE patients into lateral ventricles of mice causes impaired recognition memory after 10 days of antibody infusion, which is reversible upon antibody washout [209]. IgG binding is strongest in the hippocampus, which has a very high density of NMDAR, supporting the hypothesis that NMDAR clustering and internalization may underlie memory deficits with minimal effects on aggression, locomotion, and anxiety-like behavior [209, 210, 212, 213]. On the circuit level, mice infused with NMDARE sera were more susceptible to seizures than controls [210, 214], with similar delta-brush EEG patterns detectable in human NMDARE patients and sera-infused mice [18, 211]. NMDAR antibodies are only detectable in rodent brains after intravenous injection of patient antibodies with parallel LPS injection or in *ApoE*$^{-/-}$ mice with a defective BBB, illustrating the necessity of BBB breakdown for pathogenic binding [158, 207, 212].

Ex vivo and *in vitro* studies have proven invaluable for determining the mechanism of action of NMDAR Abs. NMDAR Ab binding interferes with EphrinB2-EPHB2R signaling that tethers NMDA receptors to their synaptic sites. Autoantibody binding thus releases NMDA receptors from the synapse, causing them to diffuse off synaptic boutons and become internalized. Accumulation of intracellular NMDAR and loss of surface NMDAR after treatment with patient antibodies is reversible with antibody washout. Treatment with EphrinB2 together with anti-NMDAR antibodies also rescues loss of NMDA receptors *in vitro* and *in vivo* [213]. It appears that internalized NMDARs are not targeted for lysosomal degradation, due to lack of involvement

of Rab proteins (endolysosomal mediators) in NMDAR internalization [215]. In recordings from acute hippocampal slices, NMDAR antibodies decreased NMDAR-dependent hippocampal long-term potentiation (LTP) in a manner similar to commercial blocking antibodies directed against extracellular domains of NR1 and NR2 subunits. Hippocampal CA1 neurons from mice infused intraventricularly with patient antibodies showed reduced excitability [214], and dentate gyrus granule cells showed smaller evoked activity, impaired LTP, and increases spike thresholds after NMDAR Ab exposure [19, 216]. Cultured neurons treated with patient antibodies showed both reduction in synaptic puncta and selective reduction in NMDA currents with no effect on AMPA, GABA, or kainate signaling [158, 212].

Substantial evidence supports the hypothesis that NMDAR Ab binding leads to cross-linking and internalization, but not necessarily destruction, of the receptor, causing deficits in synaptic and circuit function. Importantly, these models also bypass the BBB; NMDAR antibodies are efficiently excluded from the hippocampus if delivered intravenously [207]. *ApoE*$^{-/-}$ mice intravenously injected with NMDAR antibodies demonstrate Ab binding to CNS targets and decreased locomotion compared to either mice injected with control IgG, or WT mice injected with NMDAR antibodies [207]. Herpes simplex virus (HSV) infection is hypothesized to cause BBB permeability [39]; in an animal model of HSV encephalitis, a subset of mice developed anti-NMDAR antibodies and reduced NR1 subunit density in hippocampus [38]. There is a clear need to develop more animal models for NMDARE that incorporate study of BBB breach to more closely mirror the human syndrome.

1.4.2 Synaptic antigens linked to AE

Autoantibodies against proteins involved in γ-amino butyric acid (GABA)-ergic transmission, including anti-glutamic acid decarboxylase (GAD) 65, anti-GAD67, $GABA_A$ receptor, $GABA_B$ receptor, and anti-amphiphysin, are the putative autoantibodies for cerebellar ataxia, stiff person syndrome, and Batten's disease [1, 217]. $GABA_B$ receptor ($GABA_BR$) encephalitis is linked to small cell lung cancer, and patient CSF binds strongly to rodent tissue sections [26]. Slice recordings from neurons exposed to GABABR antibodies showed decreased firing reversible by washout [218]. $GABA_A$ receptor ($GABA_AR$) encephalitis antibodies have been shown histologically both on tissue sections and cultured neurons to bind to neuropil and cell surface, confirming specificity to their target through agreement with commercial $GABA_A$ antibody staining patterns [219]. Intracerebral infusion experiments have been conducted using patient samples of autoantibodies for these targets, with conflicting results. Bath application of anti-GAD65 antibodies increased inhibitory post-synaptic potential (IPSP) frequencies in cultured neurons [220]. Cerebellar infusion of GAD65 antibodies in rodents interfered with GABA synthesis in cerebellar basket cell terminals, leading to Purkinje cell hyperactivity. however, hippocampal infusion of anti-GAD65 yields no changes in synaptic transmission in acute hippocampal slice preparations that demonstrated strong effects after anti-NMDAR Ab infusion [221]. It is possible that anti-GAD65 antibodies do not strongly target hippocampal cells, or that they cannot reach their intracellular target before they are degraded or removed from the interstitial space. Rats infused with autoantibodies against amphiphysin, rather than GAD65, have been shown to exhibit behavioral symptoms of stiff-person syndrome [222]. Anti-amphiphysin antibodies are more strongly associated with tumors elsewhere in the body compared to many other AEs [223]. Methodological differences between groups and debate about pathogenicity of GAD65 autoantibodies has complicated interpretation of results to date. This is because GAD65

autoantibodies are prevalent, albeit at lower concentrations, in many type 1 diabetic patients with no neurological abnormalities. Careful screening is essential in determining a donor population for research samples in order to exclude likely non-pathogenic antibodies that present in diabetic patients.

GQ1b autoantibodies have been implicated in Miller Fisher syndrome, but limited research on the central effects of these antibodies hinders the understanding of disease pathogenesis. GQ1b antibodies have been shown to induce complement deposition; the combination of complement with antibody deposition is necessary for neuromuscular junction dysfunction *in vivo* [224]. Binding of the antibody-complement complex induces local Ca^{2+} flux into neurons *in vitro*, which alters mitochondrial function and excites the neuron [224]. Mechanistically, this provides an interesting insight into the potential role of the innate vs the adaptive immune system in AE action.

Antibodies targeting components of the voltage gated potassium channel (VGKC) complex have historically been lumped together as targeting the whole scaffolding complex, with little distinction given to individual proteins that comprise the VGKC, since the scaffold complex precipitated together with the channel in the original identification [20, 225, 226]. Recent work has defined individual targets that comprise or associate with the VGKC: Caspr2, LGI1, and Contactin2 [20]. Most investigation into the VGKC complex antibodies used rodent tissue or cultured cells to assess reactivity of patient sera or CSF. Sera from AE patients both react with rat [227] and mouse [21] hippocampal sections, as well as HeLa cells transfected with potassium channels $K_v1.1$ and $K_v1.2$, but not with *Caspr2*$^{-/-}$ mouse brain sections [21]. Adoptive transfer of patient sera or purified anti-Caspr2 IgG into mice showed that repeated immunizations with patient IgG increased quantal size and K^+-dependent amplitude of excitatory post-synaptic potentials (EPSPs) in peripheral nerves, but did not alter behavior [228].

Comparatively more is known about the mechanisms of action of LGI1 antibodies in brain. Deletion of LGI1 in all neurons, as well as conditional deletion in forebrain glutamatergic neurons using an Emx-Cre driver, resulted in epilepsy and perinatal lethality (by P25 and P32, respectively) [229, 230]. Postnatal deletion of LGI1 using the CaMKIIα-Cre driver resulted in later-onset, slightly less severe epilepsy, with premature lethality around P150 [229]. Mechanistically, LGI1 protein links presynaptic potassium channels and postsynaptic AMPAR scaffolding proteins; disruption in LGI1 structure or function selectively interferes with AMPAR-mediated signaling [230], illustrating its necessity for normal AMPAR-mediated brain function [229, 230]. Intraventricular infusion of purified patient LGI1 IgG caused hyperexcitability of hippocampal dentate gyrus granule cells and CA1 neurons, as well as memory deficits [231]. While there has been some progress in identifying potential mechanisms of action for these antibodies, initial confusion about target proteins hampered progress and left many questions unanswered.

1.4.3 Animal models of GAS-induced AE

The first group of rodent models of GAS-induced AE mirrors the EAE immunization model with an antigenic target (bacterial homogenate) in conjunction with complete Freund's adjuvant to activate the immune system and *B. pertussis* toxin to transiently permeabilize the BBB (**Figure 1.8**, left). In this model, mice and rats develop a strong humoral response against GAS and show behavioral abnormalities by motor and psychiatric metrics. GAS-immunized mice display increased rearing and decreased locomotion, as well as increased repetitive and perseverative behaviors, impaired pre-pulse inhibition and reduced serum serotonin concentrations in the prefrontal cortex, compared to controls [80, 205, 206, 232]. Histological examination of brain tissue in various studies has revealed IgG deposition in the deep cerebellar nuclei and

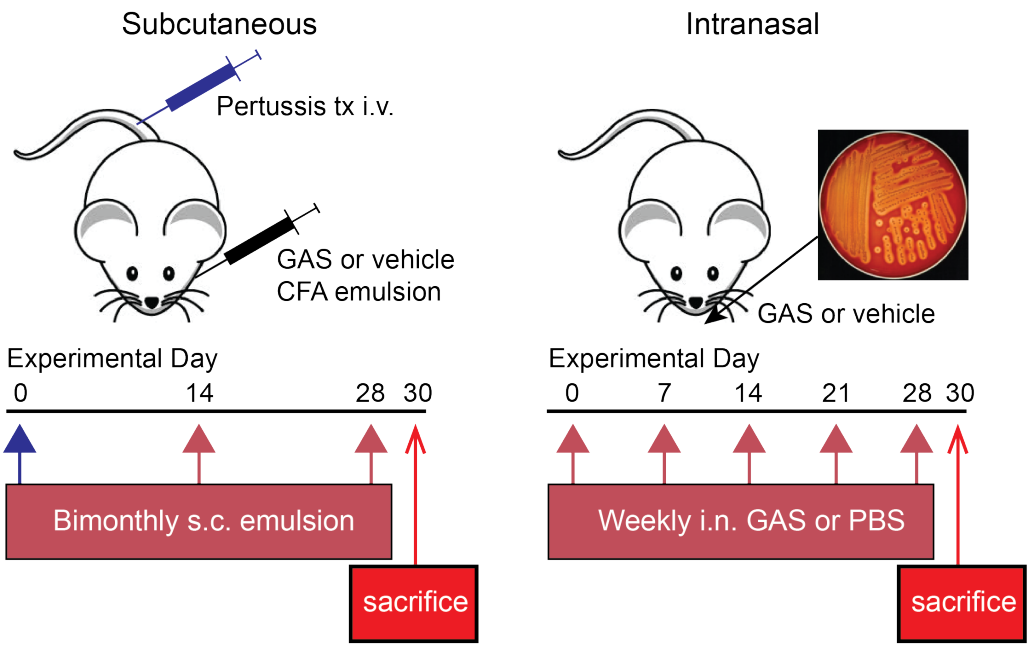

	Subcutaneous	Intranasal
T cell phenotype	Th1 (Macri, Ceci et al., 2013)	Th17 (Dileepan, Smith et al., 2016)
T cells in CNS	Few (Macri, Ceci et al., 2013)	Many (Dileepan, Smith et al., 2016)
Microglial activation	Moderate (Macri, Ceci et al., 2013)	Robust (Dileepan, Smith et al., 2016)
Neuronal dysfunction	Impaired PPI, decreased cortical 5HT (Macri, Ceci et al., 2013)	Degraded olfactory synapses (Dileepan, Smith et al., 2016)
Anti-GAS titer	High, autoreactive (Brimberg, Benhar et al., 2012; Lotan, Benhar et al., 2014)	?
BBB permeability	Not assessed	High (Dileepan, Smith et al., 2016)
Behavioral outcomes	Perseveration, Motor deficits (Yaddanapudi, Hornig et al., 2010; Brimberg, Benhar et al., 2012)	?

Figure 1.8 Comparison of two routes of GAS exposure to induce autoantibodies in rodent models. Left, repeated subcutaneous immunization with GAS-Complete Freund's adjuvant (blue and red arrows every 14 days) in combination with intravenous pertussis toxin (blue arrow on day 0 only) induces mild immunological abnormalities but replicated behavioral findings. Right, recurrent weekly intranasal inoculation with live GAS induces strong immune phenotypes. Behavioral findings are, to this point, unknown. Below, table comparing various outcome measures between the two models. Updated from [50].

hippocampus in mice, and the striatum, cortex, and thalamus in rats [80, 205, 206]. Serum isolated from immunized rodents bound to both cerebellar targets and human dopamine D1/D2 receptors

by either Western blot or ELISA [80, 206]. Motor and anxiety-like phenotypes are dominant outcomes in this model, with peripheral immune responses playing a minimal role. Comparison of findings from GAS-primed models reviewed here to Poly I:C or LPS injections show some overlap, indicating that systemic inflammation may be driving some of the psychiatric findings (reviewed in [233]).

A second mouse model that directly produces anti-GAS antibodies utilizes intranasal inoculations with live GAS bacteria (**Figure 1.8**, right). In the mouse, intranasal (i.n.) infections with live GAS bacteria polarize T cells in the nasal associated lymphoid tissue (NALT) toward a Th17 phenotype. This T cell subtype is both essential for mucosal immune protection against bacteria, and strongly implicated in many autoimmune diseases. Multiple GAS infections strengthen this Th17 immune response due to induction of IL-6 and TGF-β, two proinflammatory cytokines that drive Th17 differentiation [50, 93, 234]. IL-6 is essential for clearance of bacteria after i.n. infection; *IL-6*$^{-/-}$ mice are capable of mounting a Th1 immune response to i.n. bacterial challenge but cannot control the infection [235]. This model has been used to demonstrate that repeated i.n. GAS infections induce migration of GAS-specific Th17 cells and other T cell subtypes from the olfactory epithelium (OE) into the olfactory bulb (OB) [93]. Presence of T cells in the CNS after recurrent GAS infections also permeabilizes capillaries in several CNS regions, including the OB, amygdala, and hypothalamus, permitting deposition of serum IgG. BBB permeability in this case is largely a result of disorganization of tight junction proteins [93]. This intranasal model produces profound changes in olfactory circuitry by reducing vGluT2 expression (and, thus, excitatory input) at the presynaptic terminals of olfactory sensory axons [93]. This initiates a cascade of signaling abnormalities at the initial terminus of olfactory sensory axons. This model of GAS-induced autoimmunity demonstrates a central role for the adaptive cellular

immune response (e.g., GAS-specific Th17 cells in the CNS) in disrupting BBB function, thus promoting entry of antibodies into the CNS to allow for changes in synaptic signaling. Although a cellular adaptive immune response has not, to date, been identified in SC or PANDAS patients, GAS-specific Th17 cells can be found in the tonsils of human patients [93], making Th17 cells a potential causative agent in either initiation or persistence of AE pathogenesis.

Finally, direct injection of sera from PANDAS or SC patients allows for investigation of what cell populations are targeted by human autoantibodies. Systemic subcutaneous injection of monoclonal anti-GAS IgM, but not IgG, antibodies resulted in antibody deposition in striatum and cortex that colocalized with Fcαμ receptors. Behavioral changes and alterations in neuronal activity induced by IgM were rescued by IVIg treatment [236]. Intrastriatal infusion of serum IgG from Tourette's patients resulted in behavioral and motor stereotypy [236], while PANDAS sera infusion resulted in IgG deposition on cholinergic ($ChAT^+$), but not $parvalbumin^+$ or $nNOS^+$ striatal neurons [82]. The literature is conflicting on motor and histological findings after intrastriatal infusion of SC sera [237, 238]. Taken together, adoptive transfer of serum IgG from GAS-immunized mice into naïve recipients, or direct intracerebral infusion of human sera into rats, recapitulates some of the behavioral deficits in recipients. No effects were observed in rodents infused with IgG-depleted sera [81, 206]. There has been some investigation of what targets are recognized by infused PANDAS and SC antibodies, but more work is needed to resolve debate in this area [80, 81, 237-239]. These studies open up an avenue for further exploration of striatal involvement in these diseases.

Differences between mouse and rat GAS-induced AE models may reflect key genetic differences between the species, especially those related to the MHC locus and T cell function. All studies used inbred animals (Lewis rats, SJL or C57Bl/6 mice), so congenicity is very high in these

variable regions, but differences between strain and species may be magnified. It is also possible that different findings in mouse and rat studies could be due to variability in the humoral immune response to GAS between species or slight differences in the respective immunization protocols. Additionally, infectious load in animal colonies influences the immune response to immune challenge, requiring titration of adjuvants or infectious load [167]. Taken together, subcutaneous GAS immunization models have provided useful information regarding humoral immune response after bacterial infection, and demonstrate a link between GAS exposure and behavioral abnormalities. However, these are somewhat artificial models for immune system activation, as human GAS pharyngitis occurs primarily by the i.n. route. Moreover, these barrier-compromised AE models cannot address the question of how circulating antibodies might gain access to their CNS targets [6].

1.5 Concluding remarks

Both human studies and rodent models of AE strongly implicate the immune system in pathogenesis. While rodents provide a useful model system to study immune response to both an inciting infectious agent as well as autoimmune complications at later timepoints, mice are inherently poor models of the complex psychiatric symptoms characteristic of the AE patient population. Work that has been done thus far in rodent models has relied heavily on direction from EAE, and while it has yielded valuable insights, the role of the BBB remains underappreciated in these models. There are several different pathways for blood-borne solutes (antibodies, inflammatory cytokines, and immune cells) to enter the brain, and how antibodies may be permitted to enter the CNS is still unclear. Once in the brain, antibodies have been shown to induce defective neuronal signaling either through direct binding to their target, or indirectly by causing

destabilization or internalization of neurotransmitter receptors. Neuroinflammation is also central to AE pathogenesis. The humoral and cellular immune systems must coordinate to breach the BBB, promote inflammatory infiltrate in the CNS, and generate brain-targeting antibodies. Systematic examination of each of these different routes of barrier breach will clarify both mechanisms of disease and new therapeutic targets. Still, work using tissues or intact animals exposed to pathogenic autoantibodies has pushed the field toward understanding the basic cell biological processes underlying disease.

The importance of learning from human studies in these rare diseases is crucial, and reducing phenomena to mouse models as true to type as possible will continue to provide translatable data. Maintaining a link between the bench and the bedside remains a critical point of reference in this field, and verification of findings at multiple levels (cellular, molecular, behavioral) will lend weight to data in a relatively niche field.

Chapter 2: Materials and Methods

2.1. Experimental procedures, protocols, and reagents

All experiments were approved by the Institutional Animal Care and Use Committees at Columbia University (AAAX3452) and Duke University (#A220-15-08). Animals used for breeding and subcutaneous GAS immunization experiments were housed in the William Black building vivarium. Mice used for intranasal inoculation experiments were transferred to a BSL2+ vivarium facility in the Irving Cancer Research Center. Mice used for electrophysiological recording experiments were housed at Duke University in the Sands Research Building vivarium; recording experiments were conducted in the Bryan Research Building in the Franks lab.

2.1.1 Mice

Experimental mice were maintained on a 12-hour light/dark cycle with lights on from 6am to 6pm. Mice were housed in sex-matched cages of up to five mice with access to food and water *ad libitum*.

SJL/J

Female P25 SJL/J (Strain 000686) mice were obtained for subcutaneous immunization experiments from Jackson Labs (Bar Harbor, ME). This strain is predisposed to autoimmunity and is frequently used for EAE. SJL/J mice frequently develop reticulum small-cell carcinomas with Hodgkin's disease-like phenotypes by one year of age. Mice were housed in groups of four or five in the William Black building vivarium.

RORγt$^{GFP/GFP}$

Male and female *RORγt*$^{eGFP/+}$ [179] (B6.129P2(Cg)-*Rorc*^{tm2Litt}/J, Strain 007572) were obtained from Jackson Labs. In this strain, the coding region for *RORcγt*, a transcription factor necessary for Th17 differentiation, is replaced with eGFP. *RORγt*$^{eGFP/+}$ mice have fluorescently labeled Th17 cells (referred to as *RORγt*$^{+/-}$). *RORγt*$^{eGFP/eGFP}$ mice are unable to differentiate Th17, and have limited induction of peripheral lymph nodes and Peyer's patches (referred to as *RORγt*$^{-/-}$). *RORγt*$^{+/-}$ mice were interbred to obtain WT, *RORγt*$^{+/-}$, and *RORγt*$^{-/-}$progeny. Future mating pairs consisted of *RORγt*$^{+/-}$ crossed to *RORγt*$^{-/-}$ to obtain equal ratios of *RORγt*$^{+/-}$ and *RORγt*$^{-/-}$ progeny to be used in experiments.

CCR6 and CCR2 chemokine receptor knockouts

CCR2$^{-/-}$ [240] (B6.129S4-*Ccr2*^{tm1lfc}/J, Strain 004999) and *CCR6*$^{-/-}$ [241] (B6.129P2-*Ccr6*^{tm1Dgen}/J, Strain 005793) males were obtained from Jackson Labs and backcrossed to WT C57Bl6/J for five generations prior to use for experiments. Chemokine receptor homozygous mutant mice were interbred to obtain double mutants. *CCR6*$^{-/-}$ and *RORγt*$^{-/-}$ mice were interbred to obtain *CCR6*$^{-/-}$on the *RORγt*$^{+/-}$ background to track Th17 populations in the absence of CCR6 signaling. These strains are used to examine the role of chemokine signaling in CNS T cell homing.

2.1.1 Genotyping

DNA extraction

All mice were toe-clipped for identification and genotyping at P7-P9. Toe and/or tail samples were lysed overnight at 56°C with 400 µl lysis buffer (100 mM Tris HCl pH 8.0, 5 mM EDTA pH 8.0, 0.2% SDS, and 200 mM NaCl with 100 µg/ml proteinase K). DNA was extracted by adding 400 µl phenol/chloroform/isoamyl alcohol (25:24:1, v/v/v, Fisher) then vigorously mixed and

centrifuged at 13,200 rpm for 15 minutes at 25°C in an Eppendorf 5415D centrifuge. DNA was precipitated from 350 µl of the aqueous phase in 1 ml 95% ethanol by inverting the tube. The DNA pellet was dissolved in 100 µl TE buffer (10 mM Tris HCl pH 7.4 and 1 mM EDTA pH 8.0) overnight at 56°C.

PCR

PCR reactions were run with known positive, negative, and no-DNA controls in all reactions. Reaction components, equipment, primer sequences, and PCR protocols varied by gene target and are listed in **Table 2.1** below. PCR products were separated on a 1.5% agarose gel with 0.5% ethidium bromide at 80 V for 40 minutes.

Gene	Primer target	Primer sequence (5'-3')	Reagent	Volume per reaction (µl)	Temperature (ºC)	Time (M:SS)	No. Cycles	PCR products	Expected size (bp)	Thermal cycler
RORγt-GFP	Common forward	CCC CCT GCC CAG AAA CAC T	2x DreamTaq Master Mix	12.5	94	3:00	1	WT	174	Applied Biosystems 2720
	Wild type reverse	GGA TGC CCC CAT TCA CTT ACT TCT	Common forward primer	0.5	94	:30	35	Mutant	241	
	Mutant reverse	CGG ACA CGC TGA ACT TGT GG	Wild type reverse primer	0.5	50	1:00				
			Mutant reverse primer	0.5	72	1:00				
			ddH2O	10	72	2:00	1			
			Genomic DNA	1	4	Hold	1			
CCR2 knockout	Wild type forward	CCA CAG AAT CAA AGG AAA TGG	10x Taq buffer	5	94	3:00	1	WT	424	Applied Biosystems Veriti
	Wild type reverse	CCA ATG TGA TAG AGC CCT GTG	10mM dNTPs	1	94	:30	35	Knockout	280	
			50mM MgCl2	1	65	:30				
	Knockout forward	CTT GGG TGG AGA GGC TAT TC	125nM Forward primer	0.5	72	:30				
	Knockout reverse	AGG TGA GAT GAC AGG AGA TC	125nM Reverse primer	0.5	72	5:00	1			
			Taq enzyme	0.25	4	Hold	1			
			ddH2O	39.5						
			Genomic DNA	2						
CCR6 knockout	Wild type forward	CCC TAG AAG AGG TCA GAA ACT TCA C	2x DreamTaq Master Mix	12.5	94	3:00	1	WT	228	Applied Biosystems 2720
	Knockout forward	GGG TGG GAT TAG ATA AAT GCC TGC TCT	Common forward primer	0.5	94	:30	35	Knockout	442	
	Common reverse	AAA ACC CAA GTG TTG GTG GCA TGA G	Wild type reverse primer	0.5	57	1:00				
			Mutant reverse primer	0.5	72	1:00				
			ddH2O	10	72	8:00	1			
			Genomic DNA	1	4	Hold	1			
CD11c-eYFP	Transgene forward	TGC TGG TTG TTG TGC TGT CTC ATC	2x DreamTaq Master Mix	12.5	94	3:00	1	Transgene	550	Applied Biosystems 2720
	Transgene reverse	GGG GGT GTT CTG CTG GTA GTG GTC	Common forward primer	0.5	94	:30	35			
			Wild type reverse primer	0.5	65	:30				
			Mutant reverse primer	0.5	72	:30				
			ddH2O	10	72	2:00	1			
			Genomic DNA	1	4	Hold	1			

Table 2.1 PCR primer sequences, reaction conditions, and equipment used for genotyping.

2.1.3 Group A Streptococcus *intranasal inoculations*

Male and female littermates received a total of five weekly Group A *Streptococcus* infections prepared as described previously [93] beginning at age P21-28. Briefly, log-phase GAS cultures

($2x10^8$ CFU) were harvested, washed once in sterile PBS, then resuspended in 110 µl PBS without Ca^{2+} and Mg^{2+}. Heat-killed (HK-) GAS was used for some inoculations as described below. For these inoculations, GAS cultures were grown and harvested as described, then heat-killed for at least 30 minutes in an 85°C water bath. HK-GAS samples were streaked on blood agar plates to confirm absence of live bacteria, in parallel with a positive control from prior to heat treatment.

For inoculations, mice were lightly anesthetized with isoflurane (2.5% for induction in 1.5-2 L/min medical air), quickly removed from the induction chamber, and allowed to passively inhale the inoculum droplet dispensed from a pipet into one nostril. Mice are obligate nose-breathers, so once mice recovered from the anesthesia, the process was repeated to inoculate the other nostril. A small aliquot of the same PBS was used for vehicle inoculations. Mice were weighed at each inoculation. GAS dose is titrated up over the first two infections, so mice received inoculations of 4 µl per nostril on the first week, 6 µl per nostril on the second week, then 7.5 µl per nostril for all subsequent inoculations. This schedule minimizes death from sepsis and reduces the chance of bacterial aspiration into the lungs during inoculation.

2.1.4 Group A Streptococcus *subcutaneous immunizations*

Female P28 SJL/J mice received three total subcutaneous immunizations in the chest (near axial lymph nodes) as described in [80, 81, 205]. Briefly, 110 µl of $2x10^8$ CFU heat-killed GAS was homogenized with a mortar and pestle, then diluted into 5 ml PBS. This was mixed in Hopper glass syringes with an equal volume of Complete Freund's adjuvant containing 200 µg *Mycobacterium tuberculosis* H37Ra (DIFCO laboratories). Mice received 100 µl emulsion on experimental day 0, day 14, and day 28, in conjunction with 400 ng *Bordetella pertussis* toxin (List biological laboratories, Campbell, CA) intravenously on day 0. Vehicle control mice received

PBS/CFA emulsion and *B. pertussis* injections, and healthy control mice remained untreated. None of the control mice exhibited gross behavioral abnormalities or signs of illness.

2.1.5 Flow cytometry

Mice used for flow cytometry received an equal amount of heat-killed (HK) GAS for the last infection in lieu of live bacteria to protect the experimenter during tissue dissection. Mice were deeply anesthetized 24 h after the final infection with isoflurane and perfused briefly with ice-cold sterile PBS. Brain, spleen, NALT, and olfactory epithelia were dissected into DMEM on ice and homogenized through a 40 μm nylon mesh cell strainer with the back of a 10 ml syringe plunger. Lymphocytes from brain and NALT samples were collected from the interface of a 30%-70% Percoll gradient, then washed once in T cell media (RPMI with 10% fetal bovine serum, 1x penicillin/streptomycin, 1x glutamine, 1x non-essential amino acids, and 50 μM β-mercaptoethanol), and transferred to a 24-well tissue culture plate for cytokine stimulation or transferred to FACS tubes for transcription factor staining. Spleens were homogenized through a 40 μm nylon mesh cell strainer with a 1 ml syringe plunger, avoiding any areas of obvious necrosis. Splenocytes were collected in 5 ml DMEM and centrifuged to pellet the cells. Splenocytes were then treated with 2 ml red blood cell lysis buffer (155 mM NH_4Cl, 10 mM $KHCO_3$, 0.1 mM EDTA) for three minutes, and lysis was quenched with 8 ml DMEM. Splenocytes were washed once in 5 ml T cell media, then plated in a 24-well tissue culture plate for cytokine stimulation or transferred to FACS tubes for transcription factor staining.

For cytokine staining, cells were stimulated *in vitro* with 500x Cell Stimulation Cocktail (eBiosciences 00-4975-03) diluted to 1x in T cell media for 4h at 37°C, then transferred to FACS tubes. One third of each NALT/OE lymphocyte sample were pooled for used as single-stain and

FMO controls where possible; splenocytes were always used as a second set of single stain controls. The remaining CNS and NALT lymphocytes were transferred to FACS tubes as experimental samples; ~10^7 splenocytes were transferred to FACS tubes as splenocyte experimental samples. All washes were performed at 4°C using an Eppendorf 5810R centrifuge. Cells were washed once in FACS buffer (1% bovine serum albumin in PBS), then blocked in CD16/CD32 Fc block (BD Biosciences, 553141) diluted 1:200 in FACS buffer. Cells were washed once, then stained using the following antibodies to surface antigens: rat anti-CD4 BV605 (BD Horizon 562891, 1:100), rat anti-CD45 BV421 (BD Horizon 563890, 1:100), and Fixable Viability Dye eFluor-780 (eBiosciences 65-0865-14, 1:4000). Cells were then fixed and permeabilized with BD Cytofix/Cytoperm (BD Biosciences, 554714) and left in 1x Perm/wash buffer overnight. The following day, intracellular cytokines were stained with rat anti-IL-17A PE (BD Pharmingen, 559502), rat anti-IFNγ APC (BD Pharmingen, 554413), and rat anti-IL-10 FITC (BD Pharmingen, 554466) antibodies diluted 1:100. Cells were washed once with Perm/wash buffer, once with FACS buffer, then resuspended in 200 µl FACS buffer for analysis.

For Treg staining, cells were collected into FACS tubes without *in vitro* restimulation, blocked, and stained for the same surface antigens as above, then fixed and permeabilized using the Transcription Factor Fixation/Permeabilization kit (eBiosciences, 512343 and 522356). Following fixation, cells were washed then stained with rat anti-FoxP3 PerCP-Cy5.5 (eBiosciences, 45-5773-80, 1:100). Cells were then washed once with wash buffer, once with FACS buffer, resuspended in 200 µl FACS buffer, and analyzed. All samples were analyzed on a BD FACSCelesta (Columbia Stem Cell Initiative Flow Cytometry Core). Gates for surface stains were set with single-stain and no-stain controls; cytokine stain gates were set using fluorescence-

minus-one controls on tissue-matched lymphocytes. Compensation and analysis were performed using FlowJo software.

2.1.6 Immunohistochemistry

Mice used for immunohistochemical staining were anesthetized with isoflurane and perfused thoroughly with PBS followed by 4% PFA. Brains and livers were extracted and post-fixed for 6 h, washed three times in PBS for 30 minutes, then cryoprotected in 30% sucrose overnight and embedded in Tissue Plus O.C.T. Compound (Fisher Health Care 4585). Olfactory epithelia in the nose were decalcified with three 24 h washes in 0.5 M EDTA pH 8.0, then cryoprotected overnight in 30% sucrose and embedded in OCT. Brain and OE blocks were stored at -80°C until use. Tissues were then sectioned at 12 μm on a Leica cryostat and stored at -80°C until use. For staining, slides were air-dried for 20 minutes then placed horizontally in a humidified chamber. Slides were washed once in PBS for 10 minutes to remove excess OCT, then blocked for 1 hour in blocking buffer (10% BSA, 0.1% Triton-X-100 in 1x PBS). Primary antibodies listed in **Table 2.2** were diluted in 0.1% Triton-X-100 in PBS with 1% BSA. Primary antibody solutions were incubated overnight at 4°C. Slides were washed three times for ten minutes with PBST (0.1% Triton-X-100 in PBS), then primary antibodies were targeted using associated fluorescently tagged secondary antibodies (1:1000 for Alexa488 and Alexa594, 1:500 for Alexa647). Biotinylated tracer fluorescence was amplified with Streptavidin conjugated to Alexa594 (1:1000, Life Technologies). Secondary antibodies were diluted in PBST and incubated for two hours at room temperature. Nuclei were then labeled with DAPI (4′,6-diamidino-2-phenylindole, 1:20,000 in PBST) for 10 minutes, then slides were washed twice with PBST and twice with PBS. Slides were

coverslipped with Vectashield (Vector Labs, H-1000), sealed with clear nail polish, and stored at -20°C.

Target	Catalog Info	Dilution
Caveolin-1	Abcam ab18199	1:2000
vGluT2	Millipore AB2251-I	1:2000
GAD67	Abcam MAB5406	1:1000
CD4	BD Pharmingen 553727	1:100
Iba1	WAKO 016-20001	1:500
CD68	Abcam ab53444	1:2000
Claudin5	Invitrogen 431600	1:500
ZO-1	Life Technologies 617300	1:500
GFP	Life Technologies A11122	1:2000
GLUT1	Millipore 400060-50UG	1:4000
GLUT1 (in 2019)	Thermo Scientific RB-9052-P1	1:2000
Occludin	Invitrogen 711500	1:500
OMP	WAKO 544-10001	1:2000
Aquaporin4	Sigma A5971	1:500
LYVE1	Abcam ab14917	1:150
Group A Streptococcus	Fitzgerald 20C-CR7058RAP	1:2000

Table 2.2 Antibody information and dilutions used for immunohistochemistry.

In some cases, vasculature was stained with BSL-FITC (*Bandeiraea Simplicifolia* lectin-FITC, 1:250, Vector Laboratories, FL-1101). For BSL staining, all solutions were prepared using

PBS with Ca^{2+} and Mg^{2+}, and slides were post-fixed for ten minutes with 4% PFA following BSL-FITC staining. Imaging of brain sections was performed with a Zeiss LSM700 confocal microscope or a Zeiss AxioImager.

2.1.7 In situ hybridization

Digoxigenin-labeled probes were synthesized from plasmids grown on appropriate selection media obtained from TransOMIC using the Roche Applied Science *in vitro* transcription kit (Sigma, 11175025910). Unincorporated nucleotides were removed using a G50 column (GE Healthcare, 27533001), and probes were resuspended and stored at -20°C.

Mice used for in situ hybridization were perfused with PBS only, brains and olfactory epithelia dissected and removed, and immediately embedded in OCT and frozen on dry ice, then stored at -80°C. Sections were cut onto glass slides with samples from two mice from different treatment groups o the same slide to minimize variation between groups. For staining, slides were air-dried for 20 minutes before immersion in 4% PFA for 15 minutes, followed by three 5-minute PBS washes. Slides were acetylated (1.25% triethanolamine, 0.175% HCl, 0.25% acetic anhydride) for 10 minutes with constant stirring. Slides were blocked for 4-6 hours with hybridization buffer [50% formamide, 5x SSC, 5x Denhardt's solution, 250 µg/ml baker's yeast RNA (Sigma R6750), 100 µg/ml salmon sperm DNA (ThermoFisher, 15632011)]. Probes were diluted as below in hybridization buffer, then 100 µl probe solution was applied to slides and coverslipped (Hybrislip hybridization covers, Grace Bio 726024) for hybridization at 72°C overnight in a humidified chamber.

For alkaline phosphatase enzymatic labeling, slides were then washed for 1 h at 72°C in 0.2x SSC, 5 min at 25°C in 0.2x SSC, and 5 min at 25°C in buffer B1 (0.1 M TrisCl pH 7.5, 0.15

M NaCl). Slides were blocked at room temperature in 10% heat-inactivated normal goat serum (HINGS) in buffer B1 for 1 h in a humidified chamber. DIG-labeled probes were then targeted with an alkaline phosphatase-conjugated anti-DIG antibody (Sigma, 11093274910; 1:5000 in buffer B1 with 1% HINGS) overnight at 4°C. The following day, slides were equilibrated with four 15-minute washes with buffer B3 (0.1 M TrisCl pH 9.5, 0.1 M NaCl, 50 mM $MgCl_2$, filtered with a 0.45 μm filter). Slides were then inverted on parafilm-covered humidified trays react with 200 μl AP substrate, buffer B4 [0.24 mg/ml levamisole, 75 mg/ml 4-Nitro blue tetrazolium chloride (NBT, Roche 11383213001), 50 mg/ml BCIP 4-toluidine salt (BCIP, Roche 11383221001)]. The AP reaction was allowed to develop overnight protected from light, then checked and buffer B4 refreshed if the reaction was incomplete after 24 h. To quench the AP reaction, the chamber was flooded with water and slides were coverslipped with Glycergel warmed to 60°C (DAKO, C0563).

For fluorescent labeling of DIG-tagged probes, slides were progressed through the stringency buffers 5x SSC, 0.2x SSC, and buffer B1 as above, then endogenous peroxidase was quenched for 1 h with 3% hydrogen peroxide in methanol. Slides were then blocked with 0.5% TNB solution in buffer B1 [(Roche block, Sigma, 11096176001) w/v, dissolved at 72°C with vortexing every 15 minutes] for 1 h at room temperature. After three five-minute washes in TNT buffer (0.05% Tween-20 in buffer B1), DIG-labeled probes were targeted with an anti-DIG POD antibody [(Sigma 11207733910) 1:500 in 0.5% TNB solution] overnight in a humidified chamber at 4°C. The following day, slides were washed three times with TNT buffer, then fluorescence was amplified using Cy3 amplification for 10 minutes (Cy3 reagent 1:100 in amplification diluent). Slides were again washed three times with TNT buffer, then blocked with 10% BSA in PBST to begin immunostaining for vascular markers. Vascular antibodies were used as described above,

then slides were coverslipped and imaged on a Zeiss AxioImager or Zeiss LSM700 confocal microscope.

2.1.8 Tracer injections

Blood-brain barrier permeability was assessed using intravenous injection of fluorescent tracers. Tight junction integrity was measured using a small molecular weight dye, biocytin-tetramethylrhodamine (TMR, ThermoFisher, T12921, Waltham, Massachusetts, USA). At 48 h after the last infection, animals were anesthetized with 2% isoflurane in medical air and injected in the tail vein with 100 µl biocytin-TMR (5 mg/ml) in PBS with Ca^{2+} and Mg^{2+}. Animals were allowed to recover for thirty minutes in their home cage prior to perfusion for immunohistochemistry as described above.

2.1.9 Western blotting

Brains were collected from mice after perfusion with PBS. Collected tissue was homogenized in RIPA buffer (25mM Tris pH 7.5, 150mM NaCl, 1mM EDTA, 1% TritonX-100, 0.1% SDS) containing 1x protease and phosphatase inhibitors (ThermoFisher, 87785) using a mechanical

Target	Catalog Info	Dilution
ZO-1	ThermoFisher 33-9100	1:1000
Occludin	Invitrogen 711500	1:250
Caveolin-1	Abcam ab18199	1:1000
Cadherin-5	Abcam ab33168	1:100
VCAM-1	Abcam ab134047	1:100

Table 2.3 Antibody information and dilutions for Western blots.

homogenizer followed by 10-20 pulses of sonication. Lysates were then centrifuged for 2 minutes at 4,000rpm at 4°C, and protein concentration in the supernatant was quantified using the Pierce BCA protein assay kit (Thermo Scientific, 23225) run in parallel with BSA standards from 0.125-2 mg/ml (Bio-Rad). Protein samples were diluted in Laemmli buffer to 3 µg/µl. Protein samples (15 µl or 50 µg total protein) and prediluted protein ladder (8 µl, Bio-Rad, 1610374) were loaded into 12% or 4-15% precast gradient gels and separated by SDS-PAGE in 0.5 M glycine 4 M Tris with 1% SDS. Bands were stacked into the gel at 100V for ten minutes, then run out to separation at 150V for an additional 40 minutes. Protein gels were transferred onto polyvinylidene difluoride membranes (preactivated in methanol for two minutes then rinsed in water) in 0.5 M glycine 4 M Tris at 150 V for 65 minutes on ice. Membranes were trimmed to size, blocked for one hour in blocking buffer (1x Odyssey blocking buffer for PBS, LICOR), then incubated in primary antibodies diluted according to **Table 2.3** in blocking buffer overnight at 4°C. Following primaryantibody binding, membranes were washed three times with 1x PBS 0.1% Tween-20 for 5 minutes each. IRDye-680 and IRDye-800 conjugated secondary antibodies were used to visualize primary antibody staining (1:20,000, LICOR). Secondary antibodies were diluted in blocking buffer and incubated for one hour at room temperature. Membranes were washed three times in PBS-0.1% Tween-20 and twice in PBS prior to visualization. Protein levels in brain lysates were measured by fluorescent western blot analysis and quantitation was performed using the LICOR (LICOR, Lincoln, NE) system, as described in [91].

2.1.10 qRT-PCR

cDNA libraries were created from mRNA harvested from OB, OE, and NALT tissue. Olfactory tissues were dissected out quickly following a brief perfusion with PBS and snap-frozen on dry

Reaction component	Volume (µl)	Step	Temperature (ºC)	Time
10x Reverse transcriptase buffer	2	1	25	10:00
25x dNTP mix (100 mM)	0.8	2	37	120:00
10x RT random primers	2	3	85	5:00
MultiScribe reverse transcriptase	1	4	4	Hold
RNAse inhibitor	1			
Nuclease-free H2O	11.2			
RNA sample (0.3 µg/µl)	3			
Total	20			

Table 2.4 Reaction components and cycling information for reverse transcription reaction to create cDNA from olfactory tissues. Olfactory bulb, epithelium, and NALT samples were processed in parallel.

ice in Eppendorf tubes. RNA was extracted with the RNEasy Midi Kit (QIAGEN) according to package instructions, and stored in TE buffer (10 mM Tris HCl, 0.1 mM EDTA, pH 7.0) at -80°C until reverse transcription. RNA was reverse transcribed to create cDNA using the High-Capacity cDNA Reverse Transcription kit (Applied Biosystems) in 20 µl reactions using RNA samples

Primer	Sequence (5'-3')	Reaction component	Volume (µl)
FcγRI forward	TAA TGC CAC CAA GGT TGT GA	SYBR Green Fast Mastermix	10
FcγRI reverse	CCT GTA TTC GCC ACT GTC CT	Forward Primer 10 µM	0.4
		Reverse Primer 10 µM	0.4
FcγRIIβ forward	CGG CTG TCC ACA GTA GCA TA	H2O	7.2
FcγRIIβ reverse	TTT CAC TTC CCC ATT TGG AC	Total	18
		Sample	2
FcαµR forward	TCT TGC TCA GGA CTA ACA TGG AC		
FcαµR reverse	CTG GCA AGT GAG GTG CTT TTG		
FcRn forward	ACC CTG GAG AAG ATA TTA AAT GGG A		
FcRn reverse	TCA GGC TGC TTC ATC CAC AG		

Table 2.5 Primer sequences and reaction components for qPCR reactions. Olfactory bulb, epithelium, and NALT samples were processed in parallel.

diluted to 0.3 μg/μl according to **Table 2.4**. cDNA was used in reactions with SYBR Green master mix to probe for expression of targets using primer sequences and reaction components found in **Table 2.5**.

2.1.10 Electrophysiology

Mice used for electrophysiology experiments were infected four times with live GAS as described above. Two days after the fourth infection, mice were swabbed with a Group *A* Streptococcus clinical test (QuickVue In-Line Strep A Test, Quidel) to ensure mice were not infectious, then shipped overnight to Duke University.

Electrophysiological local field potential (LFP) recordings were performed as described previously in [242]. Briefly, following four inoculations either with PBS or live GAS, mice were surgically fitted with a custom machined head plate to allow for awake, head-fixed recording from the olfactory bulb. The head plate was positioned with a Piezo arm so the entirety of the skull overlaying the OB was visible within the head plate window. The plate was sealed to the skull with dental cement, and mice were treated post-operatively with antibiotic ointment and i.p. buprenorphine. After recovery from surgery for two days, mice were inoculated with HK-GAS or PBS to recall the immune response. Electrophysiological recordings were performed in a liquid dilution, ten channel olfactometer. The morning after recall infections, inoculated mice were anesthetized with isoflurane (1% in O_2) and a craniotomy and durotomy was opened over the posterolateral area of one olfactory bulb. A 32-site polytrode acute probe (A1 × 32-Poly3-5mm-25s-177, Neuronexus, Ann Arbor, MI) was lowered into the posterior OB to the ventromedial M/T layer, where sustained tonic activity was observed in contrast to the electrically quiet granular layer, typically at a depth of 1.5-2.2mm, at a 4° angle with respect to vertical in the coronal plane.

Once the probe was placed, blackout curtains were closed over the mouse and the recording rig was left to acclimate for 1 hour.

Signals were collected through an A32-OM32 adaptor (Neuronexus) connected to a Cereplex digital headstage (Blackrock Microsystems, Salt Lake City UT). Unfiltered signals were digitized at 30 kHz at the headstage and recorded by a Cerebus multichannel data acquisition system (BlackRock Microsystems). Experimental events and respiration signal were acquired at 2 kHz by analog inputs of the Cerebus system. Respiration was monitored with a microbridge mass airflow sensor (Honeywell AWM3300V, Morris Plains, NJ) positioned directly opposite the animal's nose. Negative airflow corresponds to inhalation and negative changes in the voltage of the sensor output. Prior to recording, the back of the probe was painted with a fluorescent dye (DiI, Life Technologies) and probe position was confirmed post hoc in histological sections. Odors were presented to the animals using a custom-made flow-dilution olfactometer at 0.04%, 0.2%, and 1% of saturated vapor with an inter-trial interval of 10 s. Odor presentation and delivery were

Vehicle	mineral oil
Neutral	ethyl butyrate
	valeraldehyde
	methyl tiglate
	isoamyl acetate
	2-hexanone
	γ-terpinene
Innately valent	peanut oil
	2-phenylethanol
	isopentylamine
	2-phenylethylamine

Table 2.6 Odorant stimuli used in electrophysiology recordings. Odors were classified as neutral or innately valent from [243]. Trials using neutral and valent odors were analyzed separately.

controlled by a custom MATLAB program. All recordings were performed blind with respect to genotype. One recording was made from each OB, for a total of two recordings per animal performed on consecutive days. Ten monomolecular odorants were diluted in mineral oil for use as odor stimuli, listed in Table 2.6. Innately valent stimuli were excluded from analysis because different anatomical circuitry processes innately valent odors through the cortical amygdala, presenting a potential confound in grouping all odors together for analysis [243]. Thus, only data for the following odor stimuli were analyzed: methyl tiglate [Alfa Aesar (Haverhill, MA) A11964], γ-terpinene (Sigma, 223190-5ML), 2-hexanone [Fluka (Mexico), 02473], isoamyl acetate [Tokyo Chemical Industry (Cambridge, MA), A0033], ethyl butyrate (Aldrich E15701), and valeraldehyde (Sigma, 110132). Fifteen trials per odor-concentration stimulus were presented for 1s each, with each trial lasting approximately 10 s; recordings typically lasted 90 min total. Single units were automatically sorted using Spyking Circus (https://www.github.com/spyking-circus). A typical recording yielded 19.7 ± 5.5 units. Analysis was performed in MATLAB (MathWorks, Natick, Massachusetts, USA). Significantly active units were defined after computing smoothed kernel density functions (KDFs) for to visualize averaged firing rates as a function of time after odor onset, and identify response latencies for each cell-odor pair. KDFs were computed for the first 500 ms following inhalation after odor onset. Response index was computed from the area under the receiver operating characteristic curve, and comparing the reliability of odor response to mineral oil response, with -1 indicating absolute suppression, 0 indicating no change, and 1 reflecting absolute activation relative to mineral oil. Significantly different responses were identified using a Wilcoxon rank-sum test with spike count distributions.

2.2 Behavioral tests

Before beginning the inoculation series, mice were handled to prevent stress responses from confounding future test sessions. For handling, mice were acclimated to the test room for 30 minutes, then individually handled for three minutes per day for three successive days.

Intranasally infected mice used for behavioral experiments received the first four infections with live GAS suspensions followed by a fifth infection using HK-GAS to minimize pathogen exposure for the experimenter. Subcutaneously immunized mice used for behavioral tests were immunized as above. Prior to beginning behavioral tests, mice were acclimated to the test room for at least 45 minutes in their home cage. In all cases where mice were tested together, groups were counterbalanced for treatment, genotype and sex where applicable.

2.2.1 Olfactory habituation-dishabituation test

Olfactory function was assessed using the olfactory habituation-dishabituation test adapted from [244] at 6 h after the last infection. Mice were habituated singly to a clean empty cage in the testing room for 30 minutes prior to testing. Animals were tested in groups of 2-3 and filmed for analysis. For testing, mice were allowed to investigate wooden long-handled Q-tips impregnated with 10µl of odorant or vehicle (water) for two minutes per trial, with approximately one minute between trials to change Q-tips. Each odorant was presented three times in succession, with water being the first odorant. Time spent sniffing the Q-tip for each two-minute trial was timed using videotapes. Data were analyzed with repeated-measures ANOVA followed by Newman-Keuls post-hoc test.

2.2.2 Open field test

Mice were tested in either black open field boxes with bedding or white open field boxes with bare bottoms. Mice were filmed from above for tracking and allowed to ambulate freely for 10 minutes. Activity was quantified with AnyMaze software.

2.2.3 Beam walking challenge

Mice were trained to cross a wide 1.5cm wooden beam covered with duct tape oriented towards their home cage until they successfully crossed three times. For testing, mice were filmed while crossing three times each on 1.5 cm, 1.0 cm, and 0.5 cm beams, with gentle assistance from the experimenter if needed. Films were analyzed for time to cross the beam, foot slips, and maximum speed in AnyMaze software.

2.2.4 Ladder beam test

Mice were trained to cross a custom machined ladder with white fiberglass sides and 100 metal rungs 4 mm in diameter until they could successfully cross the whole ladder without stopping or turning around. On test day, mice were filmed from below to capture footfalls on each rung for three trials each. Films were scored for slips of hind- and forelimbs on each rung.

2.2.5 Marble burying test

The marble burying test measures anxiety-like behavior that prompts digging and burying of items in the mouse's cage. For testing, twelve 1-cm glass marbles were arranged in a 3x4 grid atop 5 cm of corncob bedding, and mice were allowed to explore the cage and marbles for five minutes. After returning the test mouse to its home cage, the experimenter counted how many marbles were buried at the end of the testing session. Mice were filmed during testing to quantify ambulation with

AnyMaze software, and to assess marble displacement from beginning to end of the testing session.

2.2.6 Induced grooming test

This test uses water spray to prompt grooming behavior above baseline to elicit underlying repetitive behavior. Mice were acclimated singly to an empty cage for 30 minutes prior to testing. Filming then began for a 10-minute pre-spray phase. Mice were then sprayed three times with distilled water from a distance of ~20 cm, and then filmed for a 20-minute post-spray phase. Videos were analyzed for ambulation with AnyMaze, and manually scored for grooming bout number and duration, as well as rearing behavior and jumps or backflips.

2.3 Statistical analyses and figure preparation

Images were prepared using ImageJ software, and figures were assembled using Adobe Illustrator. T cell counts were performed live using a cell counter, with experimenter blind to genotype. Microglia counts were obtained from tiled images and counted using the ImageJ cell counter plugin. Electrophysiology data were analyzed in MATLAB and exported for statistical analysis. Statistical analyses of electrophysiological measures, flow cytometry data, behavioral analyses, cell count data, normalized Western blot band intensities, and barrier leakage data were performed using GraphPad Prism. Data were analyzed by Student's t-test, 1-way, 2-way, or repeated-measures (RM) ANOVA followed by Sidak's, Tukey's, or Bonferroni's post-hoc test. Significance (α) was set at 0.05. Data are represented as mean ± SEM or SD as denoted in figure legends**.**

Chapter 3: Th17 lymphocytes drive neurovascular dysfunction and olfactory circuit deficits in post-Streptococcal autoimmune encephalitis

3.1 Introduction

Antibody-mediated CNS autoimmune disease is initiated when circulating antibodies inappropriately recognize neuronal receptors or synaptic proteins as foreign epitopes. Perhaps the most well-known of these autoimmune encephalitic (AE) syndromes is anti-NMDA receptor (NMDAR) encephalitis, but limbic encephalitis and post-infectious basal ganglia encephalitis also trigger abrupt onset of neuropsychiatric symptoms in otherwise healthy individuals. Many autoantibodies that have been described to date, including anti-nuclear antibodies (ANAs), and anti-NMDAR antibodies, are pathogenically implicated in several autoimmune disorders [e.g. systemic lupus erythematosus (SLE), rheumatoid arthritis (RA), Sjögren syndrome, poly/dermato-myositis, multiple sclerosis (MS) and AE]. Group A *Streptococcus* (GAS, *S. pyogenes*) infections have been linked to later development of autoimmunity for centuries. Discovery of anti-neuronal antibodies that target dopamine D1R/D2R receptors in sera from patients with Sydenham's chorea, as well as positive response to immune treatment like IVIg, are consistent with an autoimmune mechanism for post-infectious BGE [47, 78, 156, 237]. These autoantibodies elicit behavioral abnormalities when infused directly into rodent brains, or when administered i.v. along with BBB-disrupting agents [6, 78, 80, 81, 206, 238] Because the BBB normally prevents antibody entry to the CNS parenchyma, the mechanisms by which autoantibodies may enter the brain to trigger neuropathology remain unclear for most AE syndromes.

A compelling immune-mediated mechanism for BBB disruption is through the action of T cells, which have been shown to play essential yet distinct roles in pathogenesis of MS and its animal model, experimental autoimmune encephalomyelitis (EAE) [94, 97, 100, 150]. Although

Th17 cells initiate disease and propagate pathology and neurovascular dysfunction in EAE [92, 165, 245], their contribution to AE pathogenesis remains unexplored. Postmortem and biopsy samples of AE patients have shown that $CD3^+$ T cells collect as large perivascular infiltrates in anti-Hu and anti-LGI1 AE syndromes [246]. Recent work from our lab has established a mouse model for post-infectious BGE using multiple intranasal (i.n.) inoculations with live GAS bacteria [93]. The mouse immune response closely mimics the human response to infection, inducing a GAS-specific $CD4^+$ Th17 cell response in the nasal-associated lymphoid tissue (NALT), a structural analog of the human tonsils [93, 166, 234, 235, 247]. GAS-specific T cells migrate from the nose to the parenchyma of olfactory bulbs anteriorly in the CNS before spreading more posteriorly in the brain. T cell infiltration is accompanied by impaired BBB function, deposition of IgG in the brain, activated microglial populations in the olfactory bulb (OB), and loss of excitatory synaptic proteins [93]. Although olfactory dysfunction has been reported in MS and SLE patients [248-252], as well as during EAE [253], it is unclear whether recurrent GAS infections and ensuing post-infectious BGE may impair olfactory circuit function.

Inflammatory conditions (e.g., multiple sclerosis, systemic lupus erythematosus, Alzheimer's disease, and Parkinson's disease) have been linked to olfactory dysfunction in human populations [250, 253-255] and demonstrated in rodent models of these diseases [253, 255, 256]. It is possible that inflammation in the OE alone is sufficient to affect OSN function, but the presence inflammatory cells in the OB or other brain regions (immune cells infiltrate the parenchyma in MS lesion areas) may also contribute to hyposmia observed in these conditions. Glia from the OB seem to be more plastic than glia from other brain regions, and they are more competent antigen presenters. After systemic inflammation with lipopolysaccharide (LPS), myeloid cells harvested from the OB and meninges closely interact with T cells *in vitro*, a behavior

not shared by cortical myeloid cells [256]. By contrast, local inflammation induced with LPS intranasally results in partially reversible shrinkage of the glomerular and external plexiform layers of the OB (**Figure 3.1**) [257]. In a mouse model of CNS lupus, olfactory-driven behaviors were blunted [258]. These behavioral abnormalities were accompanied by decreased cell density in the

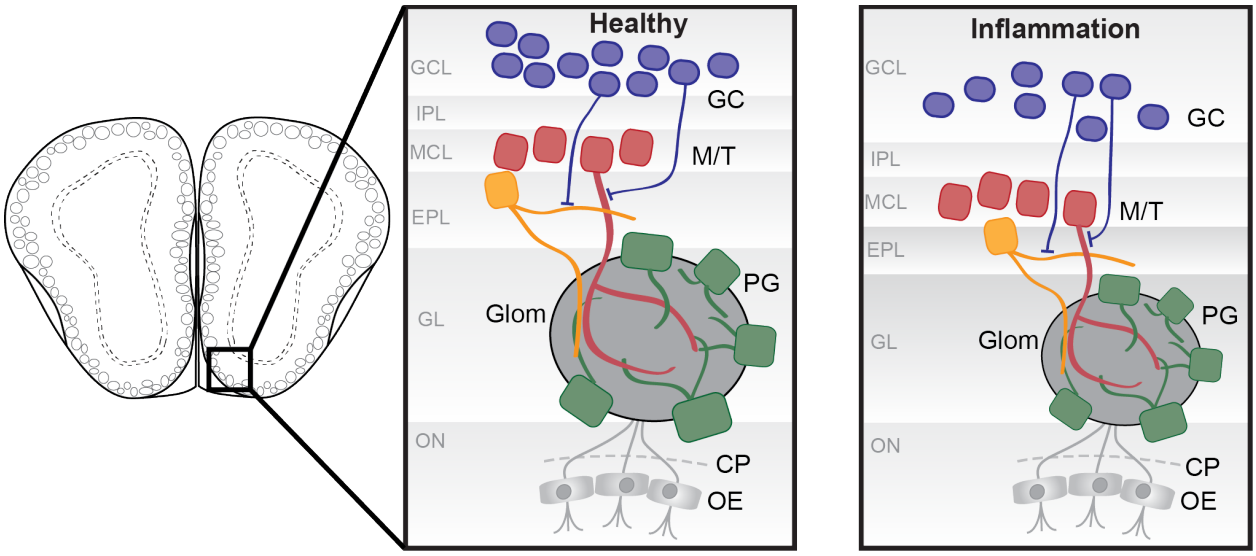

Figure 3.1 Olfactory bulb glomerular connectivity in healthy or inflammatory conditions. Odor perception is a unique sense in that the substrate, odor molecules, directly contact sensory neurons in the olfactory epithelium (OE) in the nose [259]. Each olfactory sensory neuron (OSN) expresses just one of ~1,200 odorant receptor genes, and neurons expressing a particular odorant receptor are randomly distributed within localized zones in the OE [260-262]. From the OE, OSNs project through the cribriform plate (CP) into the OB, where axons from OSNs expressing the same odorant receptor converge to terminate in roughly spherical bundles of synapses, or glomeruli (Glom), with local periglomerular interneurons (PG) and excitatory output mitral/tufted (M/T) cells [263]. Individual glomeruli are highly specific for a single odorant receptor. OB granule cells (GC) constantly turn over throughout life. A fresh supply of neuroblasts flows from the rostral migratory stream and integrates into the olfactory circuit guided by CXCL12/CXCR4 signaling, providing a way to shape adult olfactory circuitry independently of synaptic scaling mechanisms [188, 264].

rostral migratory stream, suggesting that neurogenesis may be impaired in this systemic inflammatory disease [258]. Inflammation and reduced neurogenesis in the SVZ have been reported in EAE, which would certainly affect upkeep of olfactory circuits as described above [253]. Th17 cells migrating into the brain are known to express inflammatory cytokines IFNγ, IL-6, IL-23, and IL-17A, among others [40, 265, 266]. We hypothesized that inflammatory cytokines secreted by infiltrating Th17 cells after recurrent GAS inoculations were responsible for TJ

structural abnormalities, BBB functional permeability, and microglial activation. Studies described here test the requirement of Th17 cells for these processes, as well as probing physiological consequences in olfactory circuitry in the presence of neuroinflammation after recurrent GAS infections.

3.2 Deletion of RORγt *eliminates Th17 lymphocytes after intranasal GAS inoculations*

We have previously shown that recurrent intranasal (i.n.) GAS infections promote migration of $CD4^+$ T cells from the NALT to the CNS, a subset of which are bacterial-specific Th17 ($IL\text{-}17A^+$) and autoreactive Th17 ($IL\text{-}17A^+$ $IFN\gamma^+$) [235]. To more fully understand the role

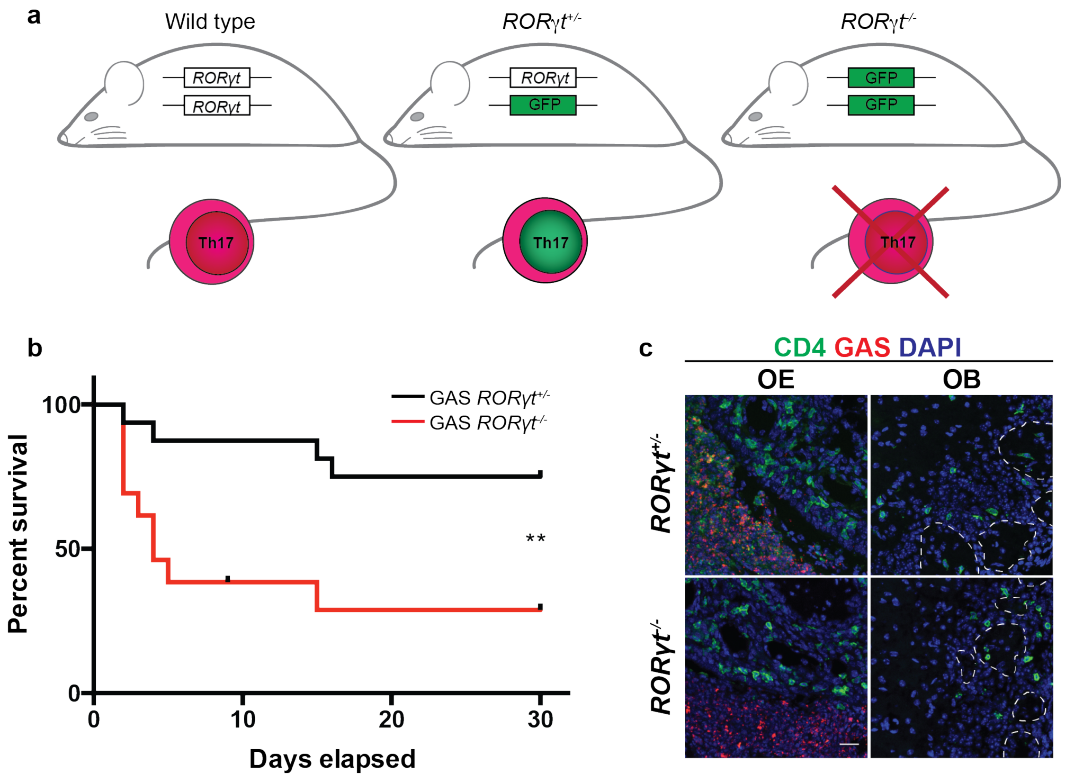

Figure 3.2 Immunocompromised *RORγt*$^{-/-}$ mice are more susceptible to sepsis than *RORγt*$^{+/-}$ mice. **a** Schematic representation of Th17 status in the *RORcγt-eGFP* mouse line, in which the *RORcγt* locus is replaced with eGFP. Survival curves in **b** for GAS-infected *RORγt*$^{+/-}$ and *RORγt*$^{-/-}$ mice after beginning infection course. *RORγt*$^{-/-}$ mice die from the infections at a higher rate than *RORγt*$^{+/-}$ mice (X^2=7.51; **p=0.0063). **c** Immunofluorescence staining for GAS surface carbohydrate (red) and CD4 (green) confirms that infection is restricted to the nose in both *RORγt*$^{+/-}$ and *RORγt*$^{-/-}$ mice. No bacterial labeling was detected in brain. Scale bar = 20 μm.

of Th17 cells in neuropathology, we performed i.n. GAS infections in the *RORcγt-eGFP* knockout-knockin mouse line, in which the *RORcγt* locus, encoding a transcription factor necessary for Th17 differentiation, is replaced with GFP (**Figure 3.2a**). Since *RORγt*$^{-/-}$ mice are immunocompromised and Th17 cells are recruited in large numbers to control GAS infections, approximately 70% of all *RORγt*$^{-/-}$ mice died from sepsis, in contrast to *RORγt*$^{+/-}$ mice, which had only a ~20% mortality rate, consistent with previous findings (**Figure 3.2b**) [93, 235]. It was important to ensure that GAS bacteria were confined to the nose in immunocompromised *RORγt*$^{-/-}$ mice, with no frank brain infection. Restriction of infection to the nose (with no spread to the brain) was confirmed with immunofluorescence for GAS surface carbohydrates (red), CD4 (green), and DAPI (**Figure 3.2c**). While CD4^{+} cells were detected in OE and OB of GAS-infected *RORγt*$^{+/-}$ and *RORγt*$^{-/-}$ mice, bacterial immunolabeling was restricted to the OE.

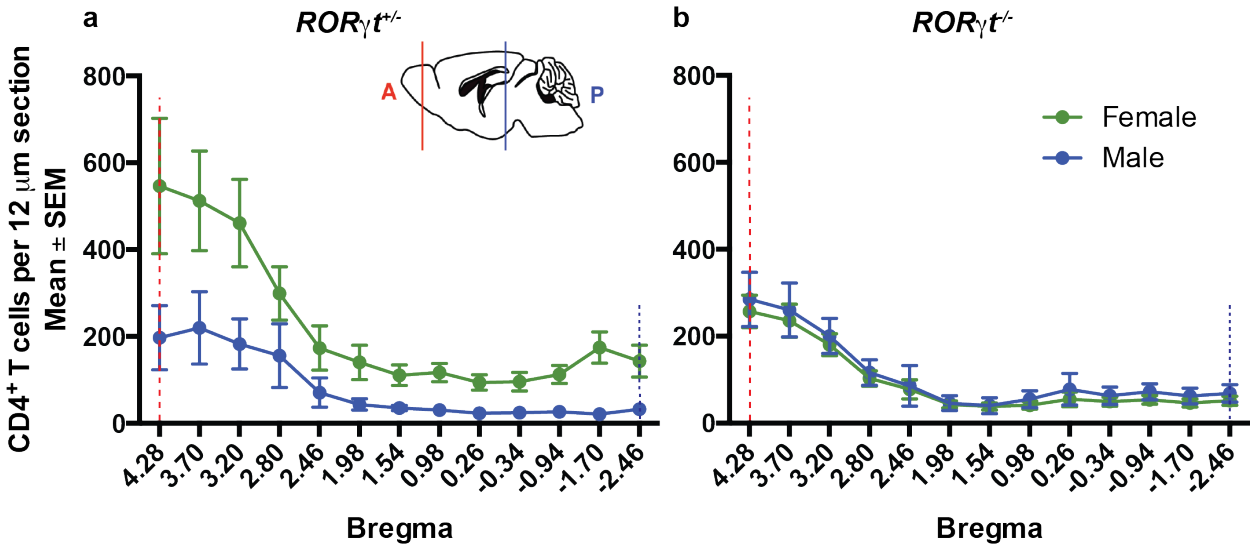

Figure 3.3 Sex-specific Th17 driven peripheral immune cell infiltration. Left, female *RORγt*$^{+/-}$ immunocompetent mice recruit more T cells to the brain than male *RORγt*$^{+/-}$ mice. There is equivalent T cell recruitment to the brain in GAS-inoculated male and female *RORγt*$^{-/-}$ mice. Data represent n=2 male *RORγt*$^{+/-}$, n=9 female *RORγt*$^{+/-}$, n=5 male *RORγt*$^{-/-}$, and n=9 female *RORγt*$^{-/-}$ mice. RM-ANOVA found no significant effects of sex and distance from bregma on T cell counts.

Pilot experiments to understand the contribution of Th17 lymphocytes to CNS pathology were initially performed using both male and female mice. Male and female *RORγt*$^{+/-}$ and *RORγt*$^{-/-}$ mice were recurrently infected with GAS, and T cell populations along the rostrocaudal axis of the brain were analyzed. Surprisingly, while *RORγt*$^{-/-}$ female mice showed a significant reduction in CNS T cell infiltration after GAS inoculations (**Figure 3.3a**), *RORγt*$^{-/-}$ males had similar numbers of CNS T lymphocytes as *RORγt*$^{-/-}$ littermates (**Figure 3.3b**). Thus, females show a Th17-dependent T cell expansion in the brain that is absent in males. Given that autoimmunity is sex-skewed to females (along with many specific autoimmune diseases), these findings agree with data showing sex differences in animal models of other autoimmune diseases [167, 267, 268]. For the rest of this study, we focused primarily on females. Phenotypes in males were analyzed separately in parallel to females.

Next, we mapped the fraction and spatial distribution of GFP$^+$ Th17 cells in the CNS after recurrent GAS infections using immunofluorescence. Consistent with previous results, ~36% of CD4$^+$ T cells were GFP$^+$ [93], indicating Th17 identity, and most GFP$^+$ CD4$^+$ Th17 cells were located in the anterior part of the brain (bregma 4.28-2.46; data not shown). In *RORγt*$^{+/-}$ mice, GFP$^+$ Th17 cells are concentrated in the olfactory bulb and anterior olfactory nucleus (AON) anteriorly (**Figure 3.4a**); in posterior brain regions, Th17 cells are mostly found in the choroid plexus and meninges (bregma -1.70, -2.46, **Figure 3.4b**). Comparison of total CD4$^+$ T cell infiltrate in GAS-infected *RORγt*$^{+/-}$ and *RORγt*$^{-/-}$ brains illustrated that in *RORγt*$^{-/-}$ mice lacking Th17 cells, total T cell infiltrate was reduced by 58%, with no detectable GFP$^+$ cells (**Figure 3.4abc**). Because the Th17 fraction in *RORγt*$^{+/-}$ brains is only 34% (**Figure 3.5b**, [93]), there must be some non-cell autonomous recruitment of other T cell populations by Th17 cells. Thus, CNS Th17 cell infiltration

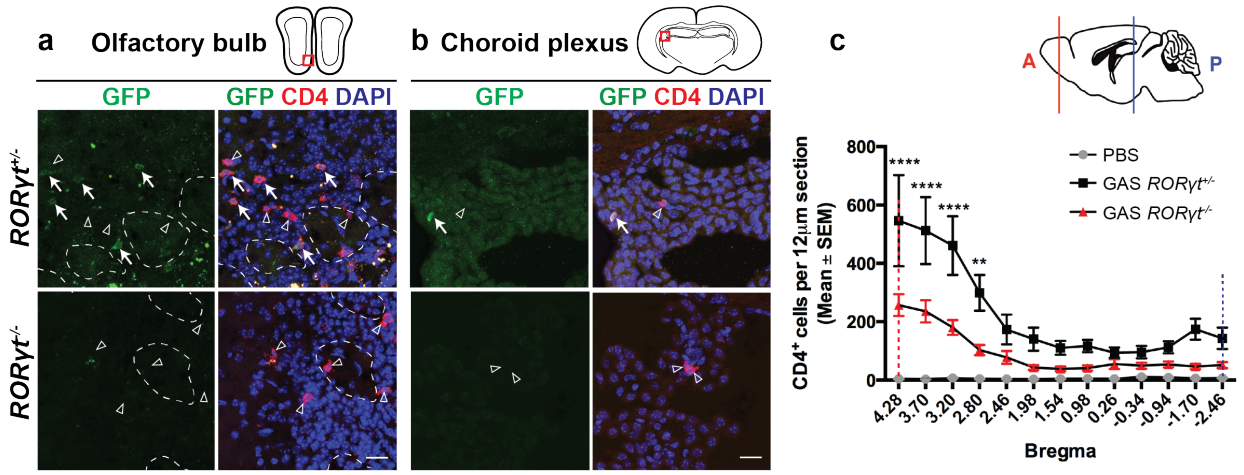

Figure 3.4 T cells infiltrate the brains of *RORγt*$^{+/-}$ and *RORγt*$^{-/-}$ mice after recurrent GAS infections. CD4^{+} T cells are visible throughout the brains of both *RORγt*$^{+/-}$ and *RORγt*$^{-/-}$ mice (anterior regions in **a** and choroid plexus in **b**). GFP^{+} CD4^{+} T cells are only found in *RORγt*$^{+/-}$ brains. **c** Quantification of total CD4^{+} T cell distribution along the anteroposterior axis of the brain in PBS (gray), GAS-infected *RORγt*$^{+/-}$ (black) and *RORγt*$^{-/-}$ (red) mice. The x-axis represents distance from bregma and the y-axis shows numbers of CD4^{+} T cells per 12 μm section. Dashed red and blue vertical lines represent relative positions in the brain cartoon above (solid lines). Data represent n=5 PBS, n=9 GAS *RORγt*$^{+/-}$, and n=9 GAS *RORγt*$^{-/-}$. RM-ANOVA found significant main effects of treatment ($F(2,20)=10.43$, $p=0.0008$) and bregma ($F(12,240)=13.4$, $p<0.0001$), as well as an interaction between treatment and bregma ($F(24,240)=4.690$, $p<0.0001$); Tukey's MC test reveals significant differences at bregmas +4.28, +3.7, +3.2 (****$p<0.0001$) and bregma 2.8 (**$p=0.0062$); Asterisks denote significance between GAS *RORγt*$^{+/-}$ and *RORγt*$^{-/-}$. Scale bar = 20 μm.

seems to have non-cell autonomous effects on other T cell subtypes, which could be due to secretion of chemokines in the nose or brain by Th17 cells.

Flow cytometric analysis of T cell subtypes in the NALT/OE and anterior CNS was then performed after recurrent i.n. GAS inoculations. In *RORγt*$^{+/-}$ brains, CD4^{+} population is comprised mainly of autoreactive IFNγ^{+} IL-17A^{+} Th17 (42.75%), followed by IFNγ^{+} Th1 (25.57%), IL-17A^{+} Th17 (19.25%), and 12.1% Tregs (**Figure 3.5abc**). The proportions of T cell subtypes are similar between brain and NALT/OE CD4^{+} populations in *RORγt*$^{+/-}$ mice (**Figure 3.5abdf**). In GAS-infected *RORγt*$^{-/-}$ mice, autoreactive Th17 (IL-17A^{+} IFNγ^{+}) and Th17 (IL-17A^{+}) populations were drastically reduced (to 10.96% and 6.4%, respectively), along with a concomitant expansion of the IFNγ^{+} population to 49.8%. Treg populations also decreased in *RORγt*$^{-/-}$ brains (7.4%, **Figure**

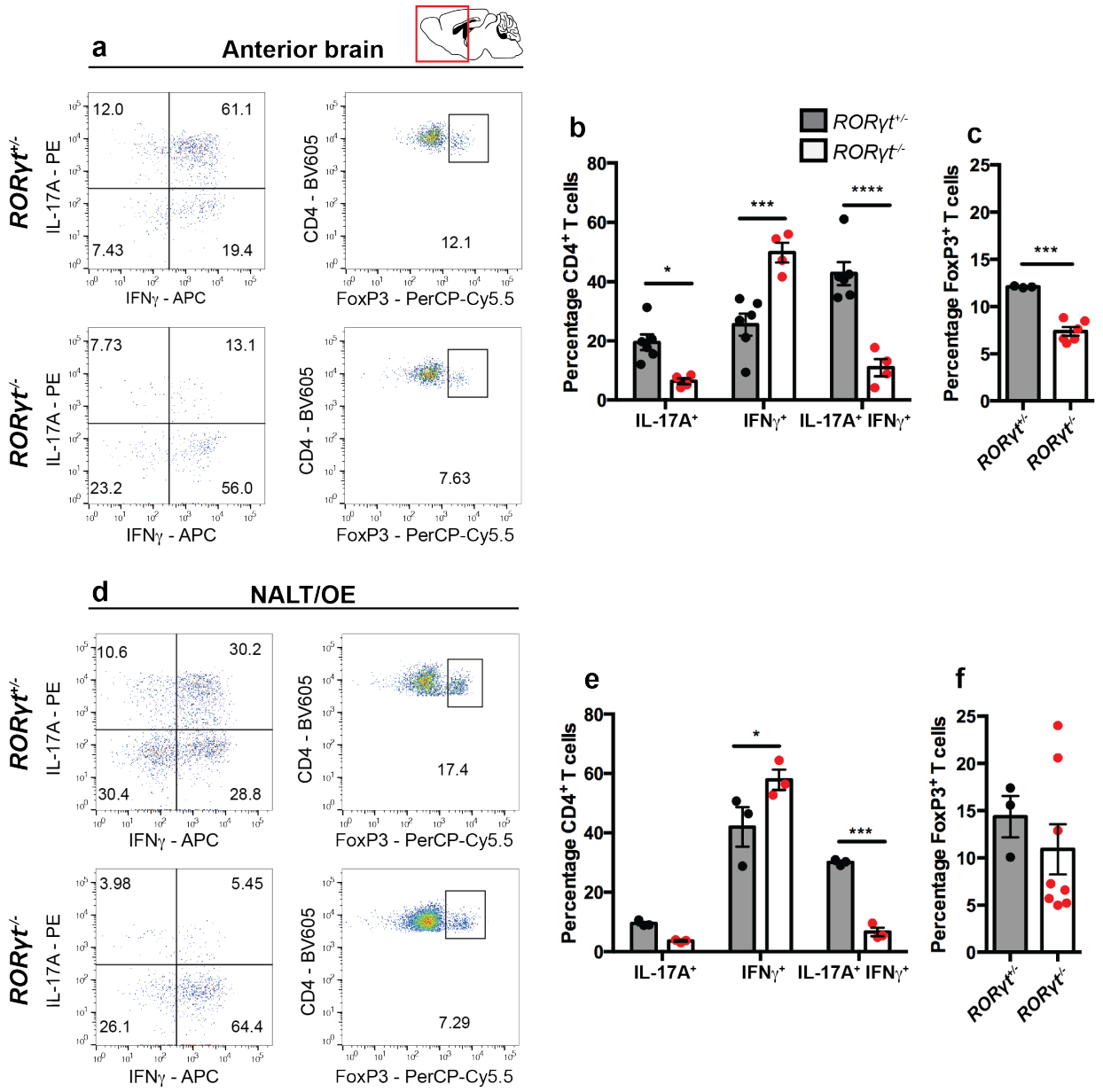

Figure 3.5 Flow cytometric analysis of lymphocytes recruited to brain and NALT/OE after recurrent GAS infections. **a** Representative flow cytometry analyses of $CD4^+$ lymphocytes purified from anterior brain tissue of *RORγt*$^{+/-}$ and *RORγt*$^{-/-}$ mice stained for intracellular cytokines (left), and representative flow cytometry for $CD4^+$ $FoxP3^+$ Treg cells from *RORγt*$^{+/-}$ and *RORγt*$^{-/-}$ brains (right). **b** Quantification of cytokine profile analysis of lymphocytes purified from brain of GAS-infected *RORγt*$^{+/-}$ and *RORγt*$^{-/-}$ mice. Data represented as mean ± SEM for n=6 GAS *RORγt*$^{+/-}$ and n=4 GAS *RORγt*$^{-/-}$ mice. Two-way ANOVA found main effects of cytokine ($F(2,16)=21.04$, $p<0.0001$) and genotype ($F(1,8)=12.58$, $p=0.0075$), as well as an interaction between cytokine and genotype ($F(2,16)=27.86$, $p<0.0001$). Sidak's post-hoc test revealed differences in $IL\text{-}17A^+$, *p=0.353; $IFN\gamma^+$ (***p=0.0001); $IL17A^+$ $IFN\gamma^+$ (****p<0.0001). **c** Treg population analysis of lymphocytes from brain in *RORγt*$^{+/-}$ and *RORγt*$^{-/-}$ mice after GAS infections. Data are represented as mean ± SEM from n=3 GAS *RORγt*$^{+/-}$ and n=6 GAS *RORγt*$^{-/-}$ mice, analyzed by two-tailed Student's t-test with Welch's correction for unequal variance (t=10.29, ***p=0.0001). (**d**, left) Representative cytokine expression profiles from lymphocytes in NALT/OE of *RORγt*$^{+/-}$ and *RORγt*$^{-/-}$ mice, and (**d**, right) representative plots of $FoxP3^+$ Tregs from NALT/OE. **e** Quantification of cytokine expression in lymphocytes purified from NALT/OE of GAS-infected *RORγt*$^{+/-}$ and *RORγt*$^{-/-}$ mice. Data represent (continued on following page)

mean ± SEM from n=3 GAS *RORγt*$^{+/-}$ and n=3 GAS *RORγt*$^{-/-}$ mice. Two-way ANOVA found a main effect of cytokine ($F(2,8)=93.14$, $p<0.0001$) but not genotype ($F(1,4)=3.675$, $p=0.1277$), and found an interaction between cytokine and genotype ($F(2,8)=17.96$, $p=0.0011$). Sidak's post-hoc test revealed differences in IFNγ$^+$ (***$p=0.0115$) and IL17A$^+$ IFNγ$^+$ (****$p=0.0006$), but not IL-17A$^+$ ($p=0.353$). **f** Quantification of FoxP3$^+$ Treg populations in NALT/OE lymphocytes from *RORγt*$^{+/-}$ and *RORγt*$^{-/-}$ mice. Data are represented as mean ± SEM from n=3 GAS *RORγt*$^{+/-}$ and n=8 GAS *RORγt*$^{-/-}$ mice; unpaired two-tailed Student's t-test showed no difference between genotypes (t=0.7416, p=0.7442).

3.5c). These changes in T cell subtype distribution in *RORγt*$^{-/-}$ brain CD4$^+$ cell populations mirror those seen in the NALT/OE (**Figure 3.5def**), reinforcing prior work suggesting that CNS T cells originate in the NALT. Despite their immunocompromised state, surviving *RORγt*$^{-/-}$ mice generate a robust CD4$^+$ cellular immune response in the NALT/OE, restricting bacterial infection to the nose.

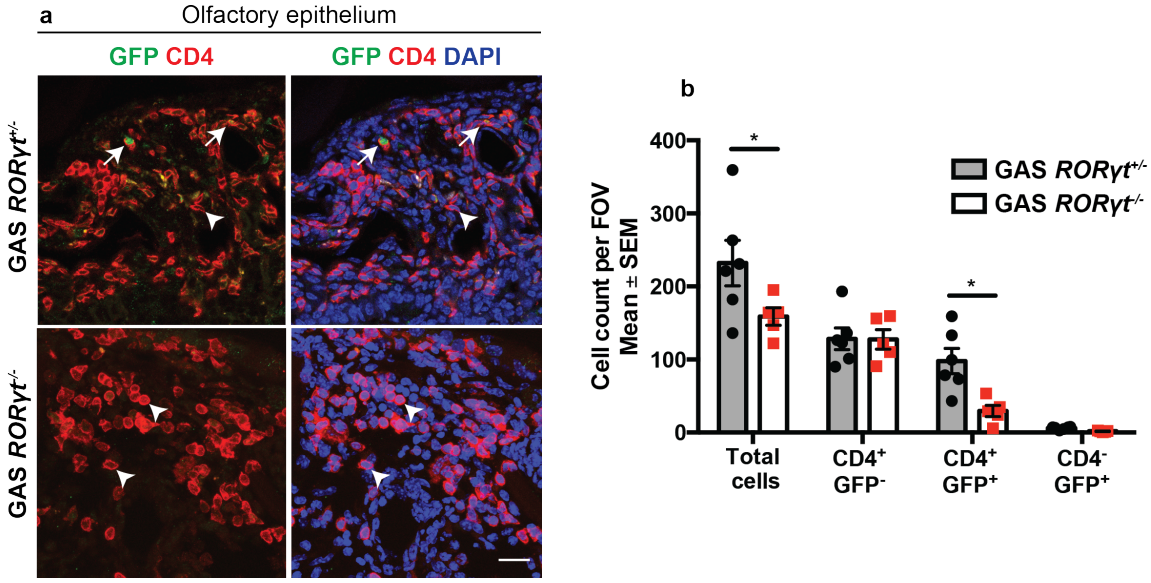

Figure 3.6 T cells recruited to the olfactory epithelium after recurrent GAS infections in *RORγt*$^{+/-}$ and *RORγt*$^{-/-}$ mice. **a** Immunofluorescence for GFP (green) and CD4 (red) shows colocalization in a subset of cells (Th17, arrows) in *RORγt*$^{+/-}$ but not *RORγt*$^{-/-}$ olfactory epithelium. Remaining cells are CD4$^+$ GFP$^-$ (arrowheads). **b** Quantification of different cell types illustrates decreased total T cell recruitment due to selective loss of CD4$^+$ GFP$^+$ Th17 cells, with no change in CD4$^+$ GFP$^-$ and CD4$^-$ GFP$^+$ cell populations. Data represent mean ± SEM from n=6 GAS *RORγt*$^{+/-}$ and n=5 GAS *RORγt*$^{-/-}$ animals. RM-ANOVA showed main effects of genotype ($F(1,9)=5.169$, $p=0.0491$) and cell type ($F(3,27)=75.42$, $p<0.0001$) on T cell populations in the nose, as well as an interaction between cell type and genotype ($F(3,27)=4.317$, $p=0.0131$). Sidak's multiple comparisons test revealed significant differences in total cells (*$p=0.0119$) and CD4$^+$ GFP$^+$ (*$p=0.0214$), but not CD4$^+$ GFP$^-$ ($p>0.999$) and CD4$^-$ GFP$^+$ ($p=0.9995$). Scale bar = 20 μm.

To confirm our findings from flow cytometric experiments, we performed immunohistochemical analysis of total $CD4^+$ and $CD4^+$ GFP^+ Th17 lymphocyte recruitment to the OE. In **Figure 3.6a**, histological examination of immunostained OE tissue sections shows recruitment of $CD4^+$ GFP^- (arrowheads) and $CD4^+$ GFP^+ cells (arrows) to the OE in *RORγt*$^{+/-}$ GAS-infected mice. However, *RORγt*$^{-/-}$ OE contain only $CD4^+$ GFP^- cells (arrowheads), with small populations of $CD4^-$ GFP^+ cells found in both genotypes (**Figure 3.6a**). GAS-infected *RORγt*$^{-/-}$ mice recruit 32.7% fewer total T cells to the OE (158.7 ± 12 T cells per FOV) compared to GAS-infected *RORγt*$^{+/-}$ mice (232.2 ± 31.1 T cells per FOV), which is accounted for by a loss of $CD4^+$ GFP^+ Th17 cells of approximately the same magnitude (decrease of 68.24 $CD4^+$ GFP^+ cells per FOV, **Figure 3.6b**).

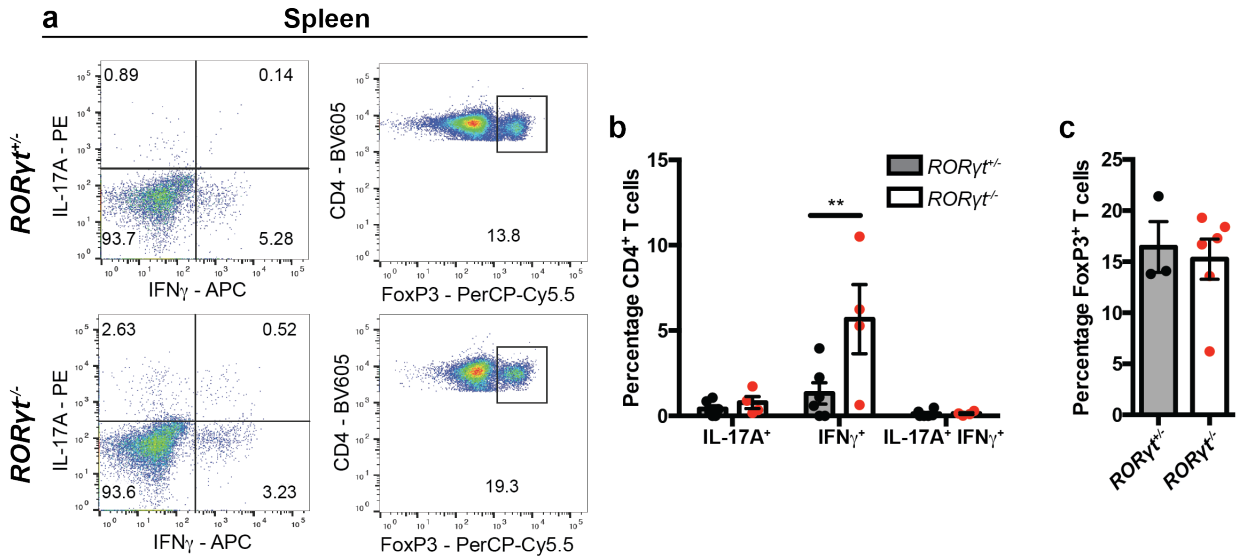

Figure 3.7 Flow cytometric analysis of splenic $CD4^+$ T cells confirms that immune response is local to olfactory tissues. Representative cytometry plots in **a** show lack of significant splenocyte activation in *RORγt*$^{+/-}$ and *RORγt*$^{-/-}$ mice after GAS infections. **b** Quantification of cytokine expression indicates only a small increase in $IFN\gamma^+$ T cells in *RORγt*$^{-/-}$ mice. Data represent mean ± SEM from n=6 GAS *RORγt*$^{+/-}$ and n=4 GAS *RORγt*$^{-/-}$ mice. Two-way ANOVA revealed a main effect of cytokine ($F(2,16)=15.23$, $p=0.0002$), but not genotype ($F(1,8)=4.731$, $p=0.0613$); there was also significant interaction between cytokine and genotype ($F(2,16)=6.660$, $p=0.0079$). Sidak's post-hoc test revealed differences in $IFN\gamma^+$ (**$p=0.0011$); but not $IL17A^+$ $IFN\gamma^+$ ($p>0.999$) or $IL\text{-}17A^+$ ($p=0.9797$). **c** Treg populations are unchanged in splenocytes from *RORγt*$^{+/-}$ and *RORγt*$^{-/-}$ mice. Data are represented as mean ± SEM from n=3 GAS *RORγt*$^{+/-}$ and n=6 GAS *RORγt*$^{-/-}$ mice. Unpaired Student's t-test showed no difference between genotypes (t=0.3559, $p=0.7324$).

The response to GAS is local to the OE and brain, as splenic lymphocytes were not activated in large numbers (**Figure 3.7a**). GAS-inoculated *RORγt*$^{+/-}$ and *RORγt*$^{-/-}$ mice show only a very small population of activated CD4^{+} IFNγ^{+} splenocytes (**Figure 3.7b)**. Moreover, the Treg population remains stable around 15%, which is typical of healthy mouse spleen (**Figure 3.7c**) [269]. Thus, in immunocompromised *RORγt*$^{-/-}$ mice, immune responses are confined to the olfactory epithelium, NALT, and brain. Both IL-17A and IFNγ are secreted by autoreactive Th17 cells found in the CNS of *RORγt*$^{+/-}$ mice infected with GAS, and these cytokines have been demonstrated *in vitro* and *in vivo* in EAE experiments to cause BBB permeability [165, 169]. BBB integrity in the presence and absence of Th17 cells recruited to the CNS after recurrent GAS infections was then investigated.

3.3 Th17 cells enhance BBB permeability in a size-dependent manner

The contribution of Th17 cells to BBB disruption after recurrent GAS infections was assessed because both IL-17A and IFNγ have been shown to disrupt endothelial tight junctions *in vitro* and *in vivo* [100, 169, 266]. First, permeability via disrupted tight junction integrity (paracellular permeability) was assessed using an i.v. injection of the small molecular weight tracer biocytin- TMR (870 Da) into PBS-inoculated controls and GAS-inoculated *RORγt*$^{+/-}$ and *RORγt*$^{-/-}$ mice at 48 h after the final infection. All GAS-inoculated mice showed increased BBB permeability in various brain regions, and heatmaps showing areas of tracer deposition in brains indicate no difference in area with BBB disruption between genotypes when compared to uninfected controls (**Figure 3.8a**). Quantification of tracer staining intensity in OB regions revealed that although both *RORγt*$^{+/-}$ and *RORγt*$^{-/-}$ mice showed increased BBB permeability in the

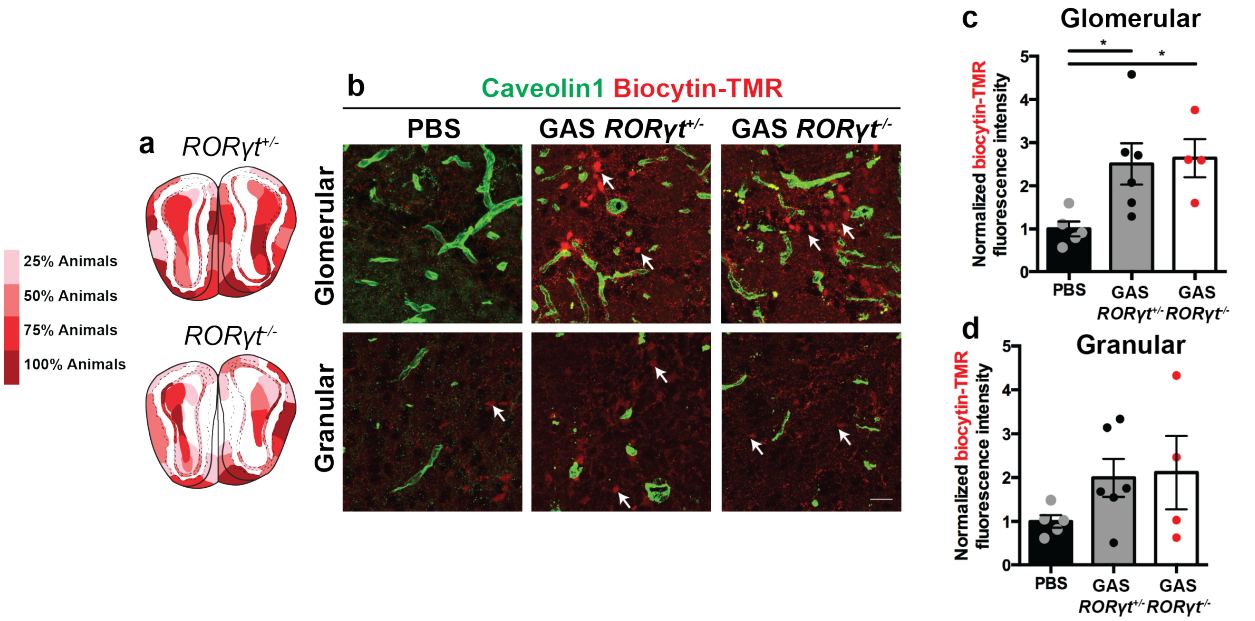

Figure 3.8 Increased permeability to a small molecular weight tracer in GAS-inoculated brains**. a** Heatmaps indicating areas of the OB with biocytin-TMR tracer deposition relative to uninfected controls. Darker red indicates more mice with biocytin-TMR staining in that region. **b** PBS-inoculated control mice show very little tracer deposition in glomerular and granular layer of the OB. GAS-inoculated mice show significant biocytin-TMR uptake by neurons (arrows) in both glomerular and granular OB layers. Quantification of biocytin-TMR staining intensity in **c** glomerular and **d** granular layers of the OB. Data were collected from n=4 PBS, n=6 GAS *RORγt*$^{+/-}$, and n=4 GAS *RORγt*$^{-/-}$ mice, represented as mean ± SEM. **c** One-way ANOVA showed significant differences in biotin intensity in glomerular layer ($F(2,12)=4.986$, $p=0.0265$). Tukey's post-hoc test revealed significant differences in PBS vs GAS *RORγt*$^{+/-}$ (*$p=0.0431$), and PBS vs GAS *RORγt*$^{-/-}$ (*$p=0.047$), but not GAS *RORγt*$^{+/-}$ vs GAS *RORγt*$^{-/-}$ ($p=0.97$). **d** No condition effect in granular biotin intensity was found by one-way ANOVA ($F(2,12)=1.519$, $p=0.2582$). Scale bar = 20 μm.

glomerular layer after GAS infections, granular layer BBB permeability was mild and not significantly different from uninfected controls (**Figure 3.8bcd**). Thus, Th17 cells are not necessary for tight junction degradation after recurrent GAS infections.

Second, permeability caused by increased transcellular vesicular traffic (by Cav1^{+} vesicles or clathrin-coated vesicles) was investigated by mapping and quantifying intensity of serum IgG deposition. Heatmaps showing areas of increased IgG deposition relative to uninfected mice again show no effect of Th17 cells on areas with BBB permeability (**Figure 3.9a**). In contrast to biocytin-TMR leakage, GAS-infected *RORγt*$^{-/-}$ mice had significantly less intense IgG staining in both

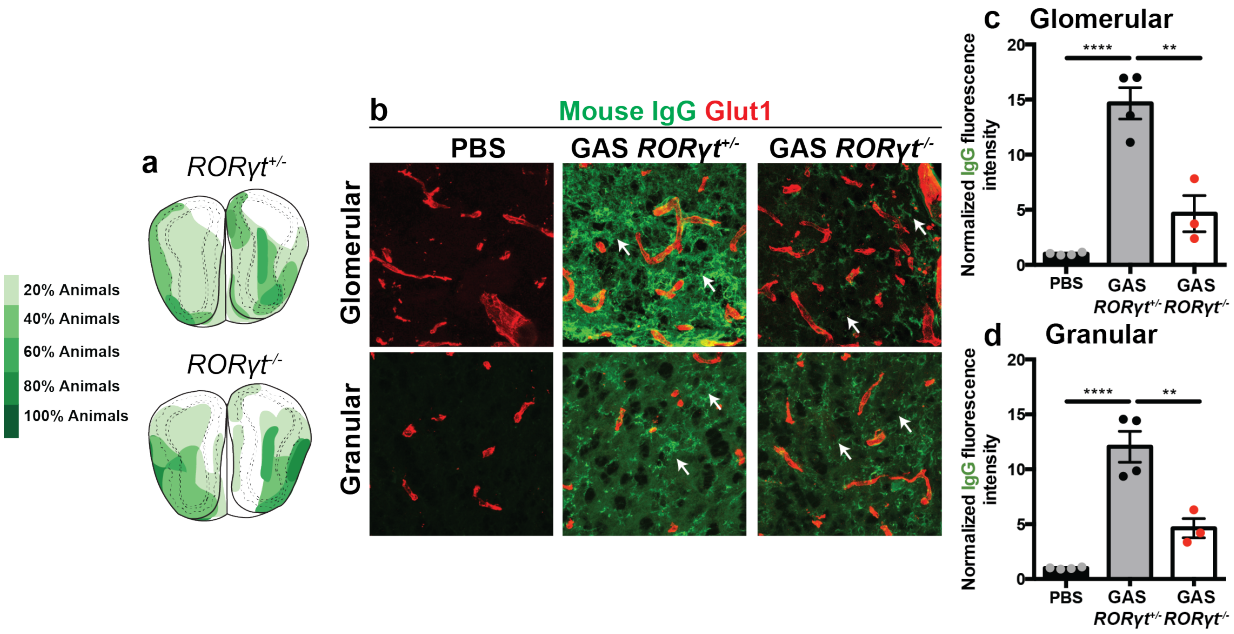

Figure 3.9 Increased deposition of IgG in OB regions in *RORγt*$^{+/-}$ but not *RORγt*$^{-/-}$ mice inoculated with GAS. **a** Heatmaps indicating areas of increased serum IgG deposition in the OB of GAS-infected *RORγt*$^{+/-}$ and *RORγt*$^{-/-}$ brains compared to PBS controls. **b** PBS-inoculated mice showed no BBB permeability to IgG in glomerular and granular OB layers. GAS *RORγt*$^{+/-}$ brains show heavy deposition of serum IgG (arrows) in both glomerular and granular layers, whereas GAS *RORγt*$^{-/-}$ mice show significantly less IgG deposition in the same regions. **c,d** Quantification of IgG leakage in glomerular and granular OB. Data represented as mean ± SEM from *n*=4 PBS, *n*=4 GAS *RORγt*$^{+/-}$, and *n*=3 GAS *RORγt*$^{-/-}$ mice. **c** One-way ANOVA was used to assess differences in IgG intensity in glomerular layer ($F(2,8)=39.01$, $p<0.0001$). Tukey's post-hoc test revealed significant differences in PBS vs GAS *RORγt*$^{+/-}$ (****$p<0.0001$), and GAS *RORγt*$^{+/-}$ vs GAS *RORγt*$^{-/-}$ (**$p=0.001$), but not PBS vs *RORγt*$^{-/-}$ ($p=0.1466$). **d** IgG deposition in the granular layer was assessed by one-way ANOVA ($F(2,8)=35.35$, $p=0.0001$). Tukey's post-hoc test revealed significant differences in PBS vs GAS *RORγt*$^{+/-}$ (****$p<0.0001$), and GAS *RORγt*$^{+/-}$ vs GAS *RORγt*$^{-/-}$ (**$p=0.0022$), but not PBS vs GAS *RORγt*$^{-/-}$ ($p=0.0829$). Scale bar = 20 µm.

granular and glomerular OB compared to GAS-infected *RORγt*$^{+/-}$ mice (**Figure 3.9bcd**). PBS-inoculated control mice had very little detectable IgG in the parenchyma, indicating an intact BBB (**Figure 3.9bcd**). Th17 cells therefore act on the endothelium directly or indirectly to modulate entry of IgG, potentially through increased rates of transcytosis or receptor-mediated transport.

Finally, to investigate the size limits of BBB leakage after GAS infections, brain sections of PBS-inoculated controls and GAS-infected *RORγt*$^{+/-}$ and *RORγt*$^{-/-}$ mice were stained for fibrinogen, a large (340 kDa) non-immunogenic serum glycoprotein that enters the CNS during

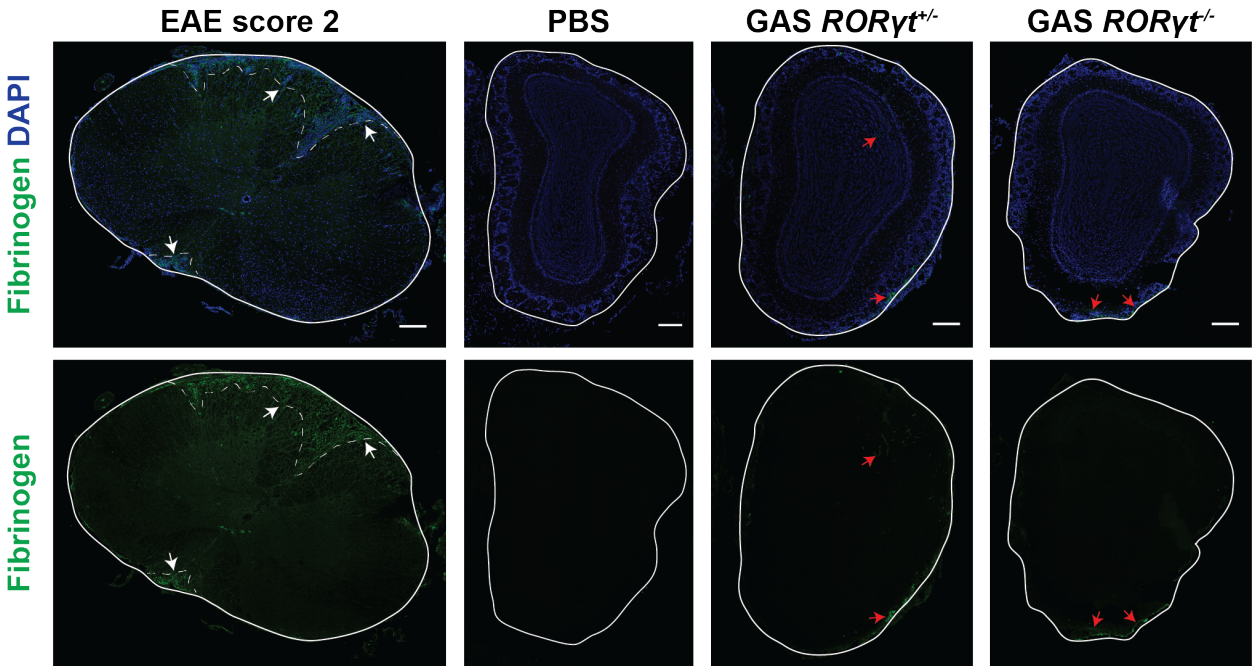

Figure 3.10 BBB permeability after recurrent GAS inoculations is size-restricted. Immunofluorescence for fibrinogen (green) in olfactory bulb tissue probes for massive disruption of TJs. EAE lumbar spinal cord served as a positive control, where fibrinogen can be seen in dorsal and ventral funiculi (dashed lines, white arrows). PBS- and GAS-inoculated *RORγt*$^{+/-}$ or *RORγt*$^{-/-}$ mice had no detectable fibrinogen deposition despite BBB permeability to biocytin-TMR and serum IgG in the same region. Intravascular and olfactory nerve (outside the BBB) fibrinogen indicated by red arrows. Scale bar = 200 μm.

massive BBB breakdown as seen in acute EAE lesions [270, 271]. **Figure 3.10** illustrates that vasculature in GAS-inoculated *RORγt*$^{+/-}$ and *RORγt*$^{-/-}$ mice remains impermeable to fibrinogen, in contrast to vessels in mice with active EAE, where fibrinogen deposition in the parenchyma can be seen in lesion areas (white arrows and dashed lines). The only detectable fibrinogen in GAS-infected brains was found in the olfactory axon tract with no BBB, or within the vasculature itself (red arrows, GAS *RORγt*$^{+/-}$ and GAS *RORγt*$^{-/-}$ panels). Increased concentration of fibrinogen in *in vitro* culture systems has been shown to alter VE-Cadherin levels and promote paracellular EC permeability, as well as promoting caveolae formation to increase transcytosis [271]. Absence of frank fibrinogen leakage in otherwise leaky brains after GAS infections indicates that either tight

junction complexes are not disrupted enough to allow passage of fibrinogen, or that transport of molecules like IgG is mediated through selective transport mechanisms.

To determine the mechanism of selective barrier exclusion of IgG in GAS-inoculated *RORγt*$^{-/-}$ mice, we analyzed expression and localization of tight and adherens junction protein

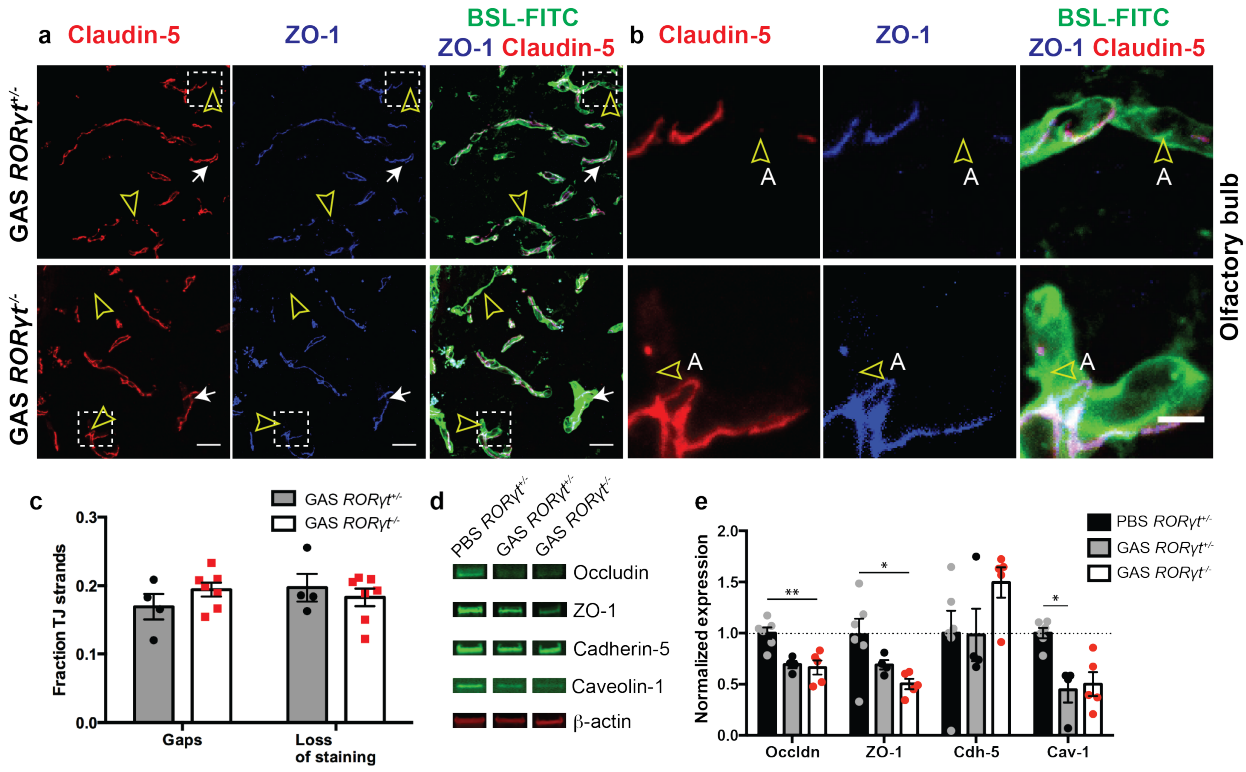

Figure 3.11 Tight junction (TJ) protein abnormalities after GAS infection in *RORγt*$^{+/-}$ and *RORγt*$^{-/-}$ brains. **a** TJ strands show abnormalities in GAS-infected *RORγt*$^{+/-}$ and *RORγt*$^{-/-}$ vessels (white arrows indicate gaps in tight junction strands, yellow arrowheads indicate extensive loss of protein staining, and green arrows point to protrusions perpendicular to the TJ strand). **b** Larger magnification images from boxed areas in **a**. Yellow arrowheads indicate absence of TJs. Scale bars are 20 µm in **a** and 5 µm in **b. c** Quantification for aberrant TJ strands in OB glomerular vessels of GAS-inoculated mice. Data were collected from n=4 GAS *RORγt*$^{+/-}$ and n=7 GAS *RORγt*$^{-/-}$ animals, expressed as mean ± SEM. Two-way ANOVA revealed no main effects of genotype ($F(1,9)=0.05095$, $p=0.4934$) or abnormality ($F(1,9)=0.1763$, $p=0.6844$) on TJ malformations, as well as no interaction between malformation and genotype ($F(1,9)=0.9943$, $p=0.3447$). **d** Representative Western blot bands for selected adherens junction, tight junction, and transcytotic proteins. **e** Quantification of protein expression. Optical density was normalized within sample to β-actin first, followed by normalization to mean PBS levels (dashed horizontal line). Data represent mean ± SEM from n=6 PBS, n=4 GAS *RORγt*$^{+/-}$, and n=5 GAS *RORγt*$^{-/-}$ animals. Significant differences in expression were detected for Occludin ($F(2,14)=7.554$, $p=0.006$) between PBS vs GAS *RORγt*$^{-/-}$ (**$p=0.0049$) but not PBS vs GAS *RORγt*$^{+/-}$($p=0.0783$); ZO-1 ($F(2,12)=3.844$, $p=0.05$) between PBS vs GAS *RORγt*$^{-/-}$ (*$p=0.0422$) but not PBS vs GAS *RORγt*$^{+/-}$($p=0.3826$); and Caveolin-1 ($F(2,13)=4.969$, $p=0.0249$) between PBS vs GAS *RORγt*$^{+/-}$ (*$p=0.036$) but not PBS vs GAS *RORγt*$^{-/-}$($p=0.0619$). Cadherin-5 levels were not significantly different between conditions ($F(2,13)=2.767$, $p=0.0997$).

levels. In OB glomerular layer vessels in *RORγt*$^{+/-}$ and *RORγt*$^{-/-}$ mice infected with GAS, immunofluorescence for TJ components Occludin and ZO-1 allowed for quantification of missing 1-3 μm lengths of TJ seams (gaps), and large >5 μm lengths of missing TJ strands (loss of staining). These abnormalities are associated with BBB dysfunction in several neurological diseases [13, 91-93]. Fractions of vessels with abnormal TJ strands were similar between GAS-inoculated *RORγt*$^{+/-}$ and *RORγt*$^{-/-}$ mice; PBS-inoculated animals showed normal TJ structures (**Figure 3.11abc**; data not shown). Protein expression of Occludin and ZO-1 were significantly reduced in GAS-inoculated *RORγt*$^{-/-}$ mice compared to PBS controls (**Figure 3.11de**). Total Caveolin-1 levels significantly decreased in GAS-inoculated *RORγt*$^{+/-}$ mice, and trended towards decreasing in *RORγt*$^{-/-}$ mice as well (p=0.0619; **Figure 3.11de**).

A second possible candidate for selective transport of IgG in *RORγt*$^{+/-}$ mice is Fc receptor-mediated transcytosis. Fc receptors (FcRs) are expressed in ECs basally and normally remove IgG from the parenchyma and shuttle it back to the bloodstream. It has been hypothesized that in certain disease states, directionality reverses and FcRs pump IgG from the blood into the brain. There are several different FcRs, each with affinity for different Ig molecules. For example, three isoforms of FcγR (FcγRI, FcγRIIα, FcγRIIβ) have affinity for IgG, while FcαμR is highly specific for IgA and IgM. We probed RNA expression from olfactory tissues isolated from mice receiving 5 PBS or GAS inoculations and sacrificed at 6 h or 48 h after the final infection. qRT-PCR revealed that FcγRI and FcRn are modestly upregulated after GAS infections, with FcγRIIβ expression increasing in OE and NALT but not brain tissue (**Figure 3.12a**). *In situ* hybridization confirmed expression of FcγRIIβ in OB. However, *FcγRIIβ* expression was not exclusively colocalized with Caveolin1 immunostaining in the OB (**Figure 3.12b**). This indicates that changes in vascular expression of Fc receptors may be drowned out by other more numerous cell types. Isolation of

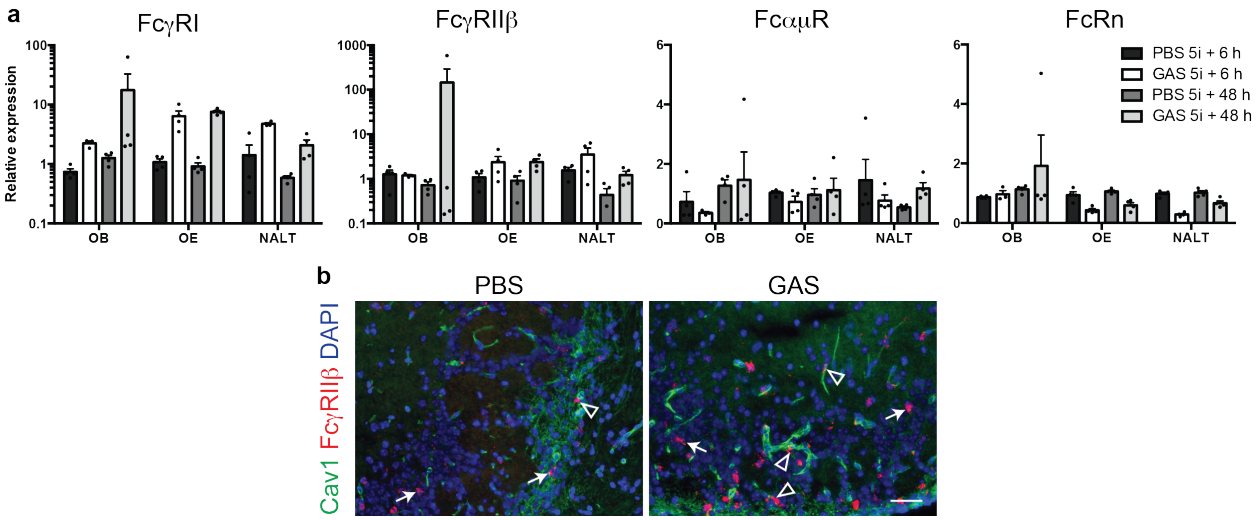

Figure 3.12 Fc receptor mRNA expression changes in olfactory tissues after recurrent PBS or GAS inoculations. **a** Quantitative real-time PCR assessed fold change in mRNA levels of *FcγRI*, *FcγRIIβ*, *FcαμR*, and *FcRn* in GAS and PBS mice at 6 h and 48 h after the final infection. None of the Fc receptor targets had significant elevation by two-way ANOVA analyzing the interaction of tissue and treatment. In situ hybridization **b** confirmed expression of *FcγRIIβ* (red) in OB brain sections, with vasculature labeled with Caveolin1 (green). mRNA expression was detected both vascularly (arrowheads) and outside of vessels (arrows) in the glomerular layer. Scale bar = 50 μm.

microvessels to examine receptor changes more closely may be necessary to fully resolve this issue. Alternatively, assays that directly test the action of Fc receptors *in vivo* without paracellular transport of solutes could clarify changes in Fc-mediated transport in BECs after GAS infections.

3.4 Neuroinflammation induces synaptic dysfunction in olfactory circuits

Elimination of Th17 cells resulting in a 48% decrease in CNS T cell burden should reduce overall cytokine load in the CNS, thus reducing microglial activation. We then examined whether loss of Th17 cells affects activation of brain-resident microglia and infiltration of peripheral macrophages after recurrent GAS infections. Compared to PBS-inoculated controls, GAS-infected *RORγt*$^{+/-}$ mice showed a 2.1-fold increase in the number of activated microglia, and GAS-infected *RORγt*$^{-/-}$ mice had a non-significant 1.4-fold increase in activated microglia relative to PBS (**Figure**

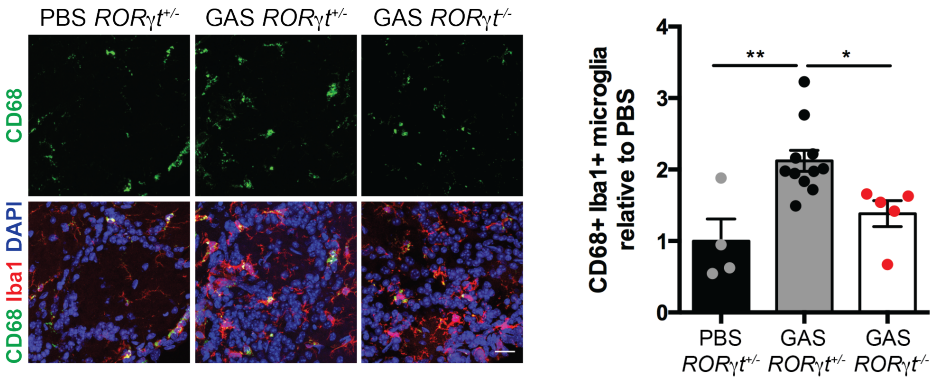

Figure 3.13 Neuroinflammation by activated microglia/macrophages after GAS inoculations. Iba1$^+$ CD68$^+$ microglia are present in the OB glomerular layer of PBS control and GAS-inoculated *RORγt*$^{+/-}$ and *RORγt*$^{-/-}$ brains by immunofluorescence, left, for CD68 (green) and Iba1 (red). Right, quantification of activated (CD68$^+$ Iba1$^+$) microglia in the glomerular layer relative to PBS microglia counts. Control and GAS-inoculated ROR-/- mice have few highly activated microglia, but GAS-inoculated *RORγt*$^{+/-}$ mice have substantial microglial activation in the glomerular layer. Data represent n=4 PBS, n=11 GAS *RORγt*$^{+/-}$, and n=5 GAS *RORγt*$^{-/-}$ animals, expressed as mean ± SEM. One-way ANOVA assessed differences in microglia levels ($F(2,17)=8.924$, $p=0.0022$). Tukey's test for multiple comparisons revealed significant differences between PBS vs GAS *RORγt*$^{+/-}$ (**p=0.0034) and GAS *RORγt*$^{+/-}$ vs GAS *RORγt*$^{-/-}$ (*p=0.0347), but not PBS vs GAS *RORγt*$^{-/-}$ (p=0.4956). Scale bar = 20 μm.

3.13). Therefore, infiltrating Th17 cells promote microglial activation or co-infiltration of peripheral macrophages after GAS infections.

We have previously shown that GAS-inoculated mice have very little vesicular glutamate transporter 2 (vGluT2) protein in olfactory bulb glomeruli [93]. To address whether these changes are Th17-dependent, we analyzed levels of vGluT2 and glutamate decarboxylase 67 (GAD67), an enzyme expressed by inhibitory periglomerular cells, within OB glomeruli of GAS-inoculated *RORγt*$^{+/-}$ and *RORγt*$^{-/-}$ mice (**Figure 3.14a**). The ratio of excitatory vGluT2 to inhibitory GAD67 in glomeruli was reduced to equal degree in GAS-infected *RORγt*$^{+/-}$ and *RORγt*$^{-/-}$ mice compared to PBS controls (**Figure 3.14b**). In conjunction with persistent loss of vGluT2 in OB glomeruli, the glomerular structures themselves are aberrant in GAS-infected *RORγt*$^{+/-}$ and *RORγt*$^{-/-}$ mice, with mean glomerular diameter reduced by 20.5% in GAS *RORγt*$^{+/-}$ and by 26.6% in GAS *RORγt*$^{-/-}$ mice compared to PBS controls (**Figure 3.14c**). This is consistent with a decrease in excitatory

input to glomeruli from OSNs onto M/T cells. Thus, Th17 cells are not required for loss of vGluT2 in OSN terminals.

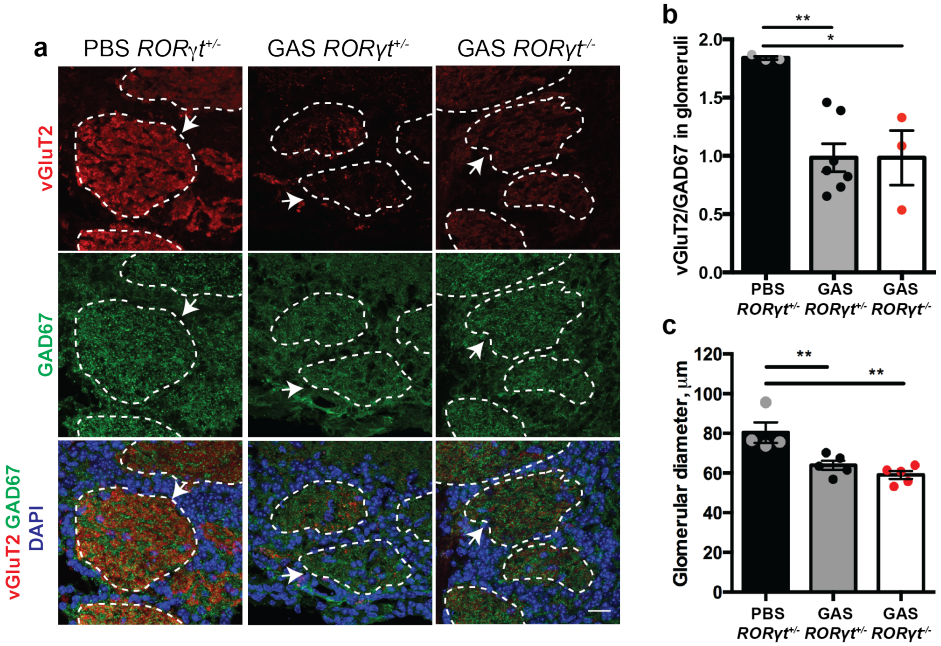

Figure 3.14 GAS-induced synapse protein degradation is Th17-independent. Synapse proteins vGluT2 and GAD67 are markers of the major components comprising the neuropil of glomeruli. PBS-inoculated mice show robust expression of both proteins, **a** however in GAS-inoculated *RORγt*$^{+/-}$ and *RORγt*$^{-/-}$ mice, vGluT2 is significantly downregulated **b** Data represented as mean ± SEM for *n*=3 PBS, *n*=7 GAS *RORγt*$^{+/-}$, and *n*=3 GAS *RORγt*$^{-/-}$. One-way ANOVA showed significant differences between conditions ($F(2,10)=9.070$, $p=0.0057$). Tukey's post-hoc test revealed differences between PBS vs GAS *RORγt*$^{+/-}$ (**p=0.0059) and PBS vs GAS *RORγt*$^{-/-}$ (*p=0.016), but not GAS *RORγt*$^{+/-}$ vs GAS *RORγt*$^{-/-}$ (p>0.999). **c** Glomerular diameter is similarly smaller in GAS-infected mice compared to PBS controls Data represented as mean ± SEM for *n*=8 PBS, *n*=5 GAS *RORγt*$^{+/-}$ and *n*=5 GAS *RORγt*$^{-/-}$ mice. One-way ANOVA revealed a condition effect ($F(2,11) = 11.93$). Tukey's multiple comparisons test revealed significant differences between PBS vs GAS *RORγt*$^{+/-}$ (**p=0.0098) and PBS vs GAS *RORγt*$^{-/-}$ (**p=0.0016), but not GAS *RORγt*$^{+/-}$ vs GAS *RORγt*$^{-/-}$ (p=0.4907). Scale bar = 20 µm.

Histological findings presented here predict that olfactory function is likely impaired in GAS-inoculated mice. This prediction was tested with a behavioral test for olfactory function, the habituation-dishabituation test [244], which leverages a mouse's innate curiosity for new stimuli to measure odor detection and discrimination. The mouse is presented for two minutes with a Q-tip impregnated with 10 µl of odorant or vehicle diluted in water. Time spent investigating (i.e., sniffing) the Q-tip is quantified, and with repeated trials using the same odorant, the mouse rapidly

loses interest and sniffs less (habituation). If the Q-tip is then odorized, the mouse increases investigation time again (dishabituation), demonstrating odor detection. Changing odorant stimulus will also prompt a dishabituation response, demonstrating odor discrimination. PBS control mice exhibit normal odor detection and discrimination (**Figure 3.15**). GAS-infected

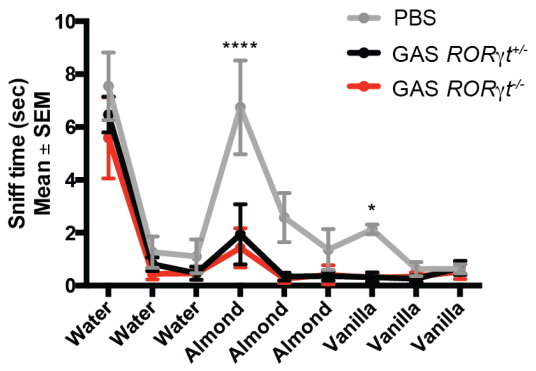

Figure 3.15 GAS-inoculated *RORγt*$^{+/-}$ and *RORγt*$^{-/-}$ mice are hyposmic. Odor detection and discrimination are impaired in GAS-inoculated *RORγt*$^{+/-}$ and *RORγt*$^{-/-}$ mice compared to PBS control *RORγt*$^{+/-}$ mice. RM-ANOVA analyzed for main effects of treatment ($F(2,13)=6.122$, $p=0.0134$) and odor ($F(8,104)=34.15$, $p<0.0001$), as well as interaction ($F(16,104)=2.163$, $p=0.0106$). Tukey's multiple comparisons test showed significantly impaired odor detection in GAS-inoculated mice compared to PBS (almond: PBS vs GAS *RORγt*$^{+/-}$ ****$p<0.0001$; PBS vs GAS *RORγt*$^{-/-}$ ****$p<0.0001$), and significantly impaired odor discrimination (vanilla: PBS vs GAS *RORγt*$^{+/-}$ *$p=0.0436$; PBS vs GAS *RORγt*$^{-/-}$ *$p=0.0456$).

RORγt$^{+/-}$ and *RORγt*$^{-/-}$ mice, however, both show blunted odor detection and no discernible odor discrimination capability (**Figure 3.15**), consistent with abnormal vGluT2 expression in glomeruli (**Figure 3.14ab**). There was no difference in baseline locomotion between treatment groups, suggesting that this result is not due to sickness behavior.

To localize deficits in olfactory processing, we recorded odor-evoked spiking activity in populations of mitral and tufted (M/T) cells from OB of awake, head-fixed mice for both *RORγt*$^{+/-}$ and *RORγt*$^{-/-}$ groups [242, 272]. We anticipated that mitral cell responses to odor in GAS-infected *RORγt*$^{+/-}$ and *RORγt*$^{-/-}$ mice would be blunted or abolished to an equal degree. To test this

prediction, multi-unit recordings using a 32-channel multi electrode probe were performed in male and female *RORγt*$^{+/-}$ and *RORγt*$^{-/-}$ mice inoculated with either PBS or GAS in the laboratory of Dr. Kevin Franks at Duke University. In these experiments, mice were presented with a battery of 11 odor stimuli listed in Table 2.6 across a 25-fold dilution range.

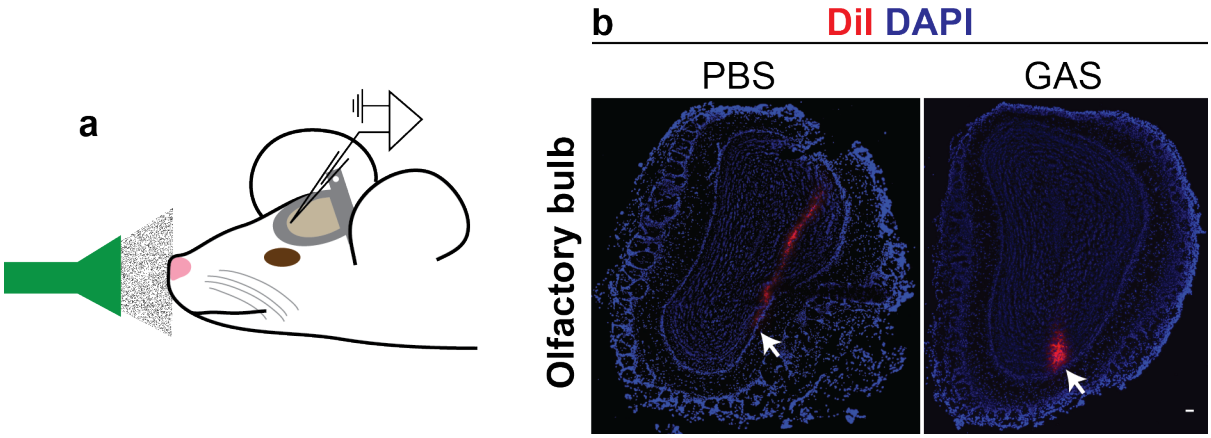

Figure 3.16 Electrophysiological recordings from mitral cell populations. **a** Schematic of headplates surgically fitted to the mouse skull prior to recording. A craniotomy was performed immediately prior to recording. **b** Representative electrode tracts in PBS and GAS mice terminating in the M/T layer of the olfactory bulb (arrow). Tracts were marked using DiI ($DiIC_{18}(3)$) painted on the reverse side of the probe. Scale bar = 100 μm.

Mice were fitted with custom headplates to allow for head-fixed, awake recordings from the OB M/T layer, as illustrated in Figure 3.16a. Probe placement within the brain was determined by breath-locked high spontaneous activity across the electrode array, ~1.5-2 mm deep from the surface of the brain. Prior to electrode insertion into the brain, the fluorescent lipophilic cationic indocarbocyanine dye DiI ($DiIC_{18}(3)$) was painted on the back face of the probe to mark the electrode tract. Electrode placement was confirmed to terminate in the M/T layer post-hoc (**Figure 3.16b**).

Mitral cells in the OB respond to odor in awake mice by modulation of a baseline firing rate. Increased concentration of odorant generally increases the magnitude of mitral cell responses. For each of four treatment groups, heatmaps showing coded responses for all mitral cells were

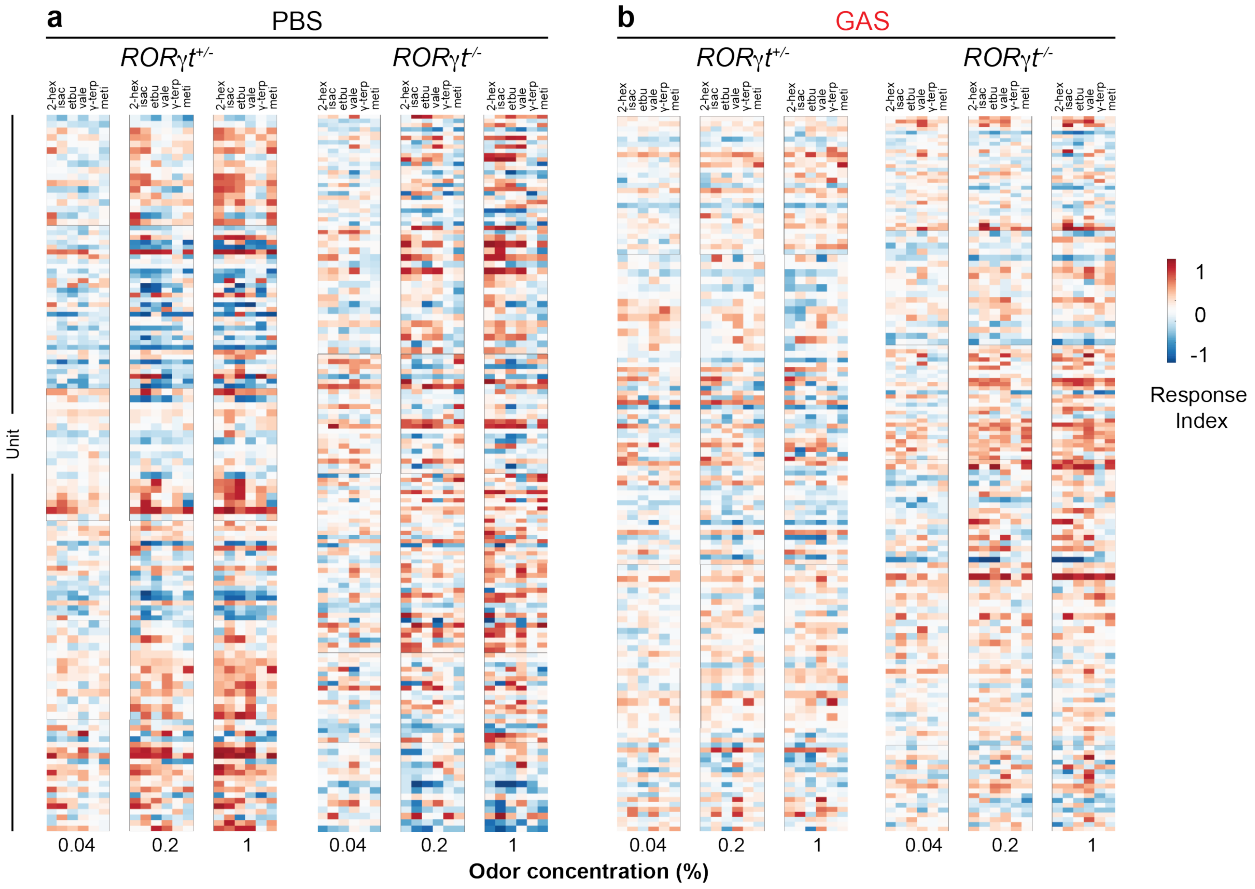

Figure 3.17 Heatmaps showing mitral cell activation and suppression responses. Changes in unit firing rate at odor onset are coded using a response index ranging from -1 to 1, with suppression indicated by negative values and activation represented by positive values. GAS-infected *RORγt*$^{+/-}$ mice have blunted responses to increased odor concentration, in contrast to PBS controls and GAS-infected *RORγt*$^{-/-}$ mice.

generated to investigate overall response quality. It is clear that PBS mice show increased activation and suppression to increased odor concentration, and that the same mitral cell may be activated or suppressed, depending on the odor (**Figure 3.17a**). GAS-infected *RORγt*$^{+/-}$ mice do show mild odor responses, but there is no readily discernible concentration-dependent increase in responsivity with concentration (**Figure 3.17b**, left). In contrast, GAS infected *RORγt*$^{-/-}$ mitral cells recapitulate concentration-dependent increase in response magnitude like PBS mice, indicating a preservation of some mitral cell function (**Figure 3.17b**, right).

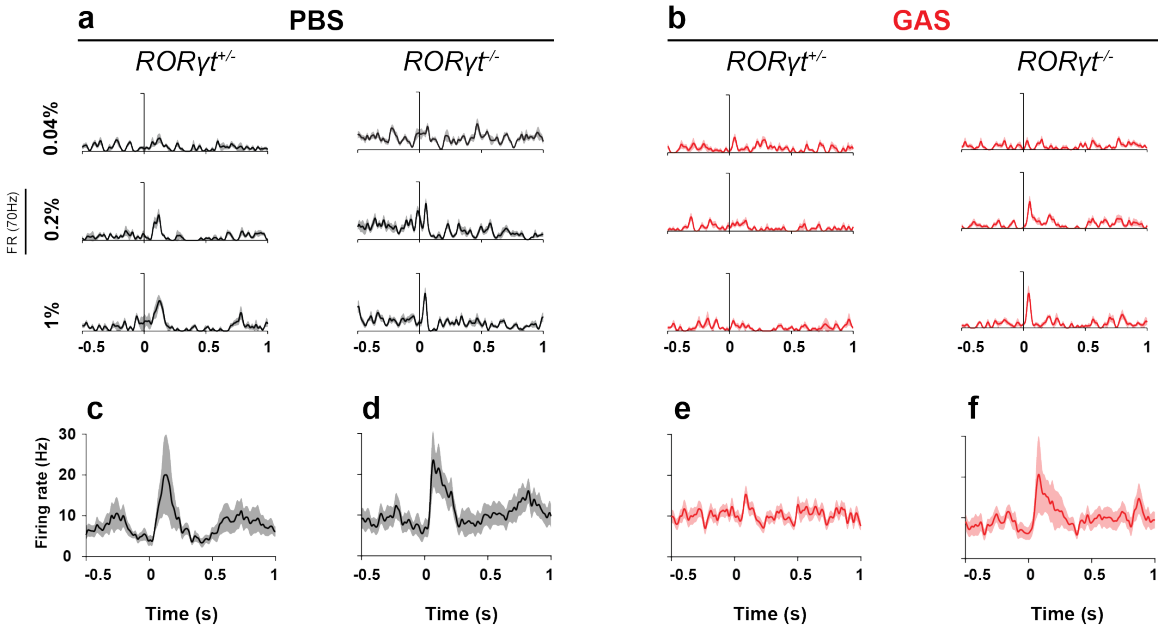

Figure 3.18 Th17-dependent ablation of mitral cell odor response in GAS-inoculated mice. Control mice **a** show increased mitral cell responses from representative units to ethyl butyrate with increased odor concentration in peri-stimulus time histograms (PSTH). In **b**, GAS-infected *RORγt*$^{+/-}$ mice have blunted odor responses to ethyl butyrate, while GAS *RORγt*$^{-/-}$ mice maintain concentration-dependent increase in mitral cell response. Vertical line denotes start of the first inhalation after odor onset. Responses averaged across all odor-concentration stimuli in **c**,**d**,**e**,**f**. Data in **c**,**d**,**e**,**f** were collected from *n*=120 cells from 6 recordings in 4 PBS *RORγt*$^{+/-}$ mice, *n*=140 cells from 7 recordings in 4 PBS *RORγt*$^{-/-}$ mice, *n*=130 cells from 7 recordings in 5 GAS *RORγt*$^{+/-}$ mice, and *n*=144 cells from 4 recordings in 5 GAS *RORγt*$^{-/-}$ mice. Scale bar at left = 70 Hz.

Odor-evoked responses were then aligned to the first inhalation after odor onset (defined as t=0 preceding a 1 sec odor stimulus) and averaged within concentration across all odor stimuli to generate a peri-stimulus time histogram (PSTH). This allows for assessment of mitral cell responses to odor over a 25-fold odor dilution series. Both *RORγt*$^{+/-}$ and *RORγt*$^{-/-}$ control PBS-inoculated mice showed increased odor-evoked response with increasing odor concentration (**Figure 3.18a**). In GAS-infected mice (**Figure 3.18b**), *RORγt*$^{+/-}$ mice do not show odor-evoked responses, even at the highest odor concentration, while *RORγt*$^{-/-}$ mice do show evoked activity in response to odor presentation. PSTHs were then averaged across concentrations to show overall odor-evoked activity; PBS *RORγt*$^{+/-}$ and *RORγt*$^{-/-}$ mice showed clear responses at odor onset (**Figure 3.18cd**). This odor response was absent in GAS-inoculated *RORγt*$^{+/-}$ mice (**Figure 3.18e**),

and partially restored in GAS-inoculated *RORγt*$^{-/-}$ mice (**Figure 3.18f**). This indicates that Th17-induced neuroinflammation may be particularly damaging to mitral cell function.

Individual mitral cells respond to input from only a few glomeruli, so only a fraction of a mitral cell population will respond to a given odor. However, the fraction of mitral cells activated by any odor should increase with odor concentration as more mitral cells get recruited. Calculations of the fraction of active cell-odor pairs for no odor (MO, mineral oil trials) through increasing odor concentrations for PBS and GAS-infected *RORγt*$^{+/-}$ or *RORγt*$^{-/-}$ mice show that mitral cell recruitment to increasing concentration of odor is impaired in GAS-infected *RORγt*$^{+/-}$

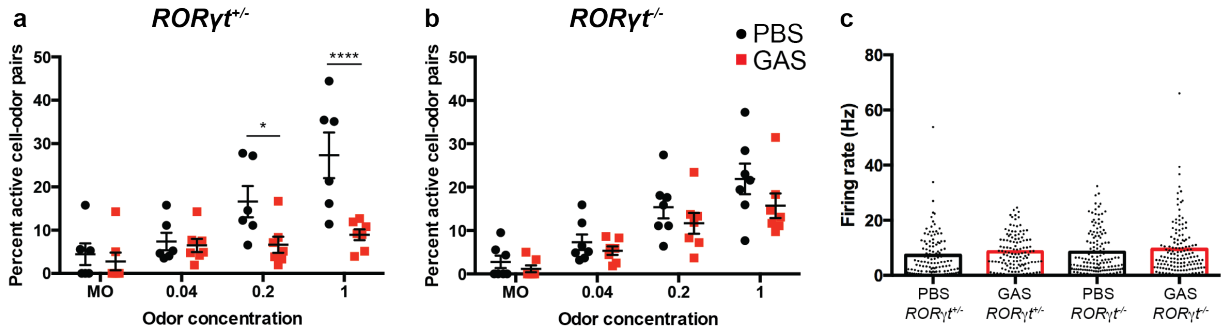

Figure 3.19 Percentage of significantly active cell-odor pairs in female *RORγt*$^{+/-}$ and *RORγt*$^{-/-}$ mice after GAS infections. **a** GAS-infected *RORγt*$^{+/-}$ mice do not show concentration-dependent increases in mitral cell recruitment, while control PBS-infected *RORγt*$^{+/-}$ mice show tonic increase in fraction of cells significantly activated by odor. *RORγt*$^{-/-}$ mice do not show a treatment effect. Data were collected from n=120 cells from 6 recordings in 4 PBS *RORγt*$^{+/-}$ mice, n=140 cells from 7 recordings in 4 PBS *RORγt*$^{-/-}$ mice, n=130 cells from 7 recordings in 5 GAS *RORγt*$^{+/-}$ mice, and n=144 cells from 4 recordings in 5 GAS *RORγt*$^{-/-}$ mice represented as mean ± SEM with symbols representing independent recordings. Two-way ANOVA assessed effects of treatment and odor concentration on activated mitral cell populations. For *RORγt*$^{+/-}$ mice, there was a treatment effect ($F(1,11)=6.381$, $p=0.0282$) and concentration effect ($F(3,33)=24.52$, $p<0.0001$) and interaction between treatment and concentration ($F(3,33)=10.34$, $p<0.0001$). Sidak's multiple comparisons test revealed differences between PBS and GAS-treated animals at 0.2% odor (*$p=0.0449$) and 1% (****$p<0.0001$), but not at baseline (MO, $p=0.9863$) or 0.04% odor ($p=0.9987$). For *RORγt*$^{-/-}$ mice, there was a main concentration effect ($F(3,36)=32.42$, $p<0.0001$), but no treatment effect ($F(1,12)=2.373$, $p=0.1494$), or interaction ($F(3,36)=0.6419$, $p=0.5931$). Sidak's multiple comparisons test indicated no significant differences between PBS and GAS-inoculated mice at any concentration. **c** Firing rate (FR) over the first inhalation after stimulus onset for 0.2% mineral oil stimuli remains constant across treatment groups. Data were collected from n=120 cells from 6 recordings in 4 PBS *RORγt*$^{+/-}$ mice, n=140 cells from 7 recordings in 4 PBS *RORγt*$^{-/-}$ mice, n=130 cells from 7 recordings in 5 GAS *RORγt*$^{+/-}$ mice, and n=144 cells from 4 recordings in 5 GAS *RORγt*$^{-/-}$ mice represented as mean (open bars) with trials (dots). One-way ANOVA found no significant differences in firing rate between treatment groups ($F(3,511)=2.323$, $p=0.0742$).

mice **(Figure 3.18a**). This effect is not observed in *RORγt*$^{-/-}$ mice, where GAS-infected mice still demonstrate concentration-dependent mitral cell recruitment (**Figure 3.18b**). These effects are not due to alterations in baseline firing rate, which remained constant across all four treatment groups (Figure 3.18c). This indicates that mechanosensitive mitral cells are responding normally after GAS infections, and that mitral cells are still healthy and fire at a normal baseline rate. Changes in responsive mitral cell fractions are therefore due to physiological changes in either input from OSNs, inflammation-induced disruption in mitral cell processing, or inflammatory effects on other cell types participating in olfactory processing (e.g., external tufted cells).

Taken together, it is clear that inflammation in the nose after GAS treatment causes frank malfunction of OB mitral neurons separated from nasal infection by a layer of synapses. Infiltration of Th17 cells from the nose into the surrounding brain parenchyma, and subsequent secretion of inflammatory cytokines, is sufficient to affect firing properties of M/T cells in the OB. These experiments show that while olfactory circuit function may be preserved in the absence of Th17 cells, functionally, GAS-infected *RORγt*$^{-/-}$ mice seem equally hyposmic. There may be a threshold of T cell infiltration or cytokine expression that dampens olfactory circuitry function.

3.5 Olfactory circuit deficits after recurrent GAS infections are Th17- and sex-dependent

Sex effects are well-documented for autoimmune conditions, including Sydenham's chorea, rheumatic fever, PANDAS, and multiple sclerosis. In the mouse model used here, female mice demonstrate a Th17-dependent recruitment of T cells to the brain after recurrent GAS infections, whereas males do not show this response (**Figure 3.3b**). Despite smaller initial CNS T cell populations in male mice, comparison of cytokine expression profiles from lymphocytes isolated from male and female *RORγt*$^{+/-}$ brains showed similar populations of IL-17A^{+}, IFNγ^{+}, and IL-17A^{+}

IFNγ^{+} lymphocytes. Both male and female *RORγt*$^{-/-}$ mice showed equivalent decreases in IL-17A^{+} and IL-17A^{+} IFNγ^{+} populations and expansion of the IFNγ^{+} population compared to *RORγt*$^{+/-}$ mice

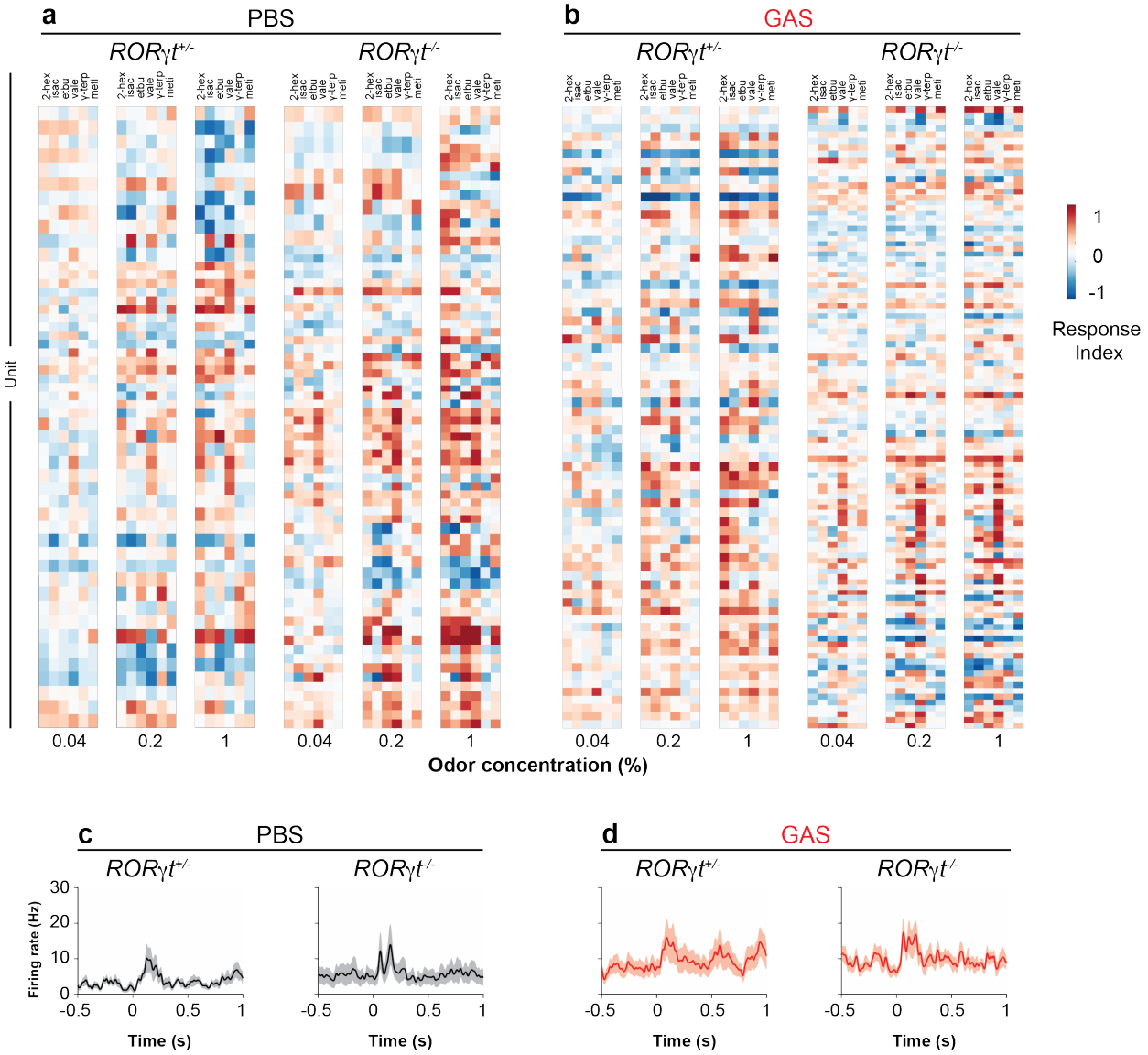

Figure 3.20 Heatmaps of mitral cell activation and suppression responses in male mice. **a** PBS and **b** GAS-inoculated mice mitral cells show relatively normal responses to odor, regardless of treatment and genotype. GAS-inoculated *RORγt*$^{-/-}$ mice appear to have blunted responses to increasing odor concentration, if anything. **c**, **d** PSTHs aligned to onset of the first inhalation after odor presentation (defined as t=0) in *RORγt*$^{+/-}$ and *RORγt*$^{-/-}$ mitral cells. PSTHs are averaged for all odor-concentration stimuli, and all groups show odor-evoked firing with stimulus onset. GAS-inoculated mice in **d** have elevated baseline firing rate before odor onset, but maintain odor-evoked activity tied to stimulus presentation. Data presented as mean ± SEM in **c** and **d** collected from *n*=48 cells from 4 recordings in 3 PBS *RORγt*$^{+/-}$ mice, *n*=65 cells from 5 recordings in 4 PBS *RORγt*$^{-/-}$ mice, *n*=71 cells from 5 recordings in 3 GAS *RORγt*$^{+/-}$ mice, and *n*=83 cells from 4 recordings in 3 GAS *RORγt*$^{-/-}$ mice.

(data not shown). It remained unclear whether the T cells that do infiltrate the brain in male *RORγt*$^{+/-}$ and *RORγt*$^{-/-}$ mice are capable of inciting the same inflammatory damage to olfactory processing seen in female *RORγt*$^{+/-}$ mice after GAS infections.

To examine olfactory circuit function in male mice, electrophysiological recordings in the mitral cell layer were performed in the same manner as in females. In male mice, electrophysiological recordings from mitral cells showed quite different trends than in female mice. In heatmaps of mitral cell activation and suppression by odor stimuli in male mice, all treatment groups showed units responding with activation and suppression to odor (**Figure 3.20ab**). PSTHs aligned to the first breath after odor presentation show that PBS control mice again demonstrate odor-evoked firing at stimulus onset, and both genotypes of GAS-inoculated mice show robust odor responses equivalent to control animals (**Figure 3.20c**). However, firing rate before odor onset appears elevated in GAS-inoculated *RORγt*$^{+/-}$ and *RORγt*$^{-/-}$ mice (**Figure 3.20d**). In male mice, mitral cells show odor-evoked activity regardless of genotype and treatment.

Population-level mitral cell responses were then examined more closely to further investigate these observations. Recruitment of mitral cells with increasing odor concentration was examined by calculating the percent of significantly activated cell-odor pairs for *RORγt*$^{+/-}$ and *RORγt*$^{-/-}$ mice. *RORγt*$^{+/-}$ mice effectively recruit mitral cells with increasing concentration of odor (**Figure 3.21a**), but GAS-inoculated *RORγt*$^{-/-}$ mice show blunted mitral cell recruitment, with a significantly smaller fraction of mitral cells responding to high odor concentrations compared to PBS *RORγt*$^{-/-}$ mice (**Figure 3.21b**). This could be due to either noisier mitral cells that are losing stimulus specificity, or a decrease in excitatory input onto mitral cells, causing them to respond less robustly to odor. Examination of firing rate during control (mineral oil) trials showed that

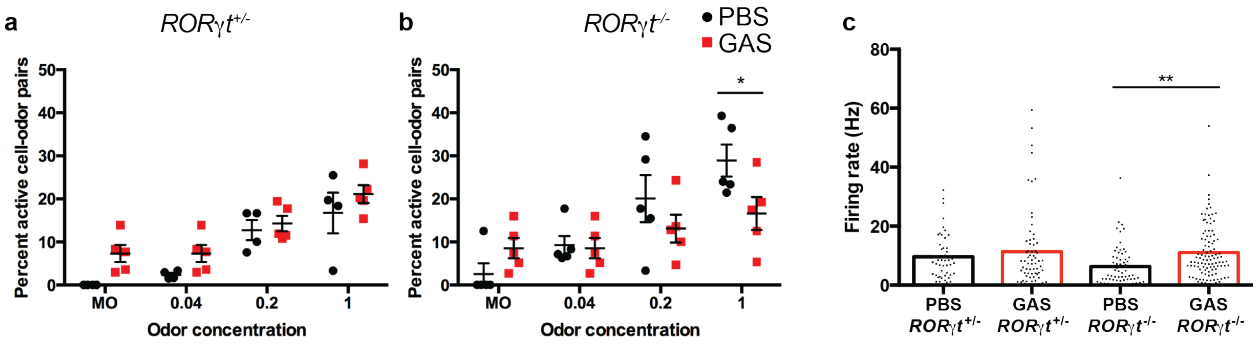

Figure 3.21 Aberrant mitral cell firing properties with increasing odor concentration in GAS-inoculated male mice. **a** Fraction of mitral cells significantly activated by odor is unchanged between PBS and GAS *RORγt*$^{+/-}$ mice. Data represented as mean ± SEM from *n*=48 cells from 4 recordings in 3 PBS *RORγt*$^{+/-}$ mice and *n*=71 cells from 5 recordings in 3 GAS *RORγt*$^{+/-}$ mice. Two-way ANOVA showed a main effect of concentration ($F(3,21)=29.14$, $p<0.0001$) but not treatment ($F(1,7)=3.450$, $p=0.1056$) or interaction ($F(3,21)=0.2728$, $p=0.8443$). **b** *RORγt*$^{-/-}$ GAS-inoculated mice showed significantly impaired mitral cell recruitment only at the highest odor concentration. Data represented as mean ± SEM from *n*=65 cells from 5 recordings in 4 PBS *RORγt*$^{-/-}$ mice and *n*=83 cells from 4 recordings in 3 GAS *RORγt*$^{-/-}$ mice. Two-way ANOVA showed a main effect of concentration ($F(3,24)=36.66$, $p<0.0001$), no main effect of treatment ($F(1,8)=1.793$, $p=0.2173$), and an interaction of concentration and treatment ($F(3,24)=3.539$, $p=0.0298$). Sidak's multiple comparisons test revealed a significant difference between PBS and GAS only at 1% odor (*p=0.0488). **c** Baseline firing rate is elevated in GAS-inoculated mice, but PBS control mice have equivalent FRs. Data are represented as mean (open bars) with individual trials (dots) from *n*=48 cells from 4 recordings in 3 PBS *RORγt*$^{+/-}$ mice, *n*=71 cells from 5 recordings in 3 GAS *RORγt*$^{+/-}$ mice, *n*=65 cells from 5 recordings in 4 PBS *RORγt*$^{-/-}$ mice, and *n*=83 cells from 4 recordings in 3 GAS *RORγt*$^{-/-}$ mice. One-way ANOVA showed significant differences between groups ($F(3,279)=4.05$, $p=0.0077$); Sidak's multiple comparisons test showed a difference in FR in *RORγt*$^{-/-}$ mice (**p=0.0042), but not *RORγt*$^{+/-}$ mice (p=0.3319).

mitral cells in male GAS-infected *RORγt*$^{-/-}$ mice had higher baseline firing rates (**Figure 3.21c**). While mitral cells in GAS-infected *RORγt*$^{-/-}$ mice are certainly able to fire, it remains unclear why they would respond with less specificity to odor in an inflammatory environment. Future experiments could parse whether mitral cells have increased AP threshold after GAS infections, or are receiving more or noisier input from OSN terminals or other cell types in the OB.

3.6 Concluding remarks

AE syndromes trigger acute neurological and psychiatric symptoms, and are widely recognized now that CNS antigens are being validated, yet the mechanisms that underlie antibody-triggered encephalitis remain poorly understood [11, 220, 231], and it is unclear how

autoantibodies breach the BBB to react with neuronal targets [50]. Neuropathological studies have shown infiltration of peripheral T cells in the brains of AE patients [246], and we have previously shown that GAS-specific Th17 cells enter the brain and are associated with vascular dysfunction, neuroinflammation, and synaptic defects in our mouse model of post-infectious BGE [93]. The precise contribution of the cellular immune mechanisms to observed neuropathology, as well as potential functional deficits, remained unclear. Here, we found that Th17 cells recruited to the NALT and OE travel to the brain, where they are required for selective permeability of the BBB, neuroinflammation, and olfactory circuit malfunction. It is necessary to consider these findings in light of what is known about other CNS autoimmune diseases (specifically MS/EAE), and to consider implications for pathogenesis of human AE.

Sex effects are described in autoimmunity overall, MS, Sydenham's chorea, PANDAS, and adults with rheumatic heart disease (but not children with rheumatic fever) [17, 150, 267, 273, 274]. Our original investigations on neuroinflammation used all female SJL/J mice prone to autoimmunity [93]. Current investigations using both male and female mice bred in-house necessitated investigation of possible sex effects in this model. We discovered that in a C57Bl6/J background, the Th17 response to recurrent GAS infections is much larger in female mice than males. This mirrors findings in EAE experiments, where female mice in the C57Bl6/J and SJL/J backgrounds are more susceptible to disease induction than males [121]. After recurrent GAS infections, both female and male mice showed recruitment of Th1/Th17 populations to the NALT and brain, but Th17 expansion in both regions was more marked in females than males (**Figure 3.3**). There was no difference in T cell infiltration in male brains in the absence of Th17 cells in *RORγt*$^{-/-}$, indicating that there may be sex-dependent changes in immune responses to pathogens.

Th17 lymphocytes and their effector cytokines mediate host defense mechanisms to extracellular bacterial infections, but also underlie pathogenesis of many autoimmune conditions [275]. For example, progression of EAE is delayed or blunted, but not completely eliminated, in mice where Th17 function or differentiation is compromised [169, 173]. Consistent with this role in EAE, Th17 cells play an important role in GAS-induced selective BBB permeability permitting antibody entry into the CNS after recurrent GAS infections. However, Th17 cells do not affect permeability to smaller molecules, nor the loss of excitatory synaptic proteins in OB glomeruli. Th1 lymphocytes present in the brains of GAS-inoculated *RORγt*$^{-/-}$ mice secrete IFNγ, which is known to induce tight junction degradation and activate microglia *in vitro* and *in vivo*, although less efficiently than IL-17A [164, 266, 276]. In addition to IFNγ, other cytokines secreted by Th17 and Th1 may contribute to persistent vascular and neuropathological dysfunction observed in our mouse model of post-infectious BGE. Both effector T cell populations are necessary to induce the full spectrum of disease pathology, similar to proposed synergistic models of inflammation and demyelination in MS/EAE [150]. Targeting CNS Th17/Th1 cells therapeutically may therefore mitigate AE disease course.

How are distinct T cell subtypes recruited to the brain during multiple GAS infections? In EAE, Th17 cell numbers peak in the spinal cord 7 days post-immunization, but Th1 cells are rare until day 14 [164]. Adoptive transfer of myelin-specific, *ex vivo* differentiated Th17 cells induces EAE than transfer of Th1 cells, suggesting that Th17 cells predominate during disease initiation, but Th1 cells are important for disease maintenance [277]. Recurrent, but not single, GAS inoculations in mice induce differentiation of IL-17A^{+} IFNγ^{+} autoreactive Th17 cells in the nose, dependent on IL-6 and TGFβ [234, 235]. This T cell population may subsequently recruit other T cell subtypes to the CNS as BGE progresses, as in EAE [165].

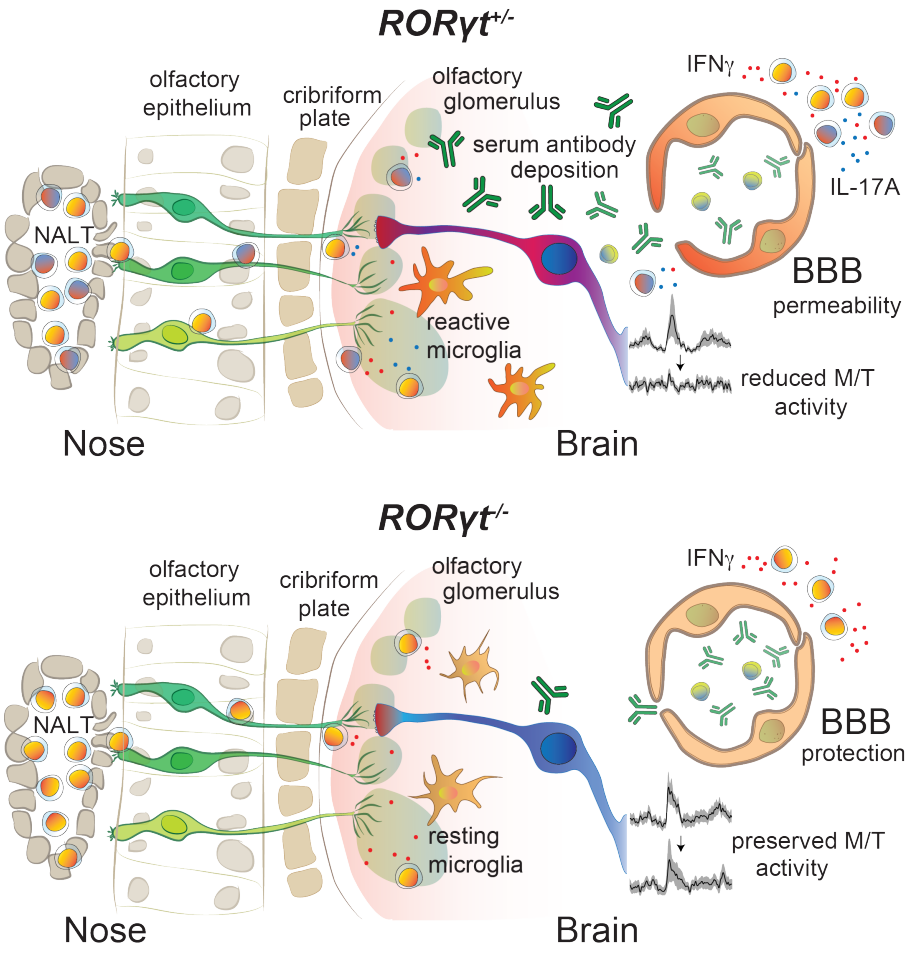

Figure 3.22 Inflammatory Th17 response after GAS infections drives selective BBB permeability, microglial activation, and aberrant mitral cell function. In *RORγt*$^{+/-}$ mice, top, Th1 and Th17 cells migrate from NALT to brain where IL-17A and IFNγ initiate BBB breakdown, neuroinflammation, and mitral cell dysfunction. At bottom, *RORγt*$^{-/-}$ female mice recruit a Th1 response in the NALT and OE. These Th1 cells then migrate in to the brain, where IFNγ secretion is less efficient at permeabilizing the BBB, activating microglia, and initiating changes to mitral cell processing.

In female mice, the role of Th17 are clear in inciting neuroinflammation after recurrent GAS infections. Th17 serve a non-cell autonomous role in T cell recruitment to the brain from OE, as Treg populations in the brain are affected by Th17 deletion (**Figures 3.5** and **3.7**). Interestingly, Tregs are not absent from the brain. The interplay between Th17 and Tregs have been noted in various autoimmune disorders, including MS, SLE, rheumatoid arthritis, and thyroid autoimmunity, and it would be interesting to examine the effects of Treg deletion in the context of

recurrent GAS infections. Exposure of Tregs to IL-1β and IL-6 can override FoxP3 binding inhibition to RORγt, allowing a second route to generate Th17 cells from Tregs [278, 279]. Disruption of the Treg/Th17 axis could therefore compensate for loss of Th17 cells in *RORγt*$^{-/-}$ mice, and provides a potential mechanism for initiation of GAS-induced autoimmunity. It is possible that Tregs serve an important role to limit inflammation after GAS infections, and further experiments should address when they are recruited to the OE and brain.

The presence of Th17/Th1 lymphocytes in the CNS is associated with BBB permeability in post-infectious BGE. Barrier malfunction is an early and persistent feature of neuroinflammation, and play a key role in MS/EAE progression, promoting microglial activation and thus further entry of peripheral immune cells and antibodies [165, 280]. Our findings reinforce the idea that BBB breakdown is not an all-or-none phenomenon, as Th17 cells are not necessary for leakage of small molecules or TJ degradation after GAS infections. Th1 cells present in the CNS can partially affect barrier permeability, degrading TJ proteins and causing structural alterations to a similar degree as Th17 cells, as has been reported for EAE [115]. Th17 cells are critical for inducing selective BBB permeability to larger molecules, as their elimination significantly reduces extravasation of IgG into the parenchyma after recurrent GAS inoculations. Conversely, cytokines secreted by Th17 cells may act indirectly on the endothelium by a different mechanism to promote BBB permeability to larger molecules [100, 280]. IL-17A or IL-23, both cytokines produced by Th17, may be important for inducing selective transport of larger proteins like albumin and IgG.

Inflammatory cytokines IL-17A and IFNγ secreted by Th17 and Th1 cells lead to local production of TNFα, IL-6, and IL-1β in the CNS, sustaining neuroinflammation. Th17 cells are more potent activators of microglia, although effects of both Th17 and Th1 can induce expression

of MHC class II on microglial membranes [164]. Our findings agree with these results from the EAE literature, with reduced microglial activation in GAS-inoculated *RORγt*$^{-/-}$ mice compared to *RORγt*$^{+/-}$ mice. In addition to their role in immune surveillance, synaptic sculpting in development and disease is dependent on microglia [180, 281-283]. Thus, microglial synaptic sculpting may partially explain synaptic deficits seen in *RORγt*$^{+/-}$ mice, as compared to *RORγt*$^{-/-}$ mice with minimal microglial activation (**Figure 3.14**).

Hyposmia and anosmia have been linked to prodromal symptoms in Alzheimer's disease, multiple sclerosis, motor neuron disease, and Huntington's disease [248, 249, 284]. Immune dysfunction in Alzheimer's disease and MS provide a further link to our mouse model of basal ganglia encephalitis with hyposmia [143, 265, 282]. Most convincingly, mouse models of Alzheimer's disease show that complement deposition guides microglia to degrade synaptic circuits [282]. Excessive immune infiltration and microglial activation in the OB of GAS-infected mice accompany hyposmia; these mice show severe physiological deficits in mitral and tufted (M/T) cell responses to odor presentation, consistent with a decrease in vesicular glutamate packing protein vGluT2 within glomeruli. While downregulation of vGluT2 in olfactory sensory neuron terminals is the parsimonious explanation for reduced neurotransmission in M/T cells, vGluT2 is also expressed in external tufted cell dendrites, which are the major drivers of mitral cell responses *in vitro* [285]. It is possible that either OSN terminals or ET dendrites contribute to the reduction in vGluT2 within glomeruli. Future experiments comparing responses in external tufted cells versus periglomerular cells versus OSN output will distinguish between these two possibilities. Nevertheless, vGluT2 loss in OB glomeruli translates to blunted odor responses of mitral cells, propagating the effects of intranasal infections down the olfactory processing pathway in GAS-infected mice. These deficits are Th17-dependent, but whether Th17 cells act directly to

impair neural function, or indirectly via activated microglia or infiltrating autoantibodies remains unclear. In the present studies, these deficits are all significantly blunted in *RORγt*$^{-/-}$ mice, so further experiments will be necessary to tease apart the mechanisms of Th17 action. It also remains unclear how long these olfactory processing deficits persist after GAS infections, and if the changes seen in OB circuits affect more complex olfactory processing dependent on the piriform, AON, or amygdala [242, 272].

These results indicate that GAS-induced neuroinflammation in mice is dependent on Th17 cells, and reinforce the multiple hit hypothesis for post-Streptococcal BGE (SC/PANDAS) pathogenesis in children. Development of rheumatic fever is directly linked to untreated GAS infections, and cross-reactive antibodies generated by these processes can act in the brain to interfere with neuronal transmission. However, BBB breakdown is a critical step in this process, and the results of experiments described here suggest that Th17 cells generated to fight infection in the NALT promote inflammation in the brain as well. Apart from facilitating BBB breach, Th17 cells may play an independent role in interfering with neuronal signaling. In the future, experiments using rodent models of post-infectious BGE should address outstanding questions about disease process such as: contribution of paracellular vs transcellular routes of BBB breach to antibody delivery to the brain; the potential role of microglia in synapse degradation; and which cells are primarily driving vGluT2 loss in olfactory circuit breakdown.

Chapter 4: Chemokine signaling via CCL2/CCR2 and CCL20/CCR6 is required for CNS T cell recruitment in post-Streptococcal BGE

4.1 Introduction

Immune cell trafficking through blood and lymphatic vasculature is regulated by interconnected networks of chemokine ligand/receptor signaling. While chemokines do not necessarily share high sequence homology, conserved structural elements link these proteins as a family [193]. In neuroinflammation, chemokines are instrumental in recruiting peripheral immune cells to the CNS. Monocytes, macrophages, dendritic cells, B cells, and T cells all respond to chemokine cues to infections, and then drain back to peripheral lymph nodes. Distinct T cell subtypes also express different chemokine receptors, summarized in **Figure 4.1**, where warmer colors indicate higher expression and cooler colors indicate lower expression. Expression of most chemokine receptors is very low on naïve T cells, and increases once T cells have differentiated to their terminal phenotype [286]. Th17 cells and regulatory T cells (Tregs) express many of the same chemokine receptors, while the chemokine receptor profile expressed on Th1 and Th2 cells is distinct from the Th17/Treg panel [286]. CCR6 is highly expressed on Th17 and Treg cells. CCR6 is unique in the chemokine receptor family because it only binds a single ligand, CCL20 [188]. CCL20 is expressed at low levels basally in mucosal epithelia, and is upregulated in olfactory epithelia under inflammatory conditions [287]. This chemokine axis is an attractive target to interfere with recruitment Th17 chemotaxis. In EAE, interfering with CCR6 function or expression limits entry of Th17 cells into the CNS via the choroid plexus [129, 165, 245]. CCR6 facilitates initial entry of T lymphocytes into the CNS [288]; this first population of T cells then recruit a second wave of immune cells to enter through the inflamed BBB [115].

CCL2 is expressed by astrocytes and neurons in the CNS to signal to microglia in inflammatory states [198, 200, 240]. Its receptor CCR2 is expressed by a large number of immune cells, including Th1 and Th2 lymphocytes. In the spinal cord in EAE, neuron- and astrocyte-derived CCL2 efficiently promote homing of Th1 and Th2 to the CNS [200, 289]. While CCR4 and CCR5 are highly expressed on Th1, Th2, and Th17 cells, the strongest evidence implicating CCR4 in CNS autoimmunity shows that it is strongly chemotactic for dendritic cells and macrophages rather than T lymphocytes [290, 291]. In EAE, it has been shown that dendritic cells

	naive	Th1	Th2	Th17	iTreg	Treg
Ccr7	14.4	12.9	11.8	13.3	14.7	12.9
Ccr6 SU	2.63	2.33	3.89	11.2	12.8	10.4
Cxcr4	12.4	9.94	10.8	10.3	9.89	11.4
Ccr4	6.14	11.4	12.2	12.3	10.1	9.63
Ccr2	3.66	13.0	13.1	7.52	3.27	8.25
Cx3cr1	4.98	3.53	3.33	6.83	6.84	5.15
Ccr5 SU	4.30	14.0	9.63	11.3	3.26	6.97

Figure 4.1 Chemokine receptor expression on T cell subsets. Relative expression (arbitrary units) of selected chemokine receptors on T lymphocyte subsets, excerpted from [286]. Warmer colors correspond to higher relative expression, cooler colors indicate lower expression.

are recruited to the CNS in a CCR2-dependent manner, and then exit via lymphatic drainage guided by CCL21/CCL19/CCR7 signaling [146, 201]. CCR2 is also expressed on microglia, which links innate and adaptive immunity in the CNS.

CCR4 and CCR5 are also highly expressed on Th1, Th2, and Th17 lymphocyte populations. The strongest evidence implicating CCR4 signaling in CNS autoimmunity is not linked to lymphocyte recruitment, but rather to dendritic cell and macrophage homing in CNS autoimmunity [288, 289]. The overarching goal of experiments described in this chapter is to investigate the temporal dynamics of T cell entry into the CNS after recurrent GAS inoculations, and how chemokines may guide T lymphocytes in this process.

4.2 Temporal dynamics of CCL2 and CCL20 expression

To assess the temporal dynamics of T cell entry into the CNS over multiple GAS inoculations, mice were inoculated intranasally with GAS as described (see Chapter 2), sacrificed at 48h after each infection, and T cell distribution was analyzed as described [93]. T cells accumulate gradually in the OB over the course of five inoculations. After 2 infections (2i), there is significant infiltration in the brain compared to PBS controls (**Figure 4.2**). However, the most significant increase in T cell numbers was seen at 4i. PBS control mice showed minimal numbers of T cells after both 1 and 5 infections, and were pooled for this analysis. Changes in T cell infiltration at 2i and 4i correspond to induction of TGFβ–1 and IL-6 in NALT, which are both essential factors for Th17 differentiation [234, 235].

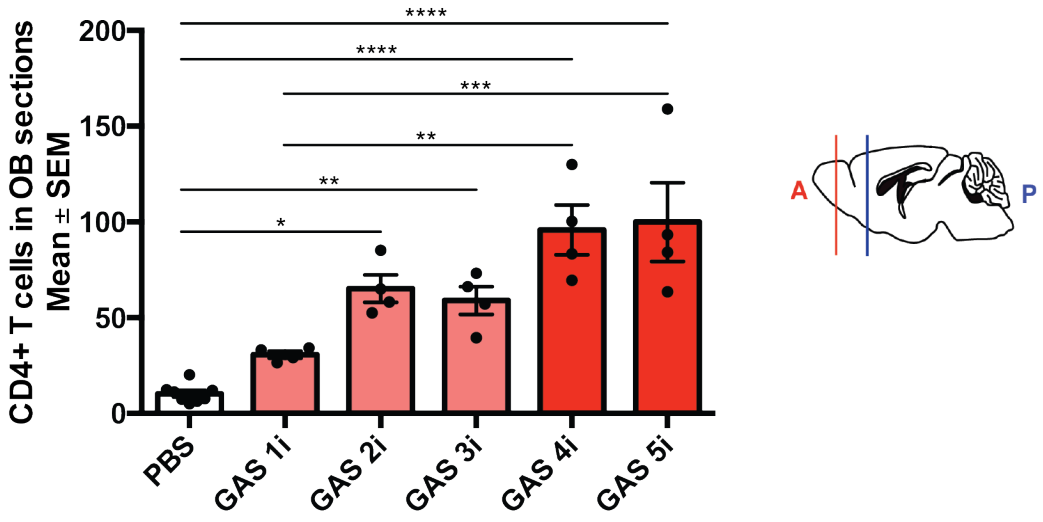

Figure 4.2 T cells accumulate in anterior brain over the course of several infections. Cohorts of mice were sacrificed 48h after 1, 2, 3, 4, and 5 GAS inoculations (i) and 1 or 5 PBS inoculations, and anterior T cell counts were assessed. Left, mean T cell count per 12 μm brain section over 4 sections spanning bregma 4.28-2.46. Schematic at right shows brain region analyzed between red and blue vertical lines. Data collected from n=4 mice per group, with PBS 1i and PBS 5i groups pooled. One-way ANOVA assessed differences between groups ($F(5,22)=17.17$, $p<0.0001$). Bonferroni's multiple comparisons test revealed significant differences between PBS vs GAS 2i (*p=0.024); PBS vs GAS 3i (**p=0.0084); PBS vs GAS 4i (****p<0.0001); PBS vs GAS 5i (****p<0.0001); GAS 1i vs GAS 4i (**p=0.0018); and GAS 1i vs GAS 5i (****p=0.0009).

Previous studies have shown that TGFβ (together with IL-6) is necessary for Th17 expansion in the NALT after GAS infections; TGFβ is significantly upregulated at 2i, and expression remains high after subsequent infections [234]. Therefore, upregulation in chemokine expression at 2i and 4i may be critical for entry of T cells into the CNS.

4.3 Chemokines CCL2 and CCL20 expressed in olfactory tissues after GAS infections

We have shown that Th17 cells enter the CNS via the olfactory route to promote neuroinflammation and neural circuit damage after recurrent GAS inoculations. In order to identify chemokine cues that may recruit T cells from OE to the CNS, 18 candidate chemokine ligands were screened for expression changes in olfactory tissues of GAS and PBS mice. OE, OB, and NALT tissue were harvested at 6 h and 48 h after the fifth infection, and cDNA was generated from RNA isolated from these tissues. We then performed qRT-PCR on OB cDNA first to assess

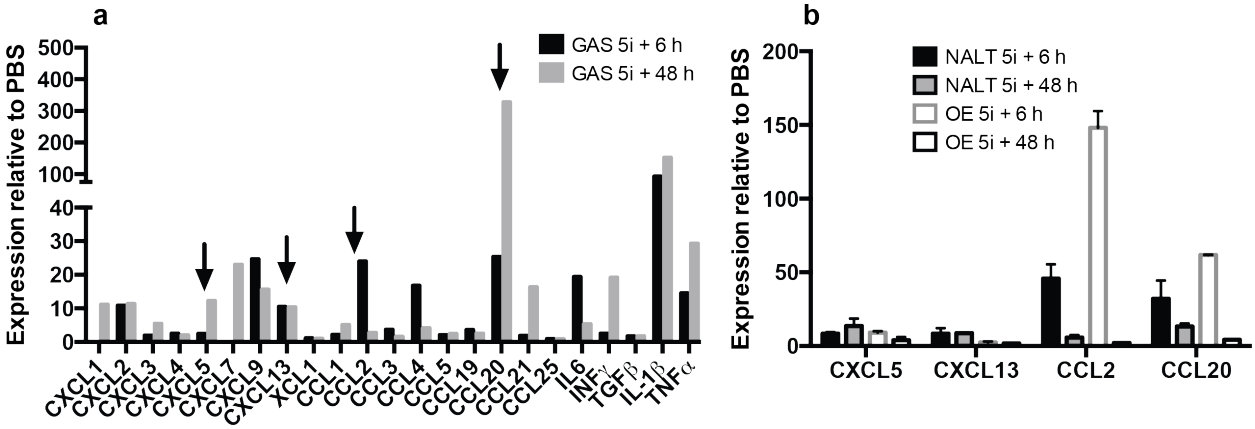

Figure 4.3 qRT-PCR screen for chemokine and cytokine expression after recurrent GAS infections in olfactory tissues. **a** Screen in olfactory bulb cDNA from control and recurrently infected mice sacrificed at 6 h and 48 h after the final GAS infection revealed candidates CXCL5, CXCL13, CCL2, and CCL20. Data represented as mean from *n*=4 PBS 6 h, *n*=4 PBS 48 h, *n*=3 GAS 6 h, and *n*=4 GAS 48 h. **b** Probing NALT and olfactory epithelium cDNA showed significant upregulation at different time points for CCL2 and CCL20, with only slight changes in expression of CXCL5 and CXCL13. All data are relative to β-actin, then normalized to PBS expression. Data represented as mean ± SEM from *n*=4 per group with matched OE and NALT samples.

chemokine ligands differentially expressed in brains of PBS and GAS-inoculated animals (**Figure 4.3a**). We identified upregulation of *CXCL5*, *CXCL13*, *CCL2*, and *CCL20* (vertical arrows) in OB cDNA from GAS-inoculated mice compared to PBS controls. These ligands are implicated in T cell chemotaxis [98, 201, 265]. Inflammatory cytokines IL-6, IFNγ, TNFα, and IL-1β were also significantly upregulated in the OB of GAS-inoculated mice compared to PBS controls. These cytokines are a known signature of bacterial GAS infection in olfactory tissues, and served as positive controls. Expression of chemokines that were upregulated in the OB of GAS-infected mice was then analyzed in NALT and olfactory epithelium. While changes in *CXCL5* and *CXCL13* expression in NALT and OE were modest, *CCL2* was highly upregulated in NALT and OE at 6 h after 5 infections, and *CCL20* was upregulated in NALT at 6 and 48 h and in OE at 6 h (**Figure 4.3b**). These data two candidate chemokines may play a role in T cell recruitment to the brain after recurrent GAS infections.

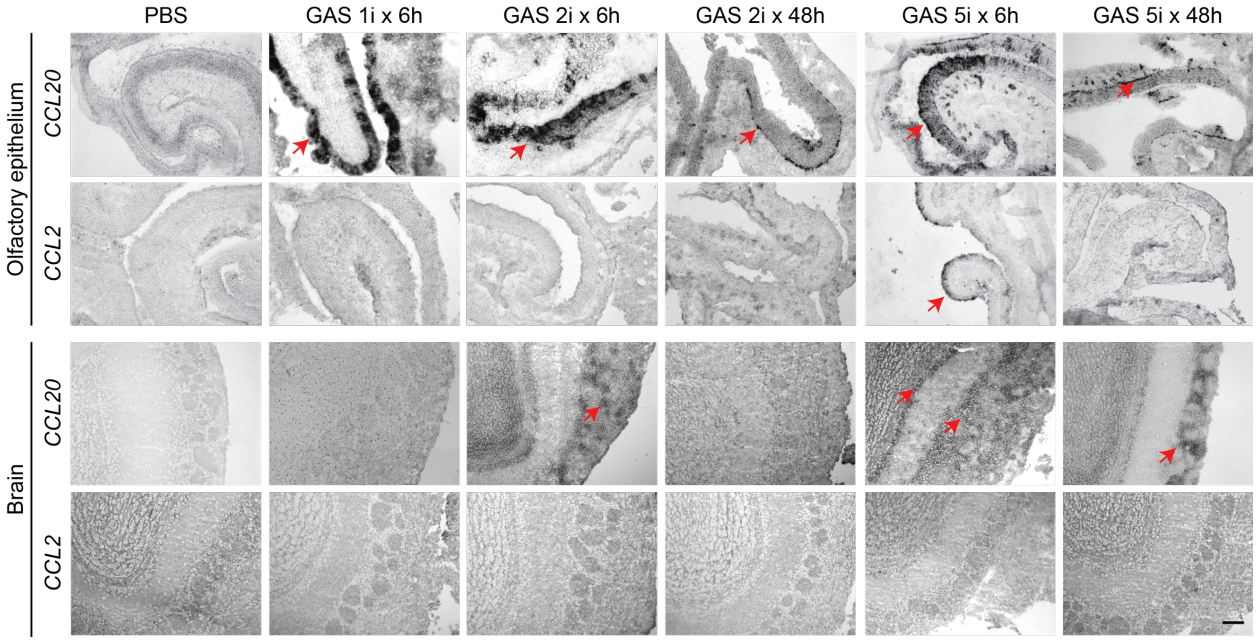

Figure 4.4 Olfactory expression of *CCL2* and *CCL20* confirmed by *in situ* hybridization. Olfactory epithelia and olfactory bulb of control and GAS-infected mice probed for *CCL2* and *CCL20* at different points after 1, 2, or 5 infections (1i, 2i, 5i). Expression of *CCL20* is visible in GAS-infected OE at all time points, while *CCL2* is only expressed after 5i. In brain, *CCL20* is expressed after 2i and 5i, while *CCL2* expression was not detected in brain at any time point. Scale bar = 100 μm.

Expression of CCL2 and CCL20 mRNA was confirmed in olfactory tissues by *in situ* hybridization. *CCL20* is expressed in OE at all time points examined after GAS infections, while OE expression of *CCL2* is robust at 6 h after 5i (**Figure 4.4**). Its expression returns to baseline by 48 h after 5i, and appears to span the olfactory sensory neuron layer. In the olfactory bulb, *CCL20* is detectable at 6 h after 2i, but is absent at later timepoints. After 5 infections, expression in the brain is robust and persists to 48 h. *CCL2* was not detected in brain at any time point. These data indicate that temporal dynamics of chemokine expression may induce migration of different T cell subsets over time both after each infection and with increasing infection number. There was only minimal expression of *CCL2* and *CCL20* mRNA in PBS-inoculated tissues at all time points (**Figure 4.4**).

4.4 CCR2 and CCR6 guide T cells into the CNS after recurrent GAS inoculations

Interfering with CCL20/CCR6 chemokine signaling in EAE delays disease onset and lessens clinical severity due to reduced Th17 cell chemotaxis into the CNS [245, 292]. Since *CCL20* is upregulated in OE, NALT, and brain after 5 GAS inoculations, we tested the role of CCL20/CCR6 signaling in T cell recruitment to the CNS after multiple GAS inoculations using CCR6-deficient mice. $CCR6^{+/-}$, $CCR6^{-/-}$, and WT littermates were recurrently infected with GAS and analyzed for T cell trafficking into the CNS. After recurrent GAS infections, $CCR6^{+/-}$ mice showed reduced T cell infiltration (65% of WT), but surprisingly, $CD4^+$ T cell numbers in $CCR6^{-/-}$ mice were equivalent to WT (**Figure 4.5a**). *CCL20* is upregulated in brain tissue after only two infections (**Figure 4.4**), giving ample time for compensatory signaling changes. Since CCR6 is highly expressed on Th17 cells (**Figure 4.1**), we investigated whether the Th17 cell fraction was affected in $CCR6^{+/-}$ and $CCR6^{-/-}$ mice after GAS infections by crossing CCR6 knockout mice to

RORγt-GFP mice, generating progeny with fluorescently labeled Th17 cells and lacking CCR6 expression. After recurrent GAS infections, we saw equivalent Th17 fractions in the brains of *CCR6*$^{+/-}$ *RORγt*$^{+/-}$ and *CCR6*$^{-/-}$ *RORγt*$^{+/-}$ (37.5% in *CCR6*$^{+/-}$ *RORγt*$^{+/-}$ and 37.7% in *CCR6*$^{-/-}$ *RORγt*$^{+/-}$, **Figure 4.5b**). The Th17 fraction in these mice was similar to Th17 fraction in *CCR6*$^{+/+}$

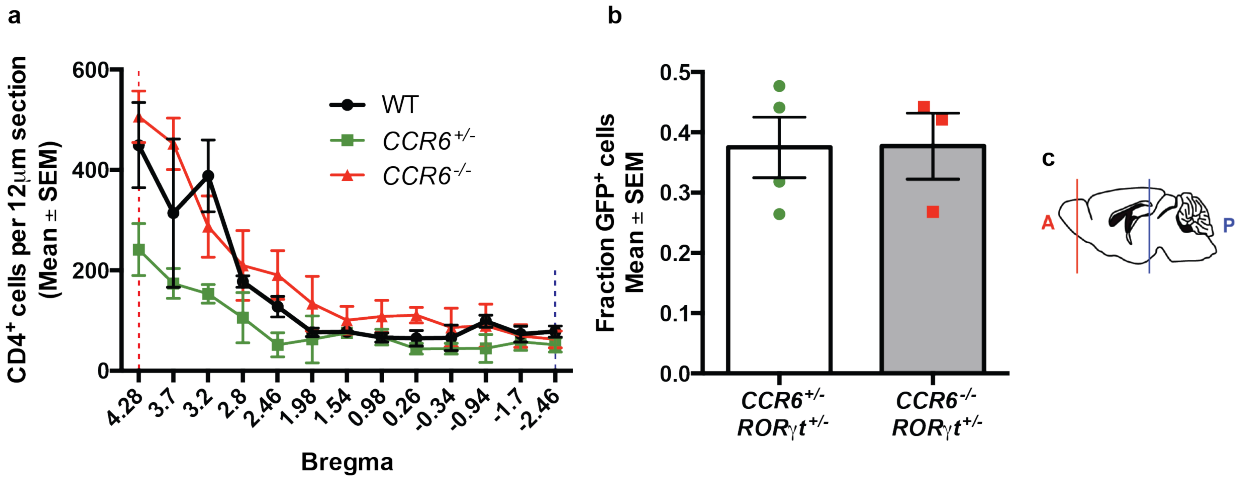

Figure 4.5 Blunted T cell infiltration in CCR6 chemokine receptor mutant mice.**. a** *CCR6*$^{+/-}$ and *CCR6*$^{-/-}$ brain CD4^{+} T cell counts along the rostrocaudal axis. Total T cell counts are reduced by 38% in *CCR6*$^{+/-}$, and increased by 145% in *CCR6*$^{-/-}$ mice compared to WT. Data represent mean ± SEM from *n*=5 WT, *n*=9 *CCR6*$^{+/-}$, and *n*=7 *CCR6*$^{-/-}$ animals. Dashed red and blue lines correspond to locations in the brain as denoted in the schematic **c**. **b** CD4^{+} GFP^{+} Th17 cells were counted in *CCR6*$^{+/-}$ *ROR*$^{+/-}$ and *CCR6*$^{-/-}$ *ROR*$^{+/-}$ brains after GAS inoculations. Data represent mean ± SEM from n=4 *CCR6*$^{+/-}$ *ROR*$^{+/-}$ and n=3 *CCR6*$^{-/-}$ *ROR*$^{+/-}$ mice. Th17 fraction was not significantly different between genotypes by Student's *t*-test (*t*=0.02672, p=0.9797).

RORγt$^{+/-}$ brains (~34%). This implies that Th17 cells may use other chemokines in addition to CCL20/CCR6 pathway to migrate from the OE/NALT to the CNS.

We then investigated the effect of CCL2/CCR2 signaling on T cell recruitment to the brain after GAS infections. Since *CCL2* is upregulated in OE after 5i, that this signaling axis might have a more modest effect on T cell infiltration than CCL20/CCR6 signaling. To this end, we analyzed T cell numbers in the brains of WT, *CCR2*$^{+/-}$ and *CCR2*$^{-/-}$ mice after 5 GAS infections. T cell infiltration was reduced in both *CCR2*$^{+/-}$ (by 53.3%) and *CCR2*$^{-/-}$ (by 44.7%) brains compared to WT (**Figure 4.6a**). In contrast to CCR6 mutants, loss of one or both alleles of CCR2 shows a

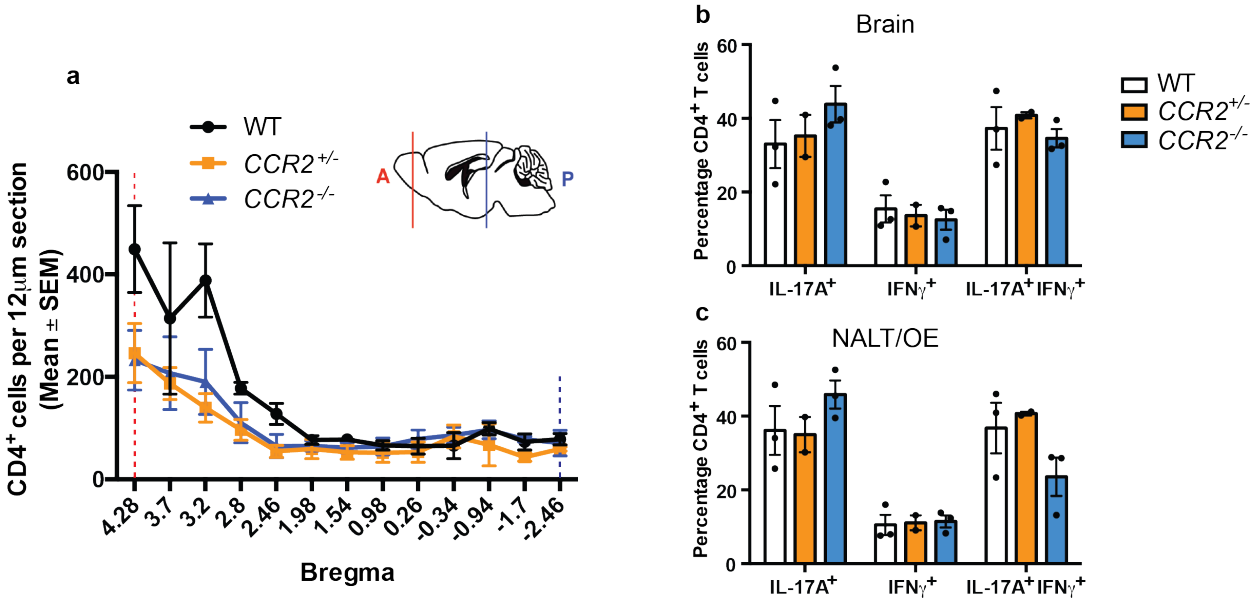

Figure 4.6 CCR2 signaling recruits T cells to the brain, but does not affect T cell differentiation. *CCR2*$^{+/-}$ and *CCR2*$^{-/-}$ brain CD4$^+$ T cell counts along the rostrocaudal axis. T cell counts are reduced by 53% in *CCR2*$^{+/-}$ and 45% in *CCR2*$^{-/-}$ mice compared to WT. Data represent mean ± SEM from n=5 WT, n=6 *CCR2*$^{+/-}$, and n=6 *CCR2*$^{-/-}$ animals. **b** Cytokine expression in brain CD4$^+$ lymphocytes was equivalent between WT, *CCR2*$^{+/-}$, and *CCR2*$^{-/-}$ mice. Data represent mean ± SEM from n=3 WT, n=2 *CCR2*$^{+/-}$, and n=3 *CCR2*$^{-/-}$ animals. Two way ANOVA showed a significant main effect of cytokine ($F(2,10)=17.64$, $p=0.0005$), but no main effect of genotype ($F(2,5)=1.044$, $p=0.4181$). **c** Cytokine expression in NALT/OE CD4$^+$ lymphocytes was equivalent between WT, *CCR2*$^{+/-}$, and *CCR2*$^{-/-}$ mice. Data represent mean ± SEM from n=3 WT, n=2 *CCR2*$^{+/-}$, and n=3 *CCR2*$^{-/-}$ animals, matched to brain samples. Two way ANOVA showed a significant main effect of cytokine ($F(2,10)=19.14$, $p=0.0004$), but no main effect of genotype ($F(2,5)=1.744$, $p=0.2663$).

similar effect on T cell trafficking, indicating that any disruption of CCL2/CCR2 signaling impairs T cell chemotaxis into the brain. To examine whether CCL2/CCR2 signaling affects recruitment of distinct lymphocyte subtypes to NALT or brain after recurrent GAS infections, or differentiation in the NALT, we examined subtype distributions by cytokine expression (IFNγ$^+$ *vs* IL-17A$^+$ *vs* IL-17A$^+$ IFNγ$^+$) using flow cytometry (**Figure 4.6bc**). Disruption of CCR2/CCL2 signaling did not affect specification of T cell subtypes in peripheral lymphoid tissue (NALT). Although T cell numbers were reduced in *CCR2*$^{+/-}$ and *CCR2*$^{-/-}$ brains, there was no difference in populations of distinct subtypes, suggesting that their recruitment to the CNS is equally affected by loss of this signaling pathway (**Figure 4.6b**). Taken together, these data indicate that CCR2 signaling contributes to CNS T cell homing, but not differentiation, after recurrent GAS inoculations.

To determine whether CCL2 and CCL20 signaling may crosstalk to recruit T cells to the CNS after GAS inoculations, *CCR6*$^{+/-}$ and *CCR2*$^{+/-}$ mice were interbred to generate mice lacking 3 or 4 alleles from both chemokine receptors. The resulting progeny (*CCR6*$^{+/-}$ *CCR2*$^{+/-}$, *CCR6*$^{+/-}$ *CCR2*$^{-/-}$, and *CCR6*$^{-/-}$ *CCR2*$^{-/-}$) were infected with GAS as described, and T cell populations in the

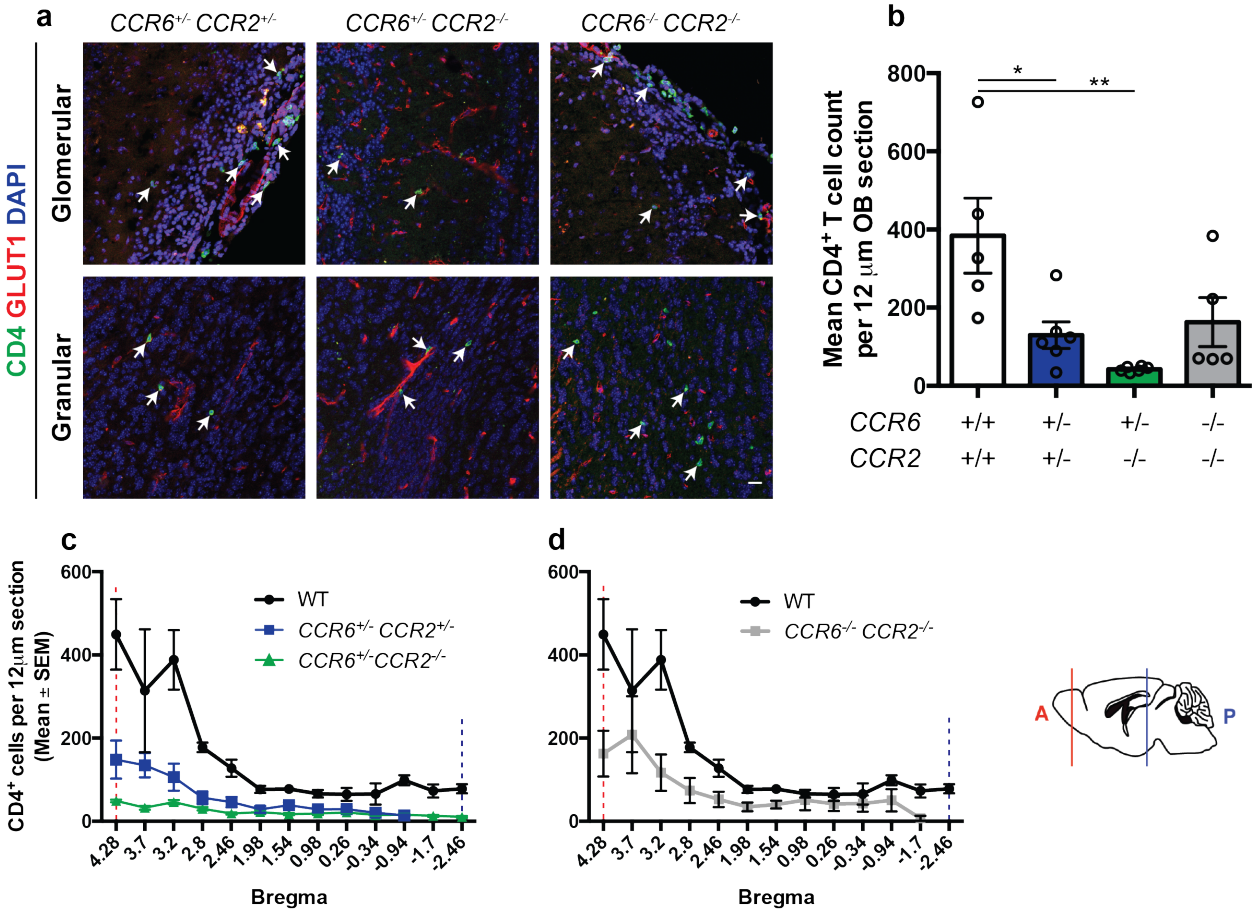

Figure 4.7 Interrupted chemokine axes influence T cell homing to brain. **a** Immunostained OB sections from *CCR6*$^{+/-}$ *CCR2*$^{+/-}$ (left), *CCR6*$^{+/-}$ *CCR2*$^{-/-}$ (center), and *CCR6*$^{-/-}$ *CCR2*$^{-/-}$ (right) brains for CD4 (green), GLUT1 (red) and DAPI (blue). CD4$^+$ T cells (arrows) are numerous in glomerular and granular layers of *CCR6*$^{+/-}$ *CCR2*$^{+/-}$ and *CCR6*$^{-/-}$ *CCR2*$^{-/-}$ brains, with less infiltrate in OB layers in *CCR6*$^{+/-}$ *CCR2*$^{-/-}$ brains. In all cases, there are more T cells in the glomerular and olfactory nerve layers than the granular layer. **b** Mean CD4$^+$ T cell count from three olfactory bulb tissue sections in WT, *CCR6*$^{+/-}$ *CCR2*$^{+/-}$, *CCR6*$^{+/-}$ *CCR2*$^{-/-}$, and *CCR6*$^{-/-}$ *CCR2*$^{-/-}$ brains. Data represent mean ± SEM from n=5 WT, n=6 *CCR6*$^{+/-}$ *CCR2*$^{+/-}$, n=6 *CCR6*$^{+/-}$ *CCR2*$^{-/-}$, and n=5 *CCR6*$^{-/-}$ *CCR2*$^{-/-}$ mice. One-way ANOVA revealed a genotype effect ($F(3,18)=6.778$, **p=0.003). Tukey's MC test revealed significant differences in WT vs *CCR6*$^{+/-}$ *CCR2*$^{+/-}$ (*p=0.0205); and WT vs *CCR6*$^{+/-}$ *CCR2*$^{-/-}$ (**p=0.0019). **c** CD4$^+$ T cell distribution along the rostrocaudal axis in WT (black), *CCR6*$^{+/-}$ *CCR2*$^{+/-}$ (blue), and *CCR6*$^{+/-}$ *CCR2*$^{-/-}$ (green) brains. Dramatic reduction in T cell counts is clear in *CCR6*$^{+/-}$ *CCR2*$^{-/-}$ brains in anterior and posterior regions. **d** CD4$^+$ T cell distribution along the rostrocaudal axis in WT (black) and *CCR6*$^{-/-}$ *CCR2*$^{-/-}$ (gray) brains. Chemokine receptor double knockout mice have a modest reduction in T cell counts, but less dramatically than genotypes represented in **c**. Dashed vertical red and blue lines (**c**, **d**) correspond to locations denoted in the brain schematic (lower right). Scale bar = 20 μm.

brain were analyzed and compared to WT mice. There was a significant reduction in numbers of $CD4^+$ T cells in brains of mice lacking 3 or 4 alleles of CCR2 and CCR6 when compared to WT controls (**Figure 4.7a**b). This decrease was most notable in and *CCR6*$^{+/-}$ *CCR2*$^{-/-}$ mice within the glomerular layer of the OB (white arrows). T cells were not associated with blood vessels (labeled with GLUT1), and most have clearly infiltrated the brain parenchyma. Comparison of average T cell counts in OB sections in chemokine receptor allele knockouts show that loss of any combination of chemokine receptor alleles results in a significant reduction in T cell populations in OB tissue sections (**Figure 4.7b**). *CCR6*$^{+/-}$ *CCR2*$^{+/-}$ and *CCR6*$^{+/-}$ *CCR2*$^{-/-}$ have significantly reduced OB T cell counts compared to WT (31.9% and 13.8% of WT levels, respectively). OB T cells in *CCR6*$^{-/-}$ *CCR2*$^{-/-}$ mice are reduced to 40.0% WT levels. The difference in T cell counts between *CCR6*$^{+/-}$ *CCR2*$^{+/-}$ and *CCR6*$^{+/-}$ *CCR2*$^{-/-}$ mice is most clear in OB sections, but T cell populations in posterior brain regions are reduced as well in *CCR6*$^{+/-}$ *CCR2*$^{+/-}$ and *CCR6*$^{+/-}$ *CCR2*$^{-/-}$ compared to WT (**Figure 4.7c**). This indicates that CCL2/CCR2 signaling may contribute to initial entry of T cells into anterior regions of the brain, as full loss of CCR2 in the *CCR6*$^{+/-}$ background more strongly affects anterior T cell populations; CCRL20/CCR6 may play a larger role in chemotaxis to posterior brain regions. Finally, *CCR6*$^{-/-}$ *CCR2*$^{-/-}$ have modest reductions in anterior T cell populations, and the loss of posterior T cells is less marked than in *CCR6*$^{+/-}$ *CCR2*$^{+/-}$ and *CCR6*$^{+/-}$ *CCR2*$^{-/-}$ brains (**Figure 4.7d**). There may be compensation for loss of CCR6 in the CCR2 axis, and when CCR2 is eliminated, T cells are particularly limited in migration into anterior brain regions.

Since loss of alleles from both chemokine receptors CCR6 and CCR2 results in reduced T cell trafficking into the CNS after recurrent GAS inoculations, we analyzed the consequences of limited CNS T cell populations on neuroinflammation. We assessed microglial activation in the

glomerular layer of the OB after recurrent GAS infections in WT, *CCR6*$^{+/-}$ *CCR2*$^{+/-}$, *CCR6*$^{+/-}$ *CCR2*$^{-/-}$, and *CCR6*$^{-/-}$ *CCR2*$^{-/-}$ mice. Microglia were highly ramified in *CCR6*$^{+/-}$ *CCR2*$^{-/-}$ brains, and more amoeboid in WT, *CCR6*$^{+/-}$ *CCR2*$^{+/-}$, and *CCR6*$^{-/-}$ *CCR2*$^{-/-}$ brains (**Figure 4.8a**). Quantification of CD68^{+} Iba1^{+} microglia in each genotype revealed that *CCR6*$^{+/-}$ *CCR2*$^{-/-}$ brains have significantly

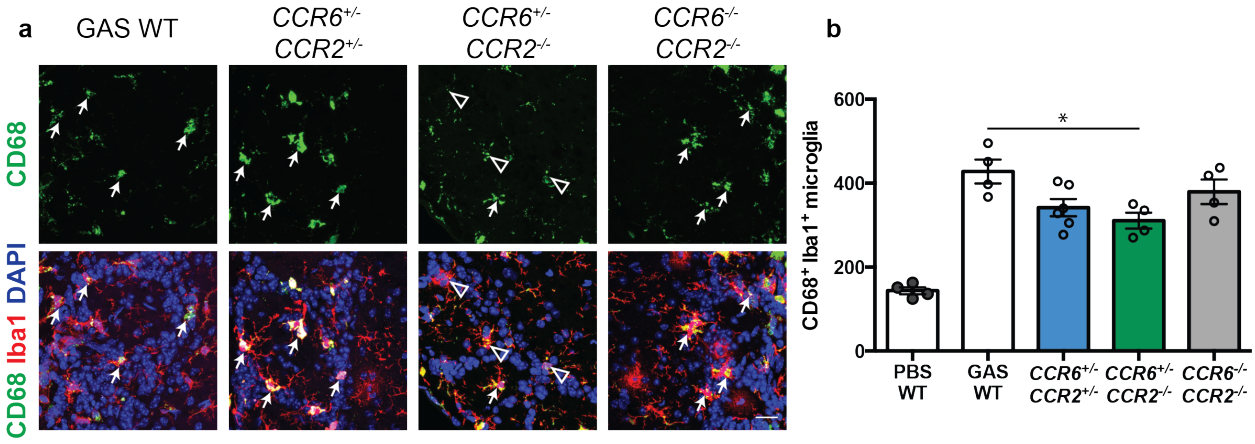

Figure 4.8 Attenuated neuroinflammation in chemokine receptor mutants. Microglial activation after recurrent GAS infections in CCR6/CCR2 chemokine receptor mutant mice. **a** Olfactory bulb microglia from WT, *CCR6*$^{+/-}$ *CCR2*$^{+/-}$, *CCR6*$^{+/-}$ *CCR2*$^{-/-}$, and *CCR6*$^{-/-}$ *CCR2*$^{-/-}$ mice shown using immunohistochemistry for Iba1 (red), CD68 (green) to mark microglial lysosomes, and DAPI (blue). Ramified resting microglia are seen in *CCR6*$^{+/-}$ *CCR2*$^{-/-}$ brains (arrowheads), and amoeboid CD68^{+} microglia are seen in WT, *CCR6*$^{+/-}$ *CCR2*$^{+/-}$, and *CCR6*$^{-/-}$ *CCR2*$^{-/-}$ brains (arrows). **b** Quantification of average CD68^{+} Iba1^{+} microglia counts from three 12 µm OB tissue sections in PBS WT, GAS WT, *CCR6*$^{+/-}$ *CCR2*$^{+/-}$, *CCR6*$^{+/-}$ *CCR2*$^{-/-}$, and *CCR6*$^{-/-}$ *CCR2*$^{-/-}$ brains. Data represent mean ± SEM from n=4 PBS WT, n=4 GAS WT, n=6 *CCR6*$^{+/-}$ *CCR2*$^{+/-}$, n=4 *CCR6*$^{+/-}$ *CCR2*$^{-/-}$, and n=4 *CCR6*$^{-/-}$ *CCR2*$^{-/-}$ mice. One-way ANOVA revealed a significant effect of genotype ($F(4,17)=21.21$, $p<0.0001$). Tukey's multiple comparisons test showed significant differences between GAS WT and *CCR6*$^{+/-}$ *CCR2*$^{-/-}$ (*$p=0.0196$), PBS WT and GAS WT ($p<0.0001$), PBS WT and *CCR6*$^{+/-}$ *CCR2*$^{+/-}$ ($p<0.0001$), PBS WT and *CCR6*$^{+/-}$ *CCR2*$^{-/-}$ ($p=0.0009$), and PBS WT vs *CCR6*$^{-/-}$ *CCR2*$^{-/-}$ ($p<0.0001$). Significance lines to PBS WT are omitted on the graph for clarity. Scale bar = 20 µm.

fewer activated microglia than WT, indicative of less neuroinflammation (**Figure 4.8b**). However, microglial activation in *CCR6*$^{+/-}$ *CCR2*$^{-/-}$ brains does not return to the level of PBS controls, indicating some residual neuroinflammation, possibly due to complement-mediated inflammation, infiltrating monocytes and macrophages, or cytokines from remaining, albeit few, infiltrating T cells.

4.5 Concluding remarks

Chemokine cues are critical for recruiting T cell populations to the site of inflammation and infection by invading pathogens. In neuroinflammatory disease, these chemokine cues are co-opted to recruit T cells to inflamed, yet sterile, brain, where they secrete inflammatory cytokines and incite damage to the surrounding tissue. In these experiments, a targeted screen identified CCL2 and CCL20 as chemokine candidates that recruit T cells to the brain from the OE after GAS infections. CCL20 is an important chemokine in the context of EAE, and is highly upregulated in the choroid plexus before disease onset to facilitate Th17 infiltration via the choroid plexus [188, 197, 287, 292]. CCL2/CCR2 signaling is critical for recruiting immune cells to the CNS in EAE [201]. After recurrent GAS inoculations, these chemokines both serve to drive lymphocytes from the NALT/OE to the brain. Chemokine expression in olfactory epithelium and brain changes over the course of five i.n. GAS infections, and rapid changes in ligand expression probably drive expansion of different T cell subsets.

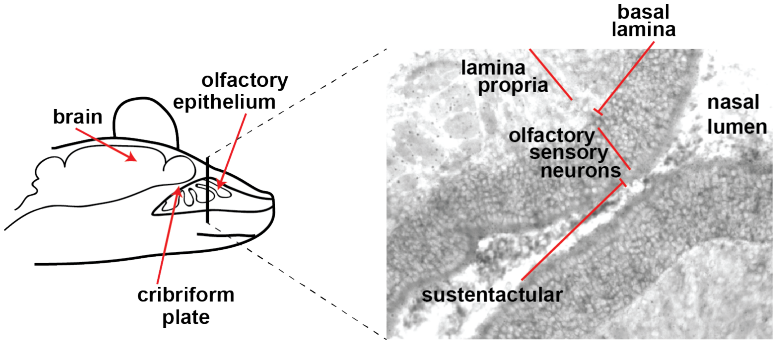

Figure 4.9 Olfactory tissues in close proximity within the skull. Schematic representation of olfactory tissues, left, show close proximity of olfactory epithelium to the brain. Right, olfactory epithelium covers olfactory turbinates in the nose. Olfactory sensory neurons are supported by a variety of tissues and cells in the OE.

In the olfactory epithelium, chemokine cues are expressed by several different cell types, but signals are frequently seen in the sustentacular layer most superficial, and in the basal lamina at the base of the olfactory sensory neuronal layer (**Figure 4.9**). Pathogens are cleared from the nasal lumen after neutralization by the action of cilia on the mucus covering the sustentacular

layer. Chemokine gradients control immune cell entry and egress from lymph nodes as well as homing to sites of infection. These gradients are maintained by tethering the secreted chemokines to glycoproteins on vascular surfaces [188, 195]. This eliminates the need to continually refresh chemokine gradients, and prolongs their signaling power. Interference with these glycoproteins that tether and maintain chemokine gradients could provide a useful target for limiting trafficking of T cells into the brain.

Chemokine signaling adapts rapidly to changes in immune status. CNS T cells both accumulate slowly over the first four infections, and persist in the brain up to 56 days post-infection [93], making chemokine signaling a dynamic process that shapes the immune profile in the brain over the course of repeated infections. Indeed, *in situ* hybridization for *CCL20* shows that it is and CNS, as their cognate receptors are expressed on different T cell populations. Therefore, it follows that early induction of TGFβ and IL-6 after 2 infections [234, 235] skew NALT and OE T cell populations to Th17, which are also recruited by CCL20 signaling. Following expansion of the Th17 population, Th1 cells respond to later induction of CCL2 signaling. As this was a limited screen that only examined a subset of all chemokines, it is possible that other chemokines recruit T cells to the OE or OB. Future experiments could examine differences between the T cell populations in the nose *vs* the brain by RNAseq, which would provide a true unbiased view of chemokine receptor expression on these populations, and give a clear idea of what may be recruiting T cells differentially to the OE or brain.

These experiments also show that near-elimination of T cell entry to the brain (in *CCR6*$^{+/-}$ *CCR2*$^{-/-}$ mice) does not abrogate microglial activation to the same extent (**Figure 4.8**). Therefore, the immune cells that do enter the brain seem capable of initiating some microglial activation, probably by secreting inflammatory cytokines known to activate microglia [164]. It is possible that

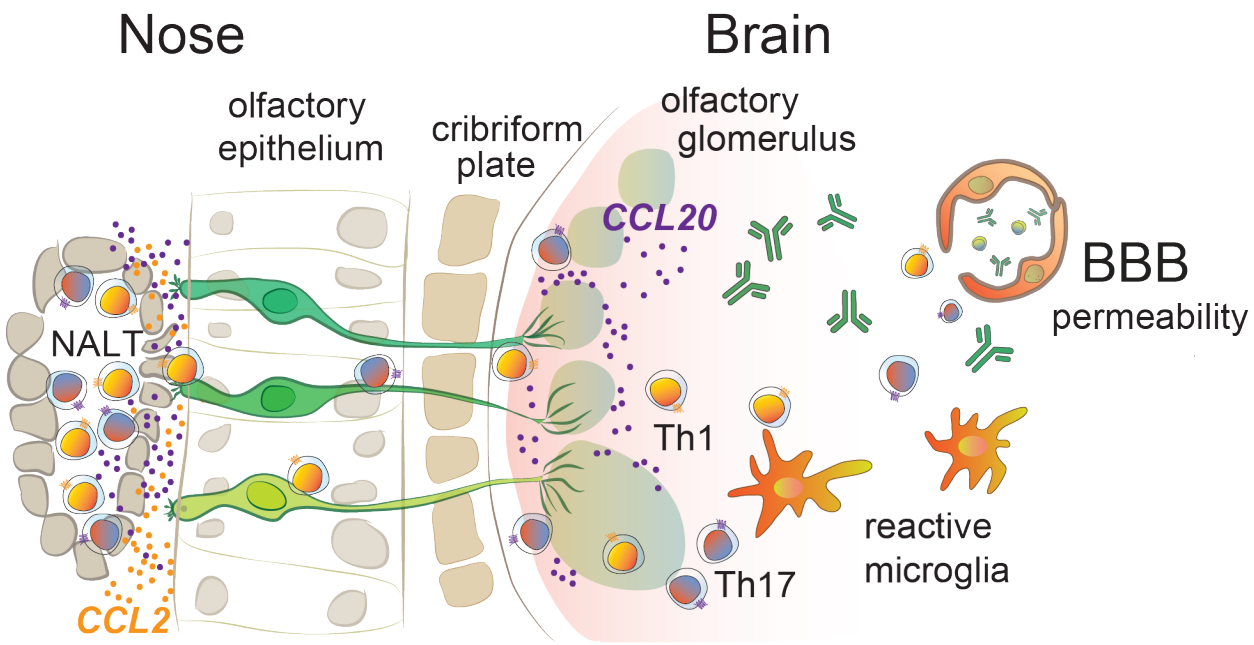

Figure 4.10 Chemokine expression influences T cell homing to the CNS after recurrent GAS inoculations. *CCL20* and *CCL2* are robustly upregulated in the NALT and olfactory epithelium, while *CCL20* is expressed periglomerularly in the olfactory bulb. Disruption of CCL2/CCR2 and CCL20/CCR6 signaling does not fully calm neuroinflammation by activated microglia.

microglia are activated via innate immunity, as the complement cascade is initiated in the OE in response to GAS infections. Complement activity may also spread to the CNS, where C1q and C3 may deposit in the OB. Microglia (and potentially infiltrating macrophages) express the C3 receptor and C1qR, allowing complement deposition to activate these cell types. While brain T cell subtype distribution is unchanged in *CCR2*$^{+/-}$ and *CCR2*$^{-/-}$ brain, NALT, and spleen CD4^{+} populations by flow cytometry (**Figure 4.6bc**, spleen data not shown), and GFP^{+} CD4^{+} Th17 populations were equivalent to WT in *CCR6*$^{+/-}$ and *CCR6*$^{-/-}$ OBs by immunohistochemistry (**Figure 4.5b**), disruption of both CCR6 and CCR2 signaling may differentially homing of T cell subtypes. Determining the identity of the T cells that do enter the brain in *CCR6*$^{+/-}$ *CCR2*$^{-/-}$ mice could provide a mechanistic explanation for reduced but not rescued microglial activation, as IFNγ produced by Th1 cells is less efficient at activating microglia than IL-17A from Th17 cells.

Recruitment of monocytes and macrophages to the CNS in EAE depends on CCR2/CCL2 signaling [150, 168, 240, 290, 293]. Peripheral macrophages extravasate through the endothelium and sometimes arrest at the basement membrane in the perivascular (Virchow-Robins) space, where their secretion of inflammatory cytokines (e.g., IL-12, TNFα) may further permeabilize the BBB [294]. In WT mice, microglial activation is robust and Th17-dependent; interfering with CCL2/CCR2 signaling may also alter microglial chemotaxis and proliferation to OB glomeruli, where their activation after recurrent GAS inoculations is high. Additionally, we cannot discount the possibility that peripheral monocytes and macrophages are recruited to the OB via CCL2 signaling. Monocytes and macrophages are potent phagocytes, and co-infiltrate the spinal cord in EAE along with adaptive immune cells [294]. It is possible that the innate immune system drives a portion of the neuroinflammation observed after recurrent GAS inoculations; indeed, the spread of macrophages from the OE to OB would complement the infiltration of T cells in the CNS.

Chemokine signaling plays an important role in recruitment of T cells to the site of infection in the OE, and our results indicate that T cells respond to chemokine cues to home to the CNS. CCL2/CCR2 and CCL20/CCR6 signaling synergize to recruit T cells to the brain after recurrent GAS inoculations, although the timing of when particular T cell subtypes might be responding to each chemokine ligand remains unclear. Importantly, disruption of chemokine signaling did not interfere with differentiation of T cells in the NALT, which might limit therapeutic use of targeting chemokine signaling to minimize contributions of specific pathogenic T cell subtypes in the brain. However, we cannot discount the possibility that other chemokine cues compensate for disruption of one chemokine signaling axis, especially after recurrent infections. Chemokine signaling may be important for initiating microglial and macrophage activation per se in the CNS, as has been shown *in vitro* [289]. Limiting T cell entry to the brain

by chemokine disruption would also reduce overall cytokine burden, thereby explaining the reduction in activated microglia. Taken together, these data provide a solid foundation for further exploration of T cell chemotaxis after recurrent GAS inoculations. To translate these findings to post-infectious BGE, it will be essential to determine inflection points for various chemokine ligands during disease progression.

Chapter 5: General discussion

The CNS has long been thought to be immune-privileged; however, recent studies have demonstrated active immune surveillance of the CNS basally and in disease states [87, 148, 192], and new mechanisms of autoimmunity against brain targets have been identified [6, 177]. Discovery of anti-NMDA receptor antibodies as the causative agent in abrupt-onset psychosis in young adults (particularly women) lent strength to the hypothesis that autoimmunity can and does target the brain [4]. Other targets of autoimmunity have been recently identified, including synaptic proteins like the AMPA receptor, $GABA_BR$, and $GABA_AR$ as well as intracellular antigens GAD65, amphiphysin, LGI1, and Caspr2 [22, 246]. Predisposition to some AE syndromes is linked to specific HLA alleles, the presence of tumors ectopically expressing neural proteins, and some infections. One particularly pressing step in AE pathogenesis remained unexplored: namely, how autoantibodies generated in the periphery enter the CNS to react with their neuronal targets.

Here, we demonstrated a vital contribution of the adaptive immune system to neuroinflammation induced in a mouse model of post-infectious basal ganglia encephalitis. Recruitment of Th17 cells to the olfactory epithelium and NALT to combat GAS infection generates populations of lymphocytes that traffic into the CNS in a sex- and Th17-dependent manner. Infiltrating lymphocytes secrete inflammatory cytokines known to damage the blood-brain barrier and activate microglia; the resulting barrier permeability is size-restricted and supports previous findings indicating separate regulation of transcellular and paracellular BBB permeability. Olfactory circuitry is profoundly affected by infiltrating T cell populations, and we observed profound mitral cell dysfunction in female mice where IL-17A-secreting cells comprise a large portion of lymphocytic infiltrate (Chapter 3). T lymphocyte infiltration and microglial activation are also regulated in part by CCR2 and CCR6 chemokine receptor signaling (Chapter

4). Below, these findings are discussed within broader contexts in the fields of immune cell trafficking, BBB structure and function, neuroinflammation, and genetic contribution to CNS autoimmunity.

5.1 T cell homing depends on concentration gradients of many signaling molecules

Homing of T cells to the site of either infection or autoimmune disease is a multi-step process that involves interaction of different signaling pathways. In these experiments, we identified CCL2 and CCL20 upregulation in olfactory tissues after recurrent GAS inoculations. Altering the expression of the cognate chemokine receptors CCR2 and CCR6 interfered with T cell homing to the CNS, but not differentiation of T cell subtypes in lymphoid tissue after GAS inoculations. Microglial activation was also reduced in *CCR6*$^{+/-}$ *CCR2*$^{-/-}$ mice with limited T cell populations. Chemokine gradients control monocyte egress from bone marrow, T cell homing to infection in the NALT, OE, and OB, and drainage of immune cells to peripheral lymph nodes for T and B cell direction to antigen [146, 193, 198, 201, 240, 290, 295]. As discussed previously, chemokine signaling plays a large role in immune cell homing to the CNS in neuroinflammation, but chemokine signaling pathways are notoriously redundant and promiscuous [193]. Lysophospholipid sphingosine-1-phosphate receptor (S1PR) signaling controls T cell egress from lymph nodes, and has been shown to sequester activated T cells in lymph nodes in EAE, as well as limiting upregulation of transcytotic BBB permeability [121]. FTY720, a lipophilic structural analog of S1P, can cross the BBB, binds 4 of the 5 S1PR isoforms, and has been approved for use in human MS patients [296]. S1PR signaling links BBB permeability with T cell entry into the CNS in inflammation, but its potential role in AE syndromes remains unexplored.

Interplay between neuroinflammation and autoantibody binding would be better understood with *in vivo* experiments where all cell types are present and may be manipulated with genetic tools. CCL2 activation of CCR2 on both microglia and neurons is implicated in the pathogenesis of neuropathic pain and itch sensation in spinal neurons [297, 298]. This provides evidence that neuronal activity can be directly modulated by inflammatory chemokines. It remains to be determined whether chemokines secreted mainly in the OE, but present at lower concentrations in the OB, directly modulate neuronal firing *in vivo*, or even what cell types secrete CCL2 detected in the OB after recurrent GAS infections. Because CCR2 is expressed on many cell types, determining the cellular components of CCL2/CCR2 interactions requires finer tools than the global receptor knockout lines used here. Selective deletion of CCR2 expression using specific genetic driver lines could define what cells actively signal through this chemokine axis during T cell chemotaxis.

Eph/Ephrin signaling has been implicated in both NMDARE pathogenesis, by tethering NMDAR to the synapse [208, 213], and in EAE, regulating T cell chemotaxis to the CNS [170]. Increased EphrinB2 signaling in NMDARE antibody-exposed mice ameliorates memory deficits, while deletion of EphrinB2 ameliorates Th1/Th17 differentiation and migration in to spinal cord lesions. These findings may be explained by differential roles of Eph/Ephrin signaling in the humoral and cellular adaptive immune system. It is possible that B cells and T cells express different Eph receptors, or are activated by different Ephrin ligands. Eph and Ephrin signaling may contribute to the pathogenesis of other AE syndromes. However, if its sole role in NMDARE pathogenesis is maintenance of NMDAR synaptic localization, Ephrins would not necessarily play a similar role in scaffolding other neurotransmitter receptors during AE pathogenesis.

5.2 Sex specificity in immune and circuit-level processing deficits

One prominent question raised in our recurrent GAS infection model is the presence of sex differences at several levels of pathogenesis. Autoimmune disease as a whole is skewed towards females, which holds true for many individual autoimmune diseases including MS, rheumatic heart disease, and Sydenham's chorea [267, 299]. Our results support hyperactivity of the Th17 axis in females, as female mice recurrently inoculated with GAS showed Th17-driven CNS lymphocyte infiltration that was absent in males (**Figure 3.3**). Given that these autoimmune diseases have reported Th17 pathology, CNS pathology we observe may be part of a larger pattern of predisposition to autoreactive Th17 phenotypes in females.

Rheumatoid arthritis (RA) is another Th17-driven autoimmune disease which manifests more severely in females than males, which holds true in animal models of the disease [300, 301]. Patient-derived samples, and *in vivo* and *in vitro* data on pathogenesis of RA provide mechanistic insight into sex differences observed in Th17-driven autoimmunity. Regulation of T cell differentiation by PPARγ is sexually dimorphic and estradiol-dependent, and Th17 differentiation in particular upon PPARγ induction was more efficient in female splenocytes than in male splenocytes [302]. In a rat RA model, both overall populations of Th17 cells, and Th17 differentiation into autoreactive Th17 (IL-17A$^+$ IFNγ$^+$) were elevated in females compared to males, correlating with symptom severity [301]. Analysis of T cell subtypes circulating in male and female RA patients indicate that anti-inflammatory Th2 cells are more numerous in male patients, perhaps indicating that in males, anti-inflammatory factors function more efficiently [300]. Strain and sex differences have been observed for EAE susceptibility, due in part to sphingosine-1-phosphate receptor-2 (S1PR-2) expression, which varies with strain and sex and has

been shown to regulate breakdown of adherens junctions and increased rates of caveolar transcytosis during disease [121].

Sex differences in neuropathology after GAS inoculations extend to physiological deficits observed in mitral cell processing. A recent study showed that combinations of activated glomeruli (representing odor identity) in female mice were more dissimilar for different odors, and that these differences were processed faster by OSNs, compared to male mice. Gonadectomy in female mice slowed OSN processing and made glomerular processing more broadly tuned, while gonadectomized male mice showed faster processing and sharper glomerular odor maps [303]. At the onset of infections (3-4 weeks of age) mice are sexually immature, but by the end of the infection paradigm (~8 weeks of age), mice have sexually matured and would presumably show sexually dimorphic processing speed by OSNs. With recurrent inflammation in the OE and, later, in the OB by infiltrating immune cells, it seems likely that the time during which infections are taking place might interfere with olfaction later in life. It remains to be seen how olfactory processing might be affected long term after cessation of recurrent GAS infections, and whether olfactory deficits might be ameliorated.

The quality of changes observed in mitral cells after recurrent GAS infections is interesting in and of itself. In females, loss of sharp odor-evoked mitral cell responses is Th17-dependent, whereas no such Th17 dependence exists in male mice (**Figures 3.18 and 3.21**). OSN function is impaired after genetically induced expression of IFNγ or TNFα by sustentacular cells in the OE, resulting in OSN apoptosis and OE inflammation; importantly, olfactory deficits are apparent before OSN death [304, 305]. Prednisone treatment to limit secondary inflammation does not restore olfactory sensory function [305]. Inflammation in the nose is therefore sufficient to interfere with OSN function. While these studies did not examine later steps in the olfactory

processing circuit, EAE studies examining lesion formation in the OB and olfactory function are informative [306]. In EAE, not only do T cells and DCs populate the OB [202], but frank lesion formation in the OB was associated with olfactory behavioral deficits [306]. Our results support the conclusion that olfactory function is differentially affected by inflammation in males and females, and that the action of Th17 cells plays a larger role in shaping responses in females. In male mice, however, Th17 are dispensable, and it appears that IFNγ^+ Th1 cells alone are sufficient to affect olfactory circuit function (**Figure 3.21**). In male *ROR$\gamma t^{-/-}$* mice, we posit that noisy OSNs drive increased firing in external tufted and mitral cells, resulting in both elevated baseline firing rate of mitral cells and may drown out odor-specific firing of OSNs. Further experiments are needed to determine what cells drive observed phenotypes in olfactory response to intranasal infection in both sexes.

Other groups have described changes in neurotransmitter metabolite concentrations in prefrontal cortex after GAS exposure [232], but no investigation of *in vivo* neuronal function has been performed to date. Although recordings from slice preparations or dissociated neurons exposed to autoantibodies have clarified mechanisms of autoantibody binding to individual receptors and neurons [19, 58, 231], but how these individual antibody binding events may affect circuit level function remains unexplored. Furthermore, circuit analyses represent a crucial step in translating molecular events to behavioral findings. Recordings from awake, behaving animals can be technically challenging, but they do represent a necessary step in understanding how BBB breach and entry of brain-targeting autoantibodies might interfere with neuronal signaling and cause some behavioral and molecular findings that have been reported [80, 205, 206]. Our experiments here show that molecular-level loss of vGluT2 in excitatory OB glomerular synapses leads to circuit-level dysfunction in OB mitral cells that may be mediated by external tufted (ET)

cells, which are the principal contributors to mitral cell output *in vitro* (**Figures 3.14, 3.17, 3.18, 3.19**) [285]. Inflammation certainly plays an essential role in this circuit, where we showed profound microglial activation and BBB dysfunction (**Figures 3.9, 3.13**). While Th17 cells were dispensable for behavioral hyposmia (**Figure 3.15**), they were necessary for inducing significant mitral cell dysfunction (**Figure 3.19**), which may represent a byproduct of inflammation or direct action of Th17 cytokines on mitral or ET populations.

5.3 Size- or route-dependent BBB dysfunction induced by Th17 lymphocytes

Breakdown of the BBB can occur via several cellular and molecular mechanisms. ECs express tight junction proteins at their apical side, sealing together spaces between adjacent cells. In an inflammatory environment, cytokines secreted by immune cells can act both directly and indirectly on TJ complexes to destabilize them [90, 94, 100, 266, 270, 280]. This permits paracellular permeability. Basal rates of transcytosis by Caveolin1^{+} vesicles, macropinocytosis, and receptor mediated vesicular transport are also very low in ECs, but inflammation causes upregulation of vesicular transport and transcellular permeability [90-92, 107, 108]. These two pathways (paracellular and transcellular) seem to operate largely independently, as shown by work in our lab where BBB permeability due to upregulation of transcytosis occurs prior to leakage induced by TJ breakdown [91]. Immune cells also appear to use these two pathways differently, as Th1 cells preferentially transmigrate transcellularly, but Th17 cells will transmigrate by either route in EAE [92]. Previous studies showed that TJ remodeling and BBB permeability occur after recurrent GAS infections [93], however, it remained unclear if this process was due to the presence of infiltrating Th17 cells. Our work indicates that breakdown of these two pathways is initiated by different processes, supporting the hypothesis that they are under independent control (**Figures**

3.8, 3.9, 3.10, 3.11). Cav1 levels were reduced significantly in *RORγt*$^{+/-}$ mice, and non-significantly in *RORγt*$^{-/-}$ mice, which seems to imply lower rates of transcytosis (**Figure 3.11**). This data bears the caveat that the phospho isoform of Cav1 has been shown to be active in internalization of TJ proteins following integrin signaling, and blots probing for the phospho-Cav1 isoform were unsuccessful [307]. We showed that IgG leakage, which can occur paracellularly or transcellularly depending on the extent of TJ disruption, was abrogated in the absence of Th17 cells, despite persistent TJ abnormalities and vascular permeability to biocytin-TMR, which traffics via the paracellular route (**Figures 3.8, 3.9, 3.11**).

Published results on this model from our lab, as well as current results, do not address temporal dynamics of BBB permeability, nor do we provide conclusive positive evidence that increased rates of transcytosis are the mechanism by which IgG deposition increases after recurrent GAS infections. Changes in transcytosis rate can be measured using tracers specifically transported via Cav1^{+} vesicles, and would be ideally suited to address this question [92, 117]. Further experiments would be needed to test when the BBB is first permeabilized (via TJ remodeling or transcytosis regulation) during the course of recurrent infections, as well as how long the BBB takes to close, if at all, after the final infection [91, 92]. Recurrent imaging using intravital microscopy may be the most well-suited tool for these experiments, and would reduce variability between mouse and bacterial cohorts.

In endothelial cells, tight junction (TJ) complexes have been hypothesized to lie in lipid rafts, specialized regional domains within the plasma membrane enriched for cholesterol, specialized proteins, and various phospholipids [308, 309]. TJ proteins Claudin-4, -5 and Occludin, but not Claudin-1, -2, or -3, have been shown both *in vivo* and *in vitro* to localize to lipid raft fractions; furthermore, infection inducing inflammatory cytokine production results in removal of

TJ proteins from rafts in epithelial cells [308-310]. In addition to localizing TJ proteins to the apical membrane, ECs may nucleate caveolae within rafts. Cholesterol and flotillin-1 may stabilize membrane regions within or around caveolae [95]. In the immune system, T cell receptors (TCRs) responsible for initiating T cell activation are also localized to raft domains, and mice deficient for raft-scaffolding protein Raftlin-1 showed ameliorated EAE. This was due to impaired TCR signaling in T cells, resulting in blunted IL-17 production [311]. Thus, membrane stabilization in both Th17 cells and in endothelial cells may play a role in vulnerability to inflammatory insult.

In addition to leakage of serum proteins through disrupted tight junctions, immune cells also cross the endothelium. The process of T cell transmigration is well described in brain and spinal cord vasculature in EAE, with some differences between these two regions [12, 103, 120]. VCAM-1, ICAM-1, MCAM, and ALCAM have all been shown to interact with T cells and promote arrest, crawling, and transmigration *in vitro* and *in vivo* [103, 105, 132, 288, 312, 313]. The roles of ICAM-1 and VCAM-1 are most well-documented in this process, and could provide a mechanism for T cell transmigration after initial BBB permeabilization. Our work supports upregulation of cell adhesion molecules in OB capillaries, but it is also possible that the leaky vasculature in the olfactory nerve provides an entry point for immune cells that then travel to the brain within the parenchyma, circumventing the BBB. While cell adhesion molecule expression was not directly investigated in these studies, the presence of T cells in the brain raises the possibility that adhesion molecules are upregulated to promote their entry later in disease course. Future experiments should address the possibility that vasculature in the OB or choroid plexus may express cell adhesion molecules to promote T cell entry into the brain via this route. It is also unclear if these changes might precede or follow initial T cell entry via the olfactory route.

The multi-hit hypothesis of post-infectious BGE necessitates BBB breakdown, but in most human pathologies, BBB permeability is localized in lesion areas [280, 314]. Seizures, whether they are caused by epilepsy or other underlying neurological condition, are both a byproduct of local disturbances in ion, metabolite, and neurotransmitter concentration from BBB permeability, as well as a cause of BBB dysfunction, owing to excitotoxic release of ions from astrocytes and neurons [315]. Over the course of NMDARE progression, patients frequently develop seizures, putatively caused by pathogenic NMDAR antibodies binding in excitable temporal lobe regions [2, 16, 246]. However, it is possible that these seizure events are actually caused by localized flares in BBB permeability, which serve to allow a fresh wave of blood-borne NMDAR antibodies to enter the CNS and progress disease. Our previous and present results indicate that BBB breakdown is neither uniform spatially across the brain, nor temporally after infection (**Figures 3.8, 3.9**) [93]. Molecular regulation of the BBB during AE disease flares is therefore a critical area of investigation. It remains unclear how BBB permeability is regulated over the course of AE syndromes, and future clinical studies examining this would significantly progress the field towards greater understanding of diseases progression.

5.4 Invitations to the T cell party in the brain

Although our experiments here did not address the role of dendritic cells in promoting neurovascular pathology after recurrent GAS infections, there is a distinct role that they may fill. $CD4^+$ T cells persist in the CNS for up to 56 days after the final infection [93], and to date we have not identified a plausible explanation for the persistence of this population in the brain so long after infection. Dendritic cells infiltrate the CNS in EAE guided by CCR2-dependent cues, and contribute to persistence of CNS-infiltrating T cells by continually presenting myelin antigen [201,

202]. DCs circulate through the brain and drain via CCR7 signaling into the deep cervical lymph nodes; epitope spreading in the nodes then contributes to disease progression; however, interference with CCR7 signaling and drainage via the cribriform plate results in DC accumulation in the brain and exacerbated clinical progression [146, 192]. DCs may also migrate to the CNS via the meningeal lymphatic vessels and passage into interstitial fluid, then drain through perivenous lymphatic vessels into deep cervical lymph nodes [316]. These data indicate that DC circulation through the CNS and back to peripheral lymph nodes drives EAE progression.

The role of dendritic cells in post-infectious autoimmune encephalitic syndromes remains unexplored, however. Our results showing upregulation of CCL2 in olfactory bulb after recurrent, but not single, infections, allow for the possibility that DCs initially recruited to the OE to respond to infection subsequently traffic into the CNS. It is possible that DCs recruited to the brain after recurrent GAS infections sample additional CNS antigens, contributing to antigen spreading after clearance to deep cervical lymph nodes [93, 235]. DCs infiltrating in the brain also provide an attractive mechanistic explanation for the of T cells in the brain for prolonged periods after GAS infections. After initial recruitment by chemokine signaling, DC populations with broadened epitope specificity may help maintain T cell presence in the CNS after resolution of frank infection. It is possible that dendritic cells do not migrate to the CNS, and are instead restricted to the OE. Preliminary results from our lab tracked dendritic cell populations after recurrent infection in the *CD11c-eYFP* transgenic mouse line, in which a fluorescent reporter is expressed under control of a DC-specific promoter (Appendix B), and indicated GAS-induced DC influx into the anterior brain. While it is unclear how long DCs persist in the brain, they could be responsible for maintenance of lymphocytes in the CNS after resolution of infection, restimulation of T cells in the CNS, or epitope spreading if DCs drain to deep cervical lymph nodes in the same manner as

in EAE [146, 235]. Examination of epitope specificity of T cells harvested from PANDAS patient tonsils could indirectly address the role of DCs in progression of GAS pharyngitis to GAS-induced autoimmunity.

One question that remains unanswered is the spatial localization of T cells along olfactory axons. While visualization of T cells along axons in a continuous path to the OB is an important step in confirming their potential use of the olfactory route to enter the CNS, the relative contributions of the olfactory tract *versus* transmigration through the endothelium remains unexplored. Preliminary experiments indicate that the majority of T cells appear to traffic along olfactory axon tracts between the axon bundles and the ensheathing glia, potentially along the lymphatics that line these tracts (Appendix C), as has been demonstrated in EAE [192, 202]. T cells appear localized along the periphery of olfactory axon bundles, with some sparse T cells present within axon bundles themselves. Live imaging experiments could track immune cells traveling over time, resolving the questions of directionality of T cell travel and how long it takes T cells to migrate from nose to brain. Future experiments using fluorescently labeled T cells in mice with i.v. fluorescent dextran to label vasculature could track T cell progress through a cranial window over the OE and cribriform plate, or in the OB to examine trafficking through the leaky BBB. It has been hypothesized that viruses and bacteria co-opt the olfactory route to cause encephalitis and infect the CNS [317]. It is possible that T cells responding to the infection in the OE use this route preferentially, with entry from a permeabilized BBB possible after initial barrier breach.

5.5 Microglia: more than neuroinflammation

Microgliosis and infiltration of peripheral macrophages into inflamed CNS lesion areas are well-described in MS, neuropsychiatric lupus, and EAE [164, 187, 318, 319]. Th17 cells expressing IL-17A or both IL-17A and IFNγ are potent activators of microglia, inducing expression of MHC-II and other costimulatory molecules [164]. IFNγ-expressing Th1 cells are less efficient in this process.

Several years ago, microglia were shown to play an active role in circuit sculpting during development, following cues from complement C1q deposition to prune underused synapses in the retinogeniculate pathway [180]. In the ensuing years, this function of microglia has been demonstrated in neurogenerative and genetic disease states as well [282, 320]. Loss of olfactory sensation has been documented for several neurodegenerative diseases, including as a prodromal biomarker for Alzheimer's disease [248, 284, 321]. In peripheral nervous autoimmunity mediated by G1q antibodies, the combination of complement and autoantibody deposition is necessary for neuromuscular junction dysfunction, indicating a role for potential peripheral synaptic tagging and innate immune mechanisms in altering neural transmission in autoimmunity [224]. Although we see microglial activation in our mouse model, the most parsimonious explanation for loss of vGluT2 staining in olfactory glomeruli would be a downregulation of this packaging protein in OSN terminals. However, mitral cells also receive input from external tufted cells (ET), and we cannot rule out the possibility that vGluT2 expression decreases in these cells [285]. Indeed, pruning of ET-mitral cell synapses by activated microglia would explain both loss of odor-driven activity in mitral cells and decreased vGluT2 expression in glomeruli. OSN-mitral cell synapses are probably not pruned by microglia, as vGluT2 loss within glomeruli was not accompanied by a decrease in post-synaptic marker PSD95 [93], which would indicate preservation of the entire synapse. Thus, if OSNs are the source of the loss-of-vGluT2 phenotype observed after GAS

infections, their presynaptic terminals are still present, but do not contain loaded glutamatergic vesicles. Further experiments using *ex vivo* OB slice preparations from GAS-inoculated mice could help determine whether OSN terminals contain either (1) an equivalent number to control mice of empty, unloaded excitatory vesicles, or (2) comparatively very few loaded glutamatergic vesicles.

The action of infiltrating monocytes and macrophages *versus* microglia in effecting circuit damage in CNS autoimmunity and neuroinflammatory diseases has not been thoroughly explored. Most of the literature discusses the coexistence of peripheral macrophage and monocyte infiltration with activated microglia in animal models of neuroinflammation, however, few have tried to untangle the specific effects of these two cell types. It may be disingenuous to attempt to separate these two immune populations, given their similar abilities as phagocytes and secreted cytokines profiles. In EAE, a recent study has shown that infiltrating macrophages and microglia may play opposite roles, where macrophages associate with nodes of Ranvier to effect myelin damage, and microglia phagocytose the debris and clean up lesion areas [322]. Specific depletion of microglia with colony stimulating factor 1 receptor (CSF1R) inhibitors (CSF1R is expressed on microglia and macrophages, but antagonists more potently affect microglial survival) would permit independent examination of microglial contributions to disease pathogenesis [281, 323]. CSF1R inhibitor treatment shows minimal effect on macrophages in healthy WT mice, but reduces macrophage presence in tumors; 99% of microglia are eliminated with CSF1R inhibitor treatment [323]. This treatment also presents an opportunity to refresh activated microglia; in acute neuroinflammation, repopulating microglia have diminished activation and more efficiently phagocytose debris [324].

Potential involvement of macrophages and monocytes has been explored very little in animal models of post-infectious BGE. Overt infection in the OE will recruit macrophages to the

nose; macrophages constitute the first line of defense upon bacterial recognition by Toll-like receptors [325]. However, while recruitment of monocytes from bone marrow upon infection is CCR2-dependent, CCR2 signaling does not determine target tissue infiltration by macrophages [295]. Induction of CCL2 in OE should recruit monocytes and macrophages to the site of infection to initiate an innate immune response. Macrophages and antibody creation are generally efficient at eliminating bacterial infection from the nose, however, GAS has been shown to create intracellular reservoirs in macrophages and epithelial cells *in vivo* [326]. T cell trafficking into the brain was hypothesized here to be CCR2-dependent, however, we cannot exclude the possibility that macrophages and monocytes recruited to the OE also traffic along olfactory sensory axons or via a disrupted BBB to enter the CNS parenchyma. To probe this question, use of live imaging of olfactory axon tracts in infected CCR2-RFP monocyte transgenic reporter mice could clarify whether monocytes in the nose directly enter the brain.

5.6 Host and pathogen genetic contribution to post-infectious BGE and other AE syndromes

Genetic vulnerability to various AE syndromes, and to their associated tumors and infectious triggers, is surprisingly variable, depending on the autoantigen implicated in pathogenesis [6, 25, 44, 57, 327]. Anti-LGI1 encephalitis has relatively stronger genetic linkage, with 27 SNPs in an HLA locus, and although it is not associated with a specific tumor, comorbid cancers have been reported [44-46]. NMDAR encephalitis has relatively weaker genetic link, but strong association with ovarian teratoma [17, 44, 207]. Species differences in the HLA locus between humans and mice complicates interpretation of immunological studies performed in mice. Use of mice with a humanized HLA locus could provide a more accurate picture of both autoimmunity initiation and epitope spreading occur in human AE. In this mouse, GAS antigen

would be processed and presented to B and T cells according to human MHC rather than mouse. Antigen processing and recognition by mouse MHC may differ significantly, especially for a uniquely human pathogen like GAS.

Even though host genetics undoubtedly play a role in either proper control of GAS infection or development of autoimmunity after recurrent infections, GAS bacterial strains have very plastic genomes. This susceptibility to genome changes may underlie shifts in the presentation of autoimmunity since the 1600s [66, 328, 329]. Historically, GAS infections caused more motor disturbances in children with rheumatic fever, with motor changes present in up to 30% of children with rheumatic fever. Today, however, pure motor symptoms in rheumatic fever are rarer, and there has been a reported increase in the frequency of psychiatric symptoms accompanying rheumatic fever [6, 65, 77]. GAS genetic drift has been posited to explain this shift in symptomatology, with mutations in superantigens and surface proteins causing slight changes in the antibody repertoire generated from GAS infections over time [63]. Our lab has access to several superantigen mutant GAS strains, with either dominant negative or deleted SAg proteins. Future experiments using the i.n. GAS infection mouse model could probe the role of SAgs in recruitment of T cells to the NALT and brain, as well as investigating the role of superantigens in generation of autoreactive Th17 cells which drive BBB permeability and microglial activation.

Olfactory function is uniquely vulnerable to repeated inflammatory insult. Olfactory sensitivity sharpens over the course of childhood, becoming sexually dimorphic as children pass through puberty [330, 331]. It would be possible to detect loss of olfactory function in children with suspected post-infectious autoimmune encephalitis, provided tests were appropriately calibrated for age and sex. If recurrent GAS infections during childhood interfere with olfactory ability later in life, this may be detectable with a clinical test. However, given sex-dependent

differences in olfactory ability over the course of development, this necessitates careful consideration of how metrics are defined for girls and boys of different ages [330]. Onset of PANDAS and SC is defined as pediatric, so use of an olfactory assay to determine either onset of symptom flares or persistent vulnerability to future flares could hold promise.

5.7 Concluding remarks

This study investigated the peripheral immune cell recruitment to the brains of mice after recurrent GAS infections. Here, we show the requirement of Th17 lymphocytes in initiating size-dependent BBB permeability, microglial activation, and olfactory bulb mitral cell dysfunction. Additionally, we identified chemokine signaling cues that contribute to CNS T cell infiltration, and show that interrupting chemokine signaling partially ameliorates neuroinflammation after recurrent GAS infections. Our results suggest that infiltrating Th17 cells in the CNS may promote BBB permeability via increased transcytosis rather than tight junction remodeling, mechanistically linking our post-infectious BGE model to EAE, another CNS autoimmune disorder.

References

1. Sinmaz, N., et al., *Autoantibodies in movement and psychiatric disorders: updated concepts in detection methods, pathogenicity, and CNS entry.* Ann N Y Acad Sci, 2015. **1351**(1): p. 22-38.
2. Leypoldt, F., T. Armangue, and J. Dalmau, *Autoimmune encephalopathies.* Ann N Y Acad Sci, 2015. **1338**: p. 94-114.
3. van Coevorden-Hameete, M.H., et al., *Molecular and cellular mechanisms underlying anti-neuronal antibody mediated disorders of the central nervous system.* Autoimmun Rev, 2014. **13**(3): p. 299-312.
4. Dalmau, J., et al., *Paraneoplastic Anti–N-methyl-D-aspartate Receptor Encephalitis Associated with Ovarian Teratoma.* Ann Neurol, 2007. **61**(1): p. 25-36.
5. Graus, F. and J. Dalmau, *Paraneoplastic neurological syndromes: diagnosis and treatment.* Curr Opin Neurol, 2007. **20**(6): p. 732-7.
6. Cutforth, T., et al., *CNS autoimmune disease after Streptococcus pyogenes infections: animal models, cellular mechanisms and genetic factors.* Future Neurol, 2016. **11**(1): p. 63-76.
7. Hornig, M., *The role of microbes and autoimmunity in the pathogenesis of neuropsychiatric illness.* Curr Opin Rheumatol, 2013. **25**(4): p. 488-795.
8. Venkatesan, A. and D.R. Benavides, *Autoimmune encephalitis and its relation to infection.* Curr Neurol Neurosci Rep, 2015. **15**(3): p. 3.
9. Dubey, D., et al., *The spectrum of autoimmune encephalopathies.* J Neuroimmunol, 2015. **287**: p. 93-7.
10. Brimberg, L., et al., *Antibodies as Mediators of Brain Pathology.* Trends Immunol, 2015. **36**(11): p. 709-24.
11. Diamond, B., et al., *Brain-reactive antibodies and disease.* Annu Rev Immunol, 2013. **31**: p. 345-85.
12. Engelhardt, B., et al., *Vascular, glial, and lymphatic immune gateways of the central nervous system.* Acta Neuropathol, 2016. **132**(3): p. 317-38.
13. Liebner, S., et al., *Functional morphology of the blood-brain barrier in health and disease.* Acta Neuropathol, 2018. **135**(3): p. 311-336.
14. Lang, K. and H. Pruss, *Frequencies of neuronal autoantibodies in healthy controls: Estimation of disease specificity.* Neurol Neuroimmunol Neuroinflamm, 2017. **4**(5): p. e386.
15. Tan, E.M., et al., *Range of antinuclear antibodies in "healthy" individuals.* Arthritis Rheum, 1997. **40**(9): p. 1601-11.
16. Heine, J., et al., *Imaging of autoimmune encephalitis--Relevance for clinical practice and hippocampal function.* Neuroscience, 2015. **309**: p. 68-83.
17. Dalmau, J., et al., *Clinical experience and laboratory investigations in patients with anti-NMDAR encephalitis.* Lancet Neurol, 2011. **10**(1): p. 63-74.
18. Graus, F., et al., *A clinical approach to diagnosis of autoimmune encephalitis.* Lancet Neurol, 2016. **15**(4): p. 391-404.
19. Hughes, E.G., et al., *Cellular and synaptic mechanisms of anti-NMDA receptor encephalitis.* J Neurosci, 2010. **30**(17): p. 5866-75.
20. Lai, M., et al., *Investigation of LGI1 as the antigen in limbic encephalitis previously attributed to potassium channels: a case series.* Lancet Neurol, 2010. **9**(8): p. 776-85.

21. Lancaster, E., et al., *Investigations of caspr2, an autoantigen of encephalitis and neuromyotonia.* Ann Neurol, 2011. **69**(2): p. 303-11.
22. Waters, P., P. Pettingill, and B. Lang, *Detection methods for neural autoantibodies.* Handb Clin Neurol, 2016. **133**: p. 147-63.
23. Cavaliere, E., et al., *Anti-NMDAR encephalitis preceded by non-herpetic central nervous system infection: Systematic literature review and first case of tick-borne encephalitis triggering anti-NMDAR encephalitis.* J Neuroimmunol, 2019. **332**: p. 1-7.
24. Nosadini, M., et al., *Herpes simplex virus-induced anti-N-methyl-d-aspartate receptor encephalitis: a systematic literature review with analysis of 43 cases.* Dev Med Child Neurol, 2017. **59**(8): p. 796-805.
25. Alves-Leon, S.V., et al., *Acute disseminated encephalomyelitis: clinical features, HLA DRB1*1501, HLA DRB1*1503, HLA DQA1*0102, HLA DQB1*0602, and HLA DPA1*0301 allelic association study.* Arq Neuropsiquiatr, 2009. **67**(3A): p. 643-51.
26. Hoftberger, R., et al., *Encephalitis and GABAB receptor antibodies: novel findings in a new case series of 20 patients.* Neurology, 2013. **81**(17): p. 1500-6.
27. Vale, T.C., et al., *Morvan syndrome as a paraneoplastic disorder of thymoma with anti-CASPR2 antibodies.* Lancet, 2017. **389**(10076): p. 1367-1368.
28. van Sonderen, A., et al., *The clinical spectrum of Caspr2 antibody-associated disease.* Neurology, 2016. **87**(5): p. 521-8.
29. Ahmad, J., et al., *Anti-n-Methyl-d-Aspartate-Receptor (NMDAR) Encephalitis in Association with Ovarian Teratoma.* Cureus, 2017. **9**(7): p. e1425.
30. Arino, H., et al., *Paraneoplastic Neurological Syndromes and Glutamic Acid Decarboxylase Antibodies.* JAMA Neurol, 2015. **72**(8): p. 874-81.
31. Dalmau, J., *NMDA receptor encephalitis and other antibody-mediated disorders of the synapse: The 2016 Cotzias Lecture.* Neurology, 2016. **87**(23): p. 2471-2482.
32. Titulaer, M.J., et al., *Late-onset anti-NMDA receptor encephalitis.* Neurology, 2013. **81**(12): p. 1058-63.
33. Murphy, T.K., et al., *Relationship of movements and behaviors to Group A Streptococcus infections in elementary school children.* Biol Psychiatry, 2007. **61**(3): p. 279-84.
34. Swedo, S.E., et al., *Pediatric autoimmune neuropsychiatric disorders associated with streptococcal infections: clinical description of the first 50 cases.* Am J Psychiatry, 1998. **155**(2): p. 264-71.
35. Takanashi, J., et al., *Late delirious behavior with 2009 H1N1 influenza: mild autoimmune-mediated encephalitis?* Pediatrics, 2012. **129**(4): p. e1068-71.
36. Tian, M., et al., *Japanese Encephalitis Virus-Induced Anti-N-Methyl-D-Aspartate Receptor Encephalitis: A Case Report and Review of Literature.* Neuropediatrics, 2019. **50**(2): p. 111-115.
37. Duarte, L.F., et al., *Herpes Simplex Virus Type 1 Infection of the Central Nervous System: Insights Into Proposed Interrelationships With Neurodegenerative Disorders.* Front Cell Neurosci, 2019. **13**: p. 46.
38. Linnoila, J., et al., *Mouse model of anti-NMDA receptor post-herpes simplex encephalitis.* Neurol Neuroimmunol Neuroinflamm, 2019. **6**(2): p. e529.
39. Liu, H., et al., *Mechanisms of Blood-Brain Barrier Disruption in Herpes Simplex Encephalitis.* J Neuroimmune Pharmacol, 2018.
40. Vezzani, A., et al., *Infections, inflammation and epilepsy.* Acta Neuropathol, 2016. **131**(2): p. 211-34.

41. Dahm, L., et al., *Seroprevalence of autoantibodies against brain antigens in health and disease.* Ann Neurol, 2014. **76**(1): p. 82-94.
42. Slight-Webb, S., et al., *Autoantibody-Positive Healthy Individuals Display Unique Immune Profiles That May Regulate Autoimmunity.* Arthritis Rheumatol, 2016. **68**(10): p. 2492-502.
43. Ronda, N., et al., *Analysis of natural and disease-associated autoantibody repertoires: anti-endothelial cell IgG autoantibody activity in the serum of healthy individuals and patients with systemic lupus erythematosus.* Int Immunol, 1994. **6**(11): p. 1651-60.
44. Mueller, S.H., et al., *Genetic predisposition in anti-LGI1 and anti-NMDA receptor encephalitis.* Ann Neurol, 2018. **83**(4): p. 863-869.
45. van Sonderen, A., et al., *Anti-LGI1 encephalitis is strongly associated with HLA-DR7 and HLA-DRB4.* Ann Neurol, 2017. **81**(2): p. 193-198.
46. Kim, T.J., et al., *Anti-LGI1 encephalitis is associated with unique HLA subtypes.* Ann Neurol, 2017. **81**(2): p. 183-192.
47. Swedo, S.E., *Sydenham's chorea. A model for childhood autoimmune neuropsychiatric disorders.* JAMA, 1994. **272**(22): p. 1788-91.
48. Joseph, N., et al., *Clinical spectrum of rheumatic Fever and rheumatic heart disease: a 10 year experience in an urban area of South India.* N Am J Med Sci, 2013. **5**(11): p. 647-52.
49. Cilliers, A.M., *Rheumatic fever and its management.* BMJ, 2006. **333**(7579): p. 1153-6.
50. Platt, M.P., D. Agalliu, and T. Cutforth, *Hello from the Other Side: How Autoantibodies Circumvent the Blood-Brain Barrier in Autoimmune Encephalitis.* Front Immunol, 2017. **8**: p. 442.
51. Gilbert, D.L. and R. Kurlan, *PANDAS: horse or zebra?* Neurology, 2009. **73**(16): p. 1252-3.
52. Singer, H.S. and C. Loiselle, *PANDAS: a commentary.* J Psychosom Res, 2003. **55**(1): p. 31-9.
53. Blackburn, J.S., *Tic Disorders and PANDAS.* Semin Pediatr Neurol, 2018. **25**: p. 25-33.
54. de Oliveira, S.K. and C.F. Pelajo, *Pediatric Autoimmune Neuropsychiatric Disorders Associated with Streptococcal Infection (PANDAS): a Controversial Diagnosis.* Curr Infect Dis Rep, 2010. **12**(2): p. 103-9.
55. Carapetis, J.R., et al., *Acute rheumatic fever and rheumatic heart disease.* Nat Rev Dis Primers, 2016. **2**: p. 15084.
56. Luleyap, H.U., et al., *Association between pediatric autoimmune neuropsychiatric disorders associated with streptococcal infections disease and tumor necrosis factor-alpha gene-308 g/a, -850 c/t polymorphisms in 4-12-year-old children in Adana/Turkey.* Indian J Hum Genet, 2013. **19**(2): p. 196-201.
57. Donadi, E.A., et al., *HLA class I and class II profiles of patients presenting with Sydenham's chorea.* J Neurol, 2000. **247**(2): p. 122-8.
58. Sabater, L., et al., *Cellular investigations with human antibodies associated with the anti-IgLON5 syndrome.* J Neuroinflammation, 2016. **13**(1): p. 226.
59. Stanevicha, V., et al., *HLA class II DR and DQ genotypes and haplotypes associated with rheumatic fever among a clinically homogeneous patient population of Latvian children.* Arthritis Res Ther, 2007. **9**(3): p. R58.

60. Stanevicha, V., et al., *HLA class II associations with rheumatic heart disease among clinically homogeneous patients in children in Latvia.* Arthritis Res Ther, 2003. **5**(6): p. R340-6.
61. Axisa, P.P. and D.A. Hafler, *Multiple sclerosis: genetics, biomarkers, treatments.* Curr Opin Neurol, 2016. **29**(3): p. 345-53.
62. Dan, J.M., et al., *Recurrent group A Streptococcus tonsillitis is an immunosusceptibility disease involving antibody deficiency and aberrant TFH cells.* Sci Transl Med, 2019. **11**(478).
63. Hurst, J.R., et al., *Streptococcal pharyngitis and rheumatic heart disease: the superantigen hypothesis revisited.* Infect Genet Evol, 2018. **61**: p. 160-175.
64. Berdeli, A., et al., *TLR-2 gene Arg753Gln polymorphism is strongly associated with acute rheumatic fever in children.* J Mol Med (Berl), 2005. **83**(7): p. 535-41.
65. Martin, W.J., et al., *Post-infectious group A streptococcal autoimmune syndromes and the heart.* Autoimmun Rev, 2015. **14**(8): p. 710-25.
66. Gray, L.A., et al., *Genome-Wide Analysis of Genetic Risk Factors for Rheumatic Heart Disease in Aboriginal Australians Provides Support for Pathogenic Molecular Mimicry.* J Infect Dis, 2017. **216**(11): p. 1460-1470.
67. Hua, R., et al., *Association of TNFAIP3 polymorphism with rheumatic heart disease in Chinese Han population.* Immunogenetics, 2009. **61**(11-12): p. 739-44.
68. Mataix-Cols, D., et al., *A total-population multigenerational family clustering study of autoimmune diseases in obsessive-compulsive disorder and Tourette's/chronic tic disorders.* Mol Psychiatry, 2018. **23**(7): p. 1652-1658.
69. Wang, H.C., et al., *Group A Streptococcal Infections Are Associated With Increased Risk of Pediatric Neuropsychiatric Disorders: A Taiwanese Population-Based Cohort Study.* J Clin Psychiatry, 2016. **77**(7): p. e848-54.
70. Orlovska, S., et al., *Association of Streptococcal Throat Infection With Mental Disorders: Testing Key Aspects of the PANDAS Hypothesis in a Nationwide Study.* JAMA Psychiatry, 2017. **74**(7): p. 740-746.
71. Kohler-Forsberg, O., et al., *A Nationwide Study in Denmark of the Association Between Treated Infections and the Subsequent Risk of Treated Mental Disorders in Children and Adolescents.* JAMA Psychiatry, 2018.
72. Song, Z., et al., *Genetic variation in the TNF gene is associated with susceptibility to severe sepsis, but not with mortality.* PLoS One, 2012. **7**(9): p. e46113.
73. McCormick, D.P., et al., *Acute otitis media severity: association with cytokine gene polymorphisms and other risk factors.* Int J Pediatr Otorhinolaryngol, 2011. **75**(5): p. 708-12.
74. Carapetis, J.R., *Rheumatic heart disease in developing countries.* N Engl J Med, 2007. **357**(5): p. 439-41.
75. Carapetis, J.R., B.J. Currie, and M.F. Good, *Towards understanding the pathogenesis of rheumatic fever.* Scand J Rheumatol, 1996. **25**(3): p. 127-31; discussion 132-3.
76. Cunningham, M.W., *Streptococcus and rheumatic fever.* Curr Opin Rheumatol, 2012. **24**(4): p. 408-16.
77. Cunningham, M.W., *Rheumatic fever, autoimmunity, and molecular mimicry: the streptococcal connection.* Int Rev Immunol, 2014. **33**(4): p. 314-29.
78. Kirvan, C.A., et al., *Streptococcal mimicry and antibody-mediated cell signaling in the pathogenesis of Sydenham's chorea.* Autoimmunity, 2006. **39**(1): p. 21-9.

79. McNamara, C., et al., *Coiled-coil irregularities and instabilities in group A Streptococcus M1 are required for virulence.* Science, 2008. **319**(5868): p. 1405-8.
80. Brimberg, L., et al., *Behavioral, pharmacological, and immunological abnormalities after streptococcal exposure: a novel rat model of Sydenham chorea and related neuropsychiatric disorders.* Neuropsychopharmacology, 2012. **37**(9): p. 2076-87.
81. Lotan, D., et al., *Behavioral and neural effects of intra-striatal infusion of anti-streptococcal antibodies in rats.* Brain Behav Immun, 2014. **38**: p. 249-62.
82. Frick, L.R., et al., *Differential binding of antibodies in PANDAS patients to cholinergic interneurons in the striatum.* Brain Behav Immun, 2018. **69**: p. 304-311.
83. Gorton, D., et al., *Repeat exposure to group A streptococcal M protein exacerbates cardiac damage in a rat model of rheumatic heart disease.* Autoimmunity, 2016. **49**(8): p. 563-570.
84. Bessen, D.E., et al., *Genetic correlates of throat and skin isolates of group A streptococci.* J Infect Dis, 1996. **173**(4): p. 896-900.
85. Ly, A.T., et al., *Differences in SpeB protease activity among group A streptococci associated with superficial, invasive, and autoimmune disease.* PLoS One, 2017. **12**(5): p. e0177784.
86. Nur-ur Rahman, A.K., et al., *The T cell receptor beta-chain second complementarity determining region loop (CDR2beta governs T cell activation and Vbeta specificity by bacterial superantigens.* J Biol Chem, 2011. **286**(6): p. 4871-81.
87. Ransohoff, R.M. and B. Engelhardt, *The anatomical and cellular basis of immune surveillance in the central nervous system.* Nat Rev Immunol, 2012. **12**(9): p. 623-35.
88. Saunders, N.R., et al., *Transporters of the blood-brain and blood-CSF interfaces in development and in the adult.* Mol Aspects Med, 2013. **34**(2-3): p. 742-52.
89. Zhao, Z., et al., *Establishment and Dysfunction of the Blood-Brain Barrier.* Cell, 2015. **163**(5): p. 1064-78.
90. Stamatovic, S.M., et al., *Endocytosis of tight junction proteins and the regulation of degradation and recycling.* Ann N Y Acad Sci, 2017. **1397**(1): p. 54-65.
91. Knowland, D., et al., *Stepwise Recruitment of Transcellular and Paracellular Pathways Underlies Blood-Brain Barrier Breakdown in Stroke.* Neuron, 2014.
92. Lutz, S.E., et al., *Caveolin1 Is Required for Th1 Cell Infiltration, but Not Tight Junction Remodeling, at the Blood-Brain Barrier in Autoimmune Neuroinflammation.* Cell Rep, 2017. **21**(8): p. 2104-2117.
93. Dileepan, T., et al., *Group A Streptococcus intranasal infection promotes CNS infiltration by streptococcal-specific T cells.* J Clin Invest, 2016. **126**(1): p. 303-317.
94. Bennett, J., et al., *Blood-brain barrier disruption and enhanced vascular permeability in the multiple sclerosis model EAE.* J Neuroimmunol, 2010. **229**(1-2): p. 180-91.
95. Doherty, G.J. and H.T. McMahon, *Mechanisms of endocytosis.* Annu Rev Biochem, 2009. **78**: p. 857-902.
96. Marchiando, A.M., et al., *Caveolin-1-dependent occludin endocytosis is required for TNF-induced tight junction regulation in vivo.* J Cell Biol, 2010. **189**(1): p. 111-26.
97. Alvarez, J.I., R. Cayrol, and A. Prat, *Disruption of central nervous system barriers in multiple sclerosis.* Biochim Biophys Acta, 2011. **1812**(2): p. 252-64.
98. Kothur, K., et al., *CSF cytokines/chemokines as biomarkers in neuroinflammatory CNS disorders: A systematic review.* Cytokine, 2016. **77**: p. 227-37.

99. Reijerkerk, A., et al., *Tissue-type plasminogen activator is a regulator of monocyte diapedesis through the brain endothelial barrier.* J Immunol, 2008. **181**(5): p. 3567-74.
100. Kebir, H., et al., *Human TH17 lymphocytes promote blood-brain barrier disruption and central nervous system inflammation.* Nat Med, 2007. **13**(10): p. 1173-5.
101. Argaw, A.T., et al., *IL-1beta regulates blood-brain barrier permeability via reactivation of the hypoxia-angiogenesis program.* J Immunol, 2006. **177**(8): p. 5574-84.
102. Lakhan, S.E., et al., *Matrix metalloproteinases and blood-brain barrier disruption in acute ischemic stroke.* Front Neurol, 2013. **4**: p. 32.
103. Vajkoczy, P., M. Laschinger, and B. Engelhardt, *Alpha4-integrin-VCAM-1 binding mediates G protein-independent capture of encephalitogenic T cell blasts to CNS white matter microvessels.* J Clin Invest, 2001. **108**(4): p. 557-65.
104. Lengfeld, J.E., et al., *Endothelial Wnt/beta-catenin signaling reduces immune cell infiltration in multiple sclerosis.* Proc Natl Acad Sci U S A, 2017.
105. Lecuyer, M.A., et al., *Dual role of ALCAM in neuroinflammation and blood-brain barrier homeostasis.* Proc Natl Acad Sci U S A, 2017. **114**(4): p. E524-E533.
106. Wu, H., et al., *Caveolin-1 Is Critical for Lymphocyte Trafficking into Central Nervous System during Experimental Autoimmune Encephalomyelitis.* J Neurosci, 2016. **36**(19): p. 5193-9.
107. Lajoie, J.M. and E.V. Shusta, *Targeting receptor-mediated transport for delivery of biologics across the blood-brain barrier.* Annu Rev Pharmacol Toxicol, 2015. **55**: p. 613-31.
108. Xiao, G. and L.S. Gan, *Receptor-mediated endocytosis and brain delivery of therapeutic biologics.* Int J Cell Biol, 2013. **2013**: p. 703545.
109. Pereira, C.D., et al., *ABC Transporters Are Key Players in Alzheimer's Disease.* J Alzheimers Dis, 2018. **61**(2): p. 463-485.
110. Goutal, S., et al., *Physical blood-brain barrier disruption induced by focused ultrasound does not overcome the transporter-mediated efflux of erlotinib.* J Control Release, 2018. **292**: p. 210-220.
111. Baburamani, A.A., et al., *Vulnerability of the developing brain to hypoxic-ischemic damage: contribution of the cerebral vasculature to injury and repair?* Front Physiol, 2012. **3**: p. 424.
112. Hara, K., et al., *Effect of bis (tributyl tin) oxide on permeability of the blood-brain barrier: a transient increase.* Occup Environ Med, 1994. **51**(11): p. 735-8.
113. Braniste, V., et al., *The gut microbiota influences blood-brain barrier permeability in mice.* Sci Transl Med, 2014. **6**(263): p. 263ra158.
114. Shigemoto-Mogami, Y., K. Hoshikawa, and K. Sato, *Activated Microglia Disrupt the Blood-Brain Barrier and Induce Chemokines and Cytokines in a Rat in vitro Model.* Front Cell Neurosci, 2018. **12**: p. 494.
115. Daneman, R. and B. Engelhardt, *Brain barriers in health and disease.* Neurobiol Dis, 2017. **107**: p. 1-3.
116. Daneman, R., et al., *Pericytes are required for blood-brain barrier integrity during embryogenesis.* Nature, 2010. **468**(7323): p. 562-6.
117. Mazzoni, J., et al., *The Wnt Inhibitor Apcdd1 Coordinates Vascular Remodeling and Barrier Maturation of Retinal Blood Vessels.* Neuron, 2017. **96**(5): p. 1055-1069 e6.

118. Bush, T.G., et al., *Leukocyte infiltration, neuronal degeneration, and neurite outgrowth after ablation of scar-forming, reactive astrocytes in adult transgenic mice.* Neuron, 1999. **23**(2): p. 297-308.
119. Bartanusz, V., et al., *The blood-spinal cord barrier: morphology and clinical implications.* Ann Neurol, 2011. **70**(2): p. 194-206.
120. Laschinger, M., P. Vajkoczy, and B. Engelhardt, *Encephalitogenic T cells use LFA-1 for transendothelial migration but not during capture and initial adhesion strengthening in healthy spinal cord microvessels in vivo.* Eur J Immunol, 2002. **32**(12): p. 3598-606.
121. Cruz-Orengo, L., et al., *Enhanced sphingosine-1-phosphate receptor 2 expression underlies female CNS autoimmunity susceptibility.* J Clin Invest, 2014. **124**(6): p. 2571-84.
122. Tavazoie, M., et al., *A specialized vascular niche for adult neural stem cells.* Cell Stem Cell, 2008. **3**(3): p. 279-88.
123. Winkler, C.W., et al., *Capillaries in the olfactory bulb but not the cortex are highly susceptible to virus-induced vascular leak and promote viral neuroinvasion.* Acta Neuropathol, 2015. **130**(2): p. 233-45.
124. Colin-Castelan, D., J. Ramirez-Santos, and G. Gutierrez-Ospina, *Differential vascular permeability along the forebrain ventricular neurogenic niche in the adult murine brain.* J Neurosci Res, 2016. **94**(2): p. 161-9.
125. Miyata, S., *New aspects in fenestrated capillary and tissue dynamics in the sensory circumventricular organs of adult brains.* Front Neurosci, 2015. **9**: p. 390.
126. Kaur, C., G. Rathnasamy, and E.A. Ling, *The Choroid Plexus in Healthy and Diseased Brain.* J Neuropathol Exp Neurol, 2016. **75**(3): p. 198-213.
127. Liddelow, S.A., *Development of the choroid plexus and blood-CSF barrier.* Front Neurosci, 2015. **9**: p. 32.
128. Liddelow, S.A., et al., *Molecular characterisation of transport mechanisms at the developing mouse blood-CSF interface: a transcriptome approach.* PLoS One, 2012. **7**(3): p. e33554.
129. Reboldi, A., Coisne, C., Baumjohann, D., Benvenuto, F., Bottinelli, D., Lira, S., Uccelli, A., Lanzavecchia, A., Engelhardt, B., and Sallusto, F. , *C-C chemokine receptor 6-regulated entry of Th-17 cells into the CNS through the choroid plexus is required for the initiation of EAE.* Nat Immunol, 2009. **10**(5): p. 514-518.
130. Rudick, R.A. and T.A. Eskin, *Neuropathological features of a lupus-like disorder in autoimmune mice.* Ann Neurol, 1983. **14**(3): p. 325-32.
131. Zameer, A. and S.A. Hoffman, *B and T cells in the brains of autoimmune mice.* J Neuroimmunol, 2004. **146**(1-2): p. 133-9.
132. Zameer, A. and S.A. Hoffman, *Increased ICAM-1 and VCAM-1 expression in the brains of autoimmune mice.* J Neuroimmunol, 2003. **142**(1-2): p. 67-74.
133. Wen, J., et al., *The role of B cells and autoantibodies in neuropsychiatric lupus.* Autoimmun Rev, 2016. **15**(9): p. 890-5.
134. Chan, O.T., M.P. Madaio, and M.J. Shlomchik, *The central and multiple roles of B cells in lupus pathogenesis.* Immunol Rev, 1999. **169**: p. 107-21.
135. Gelb, S., et al., *Mechanisms of neuropsychiatric lupus: The relative roles of the blood-cerebrospinal fluid barrier versus blood-brain barrier.* J Autoimmun, 2018. **91**: p. 34-44.
136. Wolak, D.J. and R.G. Thorne, *Diffusion of macromolecules in the brain: implications for drug delivery.* Mol Pharm, 2013. **10**(5): p. 1492-504.

137. Zhao, H., et al., *Olfactory plays a key role in spatiotemporal pathogenesis of cerebral malaria.* Cell Host Microbe, 2014. **15**(5): p. 551-63.
138. Meredith, M.E., T.S. Salameh, and W.A. Banks, *Intranasal Delivery of Proteins and Peptides in the Treatment of Neurodegenerative Diseases.* AAPS J, 2015. **17**(4): p. 780-7.
139. van Riel, D., R. Verdijk, and T. Kuiken, *The olfactory nerve: a shortcut for influenza and other viral diseases into the central nervous system.* J Pathol, 2015. **235**(2): p. 277-87.
140. Schafer, A., et al., *The role of the blood-brain barrier during Venezuelan equine encephalitis virus infection.* J Virol, 2011. **85**(20): p. 10682-90.
141. Gnann, J.W., Jr. and R.J. Whitley, *Herpes Simplex Encephalitis: an Update.* Curr Infect Dis Rep, 2017. **19**(3): p. 13.
142. Munster, V.J., et al., *Rapid Nipah virus entry into the central nervous system of hamsters via the olfactory route.* Sci Rep, 2012. **2**: p. 736.
143. Herbert, R.P., et al., *Cytokines and olfactory bulb microglia in response to bacterial challenge in the compromised primary olfactory pathway.* J Neuroinflammation, 2012. **9**: p. 109.
144. Lochhead, J.J., et al., *Rapid transport within cerebral perivascular spaces underlies widespread tracer distribution in the brain after intranasal administration.* J Cereb Blood Flow Metab, 2015. **35**(3): p. 371-81.
145. Kumar, N.N., et al., *Relative vascular permeability and vascularity across different regions of the rat nasal mucosa: implications for nasal physiology and drug delivery.* Sci Rep, 2016. **6**: p. 31732.
146. Clarkson, B.D., et al., *CCR7 deficient inflammatory Dendritic Cells are retained in the Central Nervous System.* Sci Rep, 2017. **7**: p. 42856.
147. Kaminski, M., et al., *Migration of monocytes after intracerebral injection.* Cell Adh Migr, 2012. **6**(3): p. 164-7.
148. Mohammad, M.G., et al., *Immune cell trafficking from the brain maintains CNS immune tolerance.* J Clin Invest, 2014. **124**(3): p. 1228-41.
149. Prinz, M. and J. Priller, *The role of peripheral immune cells in the CNS in steady state and disease.* Nat Neurosci, 2017. **20**(2): p. 136-144.
150. Prat, A. and J. Antel, *Pathogenesis of multiple sclerosis.* Curr Opin Neurol, 2005. **18**(3): p. 225-30.
151. Michel, L., et al., *B Cells in the Multiple Sclerosis Central Nervous System: Trafficking and Contribution to CNS-Compartmentalized Inflammation.* Front Immunol, 2015. **6**: p. 636.
152. Staun-Ram, E. and A. Miller, *Effector and regulatory B cells in Multiple Sclerosis.* Clin Immunol, 2017. **184**: p. 11-25.
153. Agahozo, M.C., et al., *CD20 therapies in multiple sclerosis and experimental autoimmune encephalomyelitis - Targeting T or B cells?* Mult Scler Relat Disord, 2016. **9**: p. 110-7.
154. Malter, M.P., C.E. Elger, and R. Surges, *Diagnostic value of CSF findings in antibody-associated limbic and anti-NMDAR-encephalitis.* Seizure, 2013. **22**(2): p. 136-40.
155. Sinclair, A.J., et al., *Clinical association of intrathecal and mirrored oligoclonal bands in paediatric neurology.* Dev Med Child Neurol, 2013. **55**(1): p. 71-5.
156. Church, A.J., et al., *CSF and serum immune parameters in Sydenham's chorea: evidence of an autoimmune syndrome?* J Neuroimmunol, 2003. **136**(1-2): p. 149-53.

157. Martinez-Hernandez, E., et al., *Analysis of complement and plasma cells in the brain of patients with anti-NMDAR encephalitis.* Neurology, 2011. **77**(6): p. 589-93.
158. Kreye, J., et al., *Human cerebrospinal fluid monoclonal N-methyl-D-aspartate receptor autoantibodies are sufficient for encephalitis pathogenesis.* Brain, 2016. **139**(Pt 10): p. 2641-2652.
159. Ehrenreich, H., *Autoantibodies against the N-Methyl-d-Aspartate Receptor Subunit NR1: Untangling Apparent Inconsistencies for Clinical Practice.* Front Immunol, 2017. **8**: p. 181.
160. Walls, A., et al., *Pediatric Autoimmune Neuropsychiatric Disorder Associated with Streptococcus Immunology: A Pilot Study.* Otolaryngol Head Neck Surg, 2015. **153**(1): p. 130-6.
161. Walls, A., et al., *Characterization of B-Cells in tonsils of patients diagnosed with pediatric autoimmune neuropsychiatric disorder associated streptococcus.* Int J Pediatr Otorhinolaryngol, 2016. **80**: p. 49-52.
162. Latimer, M.E., et al., *Therapeutic plasma apheresis as a treatment for 35 severely ill children and adolescents with pediatric autoimmune neuropsychiatric disorders associated with streptococcal infections.* J Child Adolesc Psychopharmacol, 2015. **25**(1): p. 70-5.
163. Darlington, P.J., et al., *Diminished Th17 (not Th1) responses underlie multiple sclerosis disease abrogation after hematopoietic stem cell transplantation.* Ann Neurol, 2013. **73**(3): p. 341-54.
164. Murphy, A.C., et al., *Infiltration of Th1 and Th17 cells and activation of microglia in the CNS during the course of experimental autoimmune encephalomyelitis.* Brain Behav Immun, 2010. **24**(4): p. 641-51.
165. Rostami, A. and B. Ciric, *Role of Th17 cells in the pathogenesis of CNS inflammatory demyelination.* J Neurol Sci, 2013. **333**(1-2): p. 76-87.
166. Costalonga, M., et al., *Intranasal bacteria induce Th1 but not Treg or Th2.* Mucosal Immunol, 2009. **2**(1): p. 85-95.
167. Bittner, S., et al., *Myelin oligodendrocyte glycoprotein (MOG35-55) induced experimental autoimmune encephalomyelitis (EAE) in C57BL/6 mice.* J Vis Exp, 2014(86).
168. Ifergan, I., et al., *Targeting the GM-CSF receptor for the treatment of CNS autoimmunity.* J Autoimmun, 2017. **84**: p. 1-11.
169. Komiyama, Y., et al., *IL-17 plays an important role in the development of experimental autoimmune encephalomyelitis.* J Immunol, 2006. **177**(1): p. 566-73.
170. Luo, H., et al., *EphrinB1 and EphrinB2 regulate T cell chemotaxis and migration in experimental autoimmune encephalomyelitis and multiple sclerosis.* Neurobiol Dis, 2016. **91**: p. 292-306.
171. Pare, A., et al., *IL-1beta enables CNS access to CCR2(hi) monocytes and the generation of pathogenic cells through GM-CSF released by CNS endothelial cells.* Proc Natl Acad Sci U S A, 2018. **115**(6): p. E1194-E1203.
172. Rothhammer, V., et al., *Type I interferons and microbial metabolites of tryptophan modulate astrocyte activity and central nervous system inflammation via the aryl hydrocarbon receptor.* Nat Med, 2016. **22**(6): p. 586-97.
173. Ivanov, II, et al., *The orphan nuclear receptor RORgammat directs the differentiation program of proinflammatory IL-17+ T helper cells.* Cell, 2006. **126**(6): p. 1121-33.

174. Barsheshet, Y., et al., *CCR8(+)FOXp3(+) Treg cells as master drivers of immune regulation.* Proc Natl Acad Sci U S A, 2017. **114**(23): p. 6086-6091.
175. Filatenkov, A., et al., *Persistence of parenchymal and perivascular T-cells in treatment-refractory anti-N-methyl-D-aspartate receptor encephalitis.* Neuroreport, 2017. **28**(14): p. 890-895.
176. Zeng, C., et al., *Th17 cells were recruited and accumulated in the cerebrospinal fluid and correlated with the poor prognosis of anti-NMDAR encephalitis.* Acta Biochim Biophys Sin (Shanghai), 2018. **50**(12): p. 1266-1273.
177. Sagan, S.A., et al., *Tolerance checkpoint bypass permits emergence of pathogenic T cells to neuromyelitis optica autoantigen aquaporin-4.* Proc Natl Acad Sci U S A, 2016. **113**(51): p. 14781-14786.
178. Lipp, M. and G. Muller, *Lymphoid organogenesis: getting the green light from RORgamma(t).* Nat Immunol, 2004. **5**(1): p. 12-4.
179. Eberl, G., et al., *An essential function for the nuclear receptor RORgamma(t) in the generation of fetal lymphoid tissue inducer cells.* Nat Immunol, 2004. **5**(1): p. 64-73.
180. Schafer, D.P., et al., *Microglia sculpt postnatal neural circuits in an activity and complement-dependent manner.* Neuron, 2012. **74**(4): p. 691-705.
181. Nimmerjahn, A., F. Kirchhoff, and F. Helmchen, *Resting microglial cells are highly dynamic surveillants of brain parenchyma in vivo.* Science, 2005. **308**(5726): p. 1314-8.
182. Furube, E., et al., *Brain Region-dependent Heterogeneity and Dose-dependent Difference in Transient Microglia Population Increase during Lipopolysaccharide-induced Inflammation.* Sci Rep, 2018. **8**(1): p. 2203.
183. Dudvarski Stankovic, N., et al., *Microglia-blood vessel interactions: a double-edged sword in brain pathologies.* Acta Neuropathol, 2016. **131**(3): p. 347-63.
184. Biber, K., J. Vinet, and H.W. Boddeke, *Neuron-microglia signaling: chemokines as versatile messengers.* J Neuroimmunol, 2008. **198**(1-2): p. 69-74.
185. Rappert, A., et al., *Secondary lymphoid tissue chemokine (CCL21) activates CXCR3 to trigger a Cl- current and chemotaxis in murine microglia.* J Immunol, 2002. **168**(7): p. 3221-6.
186. Mondal, T.K., et al., *Autoantibody-mediated neuroinflammation: pathogenesis of neuropsychiatric systemic lupus erythematosus in the NZM88 murine model.* Brain Behav Immun, 2008. **22**(6): p. 949-59.
187. Bialas, A.R., et al., *Microglia-dependent synapse loss in type I interferon-mediated lupus.* Nature, 2017. **546**(7659): p. 539-543.
188. Williams, J.L., D.W. Holman, and R.S. Klein, *Chemokines in the balance: maintenance of homeostasis and protection at CNS barriers.* Front Cell Neurosci, 2014. **8**: p. 154.
189. Bennett, M.L., et al., *New tools for studying microglia in the mouse and human CNS.* Proc Natl Acad Sci U S A, 2016. **113**(12): p. E1738-46.
190. Satoh, J., et al., *TMEM119 marks a subset of microglia in the human brain.* Neuropathology, 2016. **36**(1): p. 39-49.
191. Mundt, S., et al., *Conventional DCs sample and present myelin antigens in the healthy CNS and allow parenchymal T cell entry to initiate neuroinflammation.* Sci Immunol, 2019. **4**(31).
192. Hsu, M., et al., *Neuroinflammation-induced lymphangiogenesis near the cribriform plate contributes to drainage of CNS-derived antigens and immune cells.* Nat Commun, 2019. **10**(1): p. 229.

193. Proudfoot, A.E., *Chemokine receptors: multifaceted therapeutic targets.* Nat Rev Immunol, 2002. **2**(2): p. 106-15.
194. Louveau, A., T.H. Harris, and J. Kipnis, *Revisiting the Mechanisms of CNS Immune Privilege.* Trends Immunol, 2015. **36**(10): p. 569-77.
195. Holman, D.W., R.S. Klein, and R.M. Ransohoff, *The blood-brain barrier, chemokines and multiple sclerosis.* Biochim Biophys Acta, 2011. **1812**(2): p. 220-30.
196. Roberts, W.K., et al., *A destructive feedback loop mediated by CXCL10 in central nervous system inflammatory disease.* Ann Neurol, 2015. **78**(4): p. 619-29.
197. Lee, A.Y.S. and H. Korner, *The CCR6-CCL20 axis in humoral immunity and T-B cell immunobiology.* Immunobiology, 2019.
198. McManus, C., et al., *MCP-1, MCP-2 and MCP-3 expression in multiple sclerosis lesions: an immunohistochemical and in situ hybridization study.* J Neuroimmunol, 1998. **86**(1): p. 20-9.
199. Ransohoff, R.M., et al., *Astrocyte expression of mRNA encoding cytokines IP-10 and JE/MCP-1 in experimental autoimmune encephalomyelitis.* FASEB J, 1993. **7**(6): p. 592-600.
200. Conductier, G., et al., *The role of monocyte chemoattractant protein MCP1/CCL2 in neuroinflammatory diseases.* J Neuroimmunol, 2010. **224**(1-2): p. 93-100.
201. Clarkson, B.D., et al., *CCR2-dependent dendritic cell accumulation in the central nervous system during early effector experimental autoimmune encephalomyelitis is essential for effector T cell restimulation in situ and disease progression.* J Immunol, 2015. **194**(2): p. 531-41.
202. Clarkson, B.D., et al., *Mapping the accumulation of co-infiltrating CNS dendritic cells and encephalitogenic T cells during EAE.* J Neuroimmunol, 2014. **277**(1-2): p. 39-49.
203. Wang, A., et al., *Dysregulated expression of CXCR4/CXCL12 in subsets of patients with systemic lupus erythematosus.* Arthritis Rheum, 2010. **62**(11): p. 3436-46.
204. Wang, A., et al., *CXCR4/CXCL12 hyperexpression plays a pivotal role in the pathogenesis of lupus.* J Immunol, 2009. **182**(7): p. 4448-58.
205. Hoffman, K.L., et al., *A murine model for neuropsychiatric disorders associated with group A beta-hemolytic streptococcal infection.* J Neurosci, 2004. **24**(7): p. 1780-91.
206. Yaddanapudi, K., et al., *Passive transfer of streptococcus-induced antibodies reproduces behavioral disturbances in a mouse model of pediatric autoimmune neuropsychiatric disorders associated with streptococcal infection.* Mol Psychiatry, 2010. **15**(7): p. 712-26.
207. Hammer, C., et al., *Neuropsychiatric disease relevance of circulating anti-NMDA receptor autoantibodies depends on blood-brain barrier integrity.* Mol Psychiatry, 2014. **19**(10): p. 1143-9.
208. Planaguma, J., et al., *Ephrin-B2 prevents N-methyl-D-aspartate receptor antibody effects on memory and neuroplasticity.* Ann Neurol, 2016. **80**(3): p. 388-400.
209. Planaguma, J., et al., *Human N-methyl D-aspartate receptor antibodies alter memory and behaviour in mice.* Brain, 2015. **138**(Pt 1): p. 94-109.
210. Wright, S., et al., *Epileptogenic effects of NMDAR antibodies in a passive transfer mouse model.* Brain, 2015. **138**(Pt 11): p. 3159-67.
211. Wurdemann, T., et al., *Stereotactic injection of cerebrospinal fluid from anti-NMDA receptor encephalitis into rat dentate gyrus impairs NMDA receptor function.* Brain Res, 2016. **1633**: p. 10-8.

212. Wenke, N.K., et al., *NMDA receptor dysfunction via unmutated human antibodies against the NR1 subunit.* Ann Neurol, 2019.
213. Mikasova, L., et al., *Disrupted surface cross-talk between NMDA and Ephrin-B2 receptors in anti-NMDA encephalitis.* Brain, 2012. **135**(Pt 5): p. 1606-21.
214. Taraschenko, O., et al., *A mouse model of seizures in anti-N-methyl-d-aspartate receptor encephalitis.* Epilepsia, 2019. **60**(3): p. 452-463.
215. Amedonu, E., et al., *An Assay to Determine Mechanisms of Rapid Autoantibody-Induced Neurotransmitter Receptor Endocytosis and Vesicular Trafficking in Autoimmune Encephalitis.* Front Neurol, 2019. **10**: p. 178.
216. Moscato, E.H., et al., *Mechanisms underlying autoimmune synaptic encephalitis leading to disorders of memory, behavior and cognition: insights from molecular, cellular and synaptic studies.* Eur J Neurosci, 2010. **32**(2): p. 298-309.
217. Guasp, M., et al., *Cerebellar ataxia and autoantibodies restricted to glutamic acid decarboxylase 67 (GAD67).* J Neuroimmunol, 2016. **300**: p. 15-17.
218. Nibber, A., et al., *Pathogenic potential of antibodies to the GABAB receptor.* Epilepsia Open, 2017. **2**(3): p. 355-359.
219. Nikolaus, M., et al., *CSF reactivity in GABAA receptor antibody encephalitis - Immunocytochemical distribution in the murine brain.* Brain Res, 2019. **1704**: p. 249-256.
220. Haselmann, H., et al., *Interactions of Human Autoantibodies with Hippocampal GABAergic Synaptic Transmission - Analyzing Antibody-Induced Effects ex vivo.* Front Neurol, 2015. **6**: p. 136.
221. Hackert, J.K., et al., *Anti-GAD65 Containing Cerebrospinal Fluid Does not Alter GABAergic Transmission.* Front Cell Neurosci, 2016. **10**: p. 130.
222. Geis, C., et al., *Stiff person syndrome-associated autoantibodies to amphiphysin mediate reduced GABAergic inhibition.* Brain, 2010. **133**(11): p. 3166-80.
223. Pruss, H. and K. Kirmse, *Pathogenic role of autoantibodies against inhibitory synapses.* Brain Res, 2018. **1701**: p. 146-152.
224. Rodella, U., et al., *An animal model of Miller Fisher syndrome: Mitochondrial hydrogen peroxide is produced by the autoimmune attack of nerve terminals and activates Schwann cells.* Neurobiol Dis, 2016. **96**: p. 95-104.
225. Buckley, C., et al., *Potassium channel antibodies in two patients with reversible limbic encephalitis.* Ann Neurol, 2001. **50**(1): p. 73-8.
226. Thieben, M.J., et al., *Potentially reversible autoimmune limbic encephalitis with neuronal potassium channel antibody.* Neurology, 2004. **62**(7): p. 1177-82.
227. Kleopa, K.A., et al., *Neuromyotonia and limbic encephalitis sera target mature Shaker-type K+ channels: subunit specificity correlates with clinical manifestations.* Brain, 2006. **129**(Pt 6): p. 1570-84.
228. Shillito, P., et al., *Acquired neuromyotonia: evidence for autoantibodies directed against K+ channels of peripheral nerves.* Ann Neurol, 1995. **38**(5): p. 714-22.
229. Boillot, M., et al., *Glutamatergic neuron-targeted loss of LGI1 epilepsy gene results in seizures.* Brain, 2014. **137**(Pt 11): p. 2984-96.
230. Fukata, Y., et al., *Disruption of LGI1-linked synaptic complex causes abnormal synaptic transmission and epilepsy.* Proc Natl Acad Sci U S A, 2010. **107**(8): p. 3799-804.
231. Petit-Pedrol, M., et al., *LGI1 antibodies alter Kv1.1 and AMPA receptors changing synaptic excitability, plasticity and memory.* Brain, 2018. **141**(11): p. 3144-3159.

232. Macri, S., et al., *Mice repeatedly exposed to Group-A beta-Haemolytic Streptococcus show perseverative behaviors, impaired sensorimotor gating, and immune activation in rostral diencephalon.* Sci Rep, 2015. **5**: p. 13257.
233. Mora, S., et al., *Neuropsychiatric consequences of childhood group A streptococcal infection: A systematic review of preclinical models.* Brain Behav Immun, 2019.
234. Wang, B., et al., *Induction of TGF-beta1 and TGF-beta1-dependent predominant Th17 differentiation by group A streptococcal infection.* Proc Natl Acad Sci U S A, 2010. **107**(13): p. 5937-42.
235. Dileepan, T., et al., *Robust antigen specific th17 T cell response to group A Streptococcus is dependent on IL-6 and intranasal route of infection.* PLoS Pathog, 2011. **7**(9): p. e1002252.
236. Zhang, D., et al., *Anti-streptococcus IgM antibodies induce repetitive stereotyped movements: cell activation and co-localization with Fcalpha/mu receptors in the striatum and motor cortex.* Brain Behav Immun, 2012. **26**(4): p. 521-33.
237. Doyle, F., et al., *Infusion of Sydenham's chorea antibodies in striatum with up-regulated dopaminergic receptors: a pilot study to investigate the potential of SC antibodies to increase dopaminergic activity.* Neurosci Lett, 2012. **523**(2): p. 186-9.
238. Ben-Pazi, H., O. Sadan, and D. Offen, *Striatal microinjection of Sydenham chorea antibodies: using a rat model to examine the dopamine hypothesis.* J Mol Neurosci, 2012. **46**(1): p. 162-6.
239. Hallett, J.J., et al., *Anti-striatal antibodies in Tourette syndrome cause neuronal dysfunction.* J Neuroimmunol, 2000. **111**(1-2): p. 195-202.
240. Boring, L., et al., *Impaired monocyte migration and reduced type 1 (Th1) cytokine responses in C-C chemokine receptor 2 knockout mice.* J Clin Invest, 1997. **100**(10): p. 2552-61.
241. Cook, D.N., et al., *CCR6 mediates dendritic cell localization, lymphocyte homeostasis, and immune responses in mucosal tissue.* Immunity, 2000. **12**(5): p. 495-503.
242. Bolding, K.A. and K.M. Franks, *Complementary codes for odor identity and intensity in olfactory cortex.* Elife, 2017. **6**.
243. Root, C.M., et al., *The participation of cortical amygdala in innate, odour-driven behaviour.* Nature, 2014. **515**(7526): p. 269-73.
244. Yang, M. and J.N. Crawley, *Simple behavioral assessment of mouse olfaction.* Curr Protoc Neurosci, 2009. **Chapter 8**: p. Unit 8 24.
245. Robert, R., et al., *Essential role for CCR6 in certain inflammatory diseases demonstrated using specific antagonist and knockin mice.* JCI Insight, 2017. **2**(15).
246. Bauer, J. and C.G. Bien, *Neuropathology of autoimmune encephalitides.* Handb Clin Neurol, 2016. **133**: p. 107-20.
247. Park, H.S., et al., *Primary induction of CD4 T cell responses in nasal associated lymphoid tissue during group A streptococcal infection.* Eur J Immunol, 2004. **34**(10): p. 2843-53.
248. Attems, J., L. Walker, and K.A. Jellinger, *Olfactory bulb involvement in neurodegenerative diseases.* Acta Neuropathol, 2014. **127**(4): p. 459-75.
249. Barresi, M., et al., *Evaluation of olfactory dysfunction in neurodegenerative diseases.* J Neurol Sci, 2012. **323**(1-2): p. 16-24.

250. Ciurleo, R., et al., *Olfactory dysfunction as a prognostic marker for disability progression in Multiple Sclerosis: An olfactory event related potential study.* PLoS One, 2018. **13**(4): p. e0196006.
251. Devanand, D.P., *Olfactory Identification Deficits, Cognitive Decline, and Dementia in Older Adults.* Am J Geriatr Psychiatry, 2016. **24**(12): p. 1151-1157.
252. Marin, C., et al., *Olfactory Dysfunction in Neurodegenerative Diseases.* Curr Allergy Asthma Rep, 2018. **18**(8): p. 42.
253. Tepavcevic, V., et al., *Inflammation-induced subventricular zone dysfunction leads to olfactory deficits in a targeted mouse model of multiple sclerosis.* J Clin Invest, 2011. **121**(12): p. 4722-34.
254. Good, K.P., et al., *Unilateral olfactory sensitivity in multiple sclerosis.* Physiol Behav, 2017. **168**: p. 24-30.
255. Shin, T., et al., *Olfactory Dysfunction in CNS Neuroimmunological Disorders: a Review.* Mol Neurobiol, 2018.
256. Dando, S.J., et al., *Regional and functional heterogeneity of antigen presenting cells in the mouse brain and meninges.* Glia, 2018.
257. Hasegawa-Ishii, S., A. Shimada, and F. Imamura, *Neuroplastic changes in the olfactory bulb associated with nasal inflammation in mice.* J Allergy Clin Immunol, 2018.
258. Kapadia, M., et al., *Altered olfactory function in the MRL model of CNS lupus.* Behav Brain Res, 2012. **234**(2): p. 303-11.
259. Huilgol, D. and S. Tole, *Cell migration in the developing rodent olfactory system.* Cell Mol Life Sci, 2016. **73**(13): p. 2467-90.
260. Vassar, R., J. Ngai, and R. Axel, *Spatial segregation of odorant receptor expression in the mammalian olfactory epithelium.* Cell, 1993. **74**(2): p. 309-18.
261. Komiyama, T. and L. Luo, *Development of wiring specificity in the olfactory system.* Curr Opin Neurobiol, 2006. **16**(1): p. 67-73.
262. Buck, L. and R. Axel, *A novel multigene family may encode odorant receptors: a molecular basis for odor recognition.* Cell, 1991. **65**(1): p. 175-87.
263. Zou, D.J., et al., *Postnatal refinement of peripheral olfactory projections.* Science, 2004. **304**(5679): p. 1976-9.
264. Bovetti, S., et al., *Blood vessels form a scaffold for neuroblast migration in the adult olfactory bulb.* J Neurosci, 2007. **27**(22): p. 5976-80.
265. Becher, B., S. Spath, and J. Goverman, *Cytokine networks in neuroinflammation.* Nat Rev Immunol, 2017. **17**(1): p. 49-59.
266. Oshima, T., et al., *Interferon-gamma and interleukin-10 reciprocally regulate endothelial junction integrity and barrier function.* Microvasc Res, 2001. **61**(1): p. 130-43.
267. Cattalini, M., et al., *Sex Differences in Pediatric Rheumatology.* Clin Rev Allergy Immunol, 2017.
268. Li, Q., et al., *Systemic autoimmunity in TAM triple knockout mice causes inflammatory brain damage and cell death.* PLoS One, 2013. **8**(6): p. e64812.
269. Churlaud, G., et al., *Human and Mouse CD8(+)CD25(+)FOXP3(+) Regulatory T Cells at Steady State and during Interleukin-2 Therapy.* Front Immunol, 2015. **6**: p. 171.
270. Kirk, J., et al., *Tight junctional abnormality in multiple sclerosis white matter affects all calibres of vessel and is associated with blood-brain barrier leakage and active demyelination.* J Pathol, 2003. **201**(2): p. 319-27.

271. Muradashvili, N. and D. Lominadze, *Role of fibrinogen in cerebrovascular dysfunction after traumatic brain injury.* Brain Inj, 2013. **27**(13-14): p. 1508-15.
272. Bolding, K.A. and K.M. Franks, *Recurrent cortical circuits implement concentration-invariant odor coding.* Science, 2018. **361**(6407).
273. Steer, A.C., et al., *Systematic review of rheumatic heart disease prevalence in children in developing countries: the role of environmental factors.* J Paediatr Child Health, 2002. **38**(3): p. 229-34.
274. Twilt, M. and S.M. Benseler, *Childhood inflammatory brain diseases: pathogenesis, diagnosis and therapy.* Rheumatology (Oxford), 2014. **53**(8): p. 1359-68.
275. Selmi, C., J.G. Barin, and N.R. Rose, *Current trends in autoimmunity and the nervous system.* J Autoimmun, 2016. **75**: p. 20-29.
276. Calabresi, P.A., et al., *T lymphocytes conditioned with Interferon beta induce membrane and soluble VCAM on human brain endothelial cells.* J Neuroimmunol, 2001. **115**(1-2): p. 161-7.
277. Rothhammer, V., et al., *Th17 lymphocytes traffic to the central nervous system independently of alpha4 integrin expression during EAE.* J Exp Med, 2011. **208**(12): p. 2465-76.
278. Fasching, P., et al., *Therapeutic Potential of Targeting the Th17/Treg Axis in Autoimmune Disorders.* Molecules, 2017. **22**(1).
279. Yang, X.O., et al., *Molecular antagonism and plasticity of regulatory and inflammatory T cell programs.* Immunity, 2008. **29**(1): p. 44-56.
280. Alvarez, J.I., et al., *Focal disturbances in the blood-brain barrier are associated with formation of neuroinflammatory lesions.* Neurobiol Dis, 2015. **74**: p. 14-24.
281. Spangenberg, E.E. and K.N. Green, *Inflammation in Alzheimer's disease: Lessons learned from microglia-depletion models.* Brain Behav Immun, 2017. **61**: p. 1-11.
282. Hong, S., et al., *Complement and microglia mediate early synapse loss in Alzheimer mouse models.* Science, 2016. **352**(6286): p. 712-716.
283. Wu, Y., et al., *Microglia: Dynamic Mediators of Synapse Development and Plasticity.* Trends Immunol, 2015. **36**(10): p. 605-613.
284. Olichney, J.M., et al., *Anosmia is very common in the Lewy body variant of Alzheimer's disease.* J Neurol Neurosurg Psychiatry, 2005. **76**(10): p. 1342-7.
285. Gire, D.H., et al., *Mitral cells in the olfactory bulb are mainly excited through a multistep signaling path.* J Neurosci, 2012. **32**(9): p. 2964-75.
286. Stubbington, M.J., et al., *An atlas of mouse CD4(+) T cell transcriptomes.* Biol Direct, 2015. **10**: p. 14.
287. Williams, I.R., *CCR6 and CCL20: partners in intestinal immunity and lymphorganogenesis.* Ann N Y Acad Sci, 2006. **1072**: p. 52-61.
288. Larochelle, C., et al., *Melanoma cell adhesion molecule identifies encephalitogenic T lymphocytes and promotes their recruitment to the central nervous system.* Brain, 2012. **135**(Pt 10): p. 2906-24.
289. Zhang, L., et al., *Neuron-derived CCL2 contributes to microglia activation and neurological decline in hepatic encephalopathy.* Biol Res, 2017. **50**(1): p. 26.
290. Forde, E.A., R.N. Dogan, and W.J. Karpus, *CCR4 contributes to the pathogenesis of experimental autoimmune encephalomyelitis by regulating inflammatory macrophage function.* J Neuroimmunol, 2011. **236**(1-2): p. 17-26.

291. Poppensieker, K., et al., *CC chemokine receptor 4 is required for experimental autoimmune encephalomyelitis by regulating GM-CSF and IL-23 production in dendritic cells.* Proc Natl Acad Sci U S A, 2012. **109**(10): p. 3897-902.
292. Mony, J.T., R. Khorooshi, and T. Owens, *Chemokine receptor expression by inflammatory T cells in EAE.* Front Cell Neurosci, 2014. **8**: p. 187.
293. Agrawal, S.M., et al., *Extracellular matrix metalloproteinase inducer shows active perivascular cuffs in multiple sclerosis.* Brain, 2013. **136**(Pt 6): p. 1760-77.
294. Herz, J., et al., *Myeloid Cells in the Central Nervous System.* Immunity, 2017. **46**(6): p. 943-956.
295. Serbina, N.V. and E.G. Pamer, *Monocyte emigration from bone marrow during bacterial infection requires signals mediated by chemokine receptor CCR2.* Nat Immunol, 2006. **7**(3): p. 311-7.
296. Groves, A., Y. Kihara, and J. Chun, *Fingolimod: direct CNS effects of sphingosine 1-phosphate (S1P) receptor modulation and implications in multiple sclerosis therapy.* J Neurol Sci, 2013. **328**(1-2): p. 9-18.
297. Chun, S. and Y.B. Kwon, *The CCL2 elevation in primary afferent fibers produces zymosan-induced hyperalgesia through microglia-mediated neuronal activation in the spinal dorsal horn.* Brain Res Bull, 2019. **149**: p. 53-59.
298. Jiang, H., et al., *CCL2/CCR2 signaling elicits itch- and pain-like behavior in a murine model of allergic contact dermatitis.* Brain Behav Immun, 2019.
299. Brenton, J.N. and H.P. Goodkin, *Antibody-Mediated Autoimmune Encephalitis in Childhood.* Pediatr Neurol, 2016. **60**: p. 13-23.
300. Aldridge, J., et al., *Sex-based differences in association between circulating T cell subsets and disease activity in untreated early rheumatoid arthritis patients.* Arthritis Res Ther, 2018. **20**(1): p. 150.
301. Dimitrijevic, M., et al., *Sexual dimorphism in Th17/Treg axis in lymph nodes draining inflamed joints in rats with collagen-induced arthritis.* Brain Behav Immun, 2019. **76**: p. 198-214.
302. Park, H.J., et al., *Sex-Based Selectivity of PPARgamma Regulation in Th1, Th2, and Th17 Differentiation.* Int J Mol Sci, 2016. **17**(8).
303. Kass, M.D., et al., *Differences in peripheral sensory input to the olfactory bulb between male and female mice.* Sci Rep, 2017. **7**: p. 45851.
304. Pozharskaya, T. and A.P. Lane, *Interferon gamma causes olfactory dysfunction without concomitant neuroepithelial damage.* Int Forum Allergy Rhinol, 2013. **3**(11): p. 861-5.
305. Sultan, B., L.A. May, and A.P. Lane, *The role of TNF-alpha in inflammatory olfactory loss.* Laryngoscope, 2011. **121**(11): p. 2481-6.
306. Kim, J., et al., *Olfactory Dysfunction in Autoimmune Central Nervous System Neuroinflammation.* Mol Neurobiol, 2018. **55**(11): p. 8499-8508.
307. del Pozo, M.A., et al., *Phospho-caveolin-1 mediates integrin-regulated membrane domain internalization.* Nat Cell Biol, 2005. **7**(9): p. 901-8.
308. Lynch, R.D., et al., *Cholesterol depletion alters detergent-specific solubility profiles of selected tight junction proteins and the phosphorylation of occludin.* Exp Cell Res, 2007. **313**(12): p. 2597-610.
309. Sugibayashi, K., Y. Onuki, and K. Takayama, *Displacement of tight junction proteins from detergent-resistant membrane domains by treatment with sodium caprate.* Eur J Pharm Sci, 2009. **36**(2-3): p. 246-53.

310. McCaffrey, G., et al., *Tight junctions contain oligomeric protein assembly critical for maintaining blood-brain barrier integrity in vivo.* J Neurochem, 2007. **103**(6): p. 2540-55.
311. Saeki, K., et al., *A major lipid raft protein raftlin modulates T cell receptor signaling and enhances th17-mediated autoimmune responses.* J Immunol, 2009. **182**(10): p. 5929-37.
312. Cayrol, R., et al., *Activated leukocyte cell adhesion molecule promotes leukocyte trafficking into the central nervous system.* Nat Immunol, 2008. **9**(2): p. 137-45.
313. Ifergan, I., et al., *Central nervous system recruitment of effector memory CD8+ T lymphocytes during neuroinflammation is dependent on alpha4 integrin.* Brain, 2011. **134**(Pt 12): p. 3560-77.
314. Zenaro, E., G. Piacentino, and G. Constantin, *The blood-brain barrier in Alzheimer's disease.* Neurobiol Dis, 2017. **107**: p. 41-56.
315. Obermeier, B., R. Daneman, and R.M. Ransohoff, *Development, maintenance and disruption of the blood-brain barrier.* Nat Med, 2013. **19**(12): p. 1584-96.
316. Worbs, T., S.I. Hammerschmidt, and R. Forster, *Dendritic cell migration in health and disease.* Nat Rev Immunol, 2017. **17**(1): p. 30-48.
317. Harberts, E., et al., *Human herpesvirus-6 entry into the central nervous system through the olfactory pathway.* Proc Natl Acad Sci U S A, 2011. **108**(33): p. 13734-9.
318. Kuhlmann, T., et al., *An updated histological classification system for multiple sclerosis lesions.* Acta Neuropathol, 2017. **133**(1): p. 13-24.
319. Senecal, V., et al., *Production of IL-27 in multiple sclerosis lesions by astrocytes and myeloid cells: Modulation of local immune responses.* Glia, 2016. **64**(4): p. 553-69.
320. Schafer, D.P., et al., *Microglia contribute to circuit defects in Mecp2 null mice independent of microglia-specific loss of Mecp2 expression.* Elife, 2016. **5**.
321. Henkin, R.I., L. Schmidt, and I. Velicu, *Interleukin 6 in hyposmia.* JAMA Otolaryngol Head Neck Surg, 2013. **139**(7): p. 728-34.
322. Yamasaki, R., et al., *Differential roles of microglia and monocytes in the inflamed central nervous system.* J Exp Med, 2014. **211**(8): p. 1533-49.
323. Elmore, M.R., et al., *Colony-stimulating factor 1 receptor signaling is necessary for microglia viability, unmasking a microglia progenitor cell in the adult brain.* Neuron, 2014. **82**(2): p. 380-97.
324. Rice, R.A., et al., *Microglial repopulation resolves inflammation and promotes brain recovery after injury.* Glia, 2017. **65**(6): p. 931-944.
325. Valderrama, J.A. and V. Nizet, *Group A Streptococcus encounters with host macrophages.* Future Microbiol, 2018. **13**: p. 119-134.
326. Osterlund, A., et al., *Intracellular reservoir of Streptococcus pyogenes in vivo: a possible explanation for recurrent pharyngotonsillitis.* Laryngoscope, 1997. **107**(5): p. 640-7.
327. Balint, B. and K.P. Bhatia, *Stiff person syndrome and other immune-mediated movement disorders - new insights.* Curr Opin Neurol, 2016. **29**(4): p. 496-506.
328. Bryant, P.A., et al., *Some of the people, some of the time: susceptibility to acute rheumatic fever.* Circulation, 2009. **119**(5): p. 742-53.
329. McDonald, M., et al., *Apparent contrasting rates of pharyngitis and pyoderma in regions where rheumatic heart disease is highly prevalent.* Heart Lung Circ, 2007. **16**(4): p. 254-9.
330. Monnery-Patris, S., et al., *Development of olfactory ability in children: sensitivity and identification.* Dev Psychobiol, 2009. **51**(3): p. 268-76.

331. Richman, R.A., et al., *Olfactory deficits in boys with cleft palate.* Pediatrics, 1988. **82**(6): p. 840-4.
332. Kipp, M., et al., *Multiple sclerosis animal models: a clinical and histopathological perspective.* Brain Pathol, 2017. **27**(2): p. 123-137.
333. Lassmann, H. and M. Bradl, *Multiple sclerosis: experimental models and reality.* Acta Neuropathol, 2017. **133**(2): p. 223-244.
334. Kirvan, C.A., et al., *Antibody-mediated neuronal cell signaling in behavior and movement disorders.* J Neuroimmunol, 2006. **179**(1-2): p. 173-9.
335. D'Agostino, P.M., et al., *Brain dendritic cells: biology and pathology.* Acta Neuropathol, 2012. **124**(5): p. 599-614.
336. Dando, S.J., et al., *A case of mistaken identity: CD11c-eYFP(+) cells in the normal mouse brain parenchyma and neural retina display the phenotype of microglia, not dendritic cells.* Glia, 2016. **64**(8): p. 1331-49.
337. Bulloch, K., et al., *CD11c/EYFP transgene illuminates a discrete network of dendritic cells within the embryonic, neonatal, adult, and injured mouse brain.* J Comp Neurol, 2008. **508**(5): p. 687-710.

Appendix A: Comparison of route of GAS exposure: neuroinflammation and behavioral studies

Animal models of CNS autoimmunity frequently feature peripheral activation of the immune system in conjunction with permeabilization of the BBB to allow access to CNS targets. This produces a robust CNS antigen-directed response in immunized animals; in the case of MOG_{35-55} EAE immunization, demyelination, BBB breach, and immune cell infiltration occur ~8-12 days post immunization (dpi) [167]. However, many different types of EAE exist, none of which perfectly model the human disease multiple sclerosis [332, 333]. For instance, differing lengths of myelin peptide antigen produce slightly different immune cell profiles in the periphery and as CNS infiltrate. Toxin- or viral-induced demyelination models more accurately capture mechanisms of brain demyelination, as opposed to classical EAE, which primarily affects the spinal cord [333]. Differences in localization of pathology, degree of vascular dysfunction, and immune profile all separate different MS animal models [332]. Initial investigation into GAS-induced CNS autoimmunity directly translated the EAE model of antigen-directed immunization to expose rodents to GAS antigens together with adjuvants that activate the immune system and permeabilize the BBB.

The discovery that brain antigens drove pathogenic autoantibodies into the CNS in AE syndromes drew an attractive parallel to various EAE models. To investigate the pathogenesis of these diseases, new animal models of GAS-induced BGE featured immunization with GAS bacterial antigens in conjunction with adjuvants to disrupt the BBB and activate the immune system. Recurrent boosts with antigen alone every two weeks mimic recurrent exposure to GAS over long periods of time in these models. In this manner, subcutaneous (s.c.) GAS immunizations were reported to induce behavioral abnormalities reminiscent of PANDAS and SC in rats and mice

[80, 205, 206]. In addition to behavioral abnormalities, these studies described microgliosis in the striatum and deposition of serum IgG in the deep cerebellar nuclei, striatum, hippocampus, thalamus, and frontal cortex of GAS-exposed rodents [80, 81, 205, 206, 232]. In EAE, T cell, B cell, and peripheral monocyte/macrophage infiltration is a key feature of disease seen in various brain regions and in spinal cord lesion areas [115, 202, 280]. However, differences in methodology in GAS immunization models necessitates critical review in how fully their findings may be translated to human post-infectious BGE.

Behavioral and motor abnormalities were reported in subcutaneously (s.c.) GAS-immunized rodents [80, 205, 206]; however in mice, intranasal (i.n.), but not i.v. or s.c., GAS exposure generates a robust autoreactive Th17 response that mimics GAS pharyngitis in humans [93, 235]. Therefore, different routes of GAS exposure may skew immune responses. Reports of both s.c. and i.n. GAS exposure are helpful in clarifying potential mechanisms of post-infectious BGE, but thorough, direct comparison of immune and neurodegenerative outcomes in s.c. and i.n. GAS models has not been performed to date. To adequately compare s.c. GAS immunization to i.n. GAS inoculation models, experiments within our lab directly compared T cell infiltration, microglial activation, serum IgG binding profiles to GAS and brain antigens, and behavioral phenotypes.

A.1 Different immunological responses to intranasal versus subcutaneous GAS exposure

By comparing infiltration of $CD4^+$ T cells in **Figure A.1**, it is clear that i.n. inoculations are far more efficient at prompting a CNS inflammatory response, even with BBB breach in the s.c. model providing an entry to the CNS. T cells collect in i.n. brains anteriorly in the olfactory

bulb, and while some T cells are seen in the OB meninges in s.c. brains, the bulk of CD4 infiltrate in s.c. brains is periventricular and within the choroid plexus. It appears that the T cells in the

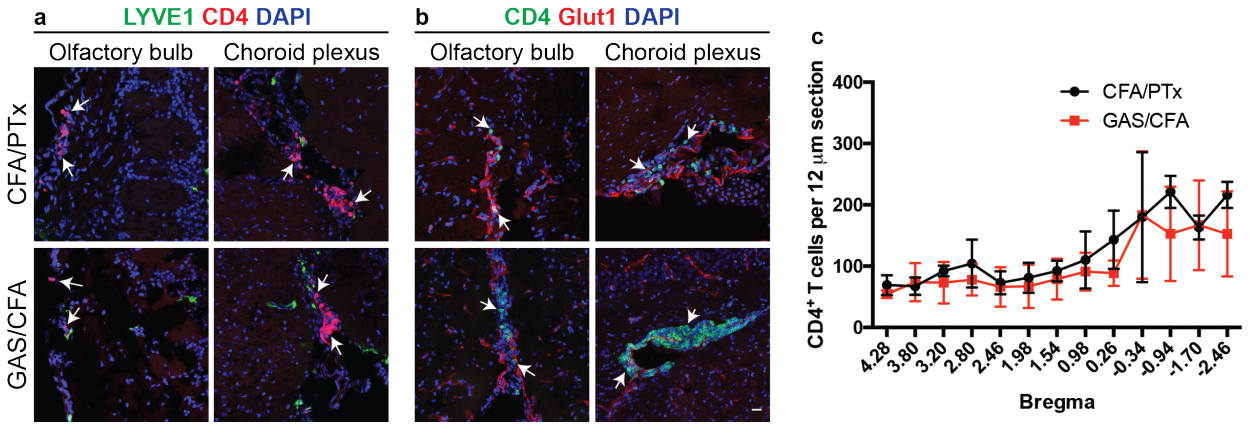

Figure A.1 $CD4^+$ T cells in brains of subcutaneously immunized SJL/J mice. **a** T cells do not colocalize with lymphatic marker LYVE1, but **b** they do colocalize with blood vessel marker GLUT1. In the choroid plexus, immunized mice show collections of $CD4^+$ T cells contained by the BCSFB. **c** Quantification of $CD4^+$ T cells over the rostrocaudal axis of the brain. Data represent mean ± SEM from *n*=4 mice per group. There was a significant effect of bregma ($F(12,72)=12.00$, $p<0.0001$), but no main treatment effect ($F(1,6)=1.439$, $p=0.2755$) or interaction between bregma and treatment ($F(12,72)=0.8039$, $p=0.6453$). Scale bar = 20 μm.

choroid plexus of s.c. GAS brains do not cross into the CSF; rather, they are limited by the BCSFB. T cell counts between i.n. and s.c. GAS brains equalize in more posterior regions of the brain.

Neuroinflammation in anterior brain regions was then assessed in s.c. and i.n. GAS-exposed mice. Microglia counts in the olfactory bulb glomerular layer of s.c. GAS-immunized mice are not significantly different from uninfected control mice, which is not surprising given the lack of peripheral immune infiltration in the OB. Intranasally-infected mice have significantly more activated microglia in the OB than s.c.-immunized mice (**Figure A.2**). Looking more posteriorly, microglia counts in the dorsal striatum are also not elevated in s.c.-GAS mice compared to vehicle controls.

A.2 Humoral anti-GAS and anti-brain immune responses induced by s.c. and i.n. GAS

Given that there seems to be a mild effect on the cellular immune system after s.c. GAS infections, we also compared humoral immune system to investigate Ab production. Serum harvested from i.n. and s.c. GAS mice (as well as their respective vehicle controls, and healthy controls) was assayed by Western blot for binding affinity for GAS bacterial protein lysate and

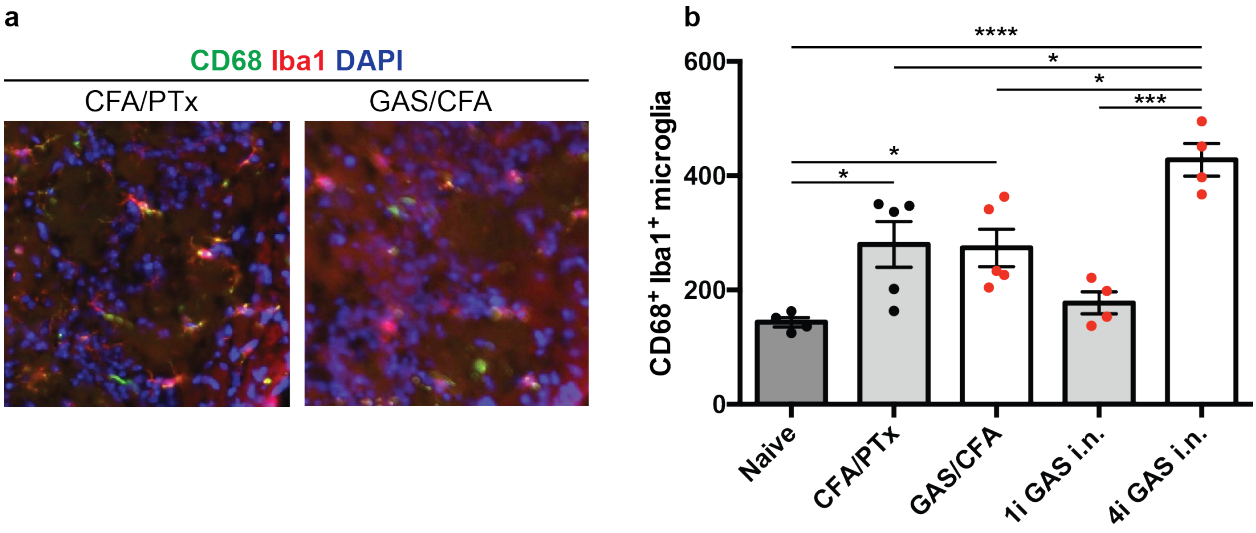

Figure A.2 Microglial activation is not GAS-specific in the s.c. GAS immunization protocol. **a** Immunohistochemical labeling of CD68 (green), Iba1 (red), and DAPI (blue) in OB tissue sections of s.c. GAS-immunized mice and CFA/PTx controls. **b** Quantification of microglia in OB sections of naïve, CFA/PTx, GAS/CFA, acutely i.n. GAS-inoculated (1i) and recurrently i.n. GAS-inoculated (4i) mice. Data represent mean ± SEM from n=4 naïve, n=5 CFA/PTx, n=5 GAS/CFA, n=4 GAS 1i, and n=4 GAS 4i animals. One-way ANOVA showed an effect of treatment ($F(4,17)=12.18$, $p<0.0001$). Tukey's MC test showed significant differences between naïve vs CFA/PTx (*p=0.0372), naïve vs GAS/CFA (*p=0.0494), naïve vs GAS 4i (****p<0.0001), CFA/PTx vs GAS 4i (*p=0.0212), GAS/CFA vs GAS 4i (*p=0.0158), and GAS 1i vs GAS 4i (***p=0.0003).

mouse brain endothelial cell (mBEC) protein lysate, and by immunofluorescence for binding affinity to fresh frozen brain tissue. These two techniques in combination allow investigation of antibodies that recognize both denatured and native protein structures, which has been a point of note in previous work [205]. Serum IgG from both i.n. and s.c. GAS mice recognize denatured GAS protein lysate, with stronger binding by i.n. GAS sera (**Figure A.3a**). Vehicle control mice do not produce antibodies against GAS. Binding affinity for mBEC lysate would be a clue towards a direct mechanism for antibodies to interact with ECs and cause BBB permeability. When serum

antibodies are reacted with mBEC lysate, some binding is evident in sera samples from i.n. and s.c. GAS-exposed mice, but binding is also clear in uninfected controls (**Figure A.3b**). This indicates that, similar to the human population, anti-EC antibodies are physiologic in a subset of mice [43]. This holds true with human patient data where anti-brain antibodies can be found in ~10% of healthy populations [14, 41].

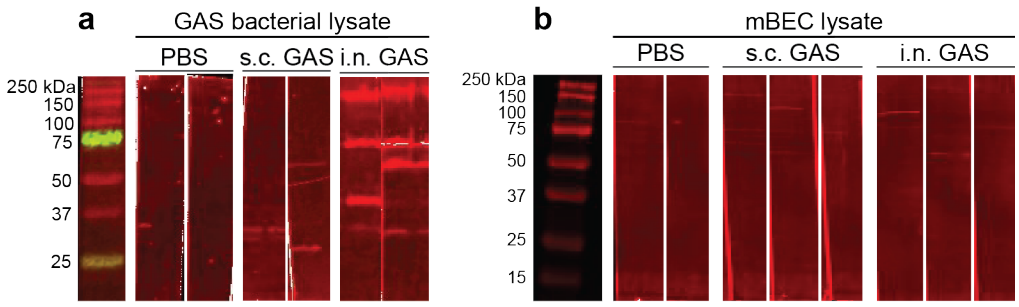

Figure A.3 Sera harvested from i.n. or s.c. GAS-exposed mice react with GAS bacterial proteins and endothelial cell antigens. **a** Western blot where GAS protein lysate is probed with diluted primary mouse sera; PBS-inoculated sera show no binding to GAS proteins on the Western membrane, but s.c. and i.n. GAS-exposed mice show robust generation of polyclonal antibodies against GAS. **b** Mouse brain endothelial cell (mBEC) protein lysate probed with diluted primary sera from PBS control mice do not show reactivity, but sera from s.c. and i.n. GAS-exposed mice do mBEC antigens.

Based on the presence of brain-binding autoantibodies in sera of s.c. GAS-immunized mice, barrier properties were investigated to ascertain whether Ab deposition via a disrupted BBB would be possible after s.c. GAS exposure. BBB integrity was measured using biocytin-TMR i.v. tracer injections after the final boost with GAS/IFA emulsion. **Figure A.4ab** details areas of BBB disruption, which were minimal in this model. Intensity of BBB leakage (i.e., amount of tracer taken up by surrounding brain tissue) was only elevated in the glomerular OB (**Figure A.4c**), compared to mice immunized without GAS homogenate. Permeability to serum IgG provides a measure of transcytotic leakage, and compared to healthy controls, there was no GAS-specific IgG leakage. In **Figure A.4d**, it is clear that there are only very small areas of BBB leakage that are different from vehicle-immunized mice, confirming that adjuvants efficiently permeabilize the

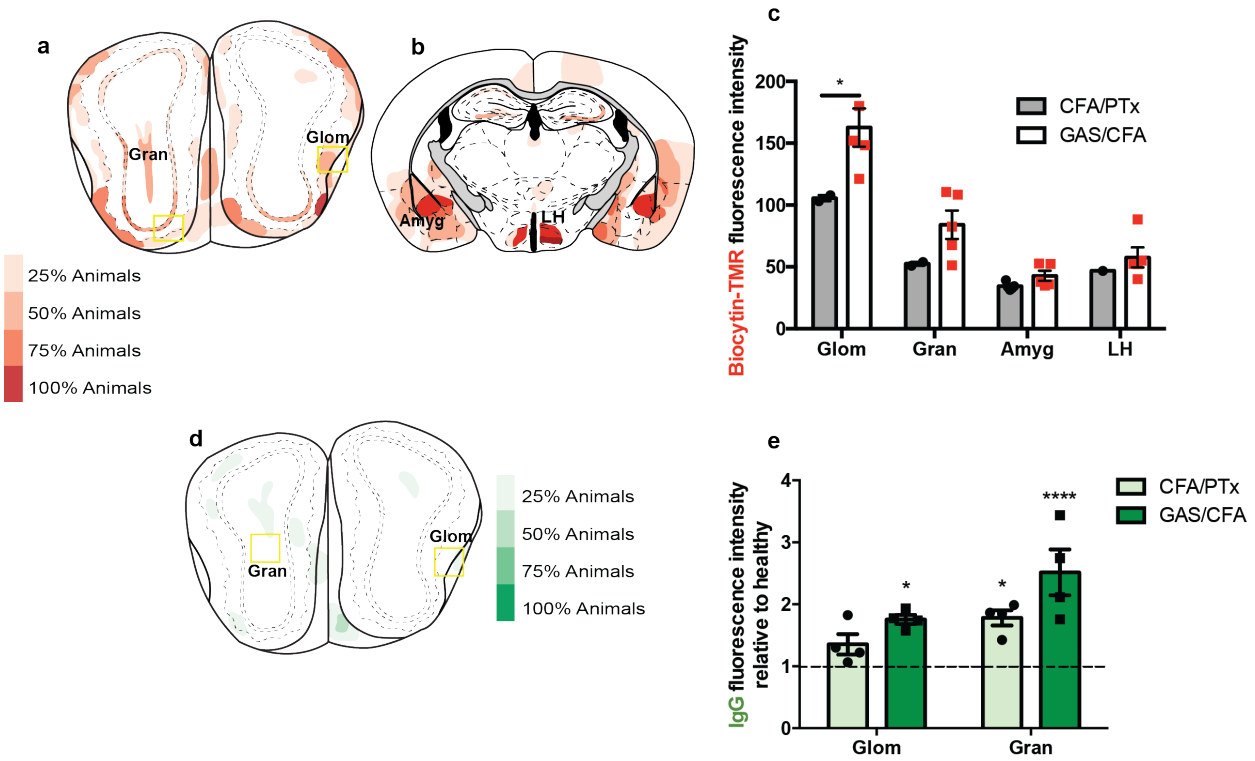

Figure A.4 GAS immunized mice have largely intact BBB. BBB permeability to small molecular weight tracer biocytin-TMR in OB regions **a** and posterior brain **b**. Quantification of tracer deposition intensity **c** shows significant BBB breakdown in OB glomerular regions. Data represent mean ± SEM from *n*=2 CFA/PTx and *n*=5 GAS/CFA mice. Glomerular vessels only were permeable to biocytin-TMR ($F(3,22)=1.926$, $p=0.1548$; OB granular, *$p=0.011$). **d** IgG deposition in GAS-immunized mice was minimal in comparison to both vehicle control and healthy mice. **e** Quantification of IgG deposition intensity immunized mice relative to IgG intensity in healthy controls. Data represent mean ± SEM from *n*=4 healthy, *n*=4 CFA/PTx, and *n*=4 GAS/CFA animals. IgG deposition was largely adjuvant-dependent and not GAS-specific ($F(2,18)=2.25$; glomerular GAS vs healthy, *$p=0.0478$; granular CFA/PTx vs healthy, *$p= 0.0315$; granular GAS vs healthy, ****$p<0.0001$).

BBB. When IgG staining intensity in vehicle- and GAS-immunized mice is normalized to staining intensity in healthy controls, IgG leakage is significantly elevated in the OB of both groups. Again, this confirms an adjuvant vehicle effect with no GAS-specific effect on IgG leakage (**Figure A.4e**). The relatively mild immune infiltration phenotype seen in s.c. GAS immunized mice led us to investigate behavioral phenotypes that have been previously reported [78, 81, 206, 334], as well as testing behavioral outcomes in i.n. GAS inoculated mice.

A.3 Behavioral phenotypes after s.c. or i.n. GAS exposure

Finally, we assessed motor and anxiety-like behaviors in i.n. and s.c. GAS exposed mice to compare published behavioral findings after s.c. GAS immunization with our i.n. GAS inoculation model (**Figure A.5**). While we replicated these assays several times, i.n. GAS-inoculated mice only showed modest alterations in behavior (representative results from one experiment showed here with no significant differences between PBS and GAS inoculated mice). In the open field assay, mice showed no differences in ambulation or pathlength (**Figure A.5a**). Gross motor behavior was intact as assayed by the ladder beam test in which mice cross a horizontal ladder and footslips are counted as errors of either forelimb or hindlimb placement (**Figure AI.5b**). In an attempt to elicit stereotypy or repetitive behaviors, we elicited grooming behavior in the induced grooming task, but found no differences in grooming bout number of bout length in GAS-inoculated mice (**Figure A.5cd**). We then compared performances by healthy unimmunized mice, s.c. CFA/PTx vehicle controls, and s.c. GAS/CFA mice in the same behavioral test battery. In the open field test, vehicle control mice traveled slightly less than healthy mice, with s.c. GAS mice showing a similar but not significant trend towards less ambulation (**Figure A.5e**; healthy vs GAS/CFA, p=0.102). GAS-immunized mice showed some motor deficiencies on the ladder beam, with GAS-immunized mice making significantly more forelimb errors than vehicle controls (**Figure A.5f**). In the induced grooming task, both vehicle and GAS s.c. immunized mice initiated fewer grooming bouts, with no significant change in bout length (**Figure A.5gh**).

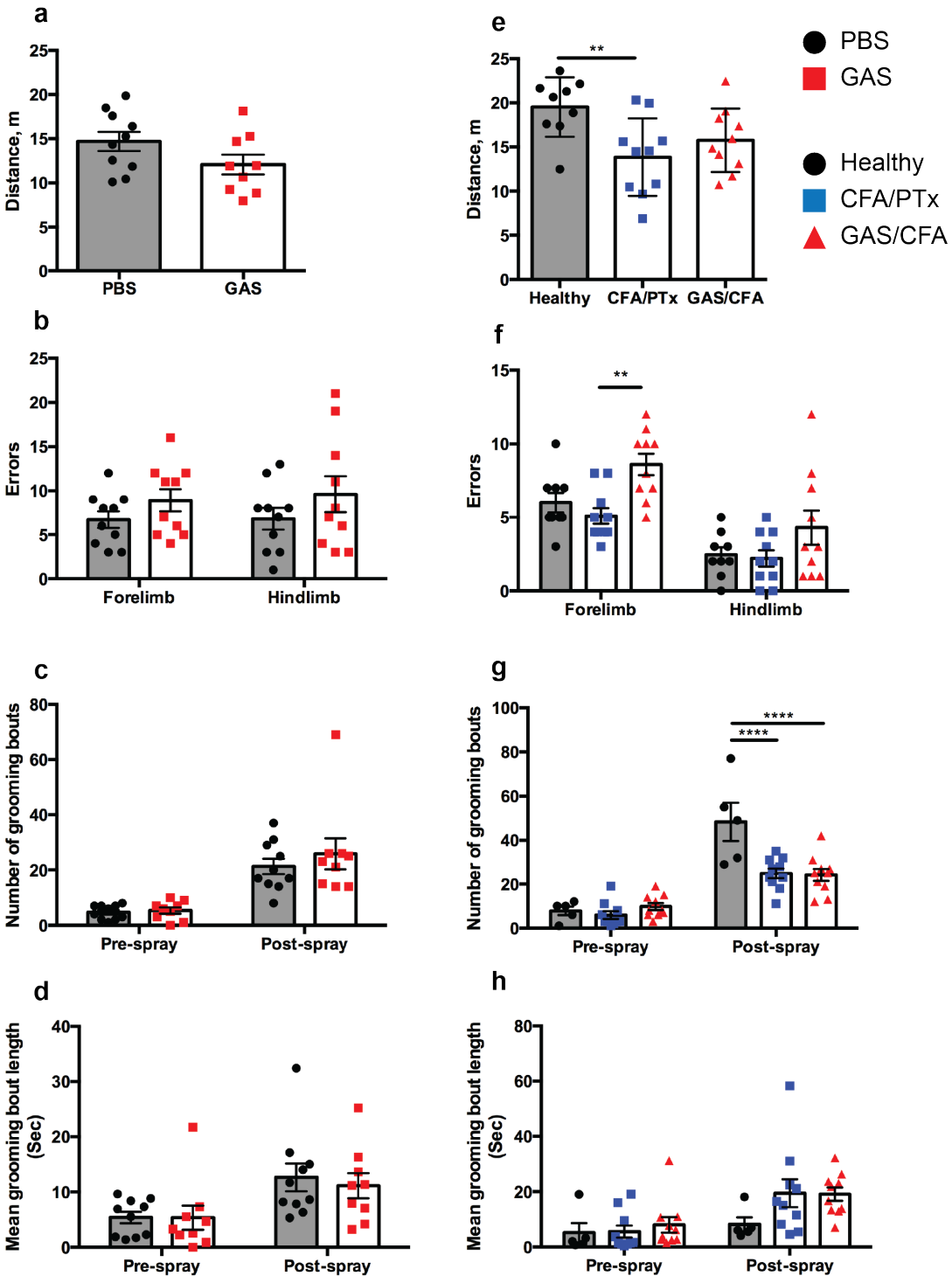

Figure A.5 Behavioral battery in i.n. and s.c. GAS-exposed mice show mild phenotypes. Intranasally-infected mice performed equivalently to controls in the open field (**a**), ladder beam (**b**), and in grooming behaviors elicited by the induced grooming test (**c,d**). Data represent mean ± SEM from n=10 PBS and n=9 GAS mice, symbols denote performance of individual animals. **e** S.c. immunized mice showed a vehicle effect in reduced ambulation in the open field ($F(2,6)=5.35$, $p=0.0113$; healthy vs CFA/PTx **$p=0.0091$). **f** In the ladder beam cross, s.c. immunized mice showed a GAS-specific effect of increased forelimb slips (continued on following page)

(treatment F(2,26)=7.654, p=0.0024; CFA/PTx vs GAS/CFA **p=0.0039). In the induced grooming assay, s.c. immunized mice again showed a vehicle effect **g** on post-spray number of grooming bouts (treatment effect F(2,22)=7.87, p=0.0026; healthy vs CFA/PTx, p<0.0001; healthy vs GAS/CFA, p<0.0001). However, no significant differences were observed in grooming bout length in s.c. immunized mice **h**. Data represent mean ± SEM from *n*=10 healthy, *n*=10 CFA/PTx mice, and *n*=10 GAS/CFA mice; symbols denote performance of individual animals.

A.4 Concluding remarks

In modeling human diseases for study in non-humans, some liberties must be taken in translating human biology into rodents. While no disease model is a perfect recapitulation of human pathology, it is critical to understand the inherent limitations of the animal model [332]. Numerous animal models of multiple sclerosis, Alzheimer's disease, Parkinson's disease, and SLE (in a very abbreviated list of diseases relevant here) exist, which capture various facets of human disease, whether it be genetic contribution to pathology, immune response, behavioral and cognitive outcomes, or vascular pathology. Here, we directly compared the cellular and humoral immune responses, BBB permeability, and behavioral abnormalities elicited by s.c. GAS immunizations and i.n. GAS inoculations.

Our experiments comparing two routes of GAS exposure show that while we confirmed previous reports of a humoral immune response following s.c. GAS immunization [81, 205, 206], the BBB remains impermeable to small molecules and serum IgG, and infiltration of peripheral immune cells is minimal (and not GAS-specific, **Figure A.1c**). Interestingly, $CD4^+$ infiltrate present in immunized mice localized to the choroid plexus, a site of initial immune infiltration in EAE [129]. We did not examine s.c. GAS-immunized animals' spinal cord or cerebellum for pathology, which are affected more by classical EAE [97], and further examination of pathology in these brain regions may indeed show immune infiltrate or serum protein deposition. Neuroinflammation was also attenuated in s.c. GAS immunized mice compared to recurrent i.n. GAS-inoculated mice (**Figure A.2b**). It is possible that neuroinflammation was only present in i.n.

inoculated mice in the OB where we examined microglia carefully, and that s.c. GAS-immunized mice would display microglial activation in other regions; however, our observations indicate that microglia in s.c. GAS immunized mice were ramified and not amoeboid, indicating low inflammation.

One hallmark of AE pathologies is the development of antibodies that cross-react with brain antigens. Sera from GAS-immunized rodents has been shown to colocalize with GAS proteins, and to bind to *ex vivo* brain tissue with native-conformation brain antigens [80-82, 206]. Some groups have illustrated the importance of using CNS antigens in their native conformation rather than denatured samples, as patient-derived autoantibodies are sensitive to tertiary structures of their antigens [1]. Current methods for detecting CNS-specific autoantibodies include cell- and tissue-based assays, Western blots with brain lysate or specific antigens, and ELISA-like plate-based assays [1, 6]. We confirmed that both s.c. and i.n. GAS exposed mice generate robust humoral immune responses targeting GAS, and that a subset of GAS-exposed mice (both s.c. and i.n.) generate antibodies recognizing brain endothelial cell lysate (**Figure A.3ab**). Importantly, anti-endothelial cell antibodies are present in a subset of the healthy population [43], and could represent non-specific inflammation in GAS-exposed animals. More convincingly, sera from GAS-exposed mice react strongly with unfixed, unpermeabilized brain tissue, whereas sera from healthy mice do not react (**Figure A.3cde**). Taken together, our results agree with previous findings of robust, specific anti-GAS and anti-brain humoral antibody responses in GAS-exposed mice, and with BBB permeability, is likely that cross-reactive anti-brain antibodies could interfere with neuronal function.

Vascular pathology in EAE begins before onset of disease, and the endothelium is permeable to Th17 cells quite early in disease course. Adjuvants used to immunize mice may

promote BBB permeability after s.c. GAS immunizations. Our results indicate that even after recurrent exposures to s.c. GAS and adjuvants, BBB permeability to the small molecular weight tracer biocytin-TMR is mild, and only deposited significantly in the OB glomerular layer (relative to CFA/PTx controls, **Figure A.4abc**). By contrast, there is an adjuvant effect on permeability to IgG, where both vehicle control and s.c. GAS immunized mice show increased IgG deposition compared to healthy mice in examined regions. These results support differential breakdown of the BBB to different size molecules, but compared to massive BBB permeability seen in i.n. GAS inoculated animals, vascular pathology in s.c. immunized mice was relatively mild.

Finally, behavioral tests showed that GAS-exposed mice had mild motor deficits on the ladder beam. GAS-immunized mice also showed mild anxiety-like phenotypes by burying more marbles than vehicle control mice, but this phenotype did not extend to repetitive behaviors assayed by the induced grooming task. To play the devil's advocate, positive results showing motor deficits in s.c. immunized mice could be due to site of injection chosen for our immunizations. We immunize for EAE and for s.c. GAS boosts in the chest, near axillary lymph nodes. In behaviors dependent on forelimb strength or walking, immunized mice may be showing deficits simply because they have large boli of emulsion on their chests. The fact that some of these findings are GAS-specific and not solely an effect of vehicle lends some weight, however, and our findings largely concur with previous reports showing motor deficits after s.c. GAS immunization or intracerebral infusion of autoantibodies. Thus, the s.c. route of GAS exposure may be a better model for the humoral immune response and circuit-level changes in behavior, but careful choice of immunization site should be considered. The s.c. GAS model is unfit for studies of how the immune response to GAS infections changes with repeated exposures, as the cellular immune system remains largely unaffected in these mice.

These experiments support validation of findings in multiple disease models, and highlight the vast differences in pathology induced by different routes of GAS exposure. It is possible that, like in EAE, pathology induced by s.c. GAS is more pronounced in the spinal cord, but given that spinal circuits were not grossly affected (MPP, personal observation), this seems unlikely. The time scale for autoantibodies generation, as well as potential changes in splenic T and B cell population remains unclear. A combined approach where i.n. and s.c. GAS are administered to the same animal may yield synergistic effects on both immune response in the CNS and behavioral changes. Future work that more closely examines changes in the B cell and plasma cell populations in both models are warranted.

Appendix B: Dendritic cells infiltrate the CNS after recurrent GAS inoculations

B.1 Dendritic cell populations increase in anterior brain after GAS infections

Dendritic cells (DCs) are the professional antigen presenting cells (APCs) of the adaptive immune system, surveying the body for foreign peptides and returning to draining lymph nodes to synapse with naïve T and B cells. This directs the effector populations to target foreign epitopes. In terminal tissues, DCs maintain T and B effector populations in situ by refreshing their antigen direction [335]. After recurrent GAS inoculations, T cells persist in the brain up to 8 weeks after the final infection. T cells should not remain in a tissue for that long without an APC to refresh their direction; after neutralizing the infection, lymphocytes exit the tissue or undergo apoptosis.

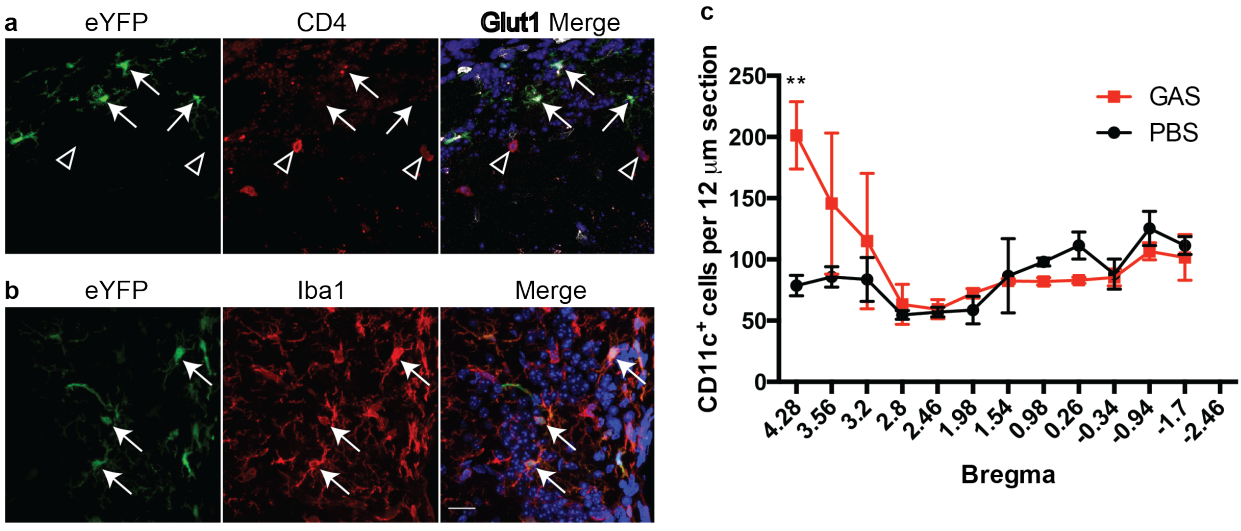

Figure B.1 Dendritic cell populations increase the CNS after recurrent GAS inoculations. **a** Immunohistochemistry for transgenic eYFP reporter shows that infiltrating DCs (green, arrows) are in close proximity to infiltrating $CD4^+$ T cells (red, open arrowheads) and not vascular (labeled with Glut1, white). **b** Immunohistochemistry for transgenic eYFP reporter shows that infiltrating DCs (green, arrows) colocalize with a subset of microglia (Iba1, red) in OB brain sections. **c** Quantification of eYFP+ DCs in brain sections shows that DCs infiltrate the brain after recurrent GAS inoculations, elevated from basal populations present in PBS controls. Data represent mean ± SEM from n=3 PBS and n=3 GAS mice. Two-way ANOVA reveals a significant main effect of bregma ($F(11,44)=3.257$, $p=0.0025$), as well as an interaction between treatment and bregma ($F(11,44)=2.335$, $p=0.0231$). Sidak's MC test shows a significant difference with treatment at bregma +4.28 (**$p=0.0012$). Scale bar = 20 μm.

We hypothesized that DC populations may be responsible for maintaining the T cell presence in the CNS for an extended period of time. To examine DC populations in mice, we

utilized the *CD11c-eYFP* transgenic line, in which eYFP is inserted in the genome under the control of the dendritic cell-specific promoter CD11c. We performed recurrent inoculations with either GAS or vehicle in this mouse line, then examined both T lymphocyte and dendritic cell populations in the brain. GAS-inoculated mice showed a specific increase in DC populations in anterior brain regions compared to vehicle control mice, indicating that they are possibly recruited to the OB along with T cells to maintain the CNS lymphocyte population (**Figure B.1**).

Next, we assessed T cell counts in parallel with DC numbers in GAS-inoculated mice. Here, it was clear that DC populations roughly correlated with T lymphocyte infiltration. In anterior brain regions where the most T cells are observed, DC populations are also elevated (**Figure B.2**). In posterior brain regions, however, T cell numbers rapidly fall, while DC populations stabilize at their baseline counts (as determined in **Figure B.1**).

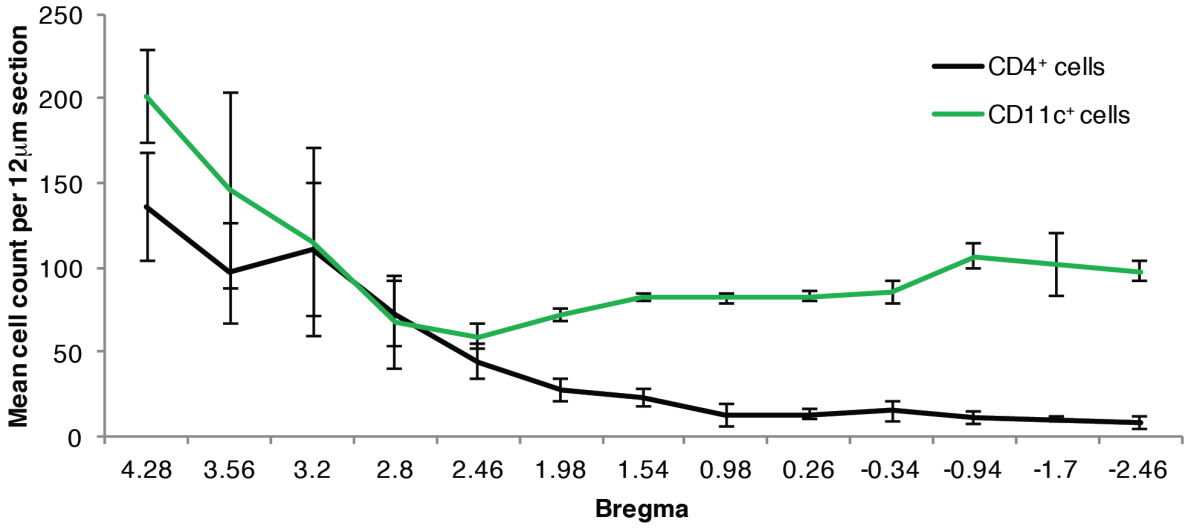

Figure B.2 T cell and dendritic cell populations are present in GAS-inoculated mice. T cell counts (black line) are elevated anteriorly in GAS-inoculated mice, and dendritic cell numbers (green line) are elevated in similar regions. Data represent mean ± SEM from n=3 GAS-inoculated mice.

B.2 Concluding remarks

Our data here agree with published studies reporting basal levels of $eYFP^+$ dendritic cells distributed throughout the brain [336, 337]. We found $eYFP^+$ DCs in the brains of both PBS control and GAS-inoculated mice, although there was an increase in DC numbers in OB brain sections. These data were collected from mice sacrificed at 48 h after the final infection. To investigate a role for DCs as potential APCs in the CNS, it will be important to verify their continued presence in the brain at longer time points. These experiments also present the opportunity to compare and contrast DC trafficking after GAS inoculations to what has been reported in EAE [146, 192, 201, 202].

Appendix C: T cells localize along olfactory axon tracts after recurrent GAS inoculations

C.1 Olfactory axon tracts connect OE with OB

Recurrent GAS inoculations in mice induce expanded T lymphocyte populations in the cervical lymph nodes (CLN), nose-associated lymphoid tissue (NALT, structural analog of the human tonsils and adenoids), and brain. $CD4^+$ T cell populations recruited to NALT and olfactory bulb express similar cytokine profiles comprised of mainly IL-$17A^+$ IFNγ^+ and IL-$17A^+$ lymphocytes; however, $CD4^+$ T cells from the CLN express mainly IFNγ [93]. This suggests that

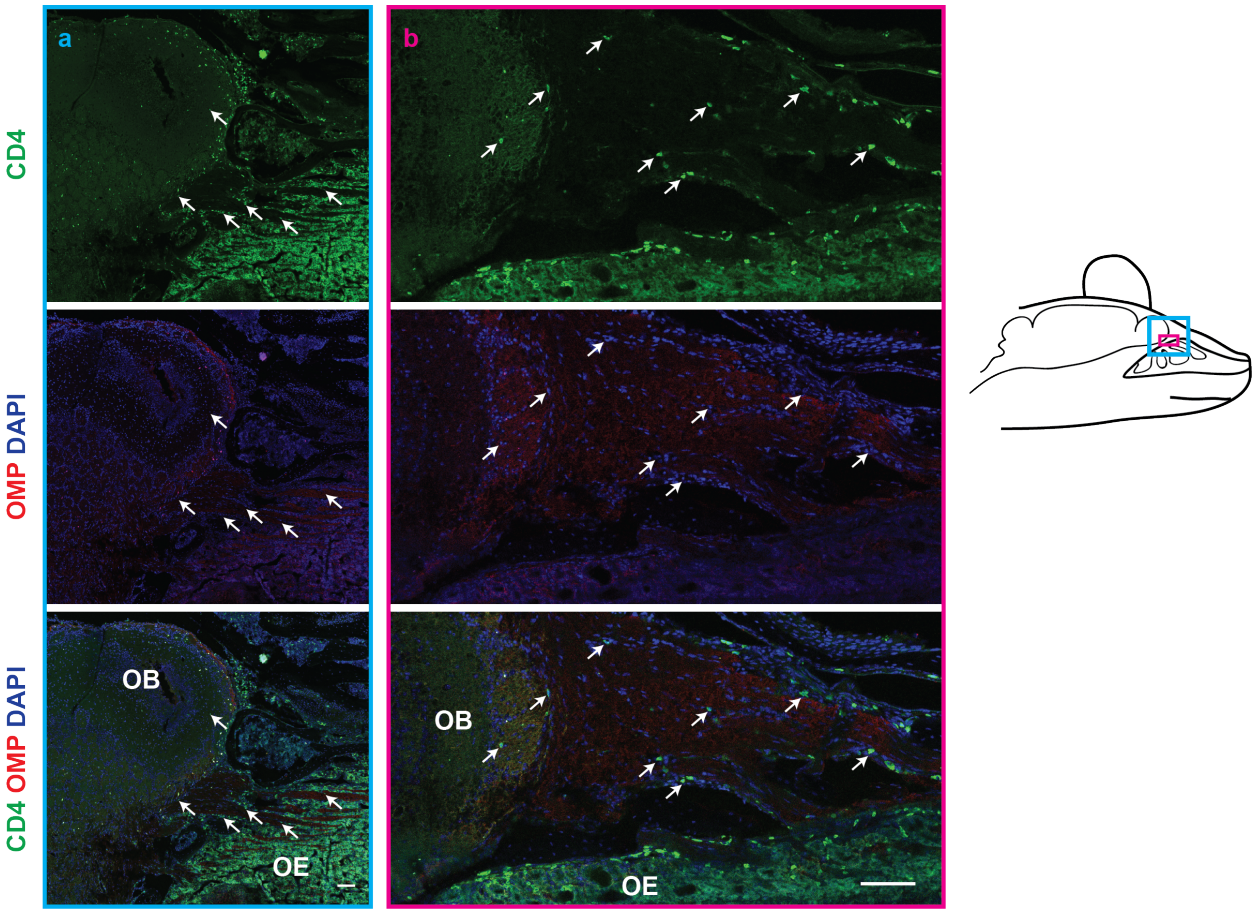

Figure C.1 Infiltrating T cells localized along olfactory sensory axon tracts. Contiguous olfactory bulb (OB) and olfactory epithelia (OE) tissue sections stained for $CD4^+$ T cells (green) and olfactory marker protein (OMP, red) show T cells localized mainly to the outer sheath of olfactory sensory axon tracts. **a** Large axon tracts contain many T cells (arrows), although mainly on the perimeter of the axon bundles, and **b** Smaller field of view image shows T cells interspersed within axon bundles and along the outside of tracts. Cyan and magenta rectangles in the schematic at right denote approximate location of images in **a** and **b**. Images are representative of n=3 GAS-inoculated *ROR*$\gamma t^{+/-}$ mice.

T cells that are recruited to the nose and secondary lymphoid tissue (NALT) migrate to the CNS, and that CLN lymphocytes are draining lymph nodes for Th1 cells from the olfactory epithelium. $CD4^+$ T cells were also detected primarily in anterior brain regions, concentrated in the olfactory bulb.

We hypothesized from these data that T lymphocytes were recruited to the site of infection in the nose and differentiated in the NALT, then migrated along olfactory sensory axon tracts that extend from the OE through the cribriform plate into the OB. Access to the brain via the olfactory route has been reported for a wide range of cargo, including peptides, small molecule drugs, viruses, bacteria, and therapeutic stem cell delivery [50, 138, 144, 145]. Convection in perivascular spaces is thought to underlie this, and delivery of biologics depends on cargo size and nasal epithelial permeability [144]. T cells are roughly uniform in size, and could conceivably traffic via this route. We assessed the feasibility of this process in a pilot experiment in which $ROR\gamma t^{+/-}$ mice were inoculated with GAS, then sacrificed at 24 h after the final infection. Skulls were dissected such that olfactory epithelia remained contiguous with the brain; skulls were then bisected sagitally and sectioned parallel to the plane of incoming olfactory axons.

C.2 Concluding remarks

Following recurrent GAS inoculations, $CD4^+$ T cells were seen in dense collections in the olfactory epithelium, within the OB, and in axon tracts connecting OE and OB (**Figure C.1**). While this data is not conclusive evidence that T cells travel from nose to brain, and not the reverse (as has been reported in EAE using newly formed lymphatic vessels [192]), it demonstrates proof-of-concept for continued investigations. Further studies should examine localization of T cells within $LYVE1^+$ lymphatics along olfactory sensory axons, proximity to blood vessels and perivascular

spaces, and whether axonal trafficking is an intrinsic property of the T cells recruited to the brain (as assessed with adoptive transfer experiments). Of course, live imaging studies would provide more conclusive evidence of both directionality of T cell flux and the speed with which lymphocytes travel along this route. Signaling pathways, including chemokine ligands, controlling this transit could also be more conclusively determined using live imaging studies. It remains to be seen whether immune cells can be seen along olfactory axons in uninfected mice, but given the relatively lower (but not absent) lymphocyte populations in uninfected olfactory epithelium, it seems likely that lymphocyte populations will be restricted to the OE. In conclusion, this work represents a proof of concept that T cells can be seen in bulk transit along olfactory sensory axons. More work is needed to determine the contribution of this pathway during T cell infiltration compared to vascular diapedesis, as well as signaling molecules that may guide T cells to home along this route to the brain.